

Earth Pressure on Walls Retaining Overconsolidated Cohesionless Soil Using the Concept of Critical State Soil Mechanics

Sergio Esteban Rosales Garzón

A Thesis
In the Department
of
Building, Civil and Environmental Engineering

Presented in Partial Fulfillment of the Requirements
For the Degree of
Doctor of Philosophy (Civil Engineering) at
Concordia University
Montreal, Quebec, Canada

June 2021

© Sergio Esteban Rosales Garzón, 2021

CONCORDIA UNIVERSITY
SCHOOL OF GRADUATE STUDIES

This is to certify that the thesis prepared

By: Sergio Esteban Rosales Garzón

Entitled: Earth Pressure on Walls Retaining Overconsolidated Cohesionless Soil Using the
Concept of Critical State Soil Mechanics

and submitted in partial fulfillment of the requirements for the degree of

DOCTOR OF PHILOSOPHY (Civil Engineering)

complies with the regulations of the University and meets the accepted standards with respect to
originality and quality.

Signed by the final examining committee:

_____ Chair
Dr. R. Sedaghati

_____ External Examiner
Dr. P. Guo

_____ External to Program
Dr. K. Skonieczny

_____ Examiner
Dr. B. Li

_____ Examiner
Dr. A. M. Zsaki

_____ Thesis Supervisor
Dr. A. M. Hanna

Approved by _____
Dr. Michelle Nokken, GPD, Department of Building, Civil & Environmental Engineering

Month/day/year _____
Dr. Mourad Debbabi
Dean, Gina Cody School of Engineering and Computer Science

Abstract

Earth Pressure on Walls Retaining Overconsolidated Cohesionless Soil Using the Concept of Critical State Soil Mechanics

Sergio Esteban Rosales Garzón, Ph.D.
Concordia University, 2021

The plane-strain (PS) critical-state (CS) friction angle is an important soil parameter in the design of several geotechnical projects. The static angle of repose, which is known to be the same as the PS-CS friction angle for normally consolidated cohesionless soil (NC), and the associated initial constant-volume friction angle were measured for three granular materials in the laboratory to validate the *flow rule* that accounts for dilatancy and accordingly the *pore pressure coefficient* A . To derive the *flow rule*, the law of conservation of energy and limit equilibrium technique were used to develop a bidimensional micromechanical model representing granular media in CS. The *flow rule* was then used to predict the at-rest coefficient $K_{\theta-OC}$ and theoretical porosity thresholds for the contractive, dilative, and collapsible behavior. The lateral stresses of silica sand under the standard and modified *Proctor energies of compaction*, and non-compacted, were measured in the laboratory for different D_r and OCR to validate the proposed $K_{\theta-OC}$. As a by-product of the previous finding, a new methodology to determine OCR in compacted backfills was developed. For the active and passive states, the variational limit equilibrium method applied on NC dry granular media and the PS-CS friction angle were adopted to derive the *nonlinear geometry of the slip-failure surface* and the associated *nonlinear coefficients* K_a and K_p . The present micromechanical model was further used to develop a numerical approach to model the *stress-strain path* and determine the *minimum wall rotation* required to develop PS-CS failure. Practical application, and design framework were prepared for various spreadsheets and illustrative examples.

Acknowledgement

My sincere gratitude to my supervisor Dr. Adel M. Hanna. He saw potential in my early idea and helped me to transform it into a thesis. His immense knowledge and vast experience in foundation engineering has substantially enriched this outcome. Thanks to his limitless generosity, his wisdom and experience were always available in many ways in the form of enlightening advice and opportune guidance to better navigate through this program. I feel proud of having him as my supervisor and professor, without him this research would not have been possible. Dr. Hanna, thank you for opening your residence to me and being there all the time during the ongoing pandemic, encouraging me to progress and complete this study despite the new limitations.

I would like to thank my colleagues Mahmoud Khalifa and Bayan Abu Safieh at Concordia University, for their calid welcoming to the research office and the various discussions that helped me settle and orient my research and TA work. Especially, I would like to thank Farhad Nabizadeh for that spontaneous kind initial introduction to the research laboratory at Concordia University.

Financial support from the Natural Sciences and Engineering Research Council of Canada (NSERC) and Concordia University is gratefully acknowledged.

Finally, my appreciation to my wife Lina Montoya for her encouragement and advice all along this journey.

Table of Content

List of Tables	xiii
List of Figures	xvi
List of Symbols	xxvii
Chapter 1: Introduction.....	1
1.1. General	1
1.2. Problem Statement	1
1.3. Motivations and applications	2
1.3.1. Development of a critical state soil mechanics CSSM model for sand	2
1.3.2. An explicit derivation	3
1.3.3. Overconsolidation	3
1.3.4. Deformation	3
1.3.5. To whom this research is directed	3
1.4. Objectives.....	3
1.5. Delimitation of the proposed explicit solution.....	4
1.6. Organization of Thesis	4
Chapter 2: Literature Review.....	7

2.1.	General	7
2.2.	Shear strength of granular cohesionless soils.....	8
2.3.	The angle of repose	12
2.3.1.	Measurement of the angle of repose	14
2.3.2.	Factors influencing the measurement of the angle of repose.....	20
2.3.3.	Theoretical relationship between the developed constant-volume friction angle and the interparticle sliding friction angle.....	21
2.3.4.	Experimental relationship between the developed constant-volume friction angle and the interparticle sliding friction angle.....	24
2.3.5.	Discussion on the angle of repose.....	27
2.4.	Prediction of lateral earth pressure.....	28
2.4.1.	Classical theory	28
2.4.2.	Analytical approaches	32
2.4.3.	Empirical approaches.....	42
2.4.4.	Limitations of existing methods.....	48
2.4.5.	Descriptive experimental work on lateral earth pressure.....	49
2.4.6.	Discussion on lateral earth pressure.....	55
2.5.	Critical state: fundamental concepts and actual practice	59

2.5.1.	Concept of critical state soil mechanics CSSM	59
2.5.2.	The micromechanical approach	59
2.5.3.	Stress-dilatancy relationship	60
2.5.4.	Actual practice for the measurement of the plane-strain critical state friction angle $\phi'_{cs,ps}$	61
2.5.5.	Actual practice for the measurement of the interparticle sliding friction angle ϕ'_{μ}	63
2.6.	General conclusion from the literature review	66
Chapter 3: Experimental Investigation		68
3.1.	General	68
3.2.	Silica Sand: basic properties	69
3.3.	Experimental investigation for critical state.....	73
3.3.1.	General.....	73
3.3.2.	Methodology of the experimental tests for critical state shear strength parameters.....	74
3.3.3.	Experimental Results	86
3.3.4.	Discussion on the role of the energy of placement based on the analysis of own experimental Results.....	91
3.4.	Experimental investigation for the at-rest lateral earth pressure incorporated with the overconsolidation ratio OCR	93

3.4.1.	General.....	93
3.4.2.	Methodology of the experimental tests for lateral stress measurement.....	93
3.4.1.	Experimental results.....	100
Chapter 4: A Critical State Soil Mechanics Plane-Strain Model for Cohesionless Soils: Derivation and Verification		
		105
4.1.	General	105
4.2.	A new theoretical model for critical state	105
4.2.1.	General definition	105
4.2.2.	New theoretical derivation for the relationship or <i>flow rule</i> between the plane-strain critical state friction angle $\phi'_{cs,ps}$ and the plane-strain constant-volume friction angle $\phi'_{cv,ps}$ 106	
4.2.3.	Porosity	117
4.2.4.	Pore pressure coefficient.....	119
4.2.5.	Critical state shear strength and critical state porosity in natural sands correlated to present <i>flow rule</i> in Eq. (4-9).....	125
Chapter 5: At-rest Lateral Earth Pressure Coefficient K_0 and K_{0-OC}		
		128
5.1.	General	128
5.2.	Derivation of K_0	128

5.2.1.	Validation of present expression (5-3) for K_{θ} with existing experimental results	132
5.3.	Derivation of $K_{\theta-OC}$	136
5.3.1.	Validation of present expression (5-7) for $K_{\theta-OC}$ with existing experimental results	139
5.4.	Experimental verification of present expressions for K_{θ} (5-3) and $K_{\theta-OC}$ (5-7).....	142
5.5.	Experimental determination of the $\sigma'_{v,max}$ corresponding to the standard, the reduced modified and the modified Proctor energies of compaction in silica sand	144
5.6.	Conclusion.....	147
Chapter 6:	Active and Passive Coefficients of Lateral Earth Pressure K_a and K_p	151
6.1.	General	151
6.2.	K_a and K_p in a wall backfill under plane-strain critical state failure	151
6.3.	K_a and K_p incorporated with the OCR effect	164
6.4.	Conclusion.....	165
Chapter 7:	Stress–Strain: A CSSM Plane-Strain Incremental Numerical Model.....	166
7.1.	General	166
7.2.	Incremental <i>flow rule</i>	166
7.3.	The principal stress ratio $(\sigma'_1/\sigma'_3)_f$ at plane-strain constant–volume failure of a prismatic soil element	167

7.4.	Stress–strain simulation of the critical state plane-strain case ($\epsilon_2=0$)	169
7.4.1.	Stress–strain and other characteristic paths according to present CSSM incremental model for cohesionless soil.....	171
7.4.2.	Validation of the Stress–Strain incremental model with existing experimental results 175	
7.5.	Conclusion.....	177
Chapter 8:	Practical Applications of Present Design Theory	179
8.1.	General	179
8.2.	Methodology to determine soil parameters according to present CSSM framework ..	179
8.3.	Soil parameters from laboratory testing	182
8.4.	Design criteria for the lateral earth pressure acting against a retaining wall	186
8.5.	Example problems.....	187
8.5.1.	Problem #1: At-rest lateral earth pressure	187
8.5.2.	Problem #2: Active lateral earth pressure	191
8.5.3.	Problem #3: Passive lateral earth pressure.....	195
8.5.4.	Problem #4: wall rotation Δ_x/H for active lateral earth pressure	199
8.5.5.	Problem #5: wall rotation Δ_x/H for passive lateral earth pressure	203
Chapter 9:	Conclusion and Recommendations.....	208

9.1. General	208
9.2. Main conclusion	209
9.3. Specific conclusions	210
9.4. Recommendation for Future Work	215
References	216
Appendices	236
Appendix A Critical Review of the Empirical K_0 Since (Jaky, 1944).	237
Appendix B Proof of Coincidence Between Common Solutions According to (Coulomb, 1776) and (Rankine, 1857).....	250
Appendix C Comparison of Lateral Earth Pressure Distribution and Slip-Failure Geometry Between Present Theory and Classical Theory According to (Coulomb, 1776) or (Rankine, 1857). 253	
Appendix D Video Recording of the Plane-Strain Constant-Volume Friction Angle Tests.....	259
Appendix E Video Recording of the Plane-Strain Critical-State Friction Angle Tests.....	260
Appendix F Video Recording of the Angle of Repose Tests in Silica Sand.	261
Appendix G Spreadsheet to Calculate $\sigma'_{v,max}$ from Experimental Results for K_{0-OC}	262
Appendix H Spreadsheet to Calculate Nonlinear Slip-Failure Surface and Lateral Stress Distribution Geometry.	265

Appendix I Spreadsheet Implanted with Present CSSM Plane–Strain Numerical Simulation for
Granular Cohesionless Soil..... 268

List of Tables

Table 2-1 Summary of assumptions and predictions of various analytical approaches for at-rest earth pressure.	57
Table 2-2 Summary of assumptions and predictions of various analytical approaches for active and passive earth pressures.	58
Table 3-1 Summary of the experimental program developed for present research.	69
Table 3-2 Silica sand physical properties adopted from (Alharthi, 2018).	71
Table 3-3 Relative density and corresponding angle of shearing resistance for silica sand 40-10 adopted from (Alharthi, 2018).	71
Table 3-4 Compressibility properties for silica sand adopted from (Hanna and Diab, 2017).	72
Table 3-5 Summary of the experimental investigation program to validate the theoretical model for critical state.	75
Table 3-6 Summary of experimental results for critical state shear strength parameters.	86
Table 3-7 Experimental results for plane-strain constant-volume friction angle $\phi'_{cv,ps} = \phi'_\mu$ on UHMW Polyethylene materials, silica sand and P50 sandpaper.	88
Table 3-8 Experimental results for the angle of repose β using the fixed base and funnel device on silica sand (see <i>Appendix F</i>).	92
Table 3-9 Summary of experimental research program for earth pressure in silica sand.	94
Table 3-10 Data collected for the calibration of each pressure sensor.	98
Table 3-11 Model properties for the four samples of silica sand.	102
Table 3-12 Experimental results for the non-compacted silica sand sample.	103
Table 3-13 Experimental results for silica sand compacted under the standard Proctor energy.	103

Table 3-14 Experimental results for silica sand compacted under the reduced modified Proctor energy.....	104
Table 3-15 Experimental results for silica sand compacted under the modified Proctor energy.....	104
Table 4-1 <i>Flow rule</i> results from Eq. (4-9) versus results from (Sadrekarimi and Olson, 2011).	114
Table 4-2 Other <i>flow rules</i> compared with present theory in Eq. (4-9).....	116
Table 5-1 Theoretical $\emptyset'_{ol}/\emptyset'_{cv}$ ratios for the interval of naturally occurring soils according to the present study.	134
Table 5-2 Experimental verification of present expressions for K_{θ} Eq. (5-3) and $K_{\theta-OC}$ Eq. (5-7) on a non-compacted sample of silica sand.....	144
Table 5-3 Experimental determination of the maximum historic vertical consolidation stress $\sigma'_{v,max}$ equivalent to the standard Proctor energy.....	146
Table 5-4 Experimental determination of the maximum historic vertical consolidation stress $\sigma'_{v,max}$ equivalent to the modified Proctor energy.....	146
Table 5-5 Experimental determination of the maximum historic vertical consolidation stress $\sigma'_{v,max}$ equivalent to the reduced modified Proctor energy.....	147
Table 7-1 Types of soil behavior according to present CSSM incremental model.	172
Table 8-1 Results from Eq. (8-2) compared to existing experimental results on natural sand from (Hanna, 2001).	185
Table 8-2 Problem #1: summary of results per unit length of wall.	190
Table 8-3 Problem #2: summary of results per unit length of wall.	194
Table 8-4 Problem #3: summary of results per unit length of wall.	197
Table 8-5 Problem #4: summary of results for dense sand under active state.....	201

Table 8-6 Problem #4: summary of results for loose sand under active state. 202

Table 8-7 Problem #5: summary of results for dense sand under passive state. 205

Table 8-8 Problem #5: summary of results for loose sand under passive state. 206

List of Figures

Fig. 2-1 Components of friction for a granular soil.....	9
Fig. 2-2 Porosity-dependant character of shear resistance as observed in experimental works: (a) according to (Bjerrum et al., 1961); and (b) according to (Sadrekarimi and Olson, 2011).....	11
Fig. 2-3 Measuring the repose angle β in a pile of granular material adapted from (Wu and Sun, 2008, p. 15).	14
Fig. 2-4 Method of loading simulated measuring box. 1: box, 2: pressure piston, 3: weight, 4: sluice and 5: slope of granular material. Adopted from (Wu and Sun, 2008, p. 16).	15
Fig. 2-5 Method of bottomless or hollow cylinder. 1: cylinder, 2: granular material. Adopted from (Wu and Sun, 2008, p. 16).	16
Fig. 2-6 Method of fixed funnel adopted from (Wu and Sun, 2008, p. 17).....	17
Fig. 2-7 Method of moving funnel adopted from (Li et al., 2005, p. 225).	17
Fig. 2-8 Method of fixed base from (Miura et al., 1997, p. 93).....	18
Fig. 2-9 Method of rotary box. 1: box, 2: frame of box, 3: rotary axis and 4: fixation plate. Adopted from (Wu and Sun, 2008, p. 17).	19
Fig. 2-10 Method of tilting cylinder adopted from (Santamarina and Cho, 2001, p. 187): (a) pour soil in a 1000 ml cylinder with water; (b) rotate the cylinder passed 60° ; (c) slowly return the cylinder to its vertical position and measure the angle of repose; and (d) the angle is measured in the middle region on the slope.	20

Fig. 2-11 Theoretical relationship between the angle of interparticle sliding friction θ'_μ and the developed constant-volume friction angle θ'_{cv} 23

Fig. 2-12 experimental setup for measuring kinetic sliding friction. A: car full of fixed particles, B: base made of the same material composing the particles adapted from (Li et al., 2005). 25

Fig. 2-13 Mobilization of passive resistance according to the Log-Spiral Hyperbolic (LSH) procedure since (Shamsabadi et al., 2007, p. 708): (a) force-displacement relationship; and (b) stress-strain relationship..... 38

Fig. 2-14 Measured diagrams of lateral earth pressure at rest on a stiff wall. 1: backfill at elevation -8.9 m; 2: backfill at elevation -6.5 m; 3: backfill at final elevation 0.00; 4: 10 months later after competition of wall backfill; 5: calculated from equation (2-39). Adopted from (Lazebnik and Tsinker, 1997, p. 202). 49

Fig. 2-15 Detection of the failure surface geometry:(a) as plotted on the shear strain map; and (b) as idealized. Adopted from (Cinicioglu et al., 2015). 50

Fig. 2-16 Path of the failure surface after (Stewart et al., 2011, p. 74)..... 54

Fig. 2-17 Components of a model viewing the concept of CSSM. 59

Fig. 2-18 Soil as an assemblage of particles, the main assumption of the micromechanics approach: (a) interparticle network of contact forces, illustrative imagen adopted from (Santamarina and Shin, 2009); (b) illustrative uniform packing investigated by (Rowe, 1962); and (c) DEM model of a polydisperse packing investigated by (Jerves and Andrade, 2016). 60

Fig. 2-19 Common techniques for the measurement of the plane-strain critical state friction angle $\phi'_{cs,ps}$ through the measurement of the static angle of repose β 63

Fig. 2-20 Scanning electron microscope micrograph of a glass microsphere mounted on an AFM cantilever beam. Illustrative imagen adopted from (Tyrrell and Cleaver, 2001)..... 64

Fig. 2-21 General scheme of inter-particle loading apparatus: (a) illustrative sketch adopted from (Senetakis and Coop, 2014); and (b) illustrative photo of the contact between the two tested particles adopted from (Senetakis et al., 2013). 65

Fig. 2-22 Experimental setup for the measurement of the interparticle sliding friction angle ϕ'_μ : (a) measurement based on forces; and (b) measurement based on the sliding angle. A: test block full of fixed artificial particles, B: base having the same sliding friction of the particles; illustrative sketch adopted from (Li et al., 2005). 66

Fig. 3-1 Particle size distribution for silica sand 40-10 adopted from (Alharthi, 2018)..... 70

Fig. 3-2 Relative density and corresponding angle of shearing resistance adopted from (Alharthi, 2018). 72

Fig. 3-3 Theoretical domain for the angle of shearing resistance contrasting the narrow window offered by natural sands only with the wider window that can be accessed if artificial granular materials are involved. 73

Fig. 3-4 Automatic rotary box: (a) conceptual cross-sectional sketch; (b) actual lateral view. ... 76

Fig. 3-5 Final vertical position of the rotary box showing the angle of repose β in the sub-step #6 (of the sequence shown in Fig. 3-6) corresponding to a single test for each of the three cohesionless granular materials: (a) UHMW polyethylene; (b) silica sand; and (c) P50 sandpaper. 78

Fig. 3-6 Illustrative sequence used to approach the plane-strain critical state friction angle by means of the static angle of repose $\beta = \phi'_{cs,ps}$ using the automatic flat-angle-of-repose-device.. 80

Fig. 3-7 *Fixed base* and *moving funnel* device after a single test on silica sand. 81

Fig. 3-8 Friction tester during a single tilt-test for measuring sliding friction in silica sand..... 82

Fig. 3-9 Blocks of silica sand: (a) front view of six actual blocks of silica sand prepared for sliding friction test on a 1 cm \times 1 cm grid; (b) block dimensions in millimeters in lateral view. 83

Fig. 3-10 Blocks of artificial materials on a grid 1 cm x 1 cm: (a) UHMW polyethylene; (b) P50 sandpaper. 85

Fig. 3-11 Experimental result for the plane-strain critical state friction angle $\phi'_{cs,ps}$ of artificial particles coated with UHMW polyethylene (see *Appendix E*). 89

Fig. 3-12 Experimental result for the plane-strain critical state friction angle $\phi'_{cs,ps}$ of silica sand (see *Appendix E*). 90

Fig. 3-13 Experimental result for the critical state friction angle $\phi'_{cs,ps}$ of artificial particles coated with P50 sandpaper (*Appendix E*). 90

Fig. 3-14 Conceptual trend between the energy of particle accommodation and the angle of repose β from the experimental results on silica sand (see Table 3-8 and numeral 3.3.3.2). 92

Fig. 3-15 Experimental setup to measure lateral stress: (a) conceptual sketch; and (b) actual setup. 95

Fig. 3-16 Dimensions of the pressure cell in millimetres: (a) plan view; and (b) section A-A'... 95

Fig. 3-17 Calibration of the sensor PSR # 3. From left to right appears the datalogger, the two aneroid manometers and the pressure cell. 97

Fig. 3-18 Correlation fit between voltage and horizontal pressure for the sensor PSR # 1..... 99

Fig. 3-19 Correlation fit between voltage and horizontal pressure for the sensor PSR # 2..... 99

Fig. 3-20 Correlation fit between voltage and horizontal pressure for the sensor PSR # 3..... 100

Fig. 4-1 Sketch of the theoretical model for the angle of repose: (a) left half of a pile of particles; (b) deformation mechanism of the unitary pack of particles. 107

Fig. 4-2 Plane-strain critical state friction angle $\phi'_{cs,ps}$ versus initial plane-strain constant-volume friction angle $\phi'_{cv,ps}$ 112

Fig. 4-3 Present experimental results for silica sand, UHMW polyethylene, and P50 sandpaper compared with present theory in Eq. (4-9). 113

Fig. 4-4 Other *flow rules* compared with present theory in Eq. (4-9)..... 115

Fig. 4-5 Cycle of porosity or relative density involved by Eqs. (4-11) to (4-14). 118

Fig. 4-6 Developed plane-strain critical state friction angle $\phi'_{cs,ps}$ versus the critical state porosity n_c , annotated with three distinctive behaviors: contractive, dilative, and collapsible..... 119

Fig. 4-7 Pore pressure coefficient $A_{cs,ps}$ at plane-strain critical state shear failure given by Eq. (4-20) compared with experimental results adopted from (Bjerrum et al., 1961, fig. 5).....	123
Fig. 4-8 Present pore pressure coefficient $A_{cs,ps}$ versus its corresponding plane-strain critical state friction angle $\phi'_{cs,ps}$	124
Fig. 4-9 Characteristic pore pressure $A_{cs,ps}$ for very loose sand according to (Bjerrum et al., 1961) and present Eq. (4-20).....	125
Fig. 5-1 Cross-sectional model used to analytically derive K_0	128
Fig. 5-2 At-rest lateral earth pressure coefficient K_0 according to Eq. (5-3) compared with the expression (2-18) since (Jaky, 1948).	130
Fig. 5-3 At-rest lateral earth pressure coefficient K_0 according to Eq. (5-3) versus relative density for silica sand.	132
Fig. 5-4 K_0 according to present Eq. (5-4) superimposed on data for K_0 : (a) for clays; and (b) for loose sands. Adapted from (Mesri and Hayat, 1993, fig. 7).	135
Fig. 5-5 K_0 according to present equation (5-4) versus initial porosity compared to original data for K_0 obtained experimentally in loose sands by (Bjerrum et al., 1961, fig. 12).	136
Fig. 5-6 Critical state parameters of some soil types in (Atkinson, 1993).....	139
Fig. 5-7 At-rest lateral earth pressure coefficient K_{0-OC} according to present Eq. (5-7) compared with the empirical formula (5-12) according to (Hanna and Al-Romhein, 2008).....	140

Fig. 5-8 At-rest lateral earth pressure coefficient $K_{\theta-OC}$ after present equation (5-7) compared with the experimental result for Toyoura sand given by equation (5-13) according to (Santana and Candeias, 2015).....	142
Fig. 5-9 Experimental results exhibiting a common alignment or link among OCR , $K_{\theta-OC}$, and D_r in present silica sand (see <i>Appendix G</i>).	149
Fig. 5-10 OCR versus D_r for silica sand (see <i>Appendix G</i>).....	150
Fig. 6-1 Slip-failure surface in cartesian coordinates and differential soil element.	153
Fig. 6-2 Slip-failure surface and known boundary conditions: (a) active state; (b) passive state.	155
Fig. 6-3 Present solution applied to experimental results of Tsagareli (1965): (a) slip-failure geometry; (b) lateral earth pressure distribution.....	158
Fig. 6-4 Active slip geometry as per Eq. (6-10) illustrated with a selection of $\phi'_{cs,ps}$	160
Fig. 6-5 Passive slip geometry as per Eq. (6-15) illustrated with a selection of $\phi'_{cs,ps}$ and H . ..	161
Fig. 6-6 Active pressure as per Eq. (6-20) illustrated with a selection of $\phi'_{cs,ps}$ and H	162
Fig. 6-7 Passive pressure as per Eq. (6-20) illustrated with a selection of $\phi'_{cs,ps}$ and H	163
Fig. 6-8 Location of the resultant horizontal force.	164
Fig. 7-1 Complete plane-strain critical state constitutive model developed by present study....	166
Fig. 7-2 Deformation mechanism: (a) the unitary pack of particles; (b) prismatic sample under the critical state plane-strain failure ($\epsilon_2 = 0$).....	169

Fig. 7-3 Characteristic curves for extensive/collapsible cohesionless granular material.	173
Fig. 7-4 Characteristic curves for extensive/dilative cohesionless granular material.....	173
Fig. 7-5 Characteristic curves for compressive/contractive cohesionless granular material.	174
Fig. 7-6 Characteristic curves for compressive/dilative cohesionless granular material.....	174
Fig. 7-7 Characteristic curves for extensive/suction-dilative cohesionless granular material....	175
Fig. 7-8 Present CSSM incremental model applied to experimental results from (Alshibli et al., 2004).	176
Fig. 8-1 Flowchart to establish porosity for present CSSM framework.....	180
Fig. 8-2 Flowchart to determine friction and other parameters in present CSSM framework. ..	181
Fig. 8-3 Plane-strain frictional parameters embedded in a single triaxial test.....	183
Fig. 8-4 Plane-strain frictional parameters versus triaxial test friction.....	184
Fig. 8-5 Comparison between the angle of shearing resistance for different tests.	186
Fig. 8-6 Problem #1: (a) wall and backfill properties; and (b) sublayers to determine <i>OCR</i>	188
Fig. 8-7 Problem #1: at-rest lateral earth pressure per unit length of wall: (a) distribution; and (b) resultant.....	191
Fig. 8-8 Problem #2: (a) wall and backfill properties; and (b) sublayers to determine the lateral stress distribution and the slip-failure surface geometry.	192

Fig. 8-9 Problem #2: (a) slip-failure surface geometry; and (b) active lateral earth pressure distribution. 195

Fig. 8-10 Problem #3: (a) wall and backfill properties; and (b) sublayers to determine the lateral stress distribution and the slip-failure surface geometry. 196

Fig. 8-11 Problem #3: (a) slip-failure surface geometry; and (b) passive lateral earth pressure distribution. 198

Fig. A-1 Stress state in a mass of earth of infinite horizontal extension taken from (Diaz-Segura, 2016) 237

Fig. A-2 Model of a pile of granular soil assumed by (Jaky, 1944) taken from (Diaz-Segura, 2016) 238

Fig. A-3 Slide planes in a motionless mass of earth taken from (Diaz-Segura, 2016)..... 239

Fig. A-4 Geometry properties and arbitrary assumption of the shear stress distribution within the zone II, figure adopted from (Diaz-Segura, 2016)..... 244

Fig. C-1 Active state characteristic curves for an extensive/collapsible cohesionless granular material: (a) slip-failure surface geometry; and (b) lateral earth pressure distribution. 254

Fig. C-2 Active state characteristic curves for an extensive/dilative cohesionless granular material: (a) slip-failure surface geometry; and (b) lateral earth pressure distribution..... 254

Fig. C-3 Active state characteristic curves for a compressive/contractive cohesionless granular material: (a) slip-failure surface geometry; and (b) lateral earth pressure distribution. 255

Fig. C-4 Active state characteristic curves for a compressive/dilative cohesionless granular material: (a) slip-failure surface geometry; and (b) lateral earth pressure distribution. 255

Fig. C-5 Active state characteristic curves for an extensive/suction-dilative cohesionless granular material: (a) slip-failure surface geometry; and (b) lateral earth pressure distribution. 256

Fig. C-6 Passive state characteristic curves for an extensive/collapsible cohesionless granular material: (a) slip-failure surface geometry; and (b) lateral earth pressure distribution. 256

Fig. C-7 Passive state characteristic curves for an extensive/dilative cohesionless granular material: (a) slip-failure surface geometry; and (b) lateral earth pressure distribution. 257

Fig. C-8 Passive state characteristic curves for a compressive/contractive cohesionless granular material: (a) slip-failure surface geometry; and (b) lateral earth pressure distribution. 257

Fig. C-9 Passive state characteristic curves for a compressive/dilative cohesionless granular material: (a) slip-failure surface geometry; and (b) lateral earth pressure distribution. 258

Fig. C-10 Passive state characteristic curves for an extensive/suction-dilative cohesionless granular material: (a) slip-failure surface geometry; and (b) lateral earth pressure distribution. 258

Fig. G-1 Spreadsheet screenshot showing the inputs and initial data processing..... 262

Fig. G-2 Spreadsheet screenshot showing the inputs and initial data processing (continued). .. 263

Fig. G-3 Spreadsheet screenshot showing the cells and formulas to process the lateral stress. . 263

Fig. H-1 Spreadsheet screenshot showing the tabulation for the slip-failure surface geometry: (a) active; and (b) passive..... 265

Fig. H-2 Spreadsheet screenshot showing the tabulation for lateral earth pressure distribution: (a) active; and (b) passive..... 266

Fig. I-1 Spreadsheet Implanted with Present CSSM Plane–Strain Numerical Simulation for Granular Cohesionless Soil..... 268

List of Symbols

A	Pore pressure coefficient in general or non-disambiguated.
A_f	Area of the failing mass associated to active and passive states of a retaining wall.
B	Horizontal distance between wall back face and the slip-failure surface outcrop at the ground level.
$A_{cs,ps}$	Pore pressure coefficient of plane-strain critical state shear failure.
$A_{cv,ps}$	Steady or intrinsic coefficient of pore pressure.
$A_{p,ps}$	Pore pressure coefficient of critical state failure due to geometrical interference.
C	Slope of the compression line under vertical loading in oedometer tests.
C_s	Slope of the swelling line under vertical unloading in oedometer tests.
D_r	Relative density.
e	Void ratio.
H	Wall height.
K_a	Active lateral earth pressure coefficient.
K_p	Passive lateral earth pressure coefficient.
K_0	At-rest lateral earth pressure coefficient of normally consolidated cohesionless soil.
K_{0-OC}	At-rest lateral earth pressure coefficient of overconsolidated and compacted soil deposits.

$K(x)$	Function for the nonlinear lateral earth pressure coefficient (includes K_a and K_p).
N	Number of steps of the stress–strain incremental numerical model.
n	Porosity.
n_c	Final porosity reached upon plane-strain critical state shear failure.
n_r	Relative porosity.
n_s	Porosity associated with a change of internal structure.
n_0	Initial porosity of the soil deposit under constant-volume or before any deviatoric shear stress.
n_0^*	Critical porosity associated with soil collapsibility potential.
OCR	Overconsolidation ratio.
$y(x)$	Function for the nonlinear slip-failure surface geometry.
α	Auxiliary angle defined herein in the particle-scale model of a pile standing at rest.
α_0	Generatrix angle of the natural exponential function.
β	Static angle of repose.
γ	Unit weight of soil (i.e., a dry unit weight of soil for present study).
ε_1	Principal axial strain.
ε_3	Secondary axial strain.
$\dot{\varepsilon}_1$	Principal axial strain rate.
$\dot{\varepsilon}_3$	Secondary strain rate.
ε_v	Volumetric strain.

$\dot{\epsilon}_v$	Volumetric strain increment.
κ	Slope of unload-reload consolidation line in \ln scale.
λ	Slope of primary consolidation line in \ln scale.
A	Plastic volumetric strain ratio.
ν	Poisson's ratio.
σ'_{v0}	Initial effective vertical stress.
$\sigma'_{v,max}$	Maximum historic effective vertical stress.
$(\sigma'_1/\sigma'_3)_{f,cs,ps}$	Principal stress ratio at critical-state plane-strain failure.
$(\sigma'_1/\sigma'_3)_{f,cv,ps}$	Principal stress ratio at constant-volume plane-strain failure.
$\sigma'_H(x)$	Function for the nonlinear horizontal earth pressure (includes $\sigma'_{a,H}$ and $\sigma'_{p,H}$).
\emptyset'	Angle of shearing resistance in general or non-disambiguated.
\emptyset'_c	Angle of grain crushing.
$\emptyset'_{cs,ps}$	External finally developed normally consolidated plane-strain critical state friction angle.
$\emptyset'_{cv,ps}$	Internal initially available normally consolidated plane-strain constant-volume friction angle.
\emptyset'_d	Angle of dilation/contraction normal to the shear plane.
\emptyset'_{ds}	Angle of shearing resistance from the direct shear test.
\emptyset'_g	Angle of geometrical interference ($\emptyset'_d + \emptyset'_p$).
$\emptyset'_{p,ps}$	Angle of pushing or rearrangement.
\emptyset'_t	Angle of shearing resistance from the triaxial test.

θ'_μ

Interparticle sliding friction angle.

Chapter 1: Introduction

1.1. General

The coefficient of lateral earth pressure K is the ratio between horizontal and vertical soil stresses at a given depth on a soil-wall interface. For design purposes, there are three distinct states. The first, named the active lateral earth pressure K_a is related to the minimum horizontal pressure that results after a soil mass fails and deforms outward against a rigid wall and both reach a point of equilibrium (e.g., a cantilever retaining wall). The second, termed the passive lateral earth pressure K_p is related to the maximum horizontal pressure that results when a soil mass fails and deforms inward due to an external action transmitted by a rigid wall (e.g., a pile carrying horizontal load or an anchor plate). The third, named the at-rest lateral earth pressure K_0 is related to the horizontal pressure a soil mass exerts against itself or against a containing structure given that no lateral deformation or failure of the soil mass occurs (e.g., a box culvert or a soil horizon). Furthermore, the lateral earth pressure can be described as the continuous transits between at-rest to active and a-rest to passive states, both mediated by the development of a nonlinear slip-failure surface in the soil mass.

1.2. Problem Statement

A generic internal friction angle of the soil ϕ' in conjunction with the problem geometry and an any assumed geometry for the slip-failure surface among other assumptions have been used in the development of mathematical, analytical and empirical models to estimate lateral earth pressures. Despite these available estimations from the existing framework having been of some help in practice; these approaches do not provide the most faithful representation of the phenomenon

resulting in high uncertainty and high discrepancies between predictions and field observations. This situation has led to underpredictions, overpredictions and unattended areas where the current theory is simply not enough to address certain problems. The specific shortcomings of current theory that constitute the problem definition for the present research are:

- The most widely used theory for at-rest lateral earth pressure coefficient K_0 is an empirical formula; consequently, we lack an explicit theoretical solution for that paramount concept in geotechnical engineering. See *Appendix A* for a critical review on this regard.
- The most widely used theory for active K_a and passive K_p lateral earth pressure coefficients assumes a straight-line slip-failure surface and triangular stress distribution behind the wall while experimental results have shown that both have a nonlinear geometry.
- Current theory for lateral earth pressure in cohesionless soils ignores *OCR* and the stress-strain evolution with deformation.

1.3. Motivations and applications

An improved lateral earth pressure theory is necessary for a better and safer geotechnical and structural design. Other motivations are:

1.3.1. Development of a critical state soil mechanics CSSM model for sand

CSSM theory has been used mainly for clay since its *critical line* approaches a straight line; however, the application of CSSM for sand remains lagged because its characteristic curved *critical line* makes analysis more difficult. Present research becomes of interest because it develops this lagged theory.

1.3.2. An explicit derivation

A complete and explicit theory for lateral earth pressure remains elusive and researchers keep in supporting their contributions on statistical fits or arbitrary assumptions that oversimplify the problem, consequently failing in this purpose (see *Chapter 2: Literature Review*). The solutions presented in this study provide the complete and explicit derivation behind each new formula.

1.3.3. Overconsolidation

Most natural soil deposits occur at a certain degree of overconsolidation and most artificial fills are compacted using standards of reference like (ASTM D698-12e2, 2012) or (ASTM D1557-12e1, 2012) gaining in this way a higher degree of overconsolidation. Consequently, overconsolidation in terms of *OCR* should be a design parameter of frequent use, however, this is not the case of the actual practice in cohesionless soils.

1.3.4. Deformation

The introduction of deformation facilitates practical applications in areas like structural monitoring, design optimization, constitutive modelling, and pushover analysis.

1.3.5. To whom this research is directed

This research is useful for various stakeholders like geosciences engineering practitioners and in industries specifically dealing with any kind of granular material (e.g., pharmaceutical, powder, agriculture, construction, mining).

1.4. Objectives

The overall objective is:

- To conduct experimental, analytical, and numerical research to formulate a new lateral earth pressure theory for cohesionless soils in terms of CSSM parameters.

The specific objectives are:

- a) To derive a theoretical constitutive model or *flow rule* for the critical state plane-strain friction angle of cohesionless soils.
- b) To perform tests for the angle of repose in extreme controlled conditions of both test procedure and particles character.
- c) To formulate a solution for the at-rest K_0 , K_{0-OCR} ; active K_a ; and passive K_p lateral earth pressure coefficients in terms of CSSM parameters observing nonlinearity and *OCR*.

1.5. Delimitation of the proposed explicit solution

The herein *explicit* lateral earth pressure theory meets the following four conditions: (i) satisfies equilibrium, (ii) satisfies a yield condition, (iii) verifies a stress–strain relationship and (iv) observes the law of conservation of energy. In addition, the present *explicit solution* excludes the arbitrary assumptions identified in the literature review (see *Chapter 2: Literature Review*) which are usually related to: (i) the slip-failure surface geometry, (ii) the lateral stress distribution, (iii) an arbitrary stress boundary condition or (iv) a pseudo-Poisson ratio.

1.6. Organization of Thesis

Apart from this introductory chapter, *Chapter 2*: presents a literature review of the friction of granular materials and the background theory for at-rest, passive, and active lateral earth pressure coefficient for cohesionless soil. It also presents a literature review on the static angle of repose of granular materials and the existing laboratory techniques for its measurement.

Chapter 3: presents all the experimental work developed in the present study. This includes a detailed description of methodologies and the raw results from measurements developed to obtain soil parameters and horizontal stresses.

Chapter 4: presents a theoretical analysis to derive the relationship or *flow rule* between the plane-strain critical state friction angle and the plane-strain constant-volume friction angle of granular materials. From this relationship, a complete model for critical state of cohesionless soils is then developed and experimentally verified.

Chapter 5: is based on the *flow rule* developed in *Chapter 4*. By applying a limit equilibrium analysis, a new formula to determine the at-rest coefficient of lateral earth pressure in normally consolidated cohesionless soil K_0 is also derived. This new formula for the at-rest coefficient of lateral earth pressure is then extended to incorporate the overconsolidated state in terms of the *OCR* parameter or K_{0-OCR} . These two formulas are validated by means of an own experimental investigation with silica sand.

Chapter 6: presents the theoretical derivation of the nonlinear active and passive coefficients of lateral earth pressure in normally consolidated cohesionless soil as a function of the plane-strain critical state friction angle. Previous derivation incorporates a new nonlinear expression for the geometry of the slip-failure surface and its associated nonlinear lateral stress distribution. Verification is provided by comparison with existing large-scale experimental results.

Chapter 7: describes an incremental numerical model to simulate the stress–strain path associated to the *flow rule* presented in *Chapter 4*. This simulation is also integrated to the rest of associated soil parameters as defined in previous chapters.

Chapter 8: presents a user-oriented set of examples to illustrate in a step-by-step fashion the practical application of the CSSM lateral earth pressure theory developed in previous chapters.

Finally, *Chapter 9:* concludes by highlighting the most relevant findings in present research and provides recommendations for future potential extensions of present work.

Chapter 2: Literature Review

2.1. General

The active, passive, and at-rest coefficients of lateral earth pressure K_a , K_p and K_0 , respectively, are important design parameters in geotechnical engineering. All of these are the ratio of the horizontal effective stress σ'_h to the vertical effective stress σ'_v , see Eq. (2-1). The active state denoted by the index “ a ” involves outward failure and deformation of the soil mass against a rigid wall until the soil-wall interaction gets a final state of equilibrium. The passive state denoted by index “ p ” involves inward failure and deformation of the soil mass. The at-rest condition denoted by index “ 0 ”, exists in-situ at a zero lateral strain state. The present literature review makes a critical analysis of the relevant state of the art around this concept. Accordingly, the explored literature includes areas like shear strength, angle of repose and prediction of active, passive and at-rest lateral earth pressure coefficients in granular materials retained by a wall.

$$K_{a|p|0} = \frac{\sigma'_h}{\sigma'_v} \quad (2-1)$$

Firstly, a review on the shear strength of granular soils is provided. Then it follows a review of the history of the angle of repose. The angle of repose is a natural phenomenon of granular materials which is recognized by geotechnical engineering. However, the theoretical treatment of this subject remains unattended. The existing geotechnical research incorporating the angle of repose has been focused mainly on experimental work leading to empirical correlations and in the development of laboratory techniques for the measurement of the angle of repose. The angle of repose is a relevant concept for present study because it is key to understanding the shear resistance developed at plane-strain critical state.

Finally, a review of the available theoretical and empirical predictions of the active, passive, and at-rest states is also provided. In this regard, the current and most widely used expression for the at-rest pressure prediction is the empirical from (Jaky, 1944). For the active and passive pressures are the analytical solutions from (Coulomb, 1776) and (Rankine, 1857). These three seminal works known as “classical theory” and an important amount of additional related research has been developed. However, a classical framework seems to prevail despite its controversial oversimplification and empirical character, in the case of the at-rest state; and despite its oversimplification and incompleteness in the case of the active and passive states. This part of the literature review highlights the main assumptions behind each reviewed approach specially those arbitrary assumptions that prevent each approach from being more precise. This, to call attention to the actual need of an explicit and complete solution for the lateral earth pressure able to overcome the shortcuts of the prevailing framework (see numeral 1.2).

2.2. Shear strength of granular cohesionless soils

As explained in (Terzaghi et al., 1996, sec. 19), the angle of shearing resistance ϕ' developed by cohesionless soils is the product of interparticle forces, governed mainly by three mechanisms that contribute to the mobilized friction angle, namely the kinetic friction ϕ'_{μ} ; rearrangement and dilation, also known as geometrical interference or interlocking ϕ'_g ; and grain crushing ϕ'_c . Accordingly, the friction developed under drained shear failure can be expressed by the Eq. (2-2) and illustrated by Fig. 2-1.

$$\phi' = \phi'_{\mu} + \phi'_g + \phi'_c \quad (2-2)$$

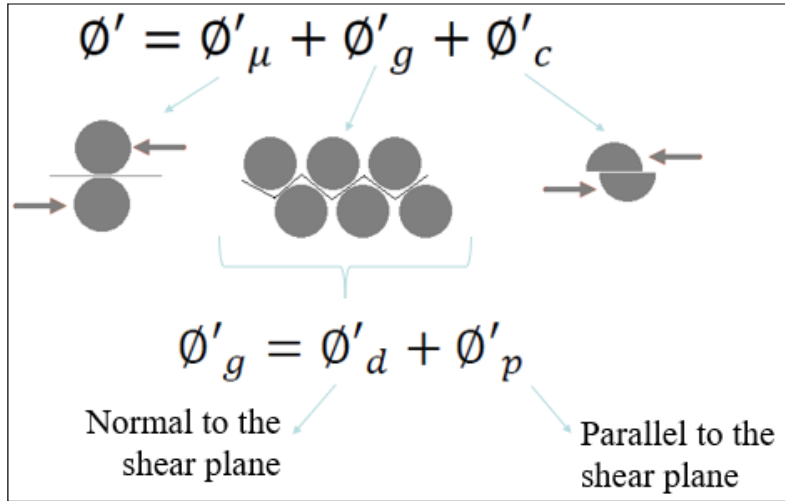


Fig. 2-1 Components of friction for a granular soil.

When a particle rolls over another, junctions form at the contact points; however, this bonding is broken in normal tension and not in tangential shear as for sliding friction. Due to an elastic rebound as the normal force is depleted, the strength at these junctions is diminished to almost zero. This explains why rolling friction is generally very small compared to interparticle sliding friction, as explained by (Lambe and Whitman, 1969, p. 65). This potential component of the shear friction is then very small and was ignored in Eq. (2-2) especially because granular cohesionless soils like sand are mostly composed by non-adhesive particles.

The relevance of the friction due to particle crushing is a function of the confinement pressure and can also be considered a steady contribution as far as the confinement pressure remains steady during the shearing process (Hamidi et al., 2009). (Bolton, 1986) and (Bolton and Arthur, 1987) observed that the tendency for particles to crush under shear is not appreciable when the confining pressure is lower than about 150 kPa, allowing dilation to be treated as an only function of relative

density under this condition (Bolton, 1986, p. 225), (Sadrekarimi and Olson, 2011). Since retaining walls as studied here are surficial structures, the confining pressure is usually below the confining pressure where the particle crushing starts being relevant permitting to draw ϕ'_c from Eq. (2-2).

On the other hand, the geometrical interference ϕ'_g is the combined effect of particle pushing and climbing. The geometrical interference ϕ'_g may be expressed as the sum of the angle of dilation ϕ'_d produced by particle climbing normal to the shear plane, and a component due to pushing or rearrangement occurring parallel to the shear plane ϕ'_p as indicated in Eq. (2-3).

$$\phi'_g = \phi'_d + \phi'_p \quad (2-3)$$

The kinetic friction ϕ'_μ also referred to as the sliding friction or the interparticle sliding friction is the intrinsic steady component of friction resisting sliding between individual grains in the tangential direction on the contact point. This interparticle sliding friction is the same constant-volume friction angle in an ampler sense $\phi'_\mu = \phi'_{cv}$. And its dominant contribution at all confining pressures depends mainly on the mineral composing the soil, the asperities at the particle-scale and the soil initial porosity n_0 . Moreover, this $\phi'_\mu = \phi'_{cv}$ is the internal friction angle initially available within the soil mass before the application of any shear failure. In other words, when the soil mass is under the at-rest state no shear failure exists, thus the “dilatancy rate” is zero and as a result, the available friction in such a state can also be deemed as a constant-volume friction angle or the *initially available constant-volume friction angle*. When a shear failure is produced in the soil mass and after enough shear deformation, the soil within the shear band will reach a porosity state n_c where two granular masses are separated by a slip-failure surface shearing at constant-volume and constant shear stress [i.e., critical state concept since (Roscoe et al., 1958)]; consequently, the

dilatancy rate again approaches zero. Thus, the finally developed friction can be deemed the *finally developed constant-volume friction angle*. To avoid confusion between these two constant-volume friction angles (the initial and the final), the developed friction angle at this porosity state known as the critical porosity n_c is then renamed in this study as the *plane-strain critical-state friction angle* $\phi'_{cs,ps}$; in fact, this *critical state* term is more appropriate here since it contains both connotations, the constant-volume, and the constant shear stress at shear failure. For this porosity n_c corresponding to the critical state, the contribution from dilation becomes zero $\phi'_d = 0$ (i.e., plane-strain condition); accordingly, the mobilized plane-strain critical state friction results to be the given by Eq. (2-4). This porosity-dependant character of shear resistance of granular soils was neatly observed by the experiments on sand developed by (Bjerrum et al., 1961) and (Sadrekarimi and Olson, 2011), see Fig. 2-2.

$$\phi'_{cs,ps} = \phi'_{cv,ps} + \phi'_{p,ps} \quad (2-4)$$

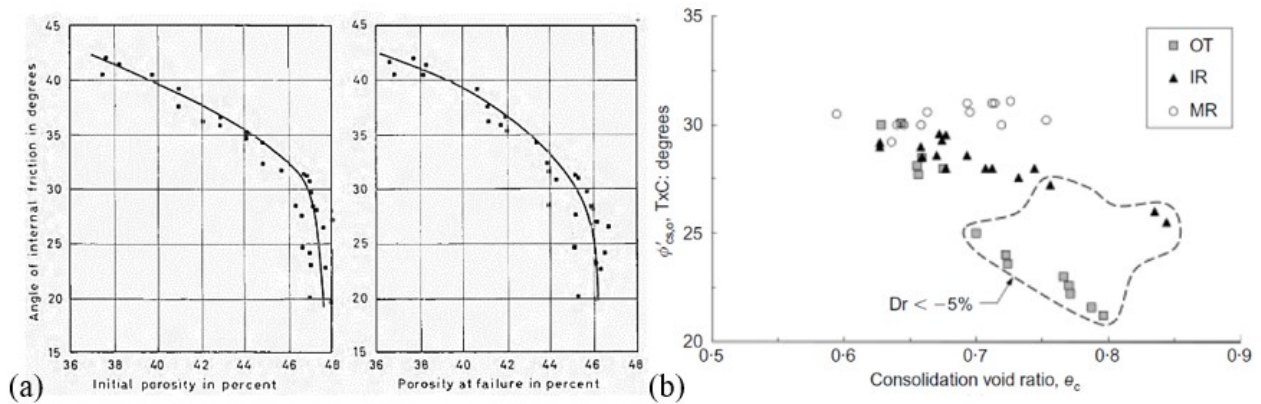


Fig. 2-2 Porosity-dependent character of shear resistance as observed in experimental works: (a) according to (Bjerrum et al., 1961); and (b) according to (Sadrekarimi and Olson, 2011).

For the particular case of normally consolidated young soil deposits, the angle of repose is equal to the plane-strain critical state friction angle $\beta = \phi'_{cs,ps}$ (Lambe and Whitman, 1969), (Cornforth, 1973), (Terzaghi et al., 1996, p. 104), (Santamarina and Cho, 2001), (Sadrekarimi and Olson, 2011). Accordingly, for this particular case under low confining pressure (i.e., no grain crushing or $\phi'_c = 0$), it is possible to rewrite Eq. (2-4) in the form of the Eq. (2-5).

$$\phi'_{cs,ps} = \beta = \phi'_{\mu,ps} + \phi'_{p,ps} \quad (2-5)$$

Equation (2-5) finally states that the static angle of repose β or the plane-strain critical-state friction angle $\phi'_{cs,ps}$ at low confining pressure and normally consolidated state (i.e., as the soil in a pile of sand standing at-rest) can be expressed as the sum of the intrinsic or steady component of friction $\phi'_{\mu,ps}$ plus an equivalent component of friction accounting for the geometrical interference in plane-strain which in critical state is given only by the interparticle pushing or rearrangement $\phi'_{p,ps}$. Note that the interparticle sliding friction angle $\phi'_{\mu,ps}$ was applied in Eq. (2-5) because it corresponds to the minimum possible initial constant-volume friction angle existing in a soil mass. For initial constant-volume friction angles higher than the interparticle sliding friction angle $\phi'_{\mu,ps}$, the more general form in Eq. (2-4) applies. Since this single case known as *the static angle of repose* β can clearly provide experimental access to the understanding of the plane-strain critical-state friction angle, the following numeral 2.3 provides specific literature review on this topic.

2.3. The angle of repose

Various definitions exist for the angle of repose β . From a phenomenological point of view, when dry material fails from a slope and flows accumulating at the toe forms a cone which angle with the horizontal is called the angle of repose (Liu, 2011). Physically, the angle of repose was defined

by (Wu and Sun, 2008) as a transition between solid and liquid phases. A more formal and common definition states the angle of repose is the steepest free standing surface of a pile of granular material under gravity can make with the horizontal before material starts to flow down (Lowe, 1976; Mehta and Barker, 1994). Karl Terzaghi defined the angle of repose as a special angle of internal friction present at a porosity equivalent to the loosest condition (Terzaghi et al., 1996).

The angle of repose is equal to the angle of shearing resistance for sedimentary, normally consolidated young materials for which the angle of repose β is equal to the critical state friction angle ϕ'_{cs} (Lambe and Whitman, 1969), (Terzaghi et al., 1996, p. 104), (Cornforth, 1973), (Santamarina and Cho, 2001), (Sadrekarimi and Olson, 2011).

Granular material susceptible of having a definite angle of repose is material composed by particles larger than a given minimum size. That minimum size depends on the substance composing the particles, but in general is the minimum particle size for which the gravity is still the source of force governing the interaction between the particles. For soils and according to geotechnical classifications the minimum particle size for a granular material is 1 μm (less than this the size is mostly colloidal particles).

In nature, the angle of repose for dry granular soils varies from 25° for smooth spherical particles to 45° for rough angular particles as indicated by (Beakawi Al-Hashemi and Baghabra Al-Amoudi, 2018, p. 399), and (Pohlman et al., 2006). This range relates in some way with the angle of interparticle sliding friction for minerals that naturally form the particles of granular soils which typically range from 26° to 37° (Terzaghi et al., 1996, p. 147).

2.3.1. Measurement of the angle of repose

The angle of repose is a limit equilibrium of the only static interaction between a mass of particles and gravity. Because of this, the measurement of the angle of repose is not an easy task. All physical methods available to measure the angle of repose are invasive and introduce additional forces altering results. All of this explains why there is no final agreement about how the angle of repose should be determined and why the results of applying certain standards or devices lacks repeatability and reproducibility.

Different instruments and techniques exist to measure the static and dynamic angle of repose. However, only those approaching the static angle of repose of soils will be reviewed here since this is the relevant for present study. The angle of repose β is commonly measured in piles of loose material produced by a given device or procedure as the maximum inclusive angle between the pile face and the horizontal, see Fig. 2-3.

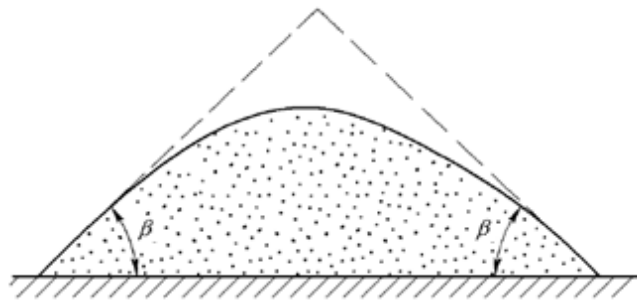


Fig. 2-3 Measuring the repose angle β in a pile of granular material adapted from (Wu and Sun, 2008, p. 15).

Numerical models that simulate granular material like distinct element method (DEM) can mimic piles of granular material; however, these piles do not reproduce the actual physical phenomena. On the contrary, the simulation of this phenomena has been used to calibrate constitutive models for granular material based on the measured-in-laboratory angle of repose (Coetzee, 2017), (Brezzi et al., 2017) and (Roessler and Katterfeld, 2018). The following numerals provide a description of the physical methods more commonly used to measure the static angle of repose.

2.3.1.1. Method of loading simulated measuring box

Loading simulated measuring box is a device to measure natural angle of repose simulating in-situ static pressure, see Fig. 2-4. First granular material is poured and leveled into the box. Then, the pressure piston is released so the weight is transferred onto the granular material. After that, the sliding door is opened, letting the granular material flows to form a slope thanks to the action of gravity and static pressure. Finally, the angle of repose can be measured on the formed slope.

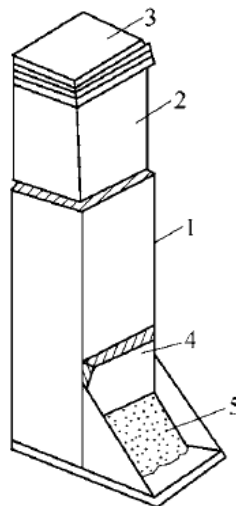


Fig. 2-4 Method of loading simulated measuring box. 1: box, 2: pressure piston, 3: weight, 4: sluice and 5: slope of granular material. Adopted from (Wu and Sun, 2008, p. 16).

2.3.1.2. Method of bottomless or hollow cylinder

The bottomless or hollow cylinder method is commonly used to assess the static angle of repose of a frictional material, see Fig. 2-5. The granular material is placed from the top into a cylinder with a ratio of diameter to height of around 1:3 and this set on a base with known friction. The diameter of the cylinder must be more than 4 to 5 times the maximum particle diameter. Then, the cylinder is carefully lifted (e.g., at a velocity of about 10 mm/s) vertically so the granular material can flow to form a cone (Wu and Sun, 2008, p. 16), (Beakawi Al-Hashemi and Baghabra Al-Amoudi, 2018, p. 401).

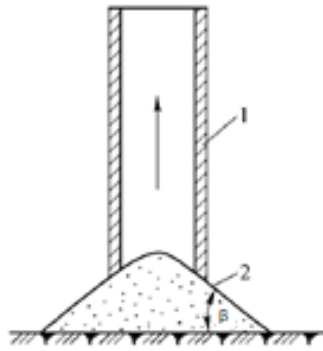


Fig. 2-5 Method of bottomless or hollow cylinder. 1: cylinder, 2: granular material. Adopted from (Wu and Sun, 2008, p. 16).

2.3.1.3. Method of funnel or falling device

The device for the method of funnel or falling method is shown in Fig. 2-6 in its fixed version and in Fig. 2-7 in its moving version. In the fixed funnel method, the granular material is first poured and leveled into the upper box. A common specification for the dimensions of this device are: 0.7

m height, 0.15 m width and 0.2 m length (Wu and Sun, 2008, p. 17). Then the funnel door is open so the granular material can fall from a certain height forming a cone onto a defined base of known friction.

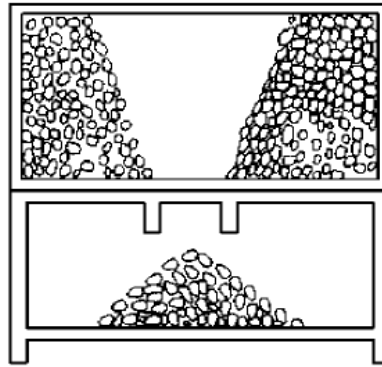


Fig. 2-6 Method of fixed funnel adopted from (Wu and Sun, 2008, p. 17).

The main difference in the moving funnel is the progressive adjustment of the falling height by means of simultaneous lifting with the pile formation. This characteristic reduces the momentum transferred to the granular soil; consequently, improving the measurement.

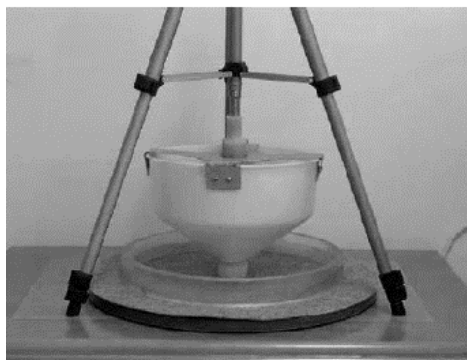


Fig. 2-7 Method of moving funnel adopted from (Li et al., 2005, p. 225).

2.3.1.4. Method of fixed base and ring

In this method the diameter of the base is fixed by using a ring or container with sharp edges. Granular material is poured onto the center from a funnel which can be adjusted to a desired height, see Fig. 2-8.

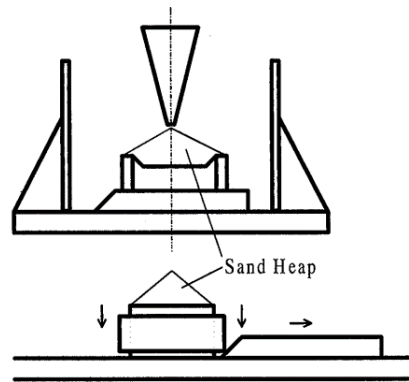


Fig. 2-8 Method of fixed base from (Miura et al., 1997, p. 93).

(Miura et al., 1997) introduced a variant which includes a pedestal with a top depression as well as a moving ring around the pedestal. After pouring the granular material on the depression the ring is lowered to finish the cone surface on a more standard manner mitigating in this way some of the factors typically influencing the measurement.

A combination of fixed funnel and fixed base was temporarily adopted by the American Society of Testing and Materials in the standard ASTM D6393 to measure the angle of repose (D18 Committee, 2014).

2.3.1.5. Method of rotary box

The Fig. 2-9 shows the rotary box device. At least one transparent wall must exist on any side of the rotary box, this to observe and measure the resulting angle of repose. The common specification for the dimensions of this rotary box is: 0.2 m height, 0.2 m width and 0.4 m length (Wu and Sun, 2008, p. 17). First, the granular material is placed on the base of the box which is rotated 90° to upright position. Then the granular material is leveled. Finally, the box is returned to its horizontal position gradually at a controlled rate of about 18°/min; in the process, the granular material will form a slope.

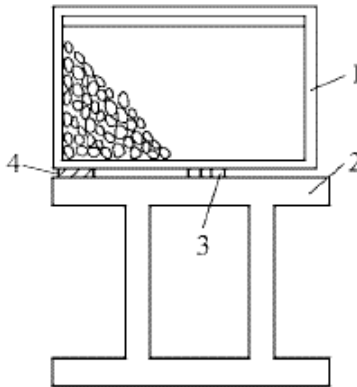


Fig. 2-9 Method of rotary box. 1: box, 2: frame of box, 3: rotary axis and 4: fixation plate.

Adopted from (Wu and Sun, 2008, p. 17).

2.3.1.6. Method of tilting cylinder

The method of tilting cylinder is explained by the Fig. 2-10. It consists in putting fine granular material in a cylinder flask full of water, saturation is used to avoid capillary effects. Then, the flask is tilted around 60° and gently returned to its vertical position. Finally, the angle of repose is

measured in the middle of the remaining slope. This method was used by (Santamarina and Cho, 2001, p. 191) to assess critical state parameter in sand. On their experiments they found that the angle of repose for the tested sand is between 0° to 2° higher than the angle of shearing resistance obtained from triaxial test results.

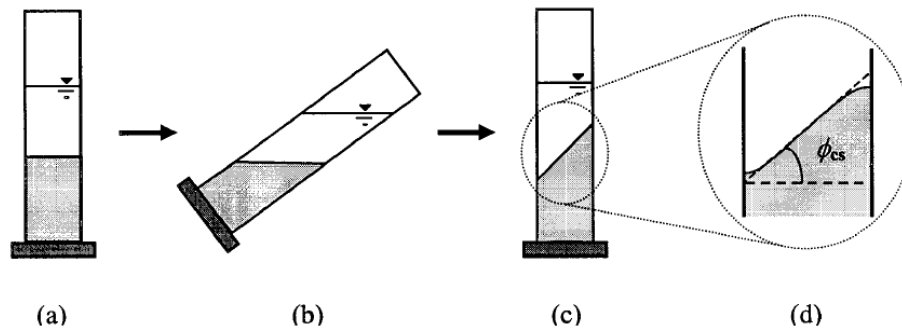


Fig. 2-10 Method of tilting cylinder adopted from (Santamarina and Cho, 2001, p. 187): (a) pour soil in a 1000 ml cylinder with water; (b) rotate the cylinder passed 60° ; (c) slowly return the cylinder to its vertical position and measure the angle of repose; and (d) the angle is measured in the middle region on the slope.

2.3.2. Factors influencing the measurement of the angle of repose

The main external influencing factors affecting the measurement of the angle of repose are the interaction of the granular material with the measuring device, the added energy due to a given height of falling, excessive height of the center of gravity of the falling mass or the added acceleration when rotation is involved. The main source of error is then the introduction of excessive momentum during the pouring of granular material. In this regard it is interesting to see

how (Kleinhans et al., 2011) improved the measurement of the static angle of repose in 5° by means of testing under reduced gravity conditions.

(Rousé, 2013) obtained the angle of repose of the same material using six different methods and six different sands. After comparing the results, it was found that the highest angle of repose came from the (C08.03 Subcommittee, 2000) withdrawn in 2005. The other methods showed a dispersion between 6% below the maximum (scoop deposition) and 35% below the maximum (fixed funnel) confirming the existence of multiple influencing factors affecting the measurement of the angle of repose.

2.3.3. Theoretical relationship between the developed constant-volume friction angle and the interparticle sliding friction angle

Some theoretical research has been devoted to the definition of the critical state friction angle ϕ'_{cv} as a function of the angle of interparticle sliding friction ϕ'_μ .

(Caquot, 1934) by integrating forces normal and tangential to the surface of a sphere on the assumption that in the ultimate state sliding occurs simultaneously on tangential planes at interparticle contacts inclined in all the tangential directions of a spherical surface (i.e., in this condition failure is not a general displacement along a definite continuous surface) derived the expression (2-6). The plot of this equation is shown in Fig. 2-11.

$$\tan \phi'_{cv} = \frac{1}{2} \pi \cdot \tan \phi'_\mu \quad (2-6)$$

(Bishop, 1954) presented two approximate solutions, one for triaxial compression (2-7) and another for plane strain (2-8). The Fig. 2-11 shows both relationships. As for Caquot's solution,

these relationships predict that the constant-volume friction angle ϕ'_{cv} increases continuously with the increment of the interparticle sliding friction angle ϕ'_μ .

$$\sin \phi'_{cv} = \frac{3}{2} \cdot \tan \phi'_\mu \quad (2-7)$$

$$\sin \phi'_{cv} = \frac{15 \cdot \tan \phi'_\mu}{10 + 3 \cdot \tan \phi'_\mu} \quad (2-8)$$

(Horne, 1969) mathematically studied an assembly of rotund, rigid, cohesionless particles and from this proposed a procedure based on the equation (2-9) and extrapolation to zero dilation of the curve (σ'_1/σ'_3) versus $(1+dV/V\varepsilon)$. Using this approach, that author provided the curve shown in Fig. 2-11.

$$\frac{\sigma'_1}{\sigma'_3} = 2 \cdot \tan^2 \left(\frac{1}{4} \pi + \frac{1}{2} \phi'_\mu \right) \quad (2-9)$$

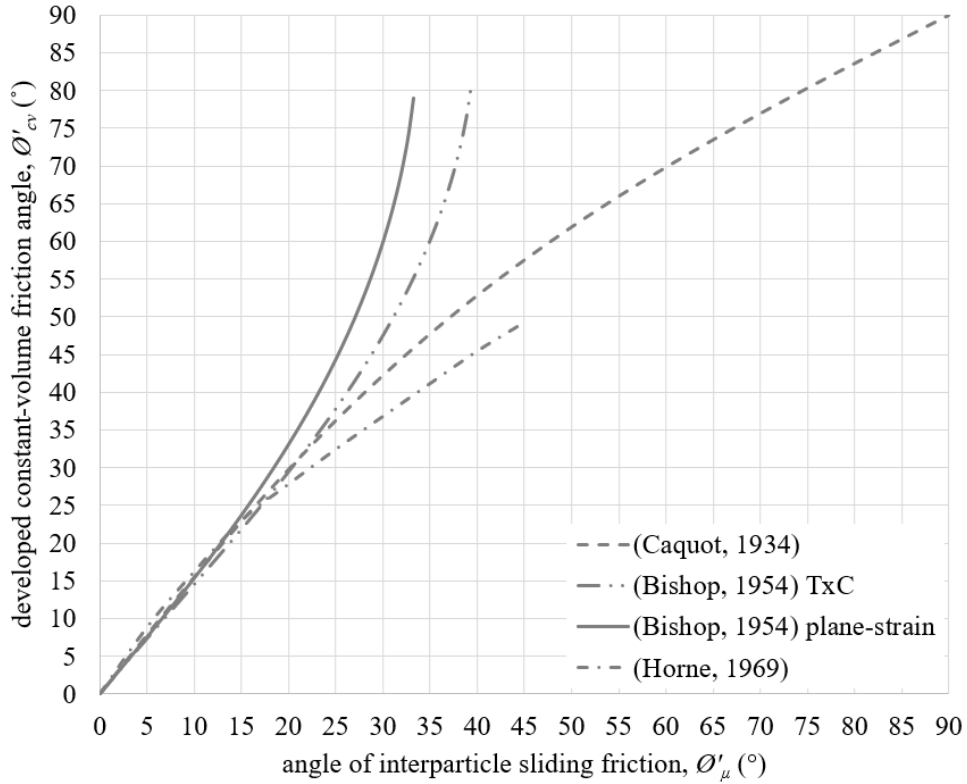


Fig. 2-11 Theoretical relationship between the angle of interparticle sliding friction ϕ'_{μ} and the developed constant-volume friction angle ϕ'_{cv} .

(Lee and Herrmann, 1993) developed a relationship between the angle of repose (i.e., the same developed ϕ'_{cv}), but in terms of the so-called angle of marginal stability and the friction angle applying the theory of molecular dynamics of granular particles in the stresses field of (Liffman et al., 1992). They found the angle of marginal stability differs from the angle of repose suggesting the angle of repose must include any effect due to the soil structure. They also concluded that the angle of repose is merely controlled by the angle of internal friction between the particles. However, the formulae derived by this approach is not of practical application since it is a function of the unknown parameter tilting angle θ_t , see equations (2-10) and (2-11).

$$\mu = \frac{R \cos(\pi/3 - \theta_t) - \cos(\pi/3 + \theta_t)}{R \sin(\pi/3 - \theta_t) + \sin(\pi/3 + \theta_t)} \quad (2-10)$$

Where:

$$R = \frac{\tan(\pi/3 + \theta_t) + \tan(\theta_r) \cos(\pi/3 + \theta_t)}{\tan(\pi/3 - \theta_t) - \tan(\theta_r) \cos(\pi/3 - \theta_t)} \quad (2-11)$$

2.3.4. Experimental relationship between the developed constant-volume friction angle and the interparticle sliding friction angle

(Zhou et al., 2002) performed numerical (DEM) and experimental research on the angle of repose of mono-sized coarse spheres. To highlight from this study is the utilization of synthetic granular material as a way of extreme control on the character of the particles. Based on the numerical results, an empirical equation (2-12) was formulated for their angle of repose Θ^* as a function of the particle to particle and particle to wall sliding and rolling frictions ($\mu_{s,pp}$, $\mu_{s,pw}$, $\mu_{r,pp}$, $\mu_{r,pw}$ respectively), the particle diameter d makes that study only applicable within a very specific set of conditions and material tested, as they declared. However, a close examination of this formula reveals ill definition; since for example, for the case of frictionless walls ($\mu_{s,pw} = \mu_{r,pw} = 0$) it is expected that any angle of repose can still be developed due to the friction in the base and between the particles; on the contrary and given the product, the formula yields an angle of repose equal to zero for this case. On the other hand, if for example the rolling coefficient was ignored ($\mu_{r,pp} = \mu_{r,pw} = 1$), which has 40 times less influence than the sliding coefficient for these experiments; then, it is expected a slightly decrease of the angle of repose but according to the expression (2-12) the angle of repose unnaturally doubles.

$$\theta^* = 102 \cdot \mu_{s.pp}^{0.27} \cdot \mu_{s.pw}^{0.22} \cdot \mu_{r.pp}^{0.06} \cdot \mu_{r.pw}^{0.12} \cdot d^{-0.2} \quad (2-12)$$

(Chik and Vallejo, 2005) experimentally studied the angle of repose developed by binary granular mixtures of coarse sand and fine sand. The influence of the friction in the base δ on the angle of repose was investigated. These authors derived the equation (2-13) from evaluating limit equilibrium in a wedge model under the action of the Rankine's active earth pressure. This in an attempt to correlate the interface friction angle δ with the angle of repose β and the angle of shear resistance of the material in the slope ϕ' . They reported this equation performed well for the case of frictionless base; however, this equation seems contradictory given that the summand $(\cos \phi' / \cos \beta)^2$ must be always less than one for the whole expression to be valid.

$$\tan \delta = \frac{\tan \beta \cos^2 \phi'}{2 + 2\sqrt{1 - (\cos \phi' / \cos \beta)^2} - \cos^2 \phi'} \quad (2-13)$$

(Li et al., 2005) developed a simple experimental method for determining the value of the kinetic friction coefficient. This experiment is based on the classical contact mechanics theory between two non adhesive spheres and accessed to a value by mean of force measurements (normal, N , and tangential, F), see Fig. 2-12 and equation (2-14).

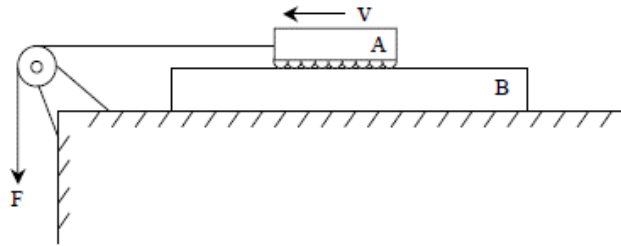


Fig. 2-12 experimental setup for measuring kinetic sliding friction. A: car full of fixed particles, B: base made of the same material composing the particles adapted from (Li et al., 2005).

$$\mu = \frac{F}{N} \quad (2-14)$$

Based on this experimental kinetic sliding friction coefficient between particles, they feed a DEM model to simulate the angle of repose; no other friction parameter was considered (e.g., rolling friction). The angle of repose was measured experimentally using a moving funnel. The material under study were rough glass beads and steel balls. For both materials they got a positive correlation for the angle of repose.

(Froehlich, 2011) measured the angle of repose ϕ_r in stockpiles of rip rap to correlate it with the granulometry of the material. Positive correlations were drawn for D_{50} and the ratio D_{85}/D_{50} , see equations (2-15) and (2-16), but with limited application to specific site conditions and assumptions. The constant ϕ_{r1} accounts for the particle character which qualitatively differentiates three types of shape: round stone, sub-round and sub-angular stone and angular stone.

$$\hat{\phi}_r = \phi_{r1} D_{50}^{0.00778} \quad (2-15)$$

$$\hat{\phi}_r = \phi_{r1} \left(\frac{D_{85}}{D_{50}} \right)^{0.125} \quad (2-16)$$

(Roessler and Katterfeld, 2018) investigated the calibration of a numerical DEM model based on the angle of repose of a natural sand measured with the method of hollow cylinder. They found that no deterministic solution exists in a DEM model since there are infinite pairs of friction coefficients: μ_s and μ_r , which can result in the same angle of repose. An additional important finding from these authors is the fact that the lifting velocity of the hollow cylinder is an important

factor influencing the measurement of the angle of repose; on this regard and according to these authors the more realistic and coherent results were obtained when slow lifting velocities were used (i.e., between 2 mm/s to 8 mm/s).

2.3.5. Discussion on the angle of repose

Researchers has been approaching the angle of repose from multiples frameworks and purposes; however, the fact that still there is no consensus on the standard of measurement and even the fact that a clear definition is still needed, make almost impossible to yield unified conclusions. Indeed, the mere action of compare between studies seems fruitless since each study may be correct but only within its own definitions, assumptions, limitations, and specific applications. The observed scatter showed by Fig. 2-11 is an evidence of previous assertion.

From the literature review about the angle of repose the main identified gaps needing further geotechnical research are:

- a) A general analytical relationship able to correlate the angle of repose with the interparticle sliding friction angle is needed.
- b) There is a need to perform tests in extreme controlled conditions of both, test procedure and particles character, in such a way that only the angle of repose is the variable under observation.

2.4. Prediction of lateral earth pressure

2.4.1. Classical theory

2.4.1.1. At-rest pressure

(Jaky, 1944) based on an equilibrium analysis of an assumed stress field in a pile of loose granular material, by assuming the internal friction angle to be the same pile angle of repose ($\phi' = \beta$) and by adding a further assumption on the shear stress distribution within the soil mass, derived the equation (2-17) for the at-rest pressure. Within the above is also the assumption of slip planes; however, in a natural mass of granular material at critical state (e.g., a pile of soil) no definite failure plane is observed. The assumption of the angle of repose equal to internal friction angle at critical state limits the expression (2-17) to normally consolidated deposits.

$$K_0 = (1 - \sin \phi') \frac{1 + (2/3) \sin \phi'}{1 + \sin \phi'} \quad (2-17)$$

In a later paper, (Jaky, 1948) decided to remove the fraction term from equation (2-17) without any further explanation, to finally arrive at the generally accepted form (2-18).

$$K_0 = 1 - \sin \phi' \quad (2-18)$$

2.4.1.2. Active and passive pressures

The classical theory of earth pressure was initially developed by (Coulomb, 1776), that author set the basic principles still widely used in earth pressure calculations. This as a by-product of his constitutive model for soils: $\tau = \sigma \tan(\phi')$, and his limit equilibrium approach. Then, by assuming

a plane slip surface and by doing equilibrium of forces of a rigid wedge on a ramp that author derived the formula (2-19) for active earth pressure on a retaining wall. The soil-structure interface friction δ , the angle of the internal wall face θ , as well as the backfill inclination α , were considered. Following this same logic for the passive condition yields the formula (2-20). The effect of an increment in friction is to reduce the active pressure and increase the passive pressure.

$$K_a = \frac{\cos^2(\phi' - \theta)}{\cos^2(\theta) \cos(\delta + \theta) \left[1 + \sqrt{\frac{\sin(\delta + \phi') \sin(\phi' - \alpha)}{\cos(\delta + \theta) \cos(\theta - \alpha)}} \right]^2} \quad (2-19)$$

$$K_p = \frac{\cos^2(\phi + \theta)}{\cos^2(\theta) \cos(\delta - \theta) \left[1 - \sqrt{\frac{\sin(\phi' + \delta) \sin(\phi' + \alpha)}{\cos(\delta - \theta) \cos(\alpha - \theta)}} \right]^2} \quad (2-20)$$

For the most common case of a vertical retaining wall (i.e., $\theta = 0$) with horizontal backfill (i.e., $\alpha = 0$) and frictionless soil-structure interface (i.e., $\delta = 0$) equations (2-19) and (2-20) reduce to (2-21) and (2-22).

$$K_a = \frac{1 - \sin \phi'}{1 + \sin \phi'} \quad (2-21)$$

$$K_p = \frac{1 + \sin \phi'}{1 - \sin \phi'} \quad (2-22)$$

(Rankine, 1857) approached the problem of plastic equilibrium within a stress field. He studied the conditions of equilibrium and failure for a differential element of earth pertaining to a semi-infinite continuum which is subjected to uniform deformation in a direction parallel to the top

surface of the soil mass. Then, by assuming plane failure surface and considering certain boundary conditions at the ground surface, Rankine developed his equation (2-23) for active condition and (2-24) for passive condition. However, this theory ignores the friction in the soil-structure interface and considers no inclination of the wall inner face.

$$K_a = \cos \alpha \left[\frac{\cos \alpha - (\cos^2 \alpha - \cos^2 \phi')^{0.5}}{\cos \alpha + (\cos^2 \alpha - \cos^2 \phi')^{0.5}} \right] \quad (2-23)$$

$$K_p = \cos \alpha \left[\frac{\cos \alpha + (\cos^2 \alpha - \cos^2 \phi')^{0.5}}{\cos \alpha - (\cos^2 \alpha - \cos^2 \phi')^{0.5}} \right] \quad (2-24)$$

If the backfill slope is horizontal (i.e., $\alpha = 0$) these equations reduce into the equations (2-25) and (2-26):

$$K_a = \tan^2 \left(45 - \frac{\phi'}{2} \right) \quad (2-25)$$

$$K_p = \tan^2 \left(45 + \frac{\phi'}{2} \right) \quad (2-26)$$

Coulomb and Rankine theories are equivalent for the case of no friction on the inner face of the vertical retaining wall and horizontal backfill [i.e., Eq. (2-25) is equivalent to Eq. (2-21) and Eq. (2-26) is equivalent to Eq. (2-21)], see *Appendix B* for the mathematical proof of this equivalency.

(Rowe, 1963) based on his research on equilibrium of assemblies of particles in contact probed that yield solutions according to his theory are identical to those based on the Coulomb equation in the special case of no volume-change during failure (i.e., $\phi' = \phi'_{cv}$). This observation indicating that the angle of friction ϕ' used by Coulomb and Rankin theories differs from the true coefficient

of solid friction between the particles ϕ'_μ was first made by (Caquot, 1934, p. 12) who called that developed friction at failure “apparent friction”. Moreover, Rowe showed that there exists an angle between failure plane and the principal stress direction which minimizes the energy of the particulate system, namely $(45^\circ - \phi'/2)$, the same angle derived by Rankine. Accordingly, in this critical state of deformation the effective friction at constant volume ϕ'_{cv} can be obtained from (2-27) given the principal stress ratio at failure.

$$\left(\frac{\sigma'_1}{\sigma'_3}\right)_f = \tan^2\left(45^\circ + \frac{\phi'_{cv}}{2}\right) \quad (2-27)$$

2.4.1.3. Discussion on the classical theory

Design of retaining walls, piles, tunnels, and buried structures in general demands knowledge of the lateral earth pressures that will be interacting with the structures or equipment. The seminal methods for the assessing of these pressures acting on structures were developed in the eighteenth and nineteenth centuries by Coulomb and Rankine. These classical theories were built based on idealized models where the retaining structure translates rigid outward or inward and soil moves as a solid wedge on a ramp. Despite the assumption of a straight-line slip-failure surface seems a reasonably valid simplification to approach the problem for the first time, this assumption overlooks the true curved failure surface observed experimentally and consequently produces a wrong distribution of stresses and location of the resultant thrust (Tsagareli, 1965), (Benmebarek et al., 2016), (Stewart et al., 2011).

On the other hand, the at-rest pressure is not better, Jakys' equation of 75 years old involves many arbitrary assumptions and lacks a rigorous demonstration. Numerous studies have confirmed the general validity of the values resulting from Eq. (2-18) (Brooker and Ireland, 1965), (Mayne and Kulhawy, 1982), (Mesri and Hayat, 1993, p. 664), (Michalowski and Park, 2004), (Michalowski, 2005); (Federico et al., 2008), (Lee et al., 2013), (Khosravi et al., 2013). However, (Michalowski, 2005, p. 1429) pointed out "*While the coefficient derived (by Jaky) is indeed a fair depiction of the stress ratio in the 'natural state,' one cannot dismiss the impression that coincidence played a role in rendering this coefficient so close to the true state at rest.*" As well as Michalowski other authors have arrived at the same conclusion agreeing on the lack of demonstration for Eq. (2-18) (Handy Richard L., 1985), (Mesri and Hayat, 1993), (Pipatpongsa et al., 2009). In short, all the evidence suggests the values obtained from Eq. (2-18) are correct (at least within the range of natural soils tested by these authors) but the derivation of Eq. (2-18) itself is unsatisfactory.

In the literature for lateral earth pressure theory, many other contributors appear, but much of these similarly are incomplete, suffer ill-derivation or lack practicality in such a way that at the end seems to prevail the classical theory. Some of these additional approaches are discussed below.

2.4.2. Analytical approaches

2.4.2.1. At-rest pressure

Based on the theory of elasticity, the value of K_0 can be calculated in a fundamental manner from Poisson's ratio ν using Hooke's law and setting lateral strain equal to zero (i.e., oedometer test case), see Eq. (2-28). However, the difficulty with this method lies in the correct estimation of Poisson's ratio.

$$K_0 = \left(\frac{\nu}{1 - \nu} \right) \quad (2-28)$$

(Terzaghi, 1923) based on the fact that the direction of the particle movement in one-dimensional compression is like that in active condition where the lateral support can move away from the soil proposed a definition of the at-rest pressure coefficient K_0 in terms of the Coulomb's active pressure and the mobilized angle shearing resistance ϕ'_o , see Eq. (2-29).

$$K_0 = \frac{1 - \sin \phi'_o}{1 + \sin \phi'_o} \quad (2-29)$$

(Hendron Jr, 1963) reported a comprehensive study on the behavior of sand in one-dimensional compression. He derived a theoretical approach to predict at-rest pressure analytically. The theoretical derivation of Hendron assumes that uniform, well-rounded, dense sand can be approximated by a face-centered array of equal radius spheres. According to this work, if this array of spheres were subjected to one dimensional compression, then the at-rest pressure can be expressed by the equation (2-30).

$$K_0 = \frac{1}{2} \left(\frac{1 + \sqrt{6}/8 - 3\sqrt{6}/8 \sin \phi'}{1 - \sqrt{6}/8 + 3\sqrt{6}/8 \sin \phi'} \right) \quad (2-30)$$

(Pruska, 1978) proposed a continuous network of inter particle stresses whose character depends on the properties and structure of the granular medium. After examining the state of stress of such a medium and assuming deformation of the medium is only due to rearrangement, he developed the expression (2-31).

$$K_0 = \tan\left(45 - \frac{\phi'}{2}\right) \quad (2-31)$$

(Evesque, 1999) combined Rowe's stress dilatancy relation (Rowe, 1962) with a stress strain-incremental modelling to yield an incremental pseudo-Poisson coefficient which varies with the principal stress ratio. Then he solved the Oedometric test case and got the expression (2-32). Where M is the slope of the critical state line according to the hardening soil standard model in the $q-p'$ space. It was shown by this author that values for K_0 compares well with Jaky equation. However, this derivation is independent of the porosity and relies on a so-called pseudo-Poisson ratio of approximate character which yields a final dilation that was not proven to correspond with a critical state condition.

$$K_0 = \frac{1 + \sqrt{8 \cdot M + 9}}{4 \cdot (M + 1)} \quad (2-32)$$

Where:

$$M = \frac{2 \cdot \sin \phi'_{cv}}{1 - \sin \phi'_{cv}}$$

(Huang et al., 2006) using a simple hypoplasticity model proposed the expression (2-33).

$$K_0 = \frac{3 - \sin \phi'_{cv}}{3 + (2 \cdot \sqrt{6} - 1) \cdot \sin \phi'_{cv}} \quad (2-33)$$

(Guo, 2010) found that density and compressibility have a role on the at-rest pressure. Based on this premise, the author developed laboratory tests to determine K_0 of two granular materials; then the experimental data was interpreted using the hypoplasticity model for sand to arrive at the expression (2-34). Where α is a scalar quantity obtained in laboratory.

$$K_0 = \frac{3 - \sin \phi'_{cv}}{3 + \left(\frac{2 \cdot \sqrt{6}}{(1 - D_r)^\alpha} - 1 \right) \cdot \sin \phi'_{cv}} \quad (2-34)$$

(Shen and Liu, 2018) reports the expression (2-35) for the lateral pressure coefficient K_0 derived from a micromechanical analysis. It was revealed that the at-rest lateral pressure coefficient increases with stiffness ratio η and fabric anisotropy β . For the case of incompressible particles expression (2-35) reduces to (2-36) indicating that K_0 is an only function of anisotropy. However, this solution seems incomplete because it does not incorporate the role of the angle of shearing resistance.

$$K_0 = \frac{2 \cdot \beta \cdot \eta}{(3 - 2 \cdot \beta) \cdot \eta + 1} \quad (2-35)$$

Where:

$$K_0 = \frac{2 \cdot \beta}{3 - 2 \cdot \beta} \quad (2-36)$$

2.4.2.2. Active and passive pressures

Analytical methods for active and passive pressures calculation can be classified in five groups: (i) limit equilibrium methods, (ii) theories of plasticity, (iii) theories of elasticity, (iv) arch methods and (v) theories using the critical state concept.

2.4.2.2.1. Limit equilibrium methods

The limit equilibrium model is usually defined as a rigid body on an inclined ramp of known geometry that can be a line, circular or a logarithmic spiral. To get satisfactory solutions in extreme

methods the unknown stresses within the failure line must be kept out from the moment equilibrium equations. This can be done by assuming only certain failure geometry. For example, when assuming a logarithmic spiral the action of these stresses passes through the pole of the spiral and thus these unknown stresses simply cancel out making possible the determination of lateral pressure (Rendulic, 1940), (Chen and Snitbhan, 1975). In the case of large enough radius of the logarithmic spiral, the spiral will tend to become a straight line; this condition is essentially that approached by (Coulomb, 1776). If the angle of apparent friction, θ' , is equal to zero, the logarithmic spiral will be a circle again allowing that simplification of moments (Fellenius, 1948). (Rahardjo and Fredlund, 1984) developed a general formulation for the lateral earth force using the generalized limit equilibrium (GLE) method of slices initially derived for slope stability computations. Accordingly, this adaptation for earth pressure inherits all the known assumptions around the GLE method. Specifically, an assumption regarding the direction or the magnitude of inter slice forces, or the position of the line of thrust are used to render the problem determinate. The lateral force can be contoured on the grid of centers of rotation as a manner of approach the most critical failure surface.

(Liu et al., 2018) proposed a modified logarithmic spiral method to determine the passive earth pressure of a frictional sloped backfill. This method is based on a limit equilibrium analysis assuming a composition of logarithmic spiral and its tangent as the failure surface. The attempt to render the failure line as a composed line formed by a segment of a logarithmic spiral (Prandtl zone) and a straight line reaching the surface (Rankine zone) is not new (Hettiaratchi et al., 1966), (Senoon, 2013), (Lee, 2019).

(Shamsabadi et al., 2007) introduced the Log-Spiral Hyperbolic (LSH) procedure to determine the passive earth pressure evolution as a function of the lateral strain. Sometimes specialized analyses like nonlinear static pushover are required for the seismic design of certain structures (e.g., bridges). Consequently, it becomes important to resolve the nonlinear force-displacement passive capacity provided by the backfill interacting with the structure. Thus, the so-called LSH model is a plane-strain model that was developed to estimate nonlinear force-displacement relationships for abutment walls based on the wall dimensions and backfill soil properties. This model is based on a limit equilibrium method for ultimate capacity that employs logarithmic spiral failure surfaces (Terzaghi, 1943), coupled with a modified hyperbolic soil stress-strain relationship (Duncan and Chang, 1970) to evaluate load-deflection behavior. Unlike classical limit-equilibrium methods, shear resistance of the soil is not assumed to be simultaneously mobilized across the full slip-failure surface, but instead varies as a function of progressive failure and strain localization in the wedge. Each progressive failure surface or “quasi-rupture line” is associated with the mobilized shear resistance and strain of the backfill as depicted in Fig. 2-13.

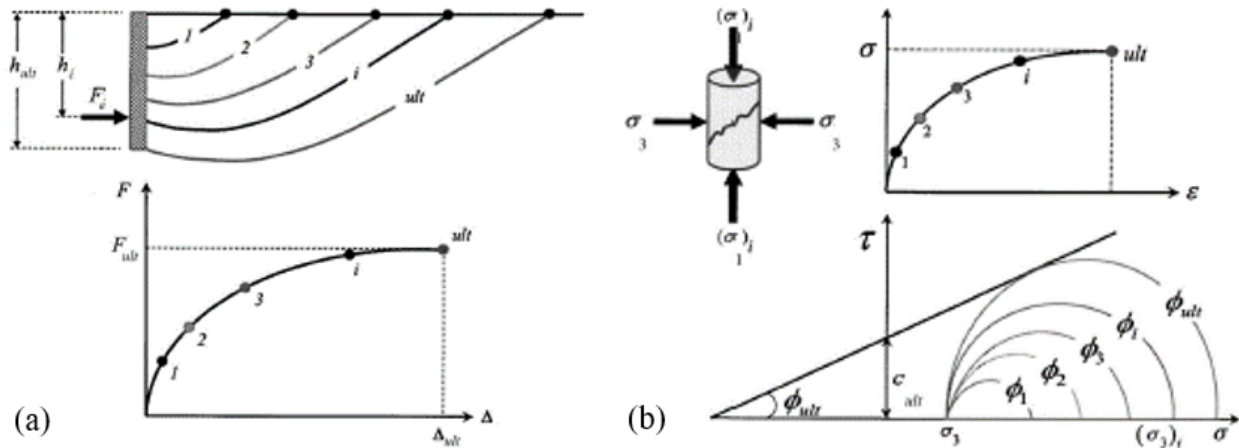


Fig. 2-13 Mobilization of passive resistance according to the Log-Spiral Hyperbolic (LSH) procedure since (Shamsabadi et al., 2007, p. 708): (a) force-displacement relationship; and (b) stress-strain relationship.

2.4.2.2.2. Theories of plasticity

Theories of plasticity assume that a state of failure exists at any point within a certain area (zone of rupture) or on a certain curve (line of failure). By means of this assumption, in connection with the equations of equilibrium is possible to get earth pressure estimations.

(Kötter, 1903) derived a differential equation governing the stresses in a curved failure surface (2-37) by considering the differential equations of equilibrium and the condition of limiting equilibrium at each point. Very little use has been made of Kötter's equation, probably because it is not simple and requires solution by numerical techniques. In two special cases it is possible to indicate simple, exact solutions of this equation, one assuming straight rupture-lines (Rankine) and another considering frictionless or weightless earth where the slip lines of at least one family are

straight, and the solution have closed form. An exact solution based on Kötter's equation satisfies the equilibrium and failure conditions. In equation (2-37) t is $(\sigma \sec \phi')$ and α is the angle between the failure line and the horizontal.

$$\frac{\partial t}{\partial s} - 2 \cdot t \cdot \tan \phi' \cdot \frac{\partial \alpha}{\partial s} - \gamma \cdot \sin(\alpha - \phi') = 0 \quad (2-37)$$

If the general shape of the failure line is known, Kötter's equation, in combination with a boundary condition at one end, enables the determination of the stresses along the failure line. A recent example of the application of this approach is in the work of (Sun and Song, 2016).

Based on Coulomb's failure model (Prandtl, 1920) determined the failure lines corresponding to the pressure of weightless ($\gamma = 0$) (or frictionless soil) on a perfectly rough wall. He found that in this case the rupture pattern (i.e., Prandtl zone) consists of a system of straight lines through the rotation point and a system of logarithmic spirals with the rotation point as their pole. The variation of stress along a spiral rupture line was found by integration of Kötter's equation for the condition of $\gamma = 0$ that can be guaranteed only by making α and t constant in (2-37).

Prandtl zones usually occur in conjunction with Rankine zones. The point of rotation is usually located at some singular point such as, for instance, the point where the backfill surface meets the wall inner face. When the wall is perfectly rough, the Prandtl zone may touch the wall in its entire length. In the general case of $\gamma \neq 0$, $\phi' \neq 0$, no exact mathematical solution exists.

(Sokolovskii, 1965) introduced the method of the Slip-Line Field. In this analysis, it is assumed that failure occurs at constant volumes of soil along slip lines that meet the Mohr-Coulomb failure criterion. This method has the advantage of providing a statically admissible stress state that

satisfies the equations of equilibrium. The Mohr-Coulomb criterion is met by the application of Kötter's equation which solution provides the orientation of the slip lines and its corresponding stresses on the failure surface. Sokolovskii accomplished this solution using numerical integration. However, the calculations needed to get a solution using this method are complex and time-consuming even for simple problems. Consequently, attempts to simplify comes from charts with solutions for certain configurations (Hettiaratchi and Reece, 1974) to addition of simplifying assumptions to oversimplify the original method and by extension the required computations (Reece and Hettiaratchi, 1989).

2.4.2.2.3. *Theories of elasticity*

Theories of elasticity are either exact or approximate. In the last case the three stresses and the two displacements at any point are, in principle, determined by Hooke's law and the equilibrium conditions for a small soil element. However, such "exact" calculations are only approached in very simple cases, ideal conditions and where a reasonable estimation of the Poisson's ratio is possible; for instance, a concentrated force on the surface of a semi-infinite elastic medium (Boussinesq, 1885). The application of theories of elasticity to lateral earth pressure problems involves very simplifying assumptions. It may be assumed, for instance, that the lateral earth pressure increases in direct proportion to the deflection of the wall, the ratio between pressure and deflection being proportional to depth.

2.4.2.2.4. *Arch methods*

(Terzaghi, 1943) introduced the concept of arching action in soils and described it as a common phenomenon encountered in soils. He used this concept qualitatively to explain observed nonhydrostatic pressure distributions of soils against retaining walls.

(Janssen, 1895) developed a differential equation for pressures in a silo by considering force equilibrium for any differential platy element in the silo under the assumption that ratio of lateral to vertical stresses is constant for grain stored in a bin. Janssen's equation has been adopted as a theoretical basis to render approximate solutions for pressure distribution in soils by adapting in some way that differential equation accounting for arching effects observed in silos.

(Spangler and Handy, 1984) based on Janssen's arching theory suggested equations to estimate the non-linear distribution of active pressure on retaining walls.

(Handy Richard L., 1985) also proposed active pressure coefficients and equations for calculating non-linear active earth pressures. This author assumed a catenary arch to describe the path of the minor principal stress. This theoretical result yields a curvilinear distribution typically centered at a height 0.42 times the height of the wall and in close agreement with existing empirical data.

(Harrop-Williams, 1989) also proposed active pressure coefficients and equations for calculating non-linear active earth pressures distributions. This author used the Coulomb's assumption of a straight slip-failure line, and his main expression requires the use of the so-called parameter β which is given as a function of the classical Coulomb's coefficient of lateral earth pressure and additionally is presented as an approximate value only applicable for the translation condition.

(Paik and Salgado, 2003) proposed a formulation for calculating the active earth pressure on a rigid retaining wall that translates horizontally away from the soil considering the arching effects in the retained soil mass. This formulation accounts for the effect of ϕ' and δ on the vertical stress at depth z in the soil. However, this approach adopts the simplifying assumption made by Coulomb considering a straight slip surface sloping at an angle of $(45^\circ + \phi'/2)$ with the horizontal. Additionally, this approach also assumes the trajectory of minor principal stresses in the form of an arc of a circle. The shape of the concave arch or the trajectory of the minor principal stresses is one of the common arbitrary assumptions in this arch method. On this regard, other authors have assumed straight line, elliptic, catenary or parabolic shape (Livingston, 1961), (Walker, 1966), (Stevic et al., 1979), (Handy Richard L., 1985), (Harrop-Williams, 1989), (Cao et al., 2019).

2.4.2.2.5. *Methods using the critical state concept*

It was not possible to find relevant research studying the active pressure in terms of critical state. However, the work developed by (Hanna and Diab, 2017) or (Fang et al., 2002) for the passive condition in terms of critical state indicates a promising line of research that can be continued in the area of active and at-rest conditions. (Fang et al., 2002) concluded that passive earth pressure at a large wall displacement can be adequately approximated by introducing the critical state concept to Coulomb theory. According to these authors, this reasonable and conservative design approach would be more likely to keep the retaining wall on the safe side.

2.4.3. Empirical approaches

Classical theory can predict the magnitude of lateral earth pressure for normally consolidated soil with adequate accuracy. Accordingly, there has not been a need of empirical approaches for this

case. However, the classical framework does not provide means to predict the lateral earth pressure for overconsolidated soil. As a result, the empirical research has been mainly focused on incorporating the *OCR* factor in the prediction of lateral earth pressure.

2.4.3.1. At-rest pressure

Numerous empirical formulas for normally consolidated soils have been developed based on laboratory testing and fitting of data and experience; however, all of them fall around Jaky simplified expression (El Sharif et al., 2011). On the other hand, for the case of overconsolidated soils there is a shortage of research. Since these empirical solutions condense observations of the actual behavior of some specific types of soil, follows is a review of the most relevant empirical relationships for at-rest pressure in overconsolidated granular soils.

(Wroth, 1972a) proposed the empirical relationship (2-38) to calculate the coefficient of earth pressure at rest for overconsolidated sand. This expression is commonly cited in literature despite it seems to be a circular reference. That is, if the expressions for K_0 according to Jaky (2-18) and that from the theory of elasticity (2-28) are plugged into this expression it turns out that $K_0 = K_0$.

$$K_{0-OCR} = (1 - \sin \phi') \cdot OCR - \left[\frac{\nu}{1 - \nu} \right] (OCR - 1) \quad (2-38)$$

(Lazebnik, 1974) proposed the expression (2-39); where: K_a is the Coulomb's active pressure, ρ_s is the unit weight of solid grains of sand t/m^3 , ρ_d is the unit weight of dray soil in t/m^3 , and α is a dimensionless parameter that characterizes roundness and sphericity of the sand particles.

$$K_{0-OCR} = K_a \left(\rho_s \tan \phi' + \frac{\alpha}{\rho_d} \right) \quad (2-39)$$

(Meyerhof, 1976) proposed the equation (2-40) to find a value for the at-rest earth pressure in overconsolidated cohesionless soil.

$$K_{0-OCR} = (1 - \sin \phi') \cdot \sqrt{OCR} \quad (2-40)$$

(Mayne and Kulhawy, 1982) based on a database containing over 170 different soils and statistical analysis of this data proposed the empirical equations (2-41) and (2-42) as a way of predicting the at-rest pressure of normally consolidated and overconsolidated soils.

$$K_{0-OCR} = (1 - \sin \phi') \cdot OCR^{\sin \phi'} \quad (2-41)$$

$$K_{0-OCR} = (1 - \sin \phi') \cdot \left[\frac{OCR}{OCR_{max}^{(1-\sin \phi')}} + \frac{3}{4} \left(1 - \frac{OCR}{OCR_{max}} \right) \right] \quad (2-42)$$

(Sherif et al., 1984) reported experimental results regarding the at-rest stresses against a rigid wall as a function of soil density. The magnitudes and distribution of static at-rest stresses against the retaining wall for loose, medium dense and dense sand was recorded from an instrumented tank. They confirmed that when the backfill behind the wall is densified either compacted or vibrated, the magnitude of the at-rest stresses increases because of densification of the backfill. The total at-rest stress exerted on the wall could be the sum of the stresses due to gravity effects and the locked-in stresses due to densification. Based on fitting of data, the empirical equation (2-43) was proposed to estimate the at-rest pressure for a compacted granular backfill. Where γ_d is the compacted dry unit weight of soil behind the wall and $\gamma_{d(min)}$ is the dry unit weight of soil in its loosest condition.

$$K_{0-OCR} = (1 - \sin \phi') + \left(\frac{\gamma_d}{\gamma_{d(min)}} - 1 \right) \cdot 5.5 \quad (2-43)$$

(Mesri and Hayat, 1993) developed exhaustive laboratory testing on undisturbed specimens from various soft clay deposits and used existing results to observe the behavior of the at-rest pressure in various conditions. For the earth pressure at-rest in sedimented, normally consolidated young deposits K_{0p} as denoted by these authors (i.e., the same K_0 in present work) was adopted the Jaky simplified solution previous validation with experimental results. Then by rewriting in terms of the critical volume friction angle ϕ'_{cv} they propose the empirical expression (2-44). For the overconsolidated condition, these authors adopted the expression according to (Mayne and Kulhawy, 1982) but rewrote it in terms of the critical volume friction angle ϕ'_{cv} in Eq. (2-45).

$$K_{0p} = 1 - \sin \phi'_{cv} \quad (2-44)$$

$$K_{0-OCR} = K_{0p} \cdot OCR^{\sin \phi'_{cv}} \quad (2-45)$$

(Hanna and Al-Romhein, 2008) developed experimental investigation of the at-rest earth pressure of overconsolidated cohesionless soil acting on retaining walls. This is based on a prototype model instrumented in laboratory. The materials under analysis were homogeneous overconsolidated dense, medium, and loose sands. Test results showed that the coefficient of at-rest earth pressure increases with the increase of the OCR . The measured lateral earth pressure according to this study agrees well with that calculated using equations (2-38), (2-40), and (2-41) but only up to an OCR of 3. In view of this and based on these experimental results, these authors proposed the empirical formula (2-46) that better predicts for a wider range of overconsolidation ratios.

$$K_{0-OCR} = (1 - \sin \phi') \cdot OCR^{(\sin \phi' - 0.18)} \quad (2-46)$$

(Lee et al., 2013) approached the at-rest pressure from its correlation with strength. For this, the authors performed basic property, oedometer, and triaxial tests on various granular samples. In this way they obtained values for the steady state angle from triaxial tests conducted up to an axial strain of 20%. Based on these results they concluded that the mobilized friction angle can be presented as a function of the steady friction angle obtained from a triaxial test and dilatancy, see Eq. (2-47). To account for the influence of dilatancy and having observed an experimental correlation between dilatancy and relative density the authors proposed the correction factor in Eq. (2-48) correlated from their experimental data. From this study is interesting to highlight that for high dilatant materials the constant-volume friction angle ϕ'_{cv} can not be obtain at this relatively low level of strain (i.e., ~20%).

$$K_0 = \frac{1 - \sin(C \cdot \phi'_{steady\ state})}{1 + \sin(C \cdot \phi'_{steady\ state})} \quad (2-47)$$

$$C = 0.494 \cdot D_r(\%)^{0.131} \quad (2-48)$$

(Santana and Candeias, 2015) presented an experimental technique using a computer controlled triaxial test to evaluate the coefficient of earth pressure at rest K_0 . As reported by these authors, this method has the advantages of being free from any side friction effects and automatically ensure that diameter change remains zero. By regression analysis these authors determined the characteristic relationship for K_{0-OCR} as a function of the overconsolidation ratio for the Toyoura sand, see equation (2-49).

$$K_{0-OCR} = 0.38 \cdot OCR^{(0.447)} \quad (2-49)$$

2.4.3.2. Passive pressure

(Hanna and Khoury Imad, 2005, p. 984) developed experimental research on overconsolidated sand to investigate the passive condition. The overconsolidation was produced by means of mechanical compaction and then the pressures on the wall were recorded with the aid of an instrumented tank. These experimental results were compared satisfactorily with theoretical predictions. After verification, these authors proposed the empirical equation (2-50) to compute the passive earth pressure in overconsolidated frictional soils accounting for rough soil-structure interface between $1/2 \varnothing' < \delta < 2/3 \varnothing'$.

$$K_{p-OCR} = K_{p-nc} \left[1.5 - \left(\frac{\delta - 25}{100} \right) \right] \cdot OCR^{\sin \delta} \quad (2-50)$$

(Hanna and Diab, 2017) investigated the passive condition applying a numerical model for a retaining wall translating horizontally into a mass of sand. The model was based on the finite-element technique, the constitutive law of the modified Cam-Clay model, and the critical state soil mechanics (CSSM) concept. After validating the numerical model with the available experimental data for normally consolidated and overconsolidated sands, the model was used to predict data from a wide range of parameters. Based on the results obtained numerically, the empirical formulas (2-51) and (2-52) were developed to predict the passive pressure for any given CSSM parameter and overconsolidation ratio.

$$K_p = (97 \cdot \tan \phi' - 21) \left[0.005 \frac{\lambda}{\kappa} + 0.125 \cdot e_{cs} - 1.25\lambda - 1.25\mu + 0.6 \right] + (2.8 \tan \phi' + 0.15) \quad (2-51)$$

$$K_{p-OCR} = K_{p-nc} \cdot R_o^{\alpha \frac{\lambda}{\lambda-\kappa}} \quad (2-52)$$

Where:

$$R_o = \frac{1 + 2 \cdot K_0}{1 + 2 \cdot K_{0-OC}} \cdot OCR$$

2.4.4. Limitations of existing methods

To be fully satisfactory, a general earth pressure theory should meet all the conditions expected from an exact solution, that is to: (i) satisfy equilibrium, (ii) satisfy a yield condition and (iii) verify a stress-strain relationship.

Empirical methods may be very useful, but their application is usually limited to such assumptions and conditions behind their derivations. Loosing in this way capacity of generalization and physical or conceptual connection; clearly, they do not satisfy the requirements. The theories of elasticity reviewed are complex for practical use, they contain very simplifying assumptions and as a result the methods usually yield too inaccurate results. In addition, theories of elasticity rely on the Poisson's ratio which is not easy to estimate for the required density conditions. Analytical derivations can be probed ill-derived or are developed in incomplete frameworks resulting in incomplete or unrealistic predictions of experimental results except for the Jaky simplified expression that coincidentally happens to yield a relatively better prediction for the at-rest pressure of natural soils.

To conclude, none of the known methods satisfies the complete set of requirements for a general active, passive and at-rest lateral earth pressure theory to be exact. Whenever the arbitrary assumption is the internal distribution of stresses, a boundary condition, or the rupture slip-failure geometry, there will be a gap between predictions and actual phenomena.

2.4.5. Descriptive experimental work on lateral earth pressure

Experimental work can show a more realistic view, for example Fig. 2-14 shows a measured diagram for at-rest pressure by SDKS-type pressure cells and the Fig. 2-15 shows the shape of the active failure wedge by Particle Image Velocimetry (PIV) analysis. Clearly there is an important gap between theoretical predictions and nature, specially in the assessment of the magnitude and distribution of pressures. Following is a mention of more relevant research involving descriptive experimental work.

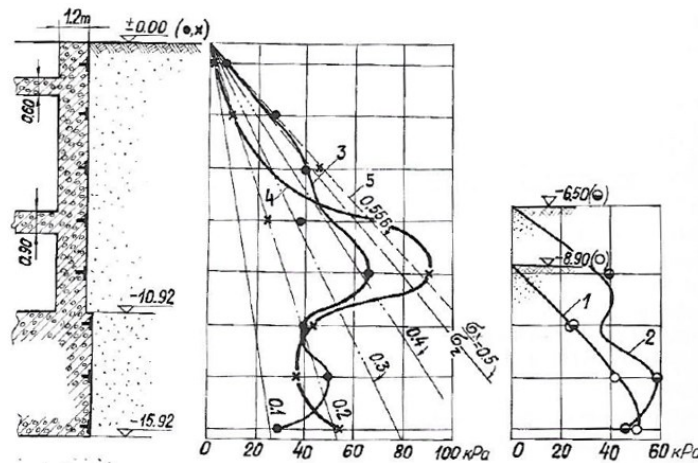


Fig. 2-14 Measured diagrams of lateral earth pressure at rest on a stiff wall. 1: backfill at elevation -8.9 m; 2: backfill at elevation -6.5 m; 3: backfill at final elevation 0.00; 4: 10 months later after completion of wall backfill; 5: calculated from equation (2-39). Adopted from (Lazebnik and Tsinker, 1997, p. 202).

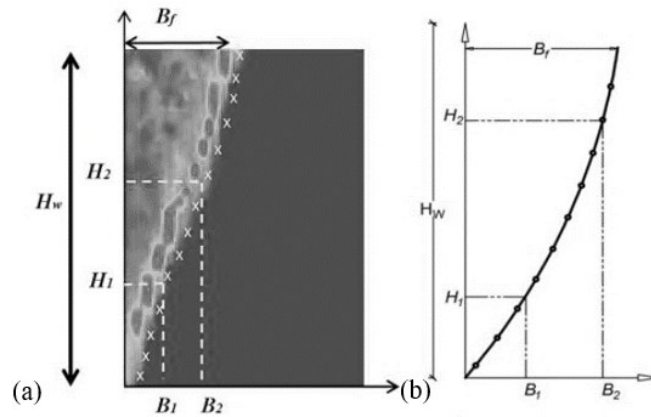


Fig. 2-15 Detection of the failure surface geometry:(a) as plotted on the shear strain map; and (b) as idealized. Adopted from (Cinicioglu et al., 2015).

(Tsagareli, 1965) investigated the lateral pressure of backfill made of loose sand on large retaining wall model (wall height between 2 m and 4 m) with a vertical back face and horizontal backfill surface and determined the magnitude, distribution, and height of resultant force of active earth pressure. This is perhaps the neatest experiment performed and various interesting conclusions can be drawn from it. On the influence of the wall displacement on the failure surface shape Tsagareli reported that little influence was observed to the point that it was possible to use only one type of displacement (i.e., translation). According to this author the experimental curve of the failure surface can be approximated by the power function in the equation (2-53) as a function of the angle of internal friction ϕ' and a coefficient C having the dimensionality of length. Moreover, Tsagareli probes this failure surface defined from equation (2-53) is the same independently of the wall height. This finding explains why research on small scale models is incomplete since the slip-failure line obtained from those small-scale experiments could be fitted by different curves without a noticeable deviation.

$$y = C \cdot (3.6 \cdot \phi' + 0.5)^{\frac{x}{c}} \quad (2-53)$$

According to Tsagareli, the normal earth pressure obtained in these experiments is equal to that calculated by Coulomb's formula for a frictionless soil-structure interface ($\delta = 0$). This indicates that the effect of the friction in the soil-structure interface is to increase the oblique resultant of stresses. Accordingly, the resultant of the total earth pressure was found to be inclined at the same angle of friction in the soil-structure interface. Tsagareli measured an angle equal to $0.75\phi'$ for smooth wall inner face and equal to ϕ' for rough walls. Finally, he determined that the location of the resultant force due to the total lateral stress is around $0.42H$ from the bottom of the wall being H the height of the wall. In conclusion, Tsagareli's experimental results probes that Coulomb theory yields approximate values for the magnitude of active force, but not for the active lateral earth pressure distribution.

(Narain et al., 1969) by means of physical tests investigated the rupture lines and earth pressure distribution on a rigid retaining wall on passive condition due to sand backfill. In accordance with some previous researchers, these authors concluded that the type of wall displacement is one of the important factors affecting the pressures distribution and the geometry of the failure surface. Additionally, they pointed out that the classical earth pressure theories are inadequate to assess passive pressures.

(Matsuo et al., 1978) investigated the lateral earth pressure evolution (at-rest-active-passive sequence) behind a retaining wall of concrete of 10 m height. The displacement of the wall to get passive and active conditions was applied by rotation around the bottom of the wall. Silty sand and slags were used as backfills material. Apparently in this full-scale setup many influencing factors

could result out of the control and measure proper of a laboratory environment. The authors report, for instance, mechanical compaction during and after backfill placement, the apparent cohesion resulted due to the various mechanical friction observed within the large sized shear apparatus, the arching effect due to the static material adjacent to the 1 m-width instrumented wall, the shear strength measured on samples prepared at lower density than that in field, the lack of capacity of the oil jacks, among others. Nevertheless, some important conclusions can be drawn from this work. The lateral pressure is non-linear and can be very irregular in layered soils (i.e., backfill compacted in layers), the active and at-rest coefficients of lateral pressure are lower and higher respectively as expected due to the mechanical compaction, after construction of the backfill the earth pressure grows gradually until it stabilizes at the at-rest condition. Additionally, it was reported an increase of the active pressure with time after the wall was rotated and fixed into its end location, sadly this apparent recovery of pressure was monitored only during a limited time so there is no evidence of its continuity or its eventual stabilization; as a result, no conclusive facts can be established from this reported time-dependant behavior. However, these authors proposed a design philosophy in which they recommend designing any retaining wall against the at-rest lateral earth pressure instead of the active lateral earth pressure, this based on that recovery trend observed.

(Fang and Ishibashi, 1986) developed experimental research to observe the distribution of the active stresses due to a sand backfill behind a rigid wall rotating about the top, the heel and in translation (wall height of 1 m). The experimental results indicated that the stress distribution is nonlinear and that the stress near the fixed point of rotation increases toward the level of the at-rest stress. As a result, the magnitude of the total lateral earth pressure for a rotating wall (either

end fixed) resulted in average about 17% higher from that given by Coulomb's solution. And the point of application of the lateral thrust can be either higher or lower than one-third from the wall base if rotation is about the top or the bottom, respectively. On the other hand, in translation mode the magnitude of the total lateral earth pressure was found to agree with Coulomb's solution and the location of the resultant active force agreed well with the reference level of $0.42H$ obtained by Tsagareli in the same translation mode.

(Stewart et al., 2011) reported experimental results of large-scale tests in passive condition. These authors tested two soil-structure specimens 2.4 m in height with identical characteristics except for the level of compaction of the sandy backfill. One specimen was compacted at relative densities ranging from approximately $D_r = 0.4-0.6$ (medium dense) and the other at a high level of compaction of $D_r = 0.9-1.0$ (very dense). Other than the degree of compaction, the two specimens were essentially identical in terms of dimensions, material gradation, and boundary conditions imposed during testing. The boundary condition imposed on the test was horizontal displacement towards the backfill without rotation (inward translation). The medium dense specimen exhibited nearly elastic-plastic response with negligible strain softening. The peak resistance corresponded to a passive earth pressure coefficient of $K_p = 10$ and occurred with a soil-structure interface friction that was approximately half of the soil friction angle. The very dense specimen exhibited a strongly strain softening response with a peak resistance and followed by a large strain approaching residual capacity. These capacities corresponded to K_p values of 24 and 17 for peak and residual conditions, respectively. As before, the soil-structure interface friction angle was approximately half of the soil friction angle. Measured earth pressure distributions against the wall were found to be linear in accordance with classical theories. The larger obtained coefficients of

passive lateral earth pressure are consistent with the degree of compaction during backfill installation (i.e., the *OCR* effect). The failure surface was reported to initiate near the base of the wall, then it extended downward about 5 cm to 10 cm to finally extend upwards toward the backfill surface 8 m apart from the wall, see Fig. 2-16.



Fig. 2-16 Path of the failure surface after (Stewart et al., 2011, p. 74).

(El-Emam, 2011) developed experimental and numerical investigation of at-rest lateral earth pressure on overconsolidated sandy soil (olivine sand). A specially instrumented container of 1.0 m high was used for this purpose. The sandy soil was compacted by vibration to increase overconsolidation. This author found the horizontal force was about three times the value calculated by classical at-rest earth pressure theory (i.e., Jaky simplified expression) for the sandy soil of $\phi'_{cv} = 46^\circ$ and the vibration compaction procedures used which were reported to be in perfect agreement with an overconsolidation ratio $OCR = 4$.

(Khosravi et al., 2013) conducted a series of physical model tests for the active and at-rest conditions of a rigid retaining wall 0.3 m height subjected to horizontal translation. The behavior of a granular retained soil was investigated experimentally using a set of precise miniature pressure cells and particle image velocimetry. The distribution of shear strain confirms that the failure zone is separated from the at-rest zone by a shear band behind the wall (i.e., a thin zone of failure rather than a surface). The active stress distribution and the at-rest stress resulting from these experiments compares well with corresponding experimental results since (Tsagareli, 1965, p. 198) and (Jaky, 1948) respectively. Additionally, the resultant lateral earth pressure equals that provided by Coulomb's solution.

2.4.6. Discussion on lateral earth pressure

As far as reviewed there is not yet an exact or complete solution for the problem of lateral earth pressure. Apart from the magnitude of the pressure, other factors like an explicit exact derivation, stress distribution, the evolution of lateral pressure with deformation and the effect of the overconsolidation ratio *OCR* are still in research and further development is required.

As explained before, figures resulting from Jaky simplified expression appear valid when compared with laboratory results; however, this expression lacks an explicit derivation. Accordingly, instead of being a well-developed theory, Jaky simplified expression can be described as a useful empirical formula to approach the magnitude of the at-rest pressure for normally consolidated young deposits. Consequently, the theory of at-rest lateral earth pressure is not well founded and is lagged compared with the theory for passive and active lateral earth pressures.

Both classical and contemporary theories are generally based on the Mohr-Coulomb criterion of failure which is fundamentally applicable to a continuum and has shown not being enough for a discrete assembly of particles. A more integral model establishing the coordination between deformation, porosity and shear strength based on the analysis of an assemblage of particles at critical state seems a more realistic approach for granular materials and is a current need. On this scope there is recent research indicating that by applying the critical state concept is possible to treat, in a more advantageous manner, the lateral earth pressure for normally and overconsolidated cohesionless soil (Hanna and Diab, 2017).

Apart from the Mohr-Coulomb criterion of failure, other principles have been adopted like for instance the principle of superposition or soil homogeneity; however, in some point within their derivation all methods resort to at least one additional simplifying assumption that usually lacks conceptual base or phenomenological link, Table 2-1 and Table 2-2 summarize the assumptions and the partial prediction associated to some of the known analytical approaches. An explicit and complete theory for lateral earth pressure on a wall retaining homogeneous overconsolidated cohesionless soil is then an oblige first step toward the appropriate understanding of more complex scenarios.

Method/Theory Name	Common arbitrary assumptions				Predictions		
	Failure shape	Stress distribution	Boundary condition	ν	constitutive model	K_0	K_{0-OC}
(Jaky, 1944)	x	x	x			✓	
Theory of elasticity		x	x	x		✓	

Method/Theory Name	Common arbitrary assumptions					Predictions	
	Failure shape	Stress distribution	Boundary condition	ν	constitutive model	K_0	K_{0-OC}
(Hendron Jr, 1963)		x				✓	
(Pruska, 1978)							
(Terzaghi, 1923)			x			✓	
(Evesque, 1999)				x		✓	
(Guo, 2010)							
(Huang et al., 2006)					x	✓	

Table 2-1 Summary of assumptions and predictions of various analytical approaches for at-rest earth pressure.

Method/Theory Name	Common arbitrary assumptions				Predictions				
	Failure shape	Stress distribution	Boundary condition	ν	Closed form solution	Pressure magnitude	Stress distribution	Failure shape	<i>OCR</i>
(Coulomb, 1776)	x				✓	✓			
(Rankine, 1857)	x		x		✓	✓			
(Kötter, 1903)	x	x	x			✓	✓	✓	
(Sokolovskii, 1965)	x		x			✓	✓		
Limit equilibrium	x	x				✓			
Logarithmic spiral	x	x			✓	✓	✓		
Elasticity		x	x	x		✓	✓		
Arch	x	x			✓		✓		

Table 2-2 Summary of assumptions and predictions of various analytical approaches for active and passive earth pressures.

2.5. Critical state: fundamental concepts and actual practice

2.5.1. Concept of critical state soil mechanics CSSM

Critical state is the ultimate state at which a soil continues to deform at constant stress and constant volume (Roscoe et al., 1958). The elements a model must contain to view this concept are indicated in the Fig. 2-17.

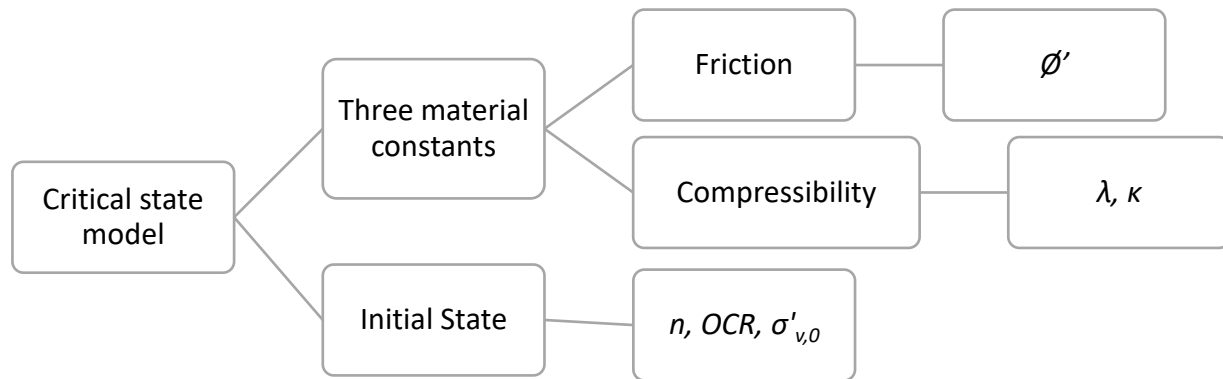


Fig. 2-17 Components of a model viewing the concept of CSSM.

2.5.2. The micromechanical approach

The micromechanics approach for constitutive modeling considers the soil as an assemblage of particles, see Fig. 2-18. Accordingly, this approach resolves soil behavior by integrating the interparticle forces at the particle scale. (Bolton, 2000) posited the micromechanics approach as a tool with the potential of overcome shortcomings in the classical continuum approach to soil mechanics.

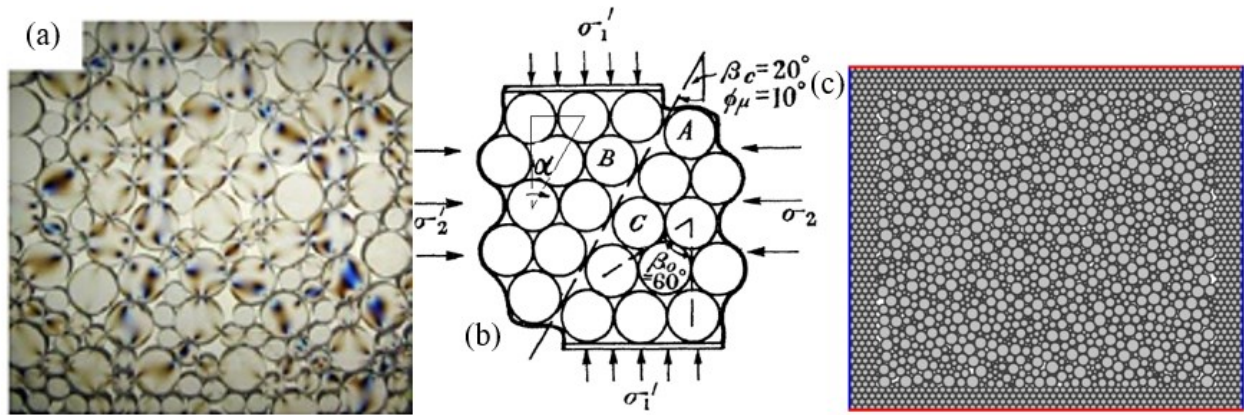


Fig. 2-18 Soil as an assemblage of particles, the main assumption of the micromechanics approach: (a) interparticle network of contact forces, illustrative imagen adopted from (Santamarina and Shin, 2009); (b) illustrative uniform packing investigated by (Rowe, 1962); and (c) DEM model of a polydisperse packing investigated by (Jerves and Andrade, 2016).

The micromechanical approach has been used mainly to investigate soil behavior; the angle of shearing resistance in general; and the definition of the constant-volume friction angle ϕ'_{cv} as a function of the interparticle sliding friction angle ϕ'_μ . The numerals 2.3 and 2.4 presented a sample of those research studies using the micromechanical approach (Caquot, 1934), (Rowe, 1963), (Rowe, 1963), (Hendron Jr, 1963), (Pruska, 1978), (Lee and Herrmann, 1993), (Jerves and Andrade, 2016), (Shen and Liu, 2018). However, few or nil relevant research can be found regarding investigation of lateral earth pressure using this approach.

2.5.3. Stress-dilatancy relationship

(Rowe, 1962) derived the stress–dilatancy relation (7-9) for plane strain conditions by using the micromechanical approach. The deformation in this relation assumes the ratio of energy absorbed

in friction to energy supplied is a constant minimum. Rowe's stress–dilatancy relation is the most widely used for granular material.

(Roscoe et al., 1963) developed another widely known stress-strain relationship based on an energy dissipation equation but specially developed for clays. (Moroto, 1987) applied a limit equilibrium approach of a block sliding on a plane to derive a stress dilatancy relation for the case of soil element under simple shear. In general, most stress-strain models for uniform sand are adaptations based on Rowe's stress-strain relations (Tatsuoka, 1976), (Bolton, 1986), (Xiang-Song et al., 1999), (Hanna, 2001), (Wan and Guo, 2004), (Chakraborty and Salgado, 2010).

2.5.4. Actual practice for the measurement of the plane-strain critical state friction angle $\theta'_{cs,ps}$

The three more common experimental techniques to measure the plane-strain critical state friction angle $\theta'_{cs,ps}$ are: the ring shear test (Sadrekarimi and Olson, 2011), the plane-strain biaxial test (Alshibli et al., 2004) and the static angle of repose (Santamarina and Cho, 2001). This last technique provides a simple but more accessible measure of this soil parameter for the punctual case of a normally consolidated soil under low confining stress and normally consolidated state. The more common techniques used for the measurement of the plane-strain critical state friction angle $\theta'_{cs,ps}$ by means of the direct measurement of the static angle of repose β were presented in detail in the numeral 2.3.1 or summarized in Fig. 2-19.

In the absence of a standard plane-strain test, the direct shear test or the triaxial test has also been used for the indirect estimation of θ'_{ps} (Taylor, 1948), (Davis, 1968), (Rowe, 1969), (Dietz, 2000),

(Hanna, 2001), (Lings and Dietz, 2004), (Lee et al., 2013) in spite of being an inappropriate stress-strain symmetry.

Previous shortcomings are still under development, for instance, some researchers have proposed the application of torsional ring shear test like that currently standardized for clay (ASTM D6467) but for cohesionless soils. The later by developing a new apparatus specially designed to cope with sand and devised to apply any given confinement pressure (Garga and Sedano, 2002), (Sadrekarimi and Olson, 2009). For instance, the critical state friction angle ϕ'_{cs} of three natural sand samples was successfully measured using one version of this experimental ring shear device and the results were satisfactorily cross validated by means of the direct measurement of the static angle of repose on a pile of sand (Sadrekarimi and Olson, 2011). Despite ring shear test for cohesionless soil is a promising laboratory technique, this seems to be still under development and no standard or commercial apparatus is currently available.

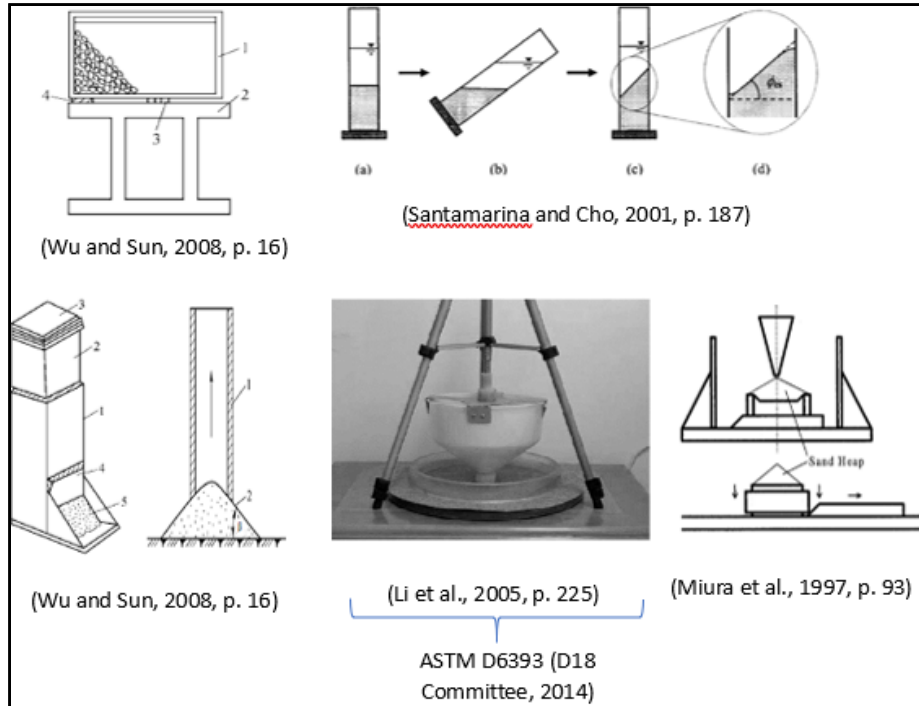


Fig. 2-19 Common techniques for the measurement of the plane-strain critical state friction angle $\phi'_{cs,ps}$ through the measurement of the static angle of repose β .

2.5.5. Actual practice for the measurement of the interparticle sliding friction angle

$$\phi'_\mu$$

The atomic force microscope (AFM) can measure the interparticle sliding friction angle ϕ'_μ of grains between clay size to fine sand size. The basic principle of the AFM is a cantilever beam of known stiffness (i.e., a proximal probe method of detection, see Fig. 2-20) used to detect normal and lateral forces between the grains surface at the contact point between two grains or between a grain and a flat surface. (Jones, 2003), for instance, reported AFM results for friction on artificial particles with size in the range 0.04 mm to 0.20 mm. However, apart from its limitation in the

maximum size of grain, this technique possesses some shortcomings like cost, the need of complicated calibration and difficulties in the appropriate manipulation of single grains (Tyrrell and Cleaver, 2001).

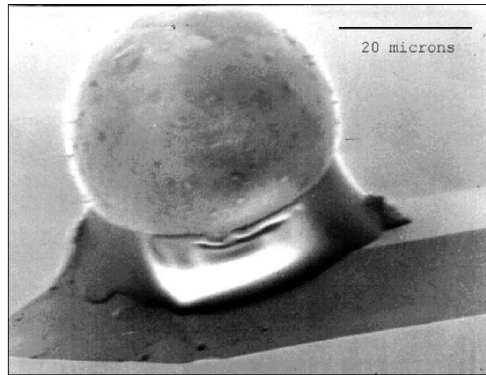


Fig. 2-20 Scanning electron microscope micrograph of a glass microsphere mounted on an AFM cantilever beam. Illustrative imagen adopted from (Tyrrell and Cleaver, 2001).

Experimental devices to develop direct shear test between two grains have also been developed for the measurement of the interparticle sliding friction angle θ'_μ (Cavarretta et al., 2011), (Senetakis et al., 2013), see Fig. 2-21.

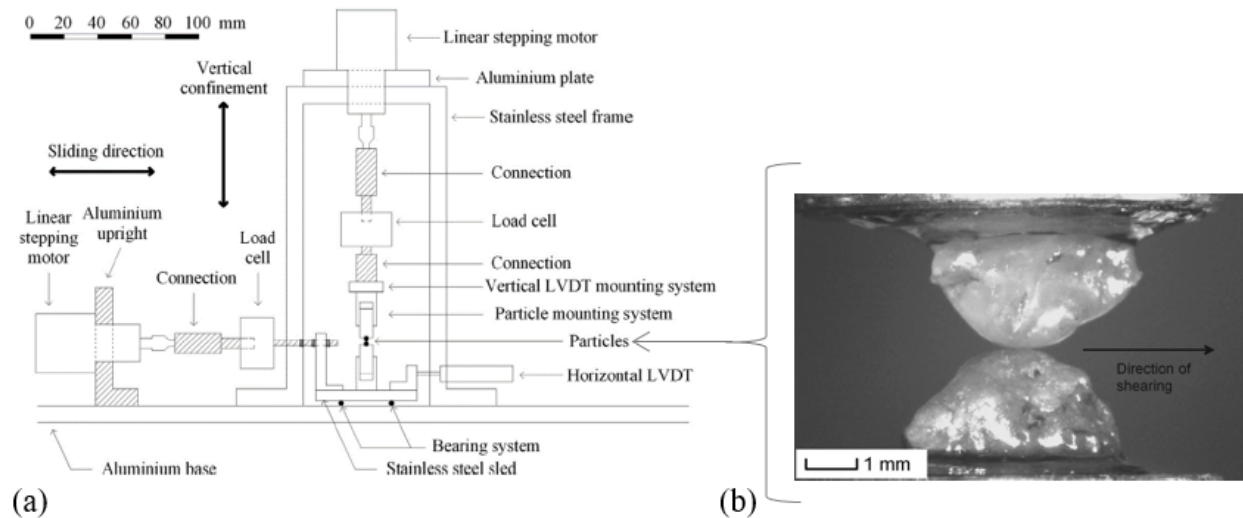


Fig. 2-21 General scheme of inter-particle loading apparatus: (a) illustrative sketch adopted from (Senetakis and Coop, 2014); and (b) illustrative photo of the contact between the two tested particles adopted from (Senetakis et al., 2013).

This kind of experiment is based on the same classical contact mechanics theory between two non-adhesive spheres and access to the tangential friction by means of force measurements (the normal N and the tangential F), as indicated by Fig. 2-22(a) and Eq. (2-54). The main drawback of this technique is its high cost and the lack of representativeness since only two grains are involved. For the case of uniform artificial particles more than two particles can be tested in a single test mitigating in this way the problem of representativeness (Li et al., 2005). However, this last approach is more difficult for natural soils due to intrinsic difficulties in sample preparation. An alternative for the determination of friction is the tilt test, in this case the same blocks “A” and “B” can be tested but in a tilt-test device as shown in Fig. 2-22(b). The angle of inclination of the table

α at the time where sliding starts (t_0) will provide the same kinetic friction angle but this time by means of the expression (2-55).

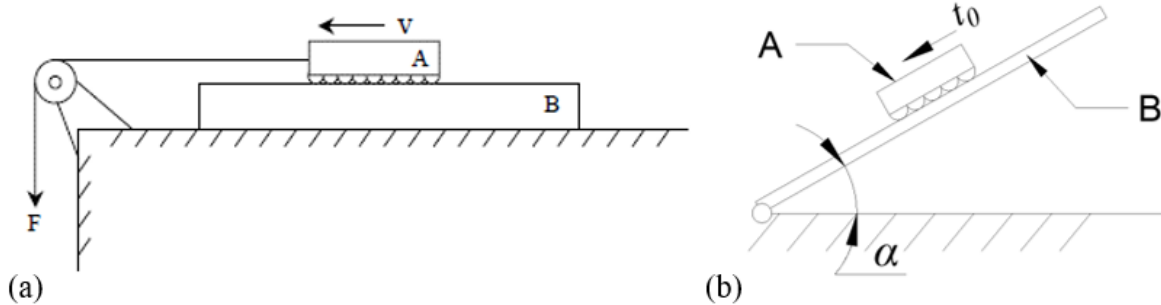


Fig. 2-22 Experimental setup for the measurement of the interparticle sliding friction angle ϕ'_μ : (a) measurement based on forces; and (b) measurement based on the sliding angle. A: test block full of fixed artificial particles, B: base having the same sliding friction of the particles; illustrative sketch adopted from (Li et al., 2005).

$$\mu = \frac{F}{N} \quad (2-54)$$

$$\mu = \tan \alpha \quad (2-55)$$

2.6. General conclusion from the literature review

Numerous studies have confirmed the empirical validity of the values resulting from Jaky simplified expression for K_0 [see formula (2-18) (Jaky, 1948)]; however, many authors agree on the lack of demonstration of this semi-empirical expression. Apart from the previous, equation (2-18) depends solely on the effective angle of shearing resistance ϕ' . Although such use is

appropriate when soil is normally consolidated, the magnitude of the earth pressure coefficient is always affected by stress history, represented by the overconsolidation ratio *OCR* as revealed by (El-Emam, 2011) and (Mayne and Kulhawy, 1982).

In theory, when soil is overconsolidated, the passive and the at-rest earth pressure coefficients exceed the value calculated by using classical theory and increases as the *OCR* increases. Many researchers, including (Hanna and Khoury Imad, 2005), (Wroth, 1972b), (Mayne and Kulhawy, 1982), (Hanna and Al-Romhein, 2008), (Hanna and Diab, 2017) and (Meyerhof, 1976) have noticed the effect of the *OCR* and thus proposed empirical equations to calculate passive and at-rest earth pressure coefficients incorporated with the *OCR*'s effect. Nevertheless, a theoretical framework for this inclusion of *OCR* is still missing.

On the other hand, the current theory for active and passive coefficients is based on an arbitrary geometry for the slip-failure surface, the more common assumption being a planar failure surface. This assumed geometry differs substantially from the geometry observed experimentally and consequently produces a wrong distribution of stresses and location of the resultant thrust behind the wall (Tsagareli, 1965), (Benmebarek et al., 2016), (Stewart et al., 2011). This is an indication that the theory for active and passive conditions is still incomplete, and more research is required specially in to capture the nonlinearity natural of this phenomenon.

Finally, current theory focuses on the stress part associated to the lateral earth pressure theory ignoring in this way the continuous stress-strain evolution proper of the actual phenomenon. Lateral earth pressure is more than the pressure by itself; in fact, this phenomenon is a continuous soil-structure interaction that should be better presented incorporating the associated strain.

Chapter 3: Experimental Investigation

3.1. General

Table 3-1 presents the summary of experimental tests developed in present study. Description of methodology and raw results for each of the tests executed to measure the soil parameters and lateral stresses are also presented in this chapter.

Experiment description	Material	Qty.	Targeted
Interparticle sliding friction angle	UHMW Polyethylene	27	$\phi'_{cv,ps}$
from the friction-tester device	Sandpaper P50	27	
	Silica sand	27	
Plane-strain critical-state friction angle	UHMW Polyethylene	5	$\phi'_{cs,ps}$
from the flat device	Sandpaper P50	5	
	Silica sand	5	
Angle of repose from the fixed base	Silica sand	5	β
and moving funnel device			
Angle of repose from the fixed base	Silica sand	5	
and fixed funnel device			
	Silica sand compacted by the standard Proctor energy	7	$K_{\theta-OC}$

Experiment description	Material	Qty.	Targeted
Lateral earth pressure on soil using an instrumented standard 4” CBR mold and surcharge transferred by a piston	Silica sand compacted by the reduced modified Proctor energy	6	
	Silica sand compacted by the modified Proctor energy	5	
	Non compacted Silica sand	6	K_0, K_{0-OC}

Table 3-1 Summary of the experimental program developed for present research.

3.2. Silica Sand: basic properties

Silica sand has been consistently used by former researchers at the geotechnical laboratory of Concordia University; consequently, our research team has gained specific knowledge on this granular material. Here some of the basic properties collected from this data set for silica sand.

(Di Camillo, 2014), (Vakili, 2015) and (Alharthi, 2018) performed laboratory tests (e.g., sieve analysis, specific gravity tests, relative density, and direct shear tests) on silica sand to determine its granulometric properties and angle of shearing resistance at different relative densities.

Results of the sieve analysis presented in Fig. 3-1 were compared by (Alharthi, 2018) to that obtained from (Vakili, 2015) who also performed the sieve analysis test on the same type of soil, indicating that the soil was uniformly graded, with a uniformity coefficient (C_u) and coefficient of curvature (C_c) of 1.88 and 1.01, respectively. According to the Unified Soil Classification System

(USCS), the soil is classified as “SP”. The compaction characteristics for this “SP” group according to USCS classifieds as good. When compacted this soil exhibits very little compressibility and expansion as well as reasonable stability when dense.

A specific gravity (G_s) test was also performed, which revealed specific gravity to be 2.62, and the maximum and minimum unit weights were 17.16 kN/m^3 and 13.98 kN/m^3 , respectively. The physical properties of silica sand are summarized in Table 3-2 adopted from (Alharthi, 2018).

Direct shear tests were also performed on silica sand. By calculating the weight of the soil required to fill the shear box for a specific relative density and by applying different compaction energy, four different relative densities were achieved and tested; 30%, 45%, 60%, and 75%. The shear box results appear in Table 3-3 and Fig. 3-2, adopted from (Alharthi, 2018).

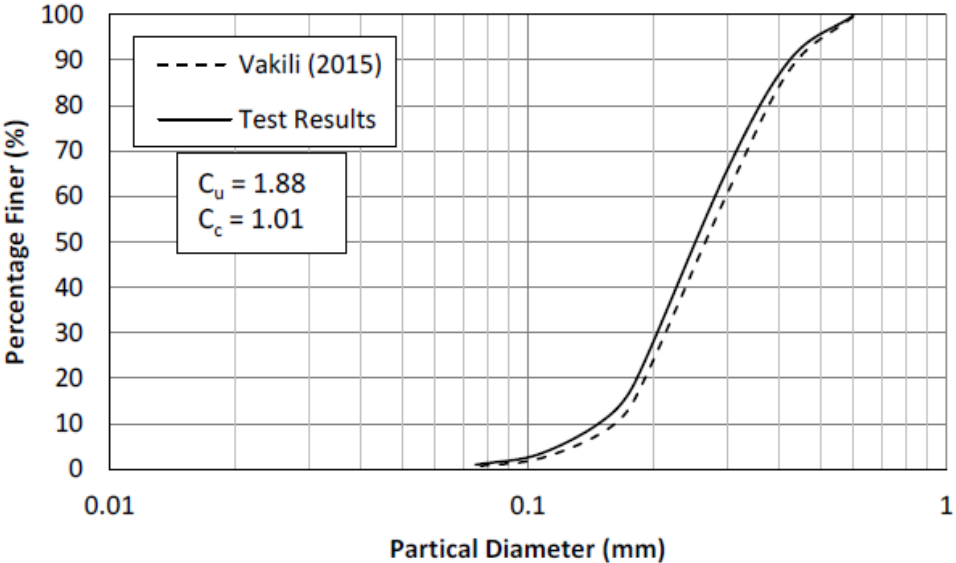


Fig. 3-1 Particle size distribution for silica sand 40-10 adopted from (Alharthi, 2018).

Test	Soil Property	Silica sand 40-10
Sieve Analysis Test	d_{10} (mm)	0.15
	d_{30} (mm)	0.21
	d_{50} (mm)	0.26
	d_{60} (mm)	0.29
	Coefficient of uniformity (C_u)	1.88
	Coefficient of curvature (C_c)	1.01
	Soil Classification (USCS)	SP
Specific Gravity Test	Specific Gravity (G_s)	2.62
Maximum and Minimum Unit Weight Test	Maximum Dry Unit Weight (kN/m^3)	17.16
	Minimum Dry Unit Weight (kN/m^3)	13.98
	Minimum Void Ratio	0.50
	Maximum Void Ratio	0.84

Table 3-2 Silica sand physical properties adopted from (Alharthi, 2018).

Relative Density	Void Ratio	Angle of Shearing
30%	0.74	32.96
45%	0.69	34.93
60%	0.63	36.80
75%	0.58	38.79

Table 3-3 Relative density and corresponding angle of shearing resistance for silica sand 40-10 adopted from (Alharthi, 2018).

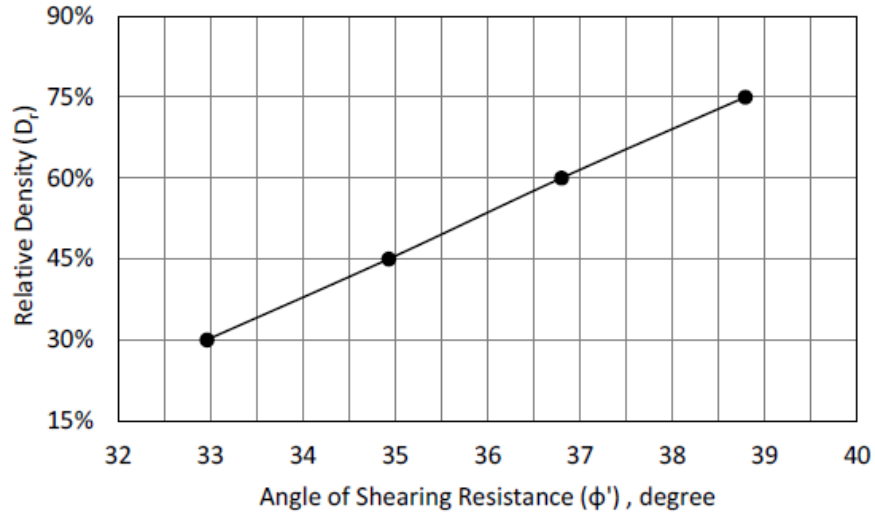


Fig. 3-2 Relative density and corresponding angle of shearing resistance adopted from (Alharthi, 2018).

(Hanna and Diab, 2017) based on (Hanna, 2001) reported compressibility properties of silica sand as shown in Table 3-4.

Sand condition	Relative density (%)	λ	κ
Loose	21	0.27	0.00720
Medium	52	0.25	0.00625
Dense/Medium	75/52	0.25/0.24	0.00581/0.00600
Medium/Dense	52/75	0.24/0.25	0.00600/0.00581
Dense	75	0.24	0.00558

Table 3-4 Compressibility properties for silica sand adopted from (Hanna and Diab, 2017).

3.3. Experimental investigation for critical state

3.3.1. General

As concluded in the literature review (see numeral 2.3.2), there are various external influencing factors affecting the measurement of the angle of repose. Among them, we have the interaction of the granular material with the measuring device, the added energy due to a given height of falling, excessive height of the center of gravity of the falling mass or the added acceleration when rotation is involved. Due to these influencing factors, measurements of the static angle of repose usually lack precision and repeatability. This unfavorable situation is added to the fact that the range of the angle of shearing resistance ϕ' of naturally occurring sands ($20^\circ < \phi' < 40^\circ$) is too narrow if compare with the complete theoretical domain of the angle of shearing resistance ($0^\circ \leq \phi' \leq 90^\circ$), see Fig. 3-3 and the state of the art tends to concentrate in this narrow segment promoting a biased view of the problem. These two problems are addressed by the experimental techniques herein adopted; these techniques are now explained in detail.

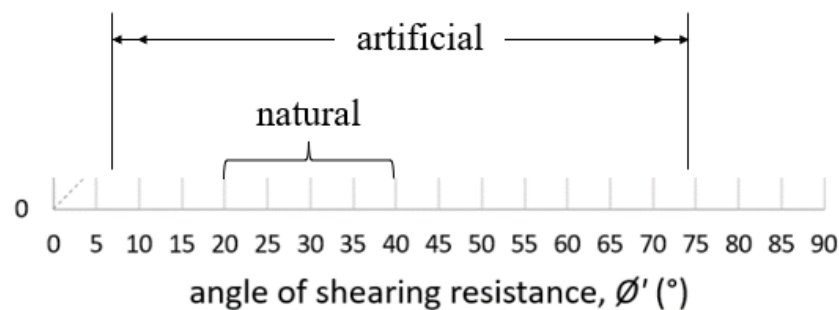


Fig. 3-3 Theoretical domain for the angle of shearing resistance contrasting the narrow window offered by natural sands only with the wider window that can be accessed if artificial granular materials are involved.

3.3.2. Methodology of the experimental tests for critical state shear strength parameters

This experimental investigation uses the specific case of critical state known as *the static angle of repose* β , see Fig. 2-3 and numeral 4.2.2. In this case the initially available friction is the interparticle sliding friction angle $\phi'_{initial} = \phi'_{cv,ps} = \phi'_\mu$ and the finally developed plane-strain critical state friction angle is the static angle of repose $\phi'_{final} = \phi'_{cs,ps} = \beta$.

From the geometry of the theoretical relationship between the plane-strain critical state friction angle $\phi'_{cs,ps}$ and the plane-strain constant-volume friction angle $\phi'_{cv,ps}$ [see Eq. (4-8) and Fig. 4-2], it seems reasonable to prove experimentally the three most characteristic points of Fig. 4-2. Consequently, three granular materials were used in this investigation, namely natural sub-rounded silica sand (see numeral 3.2) and two artificial cohesionless granular materials, one coated with ultra-high molecular weight (UHMW) polyethylene and the other coated with P50 sandpaper. The two artificial cohesionless granular materials were intentionally selected to target the two zones where the curve defined by Eq. (4-8) deviates the most from the equality line drawn in Fig. 4-2. The silica sand represents a natural material and targets the zone where the curve defined by Eq. (4-8) crosses the equality line drawn in Fig. 4-2.

The two artificial cohesionless granular materials were created from wooden discs with smooth lateral surfaces of approximately 25 mm diameter and 5 mm thickness. The curved surface of these wooden discs was coated with films of UHMW polyethylene and with P50 sandpaper to provide low- and high-friction materials, respectively. Table 3-5 summarizes the specific testing program followed during the experimental investigation for critical state.

Experiment/Test description	Material	Qty.	Targeted variable (Purpose)	Methodology description
Plane-strain critical state friction angle from the <i>flat device</i>	UHMW Polyethylene P50 Sandpaper Silica sand	5 5 5	$\theta'_{cs,ps}$	See numeral 3.3.2.1
Static angle of repose from the <i>fixed base</i> and <i>moving funnel device</i>	Silica sand	5	β (to discuss the influence of added inertial forces)	See numeral 3.3.2.2
Angle of repose from the <i>fixed base</i> and <i>fixed funnel device</i>	Silica sand	5		
Plane-strain constant-volume friction angle from the <i>friction-tester device</i>	UHMW Polyethylene P50 Sandpaper Silica sand	27 27 27	$\theta'_{cv,ps}$	See numeral 3.3.2.3

Table 3-5 Summary of the experimental investigation program to validate the theoretical model for critical state.

3.3.2.1. Methodology for the measurement of the plane-strain critical state friction angle $\phi'_{cs,ps}$ using the flat device

The rotary box method (Wu and Sun, 2008, p. 17) was adopted to measure the static angle of repose β or the plane-strain critical state friction angle $\phi'_{cs,ps}$. Note that the determination of the critical state friction angle in cohesionless soils by means of the static angle of repose is not new (Santamarina and Cho, 2001), (Atkinson, 2017, p. 135). Fig. 3-4(a) shows a conceptual sketch of the rotary box test, and Fig. 3-4(b) shows the actual rotary box developed to measure the static angle of repose. This apparatus consisted of a container made with two parallel sheets of rigid, properly framed transparent glass measuring 890 mm (width) \times 500 mm (height) and a 6 mm internal slot. An air gap in the order of 0.5 to 1.0 mm was provided between the discs and the container walls to eliminate any source of lateral constrain and facilitate the free sliding of particles within the flat container. The frame was attached to a stable, leveled base by means of hinges. The box rotated automatically at a very slow speed of 0.05 rpm via a mechanism composed of two dampers of 200 N each and a linear actuator with a capacity of 1500 N.

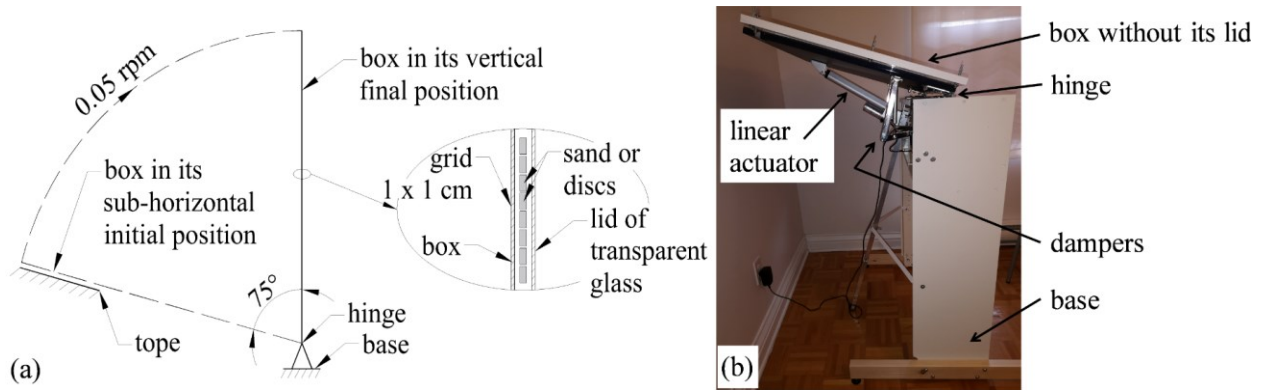


Fig. 3-4 Automatic rotary box: (a) conceptual cross-sectional sketch; (b) actual lateral view.

This mechanism allowed the gradual “activation” of gravity from the initial sub-horizontal position toward the final vertical position. This flat-angle-of-repose-device was developed to measure the static angle of repose $\beta = \phi'_{cs,ps}$ of both silica sand and artificial granular materials in a flat setup that duplicates the main characteristics of the theoretical model (i.e., a two-dimensional plane strain condition). During the rotation process, the free face of the silica sand formed a stable slope. The final steeper angle of this slope [delimited by the black arrows marking toe and crest in Fig. 3-6(b)] with the horizontal was recorded as the static angle of repose. For the two artificial cohesionless granular materials, the included angle of repose was measured as the static angle of repose, as indicated in Fig. 3-6(a). The same structure of the unitary pack of particles indicated in Fig. 4-1(b) was physically replicated for each tested slope, as highlighted in Fig. 3-5(c).

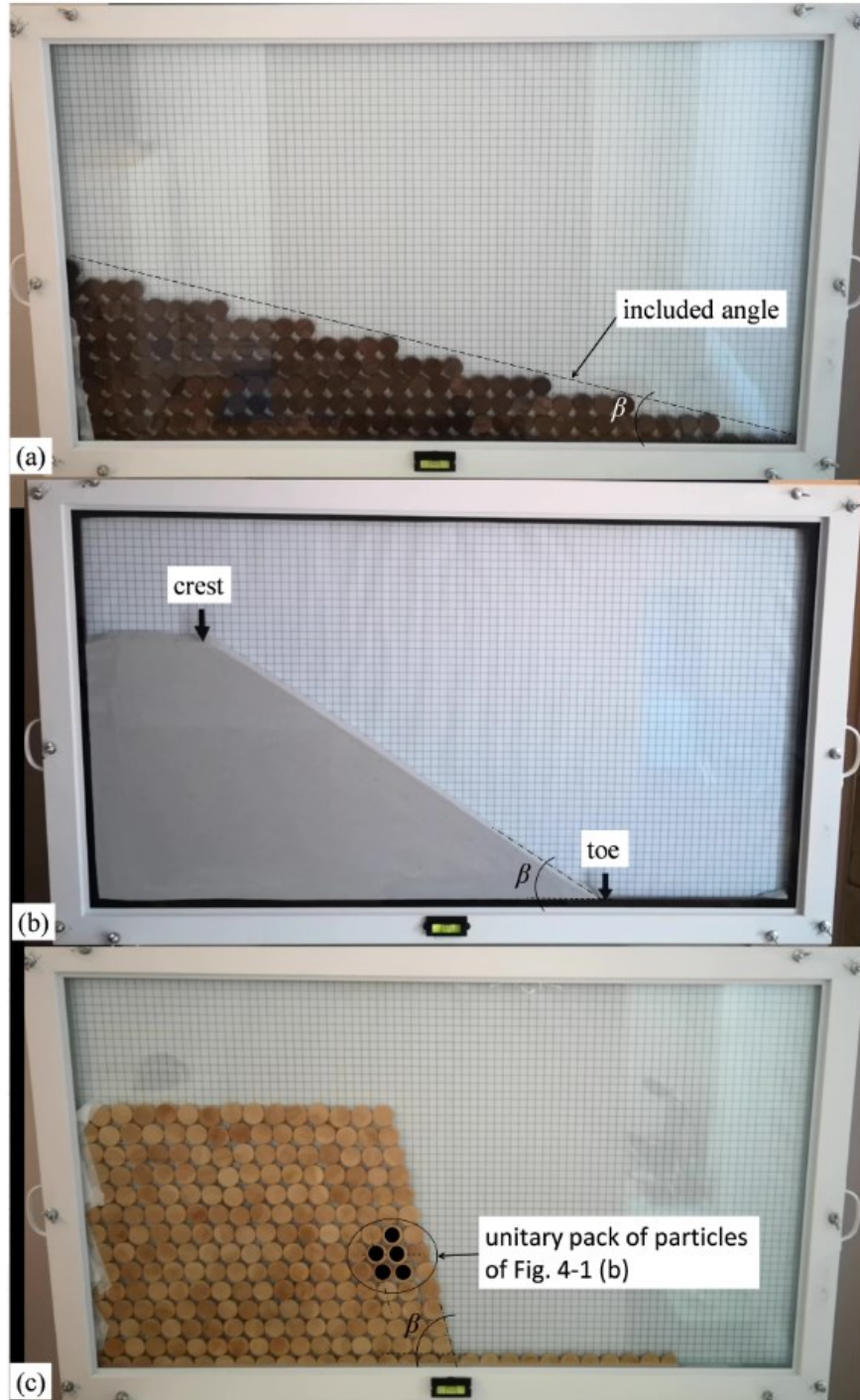


Fig. 3-5 Final vertical position of the rotary box showing the angle of repose β in the sub-step #6 (of the sequence shown in Fig. 3-6) corresponding to a single test for each of the three cohesionless granular materials: (a) UHMW polyethylene; (b) silica sand; and (c) P50 sandpaper.

The procedure followed to measure the angle of repose using this automatic flat-angle-of-repose-device resembles a slope stability analysis. The principle of this approach lays in the definition of the angle of repose as a limit; that is, a slope steeper than the angle of repose is not possible (i.e., collapse) while a slope flatter than the angle of repose remains stable. The measurement of the angle of repose was then approached by using the following procedure, (see Fig. 3-6):

- a) With the flat-angle-of-repose-device in its collapsed position a slope was built at a given arbitrary initial angle of the granular material in its loosest density (ASTM D4254-16, 2016a).
- b) Then the automatic flat-angle-of-repose-device was turn on to tilt up the display very slowly (i.e., 0.05 rpm) up to the vertical. A record on whether the slope collapses or remain stable is taken at the end of each test.
- c) If the slope in the previous step collapses steps “a” and “b” are repeated with a flatten slope. On the contrary, if the slope in the previous step remains stable steps “a” and “b” are repeated with a steeper slope.
- d) Finally, step “c” was repeated until closing the window around the angle of repose (i.e., the limit) to an interval equal or less than 3° , see an illustration of this sequence in the Fig. 3-6. The resultant angle of repose is finally adopted to be the average between the two closets slopes found bounding the limit (e.g., slopes 5 and 6 in Fig. 3-6) and the associated deviation is adopted to be the half of the difference between these to closets slopes (i.e., $SD \leq 1.5^\circ$).

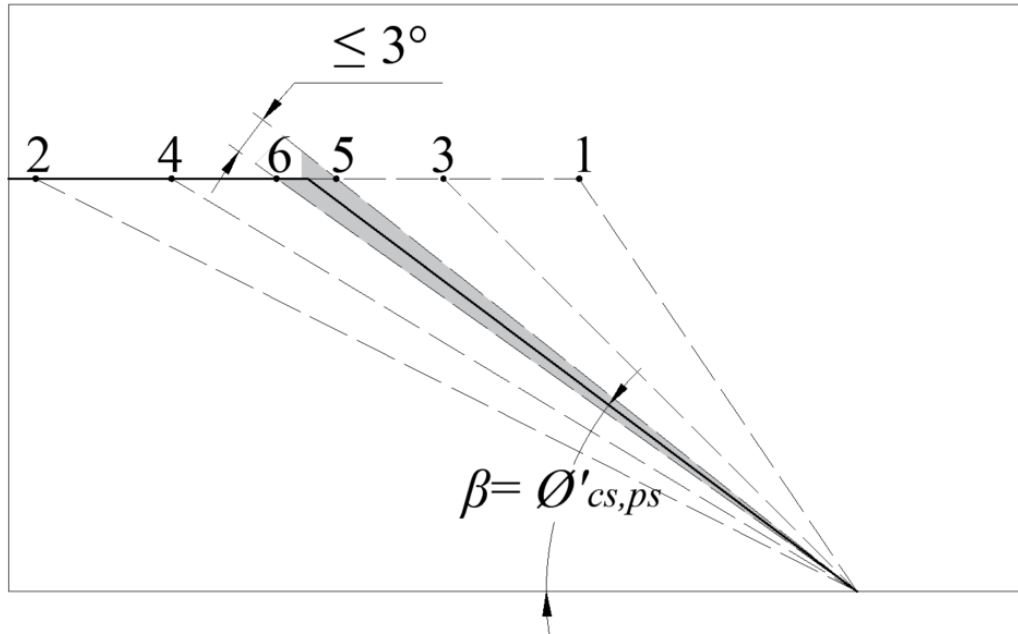


Fig. 3-6 Illustrative sequence used to approach the plane-strain critical state friction angle by means of the static angle of repose $\beta = \theta'_{cs,ps}$ using the automatic flat-angle-of-repose-device.

3.3.2.2. Methodology for the measurement of the plane-strain critical state

friction angle $\theta'_{cs,ps}$ using the flat device using funnel-based techniques

The techniques adopted to measure the static angle of repose $\beta = \theta'_{cs,ps}$ in silica sand were two: one is known as the *fix funnel with fix base* and the second is the *moving funnel with fix base*. These two techniques permit the accommodation of a pile of sand on which the direct measurement of the angle of repose can be done (see numeral 2.3.1.3). A funnel with a fixed base of 260 mm diameter was implemented, see Fig. 3-7. A linear actuator of 1500 N with auto-regulated linear speed between 0 to 5.7 mm/s was used to rise the funnel at the same pace of the pile formation, this as a measure to keep as short as possible the free fall height or vertical distance between the funnel and the peak of the pile. The previous with the aim of mitigating the potential additional

momentum transferred to the particles. A small free fall height of 3 cm to 4 cm was controlled during the *moving funnel* tests and a maximum free fall height of 13.1 cm was measured during the *fixed funnel* test. After having the pile of sand, the measurement of the angle of repose was done by means of an inclinometer of +/- 0.2 degrees accuracy.



Fig. 3-7 *Fixed base and moving funnel* device after a single test on silica sand.

3.3.2.3. Methodology for the measurement of the plane-strain constant-volume friction angle $\phi'_{cv,ps}$ using the incline plane method

The inclined plane method (Vosler, 2006), (ASTM D06 Committee, 2007) was adopted to measure the sliding friction angle $\phi'_{cv,ps}$. The automatic friction tester used in the present investigation (see Fig. 3-8) rotates at a low speed (i.e., less than or equal to 1 rpm) to facilitate precise measurements. This device was equipped with an infrared reflective sensor working as a photoelectric switch,

calibrated to stop and save the angle read by an inclinometer ($\pm 0.2^\circ$ accuracy) at the point where the upper block started to slide downward. This infrared reflective sensor was located 3–6 mm away from the upper block, which permitted a contactless setup. A speed controller to facilitate the initial leveling and a separate electric circuit serving as limiting switch were also added to make the operation easier.

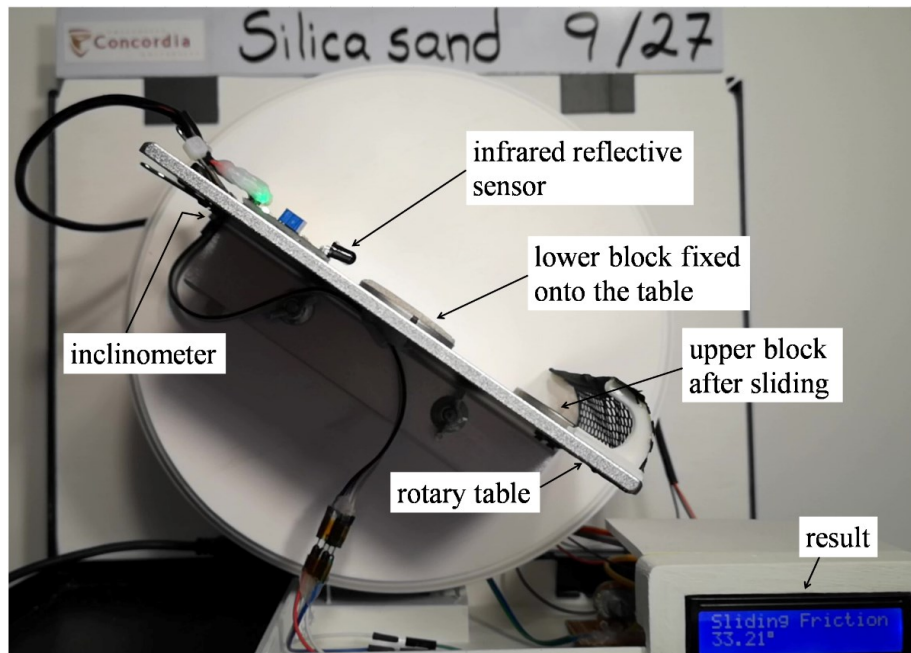


Fig. 3-8 Friction tester during a single tilt-test for measuring sliding friction in silica sand.

The raw material used to cover the curved surface of the discs for the two artificial cohesionless granular materials came in sheets facilitating the direct application of the inclined plane method. For the natural sand, blocks of silica sand were fabricated using 3D printing or additive manufacturing and covered with a circular tin of 36 mm of diameter and 3 mm depth. Fig. 3-9(a) shows the final appearance and design of these silica sand blocks. As can be seen in Fig. 3-9(b),

this test approach mitigates any kind of dilation, because any two blocks are aligned to a common tangent plane. As a result, the shear failure occurred tangentially at the grain contacts and parallel to the shear force direction in a purely constant-volume manner. To guarantee this condition, the upper block was checked prior to the test to ensure that it was firmly and uniformly in contact with the surface of the lower block; that is, the upper block did not wobble when pressed along the edge. The detailed step-by-step test procedure is described in two parts in the following numeral, the first part for sample preparation and the second part for the test itself.

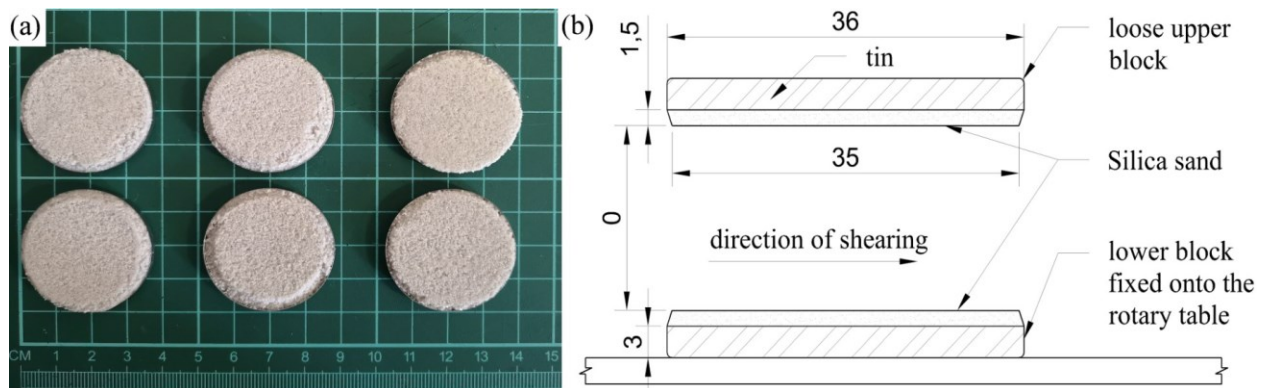


Fig. 3-9 Blocks of silica sand: (a) front view of six actual blocks of silica sand prepared for sliding friction test on a 1 cm \times 1 cm grid; (b) block dimensions in millimeters in lateral view.

3.3.2.3.1. *First part: sample preparation for silica sand*

- a) On a surface plate 229 mm width, 305 mm length, and 76 mm thick ($\pm 2 \mu\text{m}$ flatness) spread a thin layer of silica sand conforming a circular area of 35 mm of diameter.
- b) Then, apply spray adhesive on top of the previously extended layer of sand.

- c) Then, spread a new thin layer of sand in such a way that it bonds to the previous layer by means of the adhesive.
- d) Repeat steps “b” and “c” (e.g., as if following a 3D printing or additive manufacturing logic) until getting a total thickness of about 4.5 mm. Toward the end a metal tin of 36 mm of diameter and 3 mm depth is adhered to preserve the integrity of the sand block and to provide a reflective coating which is necessary for the appropriate performance of the infrared reflective sensor used in the second part. At the end, the sand block shall stick out the edge of the metal tin by about 1.5 mm. See the final appearance of the silica sand blocks in the Fig. 3-9.

3.3.2.3.2. First part: sample preparation for UHMW Polyethylene and P50

Sandpaper

- a) On a surface plate ($\pm 2 \mu\text{m}$ flatness) put a circular film of 32 mm of diameter cut out either from a sheet of UHMW Polyethylene or of P50 Sandpaper facing down against the surface plate. Then, around this circular film put a washer-like-film of 32 mm of internal diameter and at least 50 mm of out diameter. This washer-like-film has a thickness that doubles the thickness of each circular film in such a way that this washer-like-film works like a filling to let the edge of the tin at least 1.5 mm behind the surface to be tested.
- b) Separately, fill a metal tin of 36 mm of diameter and 3 mm depth with melt wax (e.g., at about 70 °C) until getting a convex wax surface sticking out the border of the metal tin.
- c) Then, take the tin full of melted wax up down, center it on the circular film prepared in the steps “a” and “b”, and press down for one or two minutes until the wax cools out.

- d) Finally, lift the metal tin from the surface plate and clean out any remaining wax burr. See the final appearance of the UHMW Polyethylene and P50 Sandpaper blocks in the Fig. 3-10(a) and (b).

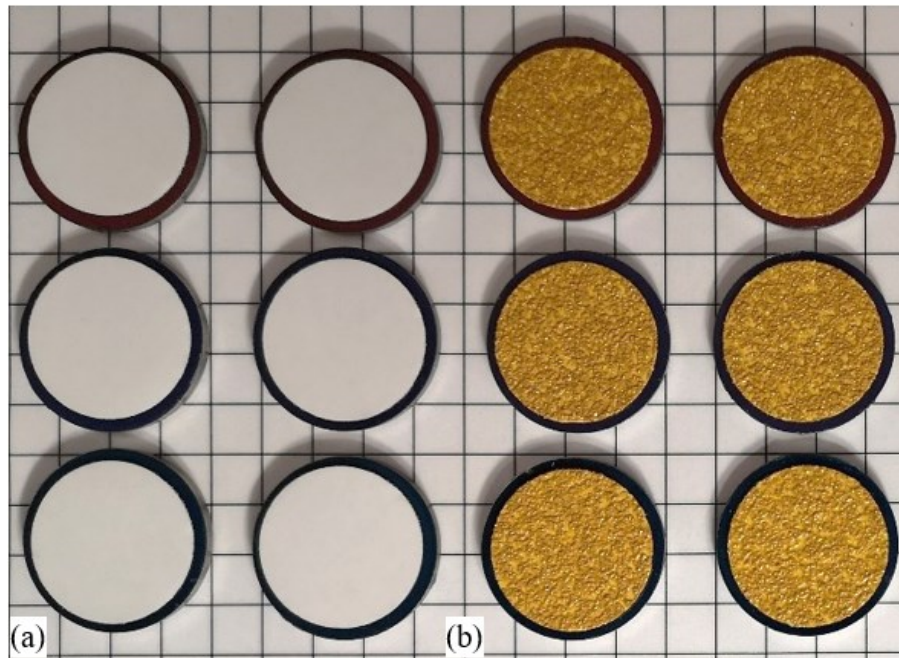


Fig. 3-10 Blocks of artificial materials on a grid 1 cm x 1 cm: (a) UHMW polyethylene; (b) P50 sandpaper.

3.3.2.3.3. *Second part: friction test*

- a) Place one of the blocks prepared in the first part and fix it on the platform of the friction tester. Double side Nano-adhesive tape of 1 mm thickness was used to fix the block on the table.

- b) Then, a second block is placed on top of the one fixed on the friction tester in the previous step. At this point the material to be tested on each of the two blocks must lay in contact against each other.
- c) Finally, the friction tester (see Fig. 3-8) was turn on to rotate the previous assemblage of blocks at a slow rate (i.e., less than or equal to 1 rpm) until the upper block begins to slide. The initial movement of the upper block defines the initial plane-strain constant-volume friction angle $\theta'_{cv,ps}$. By the time the upper block begins to slide (t_0) a photo-optical sensor automatically holds the reading from the inclinometer sensor to obtain the more precise possible reading of the sliding friction.

3.3.3. Experimental Results

Table 3-6 summarizes the three experimental points ($\theta'_{cv,ps}$, $\theta'_{cs,ps}$) obtained; these are the averages and standard deviations (*SD*), in degrees, of 27 single tests executed for each material. *Appendices D* and *E* present video recordings of all the executed tests. These video recordings are included to further illustrate the methodology behind data acquisition (see full description of the methodology in the numeral 3.3.2).

Type of granular material	$\theta'_{cv,ps}$ [$^{\circ}$ (<i>SD</i>)]	$\theta'_{cs,ps}$ [$^{\circ}$ (<i>SD</i>)]
UHMW Polyethylene	20.06 (2.57)	14.5 (0.5)
Silica sand	33.46 (3.56)	36.5 (1.5)
P50 sandpaper	62.59 (5.27)	78.5 (1.5)

Table 3-6 Summary of experimental results for critical state shear strength parameters.

For the silica sand, which is mostly quartz, the constant-volume friction angle or interparticle sliding friction angle is typically in the range 22–35° (Terzaghi et al., 1996). Moreover, for the Toyoura silica sand, a consistent constant-volume friction angle of 32–33° has been measured (Bolton, 1986), (Jamiolkowski et al., 2012), (Szypcio, 2017); consequently, the result of 33.46° presented here appears plausible. For the Toyoura silica sand, a consistent plane-strain critical state friction angle of 35–40° has been measured under a low confining pressure (i.e., $\sigma'_3 < 150 \text{ kN/m}^2$) and loose condition (Tatsuoka et al., 1986), (Bolton, 1987), (Khosravi et al., 2013); therefore, the result of 36.5° presented here again seems plausible. This positive self-evaluation of the results for silica sand reflects the soundness of the techniques adopted in this study to measure these two friction angles (i.e., $\theta'_{cv,ps}$, $\theta'_{cs,ps}$).

3.3.3.1. Raw experimental results for the plane-strain constant-volume friction angle $\theta'_{cv,ps}$

For each material (i.e., silica sand, P50 sandpaper and UHMW polyethylene) three samples were prepared, each of these samples consisting of two blocks. On each block three opposed directions were marked with the colors red, blue, and black (i.e., three marks separated 120° from each other). By combining these three directions between the two blocks results in nine different tests for each sample. Given there are three samples for each material follows the total number of tests for each material is 27. Table 3-7 shows the complete set of experimental results and the *Appendix D* contains the video recording for each of the 81 tests. The column “Name” in this table follows the color code: “color of the direction mark on block A / color of the direction mark on block B / sample number”.

Test No.	Name	UHMW	Silica sand (°)	P50 sandpaper (°)
1	Red/Red/S1	21.74	29.65	68.89
2	Blue/Red/S1	23.41	36.10	57.96
3	Black/Red/S1	21.69	33.41	56.57
4	Red/Blue/S1	19.42	35.81	59.43
5	Blue/Blue/S1	22.70	32.71	59.80
6	Black/Blue/S1	17.78	35.94	59.64
7	Red/Black/S1	16.38	32.41	61.19
8	Blue/Black/S1	20.04	27.56	70.81
9	Black/Black/S1	17.31	33.21	65.44
10	Red/Red/S2	17.31	27.28	63.41
11	Blue/Red/S2	21.87	34.35	57.76
12	Black/Red/S2	19.08	35.97	66.97
13	Red/Blue/S2	23.02	29.79	73.64
14	Blue/Blue/S2	18.71	31.18	65.57
15	Black/Blue/S2	22.96	39.17	60.94
16	Red/Black/S2	23.44	34.38	66.18
17	Blue/Black/S2	23.88	39.27	68.30
18	Black/Black/S2	22.98	30.31	49.66
19	Red/Red/S3	16.47	40.02	64.93
20	Blue/Red/S3	20.14	36.45	60.50
21	Black/Red/S3	14.55	34.03	61.53
22	Red/Blue/S3	20.66	27.65	65.89
23	Blue/Blue/S3	18.94	30.82	67.09
24	Black/Blue/S3	19.34	37.90	65.24
25	Red/Black/S3	21.52	33.99	56.85
26	Blue/Black/S3	18.98	30.93	56.56
27	Black/Black/S3	17.28	33.19	59.23

Table 3-7 Experimental results for plane-strain constant-volume friction angle $\phi'_{cv,ps} = \phi'_\mu$ on UHMW Polyethylene materials, silica sand and P50 sandpaper.

3.3.3.2. Raw experimental results for the plane-strain critical state friction angle

$$\phi'_{cs,ps}$$

For each material (i.e., UHMW polyethylene, silica sand and P50 sandpaper) five tests were required to bound a solution in the frame of the methodology explain in numeral 3.3.2.1. Fig. 3-11, Fig. 3-12, Fig. 3-13 show the iterative sequence of tests leading a result for each material and the *Appendix E* contains the video recording sequence for each of the 15 tests.

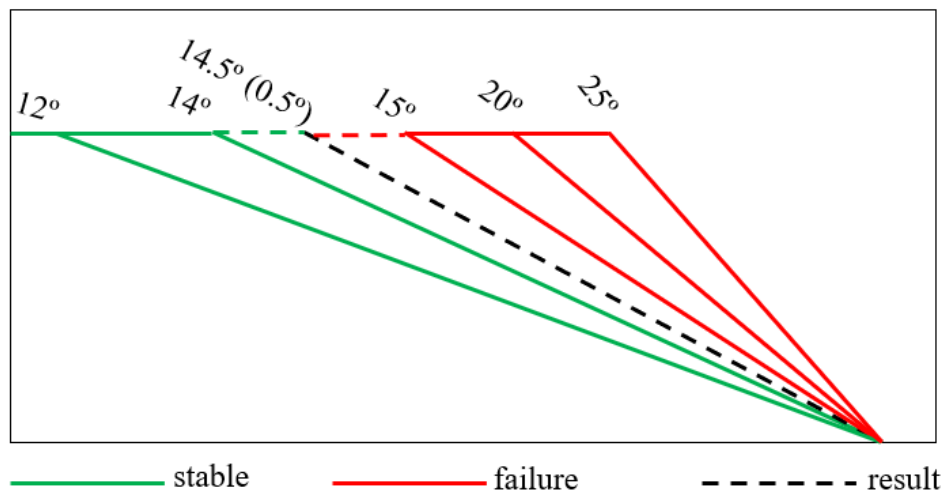


Fig. 3-11 Experimental result for the plane-strain critical state friction angle $\phi'_{cs,ps}$ of artificial particles coated with UHMW polyethylene (see *Appendix E*).

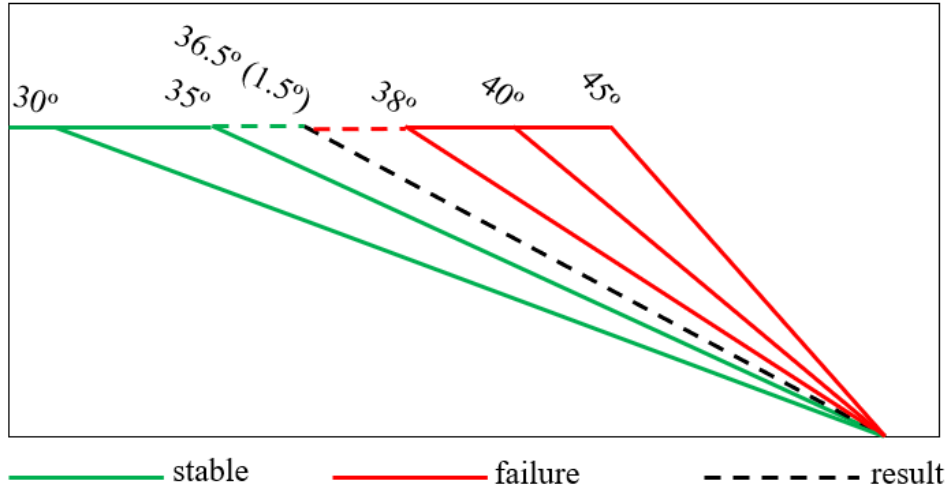


Fig. 3-12 Experimental result for the plane-strain critical state friction angle $\phi'_{cs,ps}$ of silica sand
(see Appendix E).

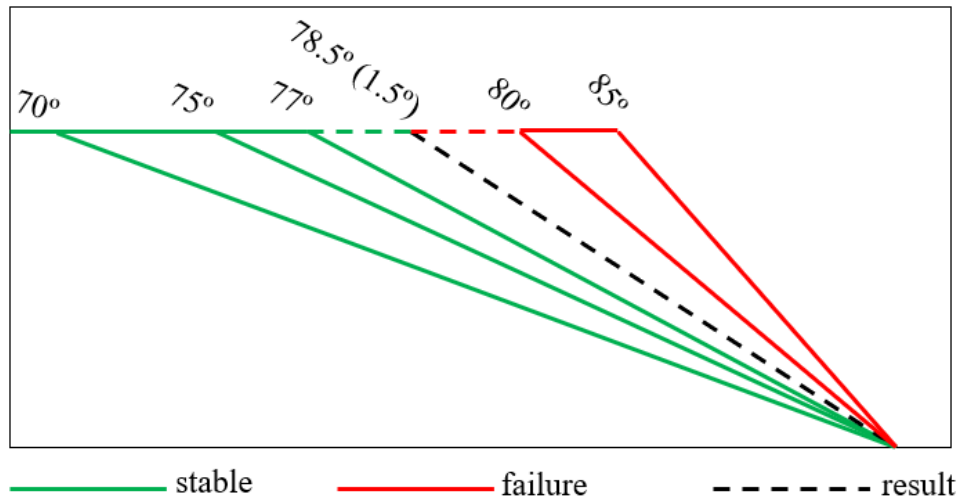


Fig. 3-13 Experimental result for the critical state friction angle $\phi'_{cs,ps}$ of artificial particles coated with P50 sandpaper (Appendix E).

3.3.4. Discussion on the role of the energy of placement based on the analysis of own experimental Results

The momentum commonly added during the measurement of the angle of repose using classical techniques (see numeral 2.3.2) is problematic because it introduces variability of what it is expected to be a deterministic soil parameter. The angle of repose measured under this condition of added momentum is always lower than the static angle of repose β that equals the plane-strain critical state friction angle $\phi'_{cs,ps}$. Experimental research was conducted here to support this discussion. Fig. 3-14 includes three experimental points and based on these a conceptual trend was drawn as indicated with the dashed line included in this figure. The first point approaches an energy of accommodation equal to zero. This point of nil added momentum adheres to the methodology presented in the numeral 3.3.2.1 and was taken from Table 3-6. The second point was determined using the *fixed base* and *fixed funnel* technique where the energy of accommodation was equivalent to a free fall height of 12.2 cm, see Table 3-8 and the corresponding video recording in the *Appendix F*. And the third point was determined using the *fixed base* and *moving funnel* technique where the energy of accommodation was equivalent to a free fall height of 3.5 cm, see Table 3-8 and the corresponding video recording in the *Appendix F*.

The conceptual trend observed in Fig. 3-14 supports the following the definition for the plane-strain critical state friction angle developed by a pile of sand or by a sedimentary horizon of normally consolidated young cohesionless granular soil: *The static angle of repose is the steepest freestanding angle a pile of loose granular material can hold given an energy of particle accommodation equal to zero.*

Test No.	β from the fixed base and fixed	β from the fixed base and
1	33.98	34.70
2	32.44	34.33
3	34.57	35.03
4	33.28	34.05
5	33.70	34.66
Average (SD):	33.59 (0.80)	34.55 (0.38)

Table 3-8 Experimental results for the angle of repose β using the fixed base and funnel device on silica sand (see *Appendix F*).

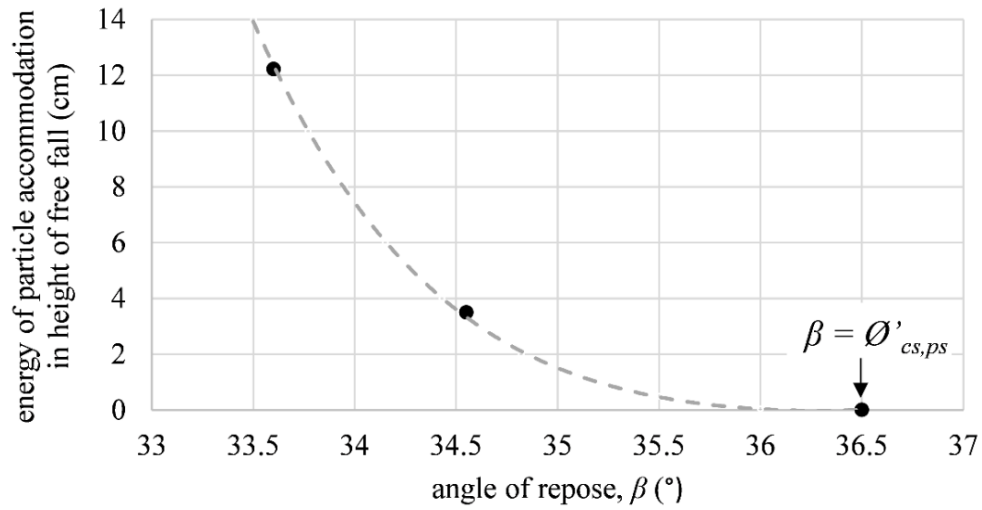


Fig. 3-14 Conceptual trend between the energy of particle accommodation and the angle of repose β from the experimental results on silica sand (see Table 3-8 and numeral 3.3.3.2).

3.4. Experimental investigation for the at-rest lateral earth pressure incorporated with the overconsolidation ratio *OCR*

3.4.1. General

The *OCR* parameter in cohesionless soils is known to be bounded by the relative density D_r or porosity n of the cohesionless soil deposit. Present experimental investigation limits the study to the densities yielded in silica sand by the two known Proctor energies of compaction, this is because these two cases are the most widely use in backfills behind retaining wall.

3.4.2. Methodology of the experimental tests for lateral stress measurement

A sensing ring built from a standard 4" (101.6 mm) CBR mold and a piston to transfer vertical load were developed to measure the lateral stress transmitted by a normal stress acting through different samples of silica sand, see Fig. 3-15. Numeral 3.2 provides the physical properties of the silica sand selected for present study. The first objective was to obtain a series of experimental results for the K_0 and K_{0-OC} for a non-compacted sample. The second objective was to obtain a series of experimental results for the K_0 and K_{0-OC} for the two given standard energies of compaction, namely: the standard Proctor energy 591.3 kJ/m^3 (ASTM D698-12e2, 2012) and the modified Proctor energy 2696.0 kJ/m^3 (ASTM D1557-12e1, 2012) and an additional intermediate energy noted as the reduced modified Proctor energy 1308.8 kJ/m^3 .

The setup uses a 4" (101.6 mm) cylindrical mold that conforms to the standards (ASTM D698-12e2, 2012) and (ASTM D1557-12e1, 2012). Three pressure transducers (i.e., RP-S40-ST) were mounted on the inner side of the mold spaced 120° from each other as indicated in Fig. 3-16. The surcharge was transferred onto the soil sample by means of a steel piston and dead weights. Then,

the lateral stress transferred through the soil transduces into a voltage output signal, which is finally read in a datalogger. Each sensor has its own separate circuit to collect three independent results per reading. Table 3-9 presents the testing program. Seven points of *OCR* were reached for the standard Proctor energy, five for the modified Proctor energy, six for the reduced modified Proctor energy and six for the non-compacted sand. Various levels of *OCR* were reached on each of these three samples following the procedure described in the next numeral.

Experiment/Test	Energy (kJ/m³)	Qty.	Targeted variable	Standard
at-rest coefficient of lateral	591.3	7	$K_{\theta-OC}$	(ASTM D698-12e2, 2012)
earth pressure on soil using	2696.0	5		(ASTM D1557-12e1, 2012)
an instrumented standard 4"	1308.8	6		
CBR mold and surcharge	None	6	$K_{\theta}, K_{\theta-OC}$	(ASTM D4254-16, 2016b)
Porosity	N/A	4	n	

Table 3-9 Summary of experimental research program for earth pressure in silica sand.

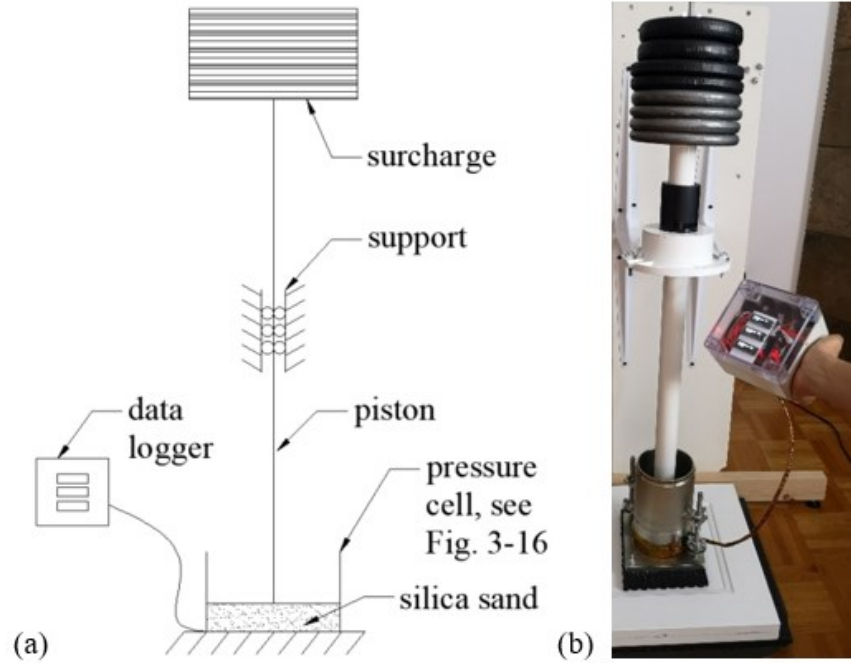


Fig. 3-15 Experimental setup to measure lateral stress: (a) conceptual sketch; and (b) actual setup.

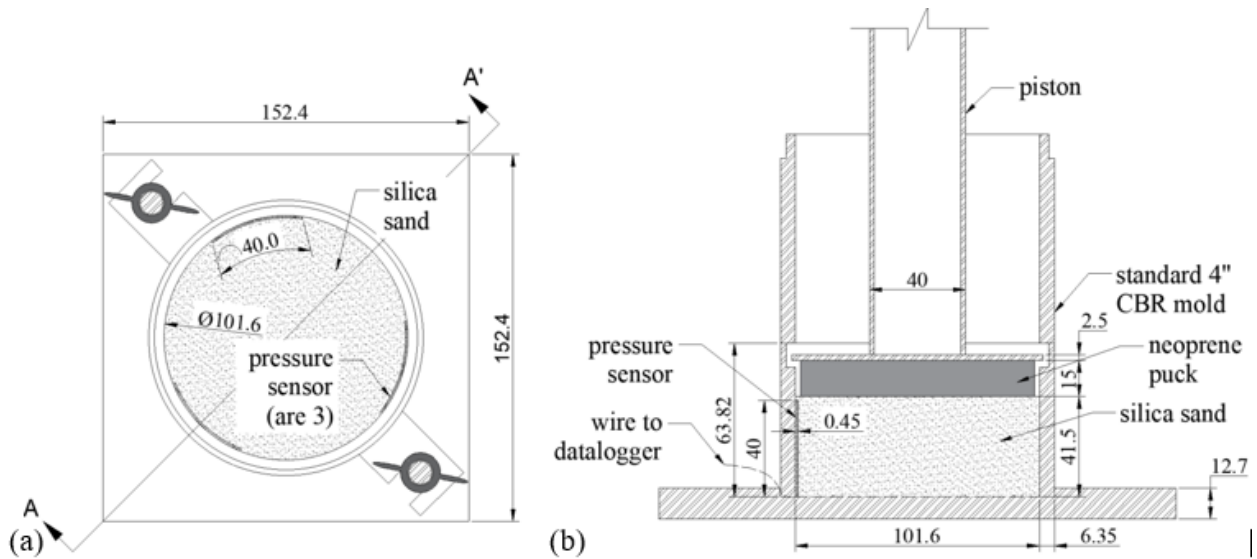


Fig. 3-16 Dimensions of the pressure cell in millimetres: (a) plan view; and (b) section A-A'.

3.4.2.1. Methodology of measurement for K_0 and K_{0-OC}

Three samples were tested, and various levels of *OCR* were reached on each one by following the next procedure:

- a) Place and level off a layer of loose silica sand to target a compacted layer of 39 mm or 22.5 mm thick according to the case. The sand was dropped no more than 13 mm this to guarantee an initial loosest state as suggested in (ASTM D4254-16, 2016a).
- b) After placement compact the sample as specified for the standard test *Method A* as per (ASTM D698-12e2, 2012) for the standard Proctor energy and as per (ASTM D1557-12e1, 2012) for the modified Proctor energy. In the last case repeat step “a” and “b” to complete a compacted thickness of 45 mm. To reach the reduced modified Proctor energy a reduced number of blows was used (i.e., 11 blows per layer). This step “b” was omitted for the non-compacted sample.
- c) Then, the total surcharge was transferred onto the sample. This maximum surcharge consisted of 19.88 kg for the standard Proctor energy and the non-compacted sample, 15.35 kg for the reduced modified Proctor energy, and 10.77 kg for the modified Proctor energy test.
- d) After 24 h, follows the unloading increments, each with a duration of at least 24 h or until a steady output signal was recorded. Outputs are registered at the end of each increment.

3.4.2.2. Calibration

Two calibrated aneroid manometers (± 1 mm Hg accuracy) were used for the calibration of each of the three pressure sensors. Fig. 3-17 shows a point of calibration for the sensor PSR#3 at the specific pressure of 130 mm Hg (i.e., 17.33 kPa) as illustration of this procedure. The range of calibration is from 50 mm Hg to 130 mm Hg in incremental steps of 5 mm Hg; accordingly, 17 points of calibration were executed for each sensor. Each point of calibration is composed by a known applied pressure (read in mm Hg) versus its corresponding voltage output (read in Volts).

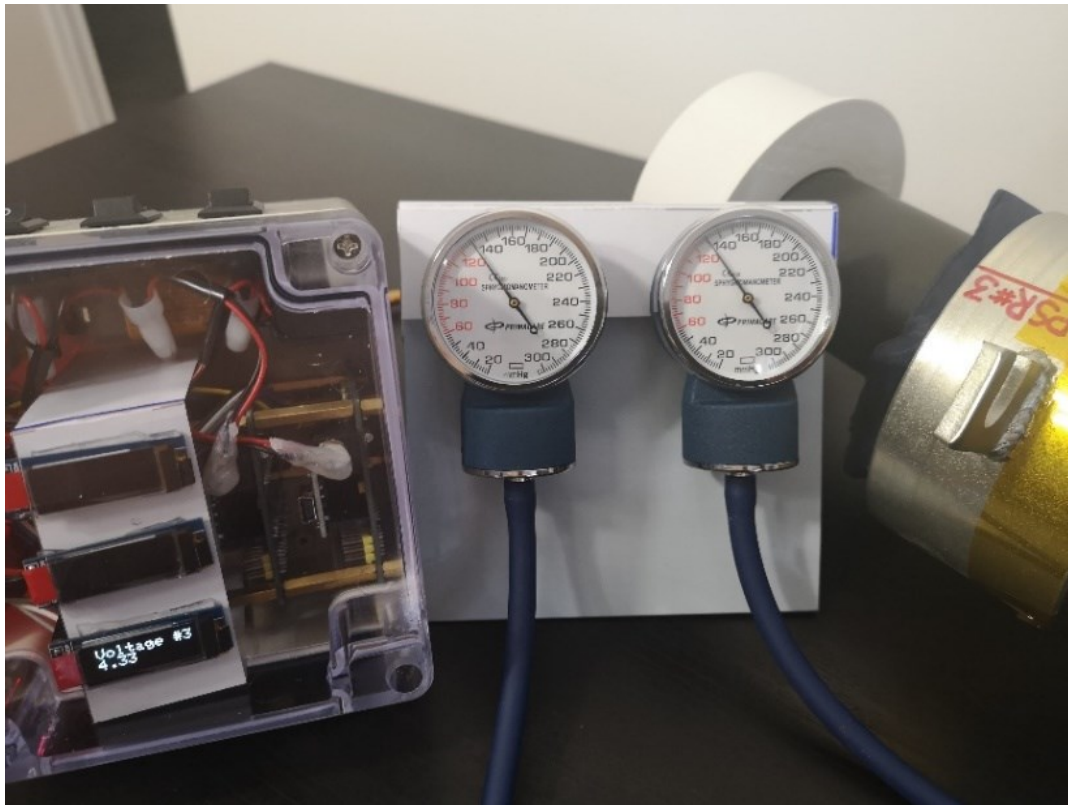


Fig. 3-17 Calibration of the sensor PSR # 3. From left to right appears the datalogger, the two aneroid manometers and the pressure cell.

The data collected in this way is presented in Table 3-10 for each of the sensors. Then, these data were fitted to obtain a function to convert the voltage read in the datalogger into a horizontal pressure in kPa. The process of correlation using the function for each sensor involves a relative error of +/- 2%. Fig. 3-18, Fig. 3-19 and Fig. 3-20 show the correlation function for each sensor in the pressure cell.

Pressure applied by aneroid		Corresponding output voltage read in datalogger (V)		
mm Hg	kPa	PSR # 1	PSR # 1	PSR # 3
50	6.67	1.41	1.47	1.52
55	7.33	1.95	1.93	1.96
60	8.00	2.34	2.46	2.39
65	8.67	2.73	2.87	2.74
70	9.33	3.04	3.17	3.07
75	10.00	3.30	3.36	3.37
80	10.67	3.50	3.49	3.51
85	11.33	3.64	3.62	3.66
90	12.00	3.76	3.73	3.80
95	12.67	3.89	3.86	3.92
100	13.33	3.99	3.96	4.03
105	14.00	4.10	4.03	4.13
110	14.67	4.15	4.10	4.18
115	15.33	4.21	4.16	4.21
120	16.00	4.27	4.21	4.26
125	16.67	4.31	4.27	4.30
130	17.33	4.35	4.32	4.33

Table 3-10 Data collected for the calibration of each pressure sensor.

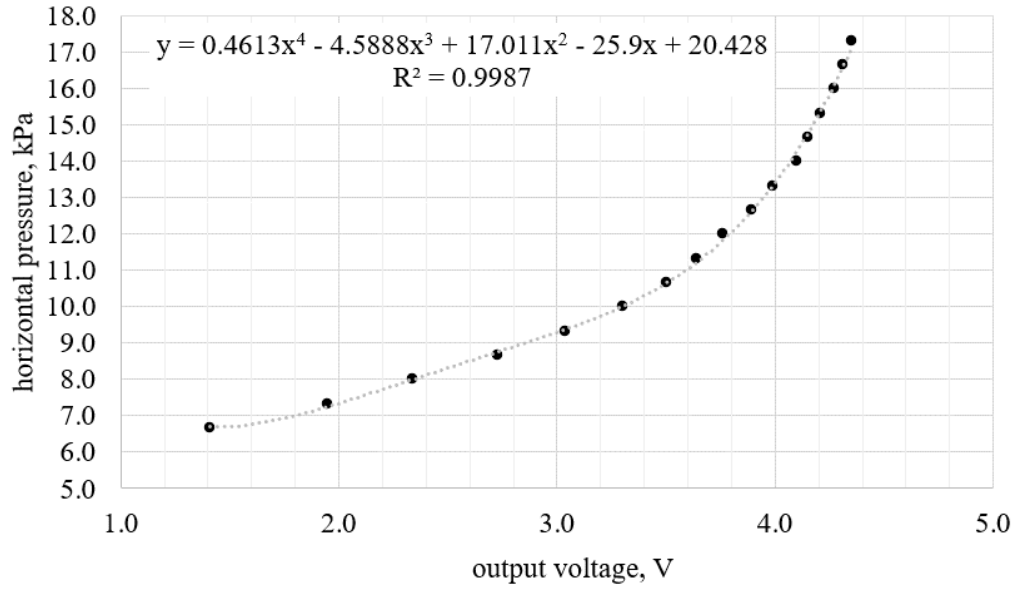


Fig. 3-18 Correlation fit between voltage and horizontal pressure for the sensor PSR # 1.

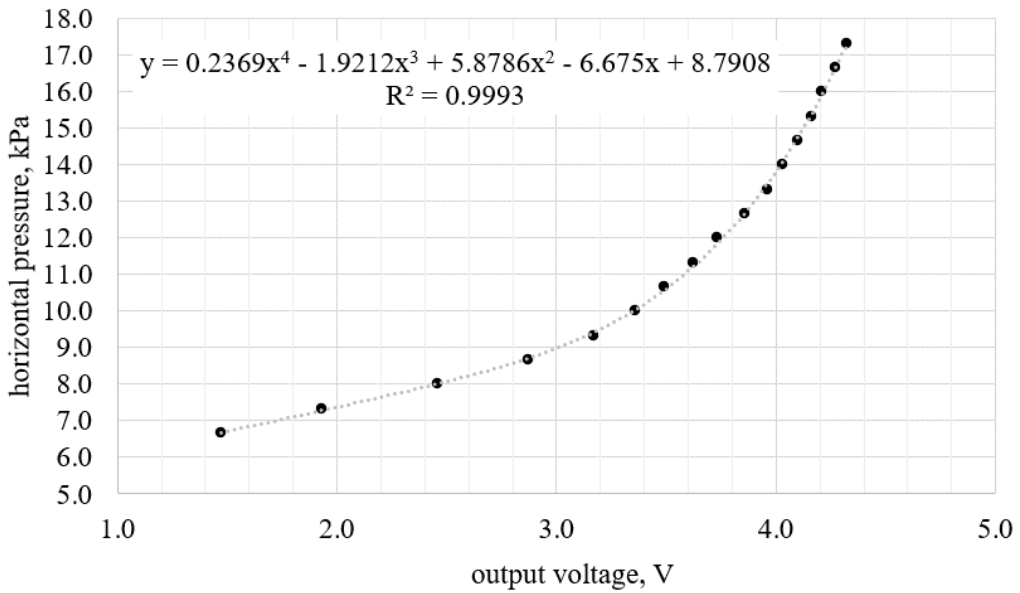


Fig. 3-19 Correlation fit between voltage and horizontal pressure for the sensor PSR # 2.

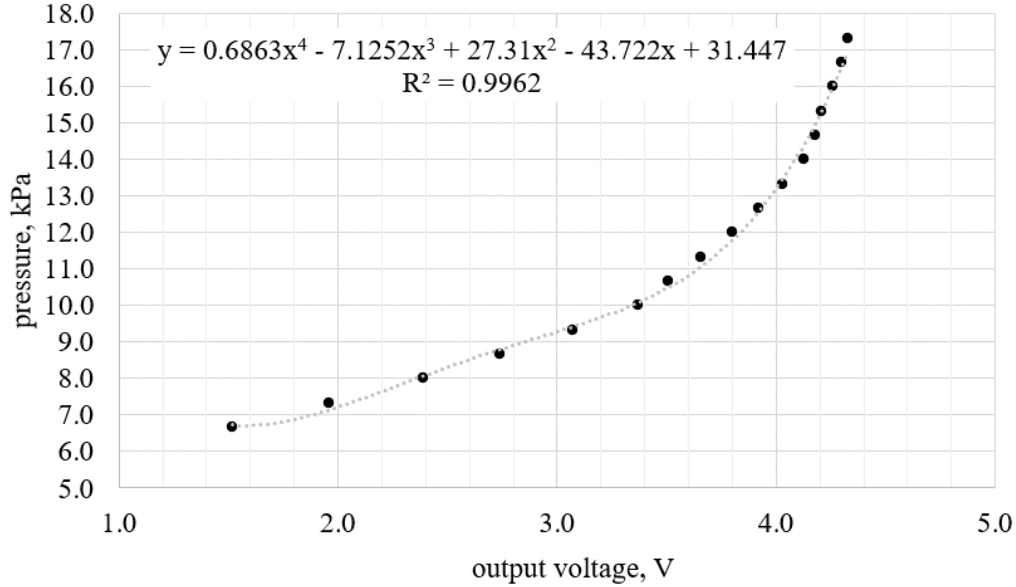


Fig. 3-20 Correlation fit between voltage and horizontal pressure for the sensor PSR # 3.

3.4.1. Experimental results

The experimental results can be presented in two parts, the first includes the model parameters for the four samples of silica sand after placement in the pressure cell but before loading and the second part includes the results for lateral earth pressure after loading and unloading. The first set of results is summarized in the Table 3-11. The plastic volumetric strain ratio A was adopted from the existing data set for this same silica sand (Hanna and Diab, 2017), (Hanna, 2001), see numeral 3.2. The weight, height, volume, dry unit weight γ_d , initial porosity $n_{c,sand}$ and the initial relative density of each sand sample $D_{r,c,sand}$ are direct laboratory measurements. Then and to correlate with present theoretical model, a relative porosity $n_{c,r}$ and its corresponding model critical porosity $n_{c,model}$ were computed for each sample [i.e., by applying Eqs. (4-21) and (4-22)]. Then, the plane-strain critical state friction angle $\phi'_{cs,ps}$ was determined with Eq. (4-11) to satisfy the model critical

porosity $n_{c,model}$ of each silica sand sample. Finally, the plane-strain constant-volume friction angle $\phi'_{cv,ps}$ was determined replacing $\phi'_{cs,ps}$ in Eq. (4-9) and the associated at-rest coefficient of lateral earth pressure was determined by applying these strength parameters in Eq. (5-4). The *Appendix G* presents all previous computations in an Excel spreadsheet.

Table 3-12 presents the experimental results for the non-compacted sample. The first line in Table 3-12 corresponds to the normally consolidated condition and the rest of lines represent a different independent unload step. Table 3-13, Table 3-14 and Table 3-15 present the experimental results for each of the three compacted samples. The first line these tables corresponds to the maximum applied surcharge and the rest of lines represent a different independent unload step. The outputs are presented in Volts which is the original signal as given by the datalogger as well as their corresponding horizontal stresses in kPa after correlating with the corresponding calibration functions, see previous numeral 3.4.2.2. For all the cases, the overconsolidated at-rest coefficient of lateral earth pressure $K_{\theta-OC}$ was computed as the ratio between the average horizontal stress given by the pressure sensors and the known applied vertical stress $\sigma'_{v,\theta}$.

Energy	Weight	Height	Volume	γ_d	$n_{c,sand}$	$n_{c,r}$	$n_{c,model}$	$D_{r,c,sand}$	Λ	$\phi'_{cs,ps}$	$\phi'_{cv,ps}$	K_0
(kJ/m³)	(gr)	(m)	(10⁻⁴ m³)	(kN/m³)	(%)		(%)	(%)		(°)	(°)	
N/A	524.41	0.040	3.24	15.86	38.28	0.598	34.66	64.63	0.97605	36.740	33.562	0.444
590	517.52	0.039	3.16	16.05	37.53	0.659	33.34	70.36	0.97641	38.236	34.298	0.433
1346	556.57	0.041	3.32	16.42	36.09	0.776	30.81	80.94	0.97707	40.821	35.540	0.413
2787	636.05	0.045	3.65	17.10	33.46	0.990	26.17	99.16	0.97822	44.829	37.420	0.385

Table 3-11 Model properties for the four samples of silica sand.

$\sigma'_{v,0}$ (kPa)	voltage from datalogger (V)			σ'_h (kPa)			$K_{\theta-OC}$	OCR
	PSR # 1	PSR # 2	PSR # 3	PSR # 1	PSR # 2	PSR # 3		
24.06	3.49	3.49	3.48	10.61	10.57	10.40	0.438	1.000
21.31	3.33	3.33	3.34	10.09	9.94	10.00	0.470	1.129
18.57	2.90	3.13	3.12	9.09	9.32	9.51	0.501	1.295
15.77	2.63	2.62	2.63	8.57	8.27	8.58	0.537	1.525
13.03	2.25	2.24	2.25	7.82	7.71	7.76	0.596	1.846
10.07	1.45	1.44	1.46	6.69	6.65	6.77	0.666	2.390

Table 3-12 Experimental results for the non-compacted silica sand sample.

$\sigma'_{v,0}$ (kPa)	voltage from datalogger (V)			σ'_h (kPa)			$K_{\theta-OC}$
	PSR # 1	PSR # 2	PSR # 3	PSR # 1	PSR # 2	PSR # 3	
24.06	4.42	4.39	4.42	18.10	18.23	18.41	0.758
21.31	4.34	4.32	4.29	16.98	17.28	16.39	0.792
18.57	4.18	4.18	4.15	15.08	15.61	14.65	0.814
15.77	3.89	4.14	4.05	12.60	15.18	13.64	0.876
13.03	3.76	3.77	3.76	11.81	12.09	11.57	0.907
10.07	2.90	3.23	3.22	9.09	9.61	9.72	0.941
7.38	1.76	2.29	2.40	6.95	7.78	8.09	1.031

Table 3-13 Experimental results for silica sand compacted under the standard Proctor energy.

$\sigma'_{v,0}$ (kPa)	voltage from datalogger (V)			σ'_h (kPa)			K_{0-OC}
	PSR # 1	PSR # 2	PSR # 3	PSR # 1	PSR # 2	PSR # 3	
18.570	4.42	4.41	4.42	18.10	18.51	18.41	0.988
15.771	4.30	4.29	4.29	16.46	16.90	16.39	1.052
13.028	4.13	4.14	4.15	14.57	15.18	14.65	1.136
10.065	3.78	3.79	3.77	11.92	12.22	11.62	1.184
7.377	3.35	3.36	3.34	10.15	10.05	10.00	1.365
4.470	2.49	2.47	2.46	8.30	8.03	8.22	1.831

Table 3-14 Experimental results for silica sand compacted under the reduced modified Proctor energy.

$\sigma'_{v,0}$ (kPa)	voltage from datalogger (V)			σ'_h (kPa)			K_{0-OC}
	PSR # 1	PSR # 2	PSR # 3	PSR # 1	PSR # 2	PSR # 3	
13.03	4.54	4.53	4.53	20.04	20.35	20.46	1.557
10.07	4.40	4.41	4.40	17.81	18.51	18.07	1.800
7.38	4.19	4.18	4.17	15.18	15.61	14.88	2.063
4.47	4.02	3.98	4.02	13.58	13.66	13.37	3.028
1.73	3.66	3.64	3.67	11.30	11.31	11.12	6.501

Table 3-15 Experimental results for silica sand compacted under the modified Proctor energy.

Chapter 4: A Critical State Soil Mechanics Plane-Strain Model for Cohesionless Soils: Derivation and Verification

4.1. General

Present research adheres to the general established concept indicating that the static angle of repose β for sedimentary, normally consolidated young materials equals the plane-strain critical state friction angle $\phi'_{cs,ps}$, (Lambe and Whitman, 1969), (Terzaghi et al., 1996, p. 104), (Cornforth, 1973), (Santamarina and Cho, 2001), (Sadrekarimi and Olson, 2011). However, this definition does not precise what the angle of repose is by itself.

During the pile formation in the context of a static angle of repose test, the process of placement occurs under the influence of gravity and is controlled by the frictional contact between the particles and the structural interference. When the granular media stabilizes the strains become zero and the gravitational and horizontal stresses become principal stresses. This effective stress state is known to be the at-rest condition define as $K_0 = \sigma'_h / \sigma'_v$. From this is possible to posit the static angle of repose is a buttress naturally formed to counteract the at-rest lateral earth pressure. Therefore, it is reasonable to assert that the at-rest lateral earth pressure is a function of the static angle of repose. Present chapter provides a theoretical derivation to put K_0 in terms of $\beta = \phi'_{cs,ps}$ and presents the corresponding experimental proof.

4.2. A new theoretical model for critical state

4.2.1. General definition

Retaining walls are longitudinal structures where relevant strain occurs within the plane normal to the wall and strain out of this plane is virtually zero. This means the stress-strain behavior in the

backfill material can be treated as a plane-strain two-dimensional problem. In short, the herein proposed theoretical constitutive model for granular materials at critical state can be described as *a two-dimensional, plane strain, nonlinear, micromechanical model*.

4.2.1.1. Selection of the micromechanics technique

Most constitutive soil models are formulated in the *paradigm of continuum*. Their development has been based on laboratory test results on a given sample of soil which is treated as a solid unit as it is done for other non-granular materials like steel or concrete. Accordingly, these models read the soil behavior by means of interpreting different measures from the specimen's contour (e.g., strains, stresses, pore water pressure, among others). However, granular soil is an assemblage of discrete solid particles. This diametric difference between the *paradigm of continuum* usually adopted in the state of the art and the actual nature of soil is an obstacle for the fundamental understanding of soil behavior. Viewing this problem, present research proposes the development of a theoretical model based on a *micromechanical* analysis. *Micromechanical* techniques permit the analysis of soil at the particle-scale level where interparticle interactions govern the macroscopic soil behavior, see numeral 2.5.2.

4.2.2. New theoretical derivation for the relationship or *flow rule* between the plane-strain critical state friction angle $\theta'_{cs,ps}$ and the plane-strain constant-volume friction angle $\theta'_{cv,ps}$

The theoretical model developed in the present study consists of a pile of circular particles of the same unitary diameter that corresponds to the plane view of a packing of uniform spheres, as shown in Fig. 4-1(a). The placement process occurs only under the gravitational force exerted by

the self-weight of the particles. Thus, the mass deforms from the loosest possible arrangement (e.g., stacked) to a more compact condition at the end of the self-stabilization process by means of the interparticle mechanism, as illustrated in Fig. 4-1(b). The column of particles “ m ” tends to penetrate the already-settled material by moving the row of particles “ n ” toward the left, as it cannot move toward the right due to the axial symmetry of the pile. Furthermore, parallel radial planes of particles are falling and slipping simultaneously, accordingly, there is no relative velocity between adjacent planes of particles. In other words, during the placement process, the lateral friction is zero and consequently a non-lateral constraint is considered (i.e., the plane-strain condition). Finally, when this mechanism self-stabilizes and deformation ceases, the column of particles m will have penetrated a vertical distance Δ_y , causing the row of particles n to slip a horizontal distance Δ_x .

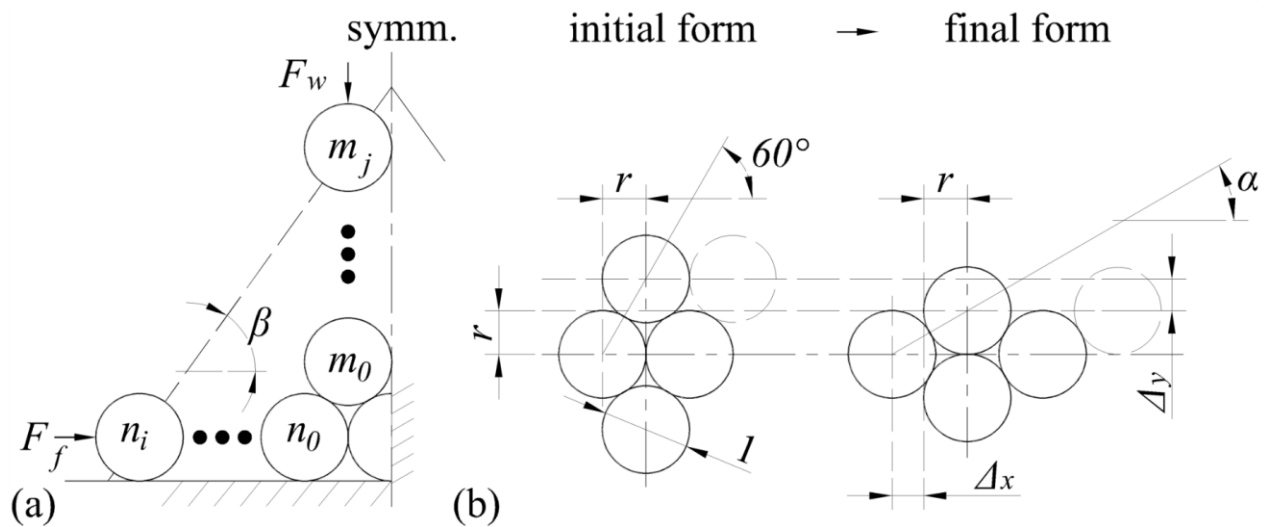


Fig. 4-1 Sketch of the theoretical model for the angle of repose: (a) left half of a pile of particles; (b) deformation mechanism of the unitary pack of particles.

This model makes the following assumptions:

- a) The model is in a normally consolidated condition;
- b) During deformation, particles can only slide (i.e., rolling friction equal to zero, $\phi'_{\mu r} = 0$);
- c) The individual circular particles remain solid (i.e., no crushing occurs, $\phi'_c = 0$) and do not contribute to any elastic response toward deformation (i.e., $C \gg C_s$);
- d) The angle of repose is independent of scale;
- e) The particle size is small compared with the scale of the set-up;
- f) The angle of friction along the pile base is the same as the angle of interparticle sliding friction ϕ'_μ ; and,
- g) Deformation occurs with plain-strain symmetry; consequently, the plane model in Fig. 1(b) refers to a slice of unitary thickness.

To conform to the law of conservation of energy, this interparticle deformation mechanism must exhibit a work equilibrium at the final stage in critical-state; therefore, the acting work produced by the gravitational force transforms into reactive work done by the frictional resisting force, which can be expressed by Eq. (4-1).

$$F_f \cdot \Delta_X = F_W \cdot \Delta_Y \quad (4-1)$$

The vertical penetration of column m , named Δy , and the horizontal slip of row n , named Δx , can be derived from the geometry of the model given in Fig. 4-1(b) resulting in the expressions (4-2) and (4-3), respectively.

$$\Delta_y = (\sin 60^\circ - \sin \alpha) \quad (4-2)$$

$$\Delta_x = (\cos \alpha - \cos 60^\circ) \quad (4-3)$$

The frictional resisting force F_f developed during the slip of row n is given by Eq. (4-4).

$$F_f = i \cdot \gamma \cdot d^2 \cdot \tan \phi'_\mu \cdot 1 \quad (4-4)$$

where d is the diameter of a single particle (i.e., $d = 1$); γ is the dry unit weight of the particulate assemblage; and the index i accounts for the number of particles in row n . The gravitational force F_W developed by the mass of column m is defined by Eq. (4-5).

$$F_W = j \cdot \gamma \cdot d^2 \cdot 1 \quad (4-5)$$

where j is the number of particles in column m .

Substituting Eqs. (4-2) to (4-5) in Eq. (4-1) yields Eq. (4-6):

$$\begin{aligned} & (i \cdot \gamma \cdot d^2 \cdot \tan \phi'_\mu \cdot 1) \cdot (\cos \alpha - \cos 60^\circ) \\ & = (j \cdot \gamma \cdot d^2 \cdot 1) \cdot (\sin 60^\circ - \sin \alpha) \end{aligned} \quad (4-6)$$

From the pile-scale model shown in Fig. 4-1(a) the angle of repose β is define by Eq. (4-7).

$$\tan \beta = \frac{j}{i} \quad (4-7)$$

Substituting Eq. (4-7) into Eq. (4-6) and setting $\alpha = \beta$ and $d = 1$, the final state of equilibrium can be expressed as in Eq. (4-8).

$$\tan \phi'_{\mu} = \tan \beta \frac{(\sin 60^{\circ} - \sin \beta)}{(\cos \beta - \cos 60^{\circ})} \quad (4-8)$$

Equation (4-8) defines the angle of repose β as a unique function of the angle of interparticle sliding friction ϕ'_{μ} . Furthermore, it presents a more general definition in terms of the initial internal friction versus the developed boundary friction, thus, Eq. (4-8) can be rewritten as in Eq. (4-9).

$$\tan(\phi'_{cv,ps}) = \tan(\phi'_{cs,ps}) \frac{\sin 60^{\circ} - \sin(\phi'_{cs,ps})}{\cos(\phi'_{cs,ps}) - \cos 60^{\circ}} \quad (4-9)$$

Where the initial internal friction in the pile of granular material standing at rest corresponds to the plane-strain constant-volume friction angle $\phi'_{\mu} = \phi'_{cv,ps}$. In the normally consolidated condition, this corresponds to the plane-strain critical state friction angle $\beta = \phi'_{cs,ps}$ (Lambe and Whitman, 1969), (Terzaghi et al., 1996, p. 104), (Cornforth, 1973), (Santamarina and Cho, 2001), (Sadrekarimi and Olson, 2011). The present analytical $\phi'_{cv,ps}$ is a friction angle that can be determined in the laboratory by the constant-volume RS test (Sadrekarimi and Olson, 2011) or undrained TxC shear test. The present analytical $\phi'_{cs,ps}$, also referred to in the literature as the plane-strain friction angle ϕ'_{ps} , is a friction angle that can be determined in the laboratory by techniques such as the RS test (Sadrekarimi and Olson, 2011), the large-displacement DS test

(Lings and Dietz, 2004), the plane-strain biaxial test (Alshibli et al., 2004) or the static angle of repose as done in present study for the particular case where $\varnothing'_{cv,ps} = \varnothing'_{\mu}$.

It should be noted that Eq. (4-9) includes the plane-strain angle of pushing or rearrangement $\varnothing'_{p,ps}$ as an implicit value. In other words, $\varnothing'_{p,ps}$ is a function of the initial state $\varnothing'_{cv,ps}$. This implies that, known the initial state $\varnothing'_{cv,ps}$, the ultimate state $\varnothing'_{cs,ps}$ can be directly determined from Eq. (4-9) and accordingly, $\varnothing'_{p,ps}$ can be obtained from Eq. (2-4). Currently, based on Rowe's theory (Rowe, 1962), (Rowe, 1969); the most widely used expression for the plane-strain critical state shear strength for cohesionless soils is the Eq. (4-10).

$$\sin(\varnothing'_{cs,ps}) = \frac{\sin(\varnothing'_{cv,ps}) + \sin(\varnothing'_{p,ps})}{1 + \sin(\varnothing'_{cv,ps}) \cdot \sin(\varnothing'_{p,ps})} \quad (4-10)$$

Equation (4-10) contains $\varnothing'_{p,ps}$ as an independent variable; consequently, the proposed expression in Eq. (4-9) reduces the number of unknowns as compared with the widely used expression in Eq. (4-10). Thus, Fig. 4-2 illustrates Eq. (4-9) alongside Rowe's Eq. (4-10). In Fig. 4-2, the same $\varnothing'_{cv,ps}$ and $\varnothing'_{p,ps}$ values used to plot Eq. (4-9) were used as the input parameters of Eq. (4-10). As the values for $\varnothing'_{cs,ps}$ obtained from Rowe's theory are relatively lower than the values produced by the present theory, especially for $\varnothing'_{cv,ps}$ values above 30°, Rowe's Eq. (12) does not fully satisfy the conceptual expression of Eq. (2-4).

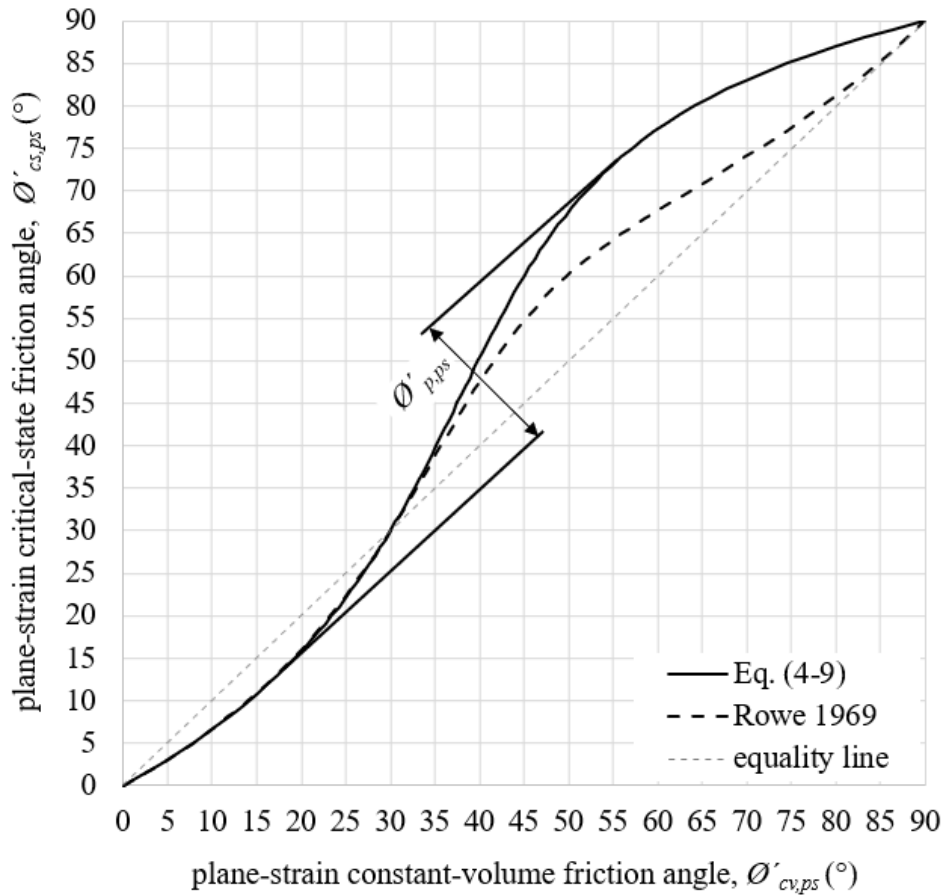


Fig. 4-2 Plane-strain critical state friction angle $\phi'_{cs,ps}$ versus initial plane-strain constant-volume friction angle $\phi'_{cv,ps}$.

From previous analysis is clear the fact that the static angle of repose is not the same as the interparticle sliding friction angle as evidenced by the equality line in Fig. 4-2.

The Fig. 4-3 presents the three experimental points ($\phi'_{cv,ps}$, $\phi'_{cs,ps}$) determined for the three materials, along with the *flow rule* Eq. (4-9). There is a good agreement between the present theory and our experimental measurements.

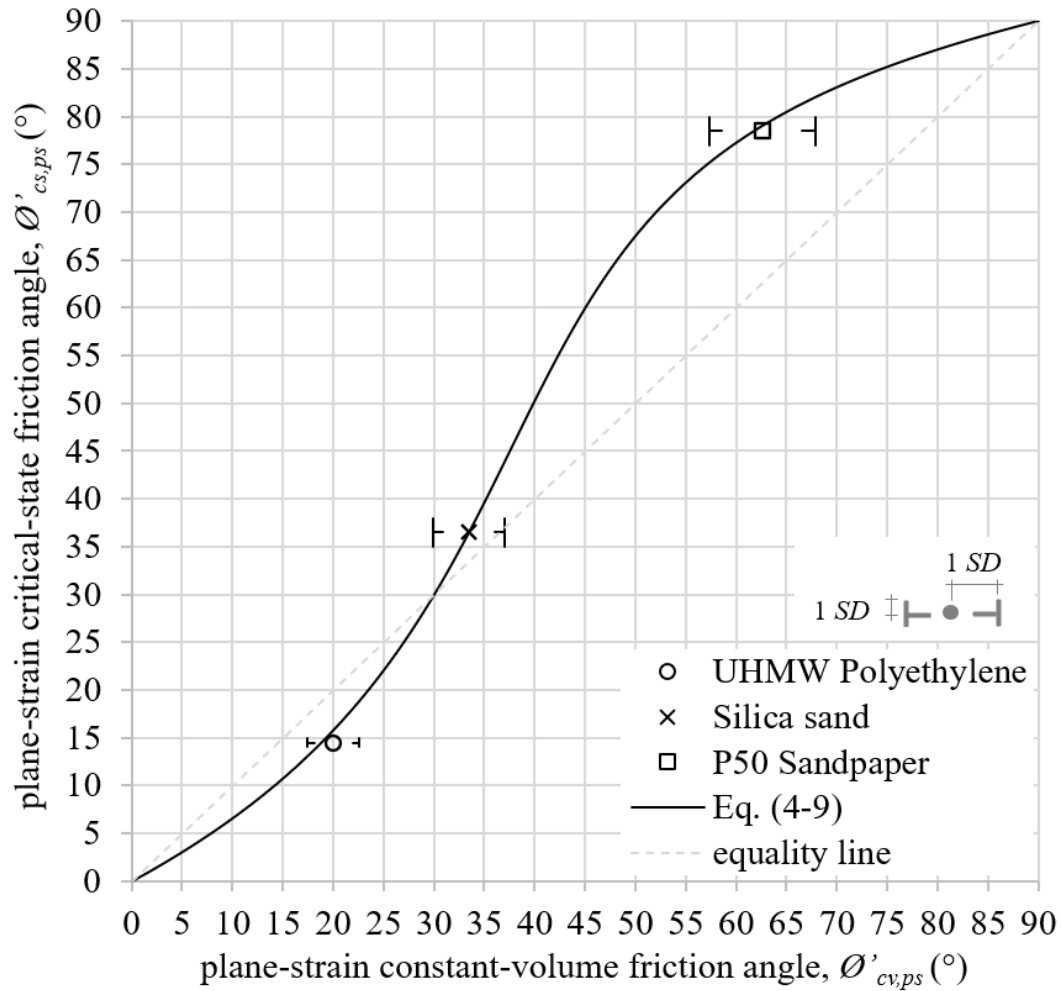


Fig. 4-3 Present experimental results for silica sand, UHMW polyethylene, and P50 sandpaper compared with present theory in Eq. (4-9).

4.2.2.1. Validation of present flow rule Eq. (4-9) using empirical existing data

(Sadrekarimi and Olson, 2011) investigated yield and critical state friction angles of sands using triaxial compression and ring shear tests on air-pulvinated and moist-tamped specimens of three different sands. The sands under observation were Ottawa 20/40 (OT), Illinois River (IR) and Mississippi River (MR). From their results for the ring shear tests they found that under small

confining stresses ($\rightarrow 0$ kPa), the constant-volume friction angle ϕ'_{cv} is approximately 32° , 36° and 38° in OT, IR, and MR sands, respectively. These authors refer to this angle as the critical state friction angle without particle crushing and identify it with the notation: $\phi'_{cs,o}$, where the sub index “O” stands for original sand or non-crushed sand. (Sadrekarimi and Olson, 2011, figs. 14-b). On the other side, under larger confining stresses ($\rightarrow 800$ kPa) the developed plane-strain constant-volume friction angle of shearing resistance asymptotically stabilizes in 31° , 33° and 34° in OT, IR and MR sands respectively, see (Sadrekarimi and Olson, 2011, figs. 14-b). This last measurement obtained after large confining pressure and shear strain corresponds to the steady internal friction angle ϕ'_μ . Accordingly, it is possible a positive direct verification of the present expression (4-9) for each of these three sands as presented in the Table 4-1.

Sand type	Ring shear test results according to (Sadrekarimi and Olson, 2011)		Angle of repose according to Eq. (4-9)
	$\phi'_{cs,ps}$ ($^\circ$)	ϕ'_μ ($^\circ$)	β ($^\circ$) = $\phi'_{cs,ps}$ (ϕ'_μ)
Ottawa 20/40 (OT)	32	31	31.80
Illinois River (IR)	36	33	35.61
Mississippi River (MR)	38	34	37.62

Table 4-1 *Flow rule* results from Eq. (4-9) versus results from (Sadrekarimi and Olson, 2011).

In the Fig. 4-2 (numeral 4.2.2), present *flow rule* was compared with Rowe’s semi-empirical *flow rule*. In general, the differences of Eq. (4-9) compared to other *flow rules* for cohesionless soils in the range of natural sands is relatively small (see Fig. 4-4); however, it is important to notice that

present Eq. (4-9) is the product a fully theoretical derivation for the specific plane-strain condition that reduces the number of unknowns by one making the solution more deterministic which permits a more ample application and understanding of the behavior of sand as demonstrated in many instances along present study. The Table 4-2 compares *flow rules* including the present to highlight the reduction in the number of unknowns explained before.

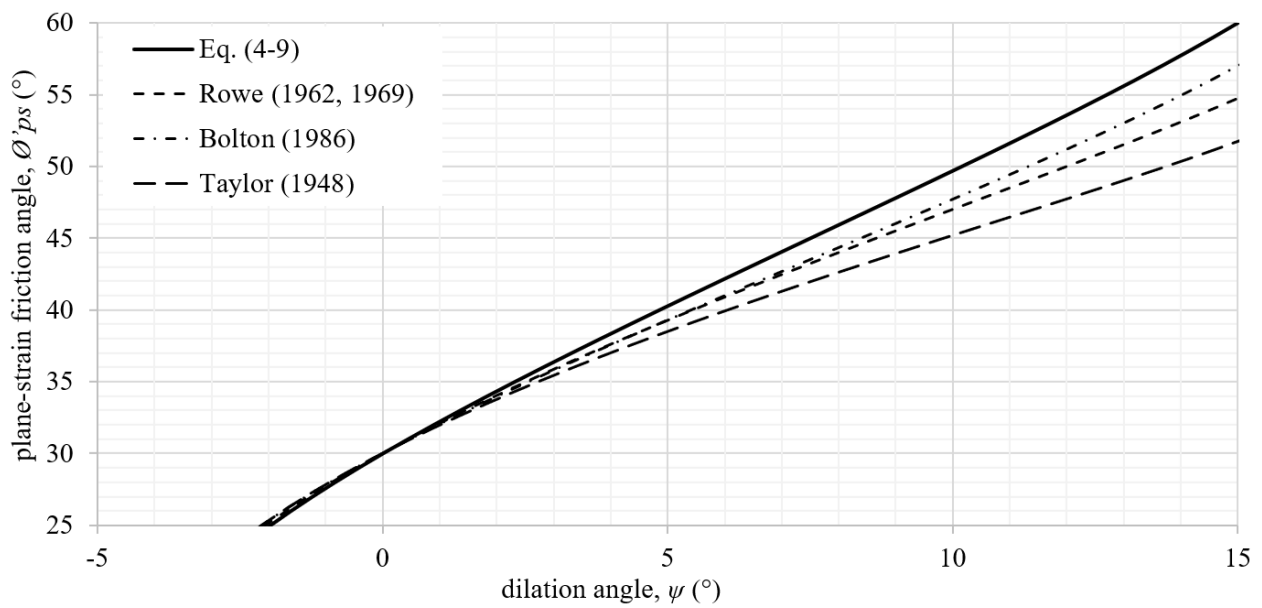


Fig. 4-4 Other *flow rules* compared with present theory in Eq. (4-9).

Author	Flow rule	Variables
Present study in Eq. (4-9)	$\tan(\varnothing'_{cv,ps}) = \tan(\varnothing'_{cs,ps}) \frac{\sin 60^\circ - \sin(\varnothing'_{cs,ps})}{\cos(\varnothing'_{cs,ps}) - \cos 60^\circ}$	$\varnothing'_{cv,ps}, \varnothing'_{cs,ps}$
(Rowe, 1962), (Rowe, 1969)	$\sin(\varnothing'_{cs,ps}) = \frac{\sin(\varnothing'_{cv,ps}) + \sin(\varnothing'_{p,ps})}{1 + \sin(\varnothing'_{cv,ps}) \cdot \sin(\varnothing'_{p,ps})}$	$\varnothing'_{cv,ps}, \varnothing'_{cs,ps}, \varnothing'_{p,ps}$
(Bolton, 1986)	$\varnothing'_{cs,ps} = \varnothing'_{cv,ps} + 0.8 \cdot \varnothing'_{p,ps}$	
(Taylor, 1948)	$\tan(\varnothing'_{cs,ps}) = \tan(\varnothing'_{cv,ps}) + \tan(\varnothing'_{p,ps})$	

Table 4-2 Other *flow rules* compared with present theory in Eq. (4-9).

Finally, for the sake of comparison, is important to notice that the notation for friction angle may differs between authors; nevertheless, the conditions at which those friction angles were originally determined or stablished permits the “translation” between notations. In the research according to (Rowe, 1969), for instance: the developed friction \varnothing'_{ps} corresponds with the present $\varnothing'_{cs,ps}$; the constant-volume friction angle \varnothing'_{cv} corresponds with the present $\varnothing'_{cv,ps}$; and the dilatancy ψ corresponds with the present $\varnothing'_{p,ps}$. In the research developed by (Lings and Dietz, 2004), for instance: the developed plane-strain friction angle \varnothing'_{ps} corresponds with the present $\varnothing'_{cs,ps}$; the critical state (plane strain) friction angle \varnothing'_{crit} corresponds with the present $\varnothing'_{cv,ps}$; and the dilation angle ψ corresponds with the present $\varnothing'_{p,ps}$. In the empirical research after (Bolton, 1986), for

instance: the maximum friction \varnothing'_{max} corresponds with the present $\varnothing'_{cs,ps}$; the critical friction \varnothing'_{crit} corresponds with the present $\varnothing'_{cv,ps}$; and the dilatancy term 0.8ψ corresponds with the present $\varnothing'_{p,ps}$. In the research according to (Atkinson, 1973), for instance: the mobilized friction \varnothing'_{mob} corresponds with the present $\varnothing'_{cs,ps}$; the plane-strain constant-volume friction angle \varnothing'_{cv} corresponds with the present $\varnothing'_{cv,ps}$; and the dilation angle ψ corresponds with the present $\varnothing'_{p,ps}$.

4.2.3. Porosity

According to the present particle-scale model (i.e., a packing of uniform spheres), the corresponding analytical porosity at critical state failure n_c can be computed from the geometry shown in Fig. 4-1(b) when the auxiliary pile angle α reaches equilibrium; that is, $\alpha = \beta = \varnothing'_{cs,ps}$. Equations (4-11) and (4-12) provide the critical porosity n_c for the intervals $0^\circ \leq \varnothing'_{cs,ps} \leq 45^\circ$ and $45^\circ \leq \varnothing'_{cs,ps} \leq 90^\circ$, respectively. Similarly, Equations (4-13) and (4-14) provide the initial porosity n_0 for the intervals $0^\circ \leq \varnothing'_{cv,ps} \leq 45^\circ$ and $45^\circ \leq \varnothing'_{cv,ps} \leq 90^\circ$, respectively. In general, the porosity in the assemblage of particles ranges from a minimum possible porosity $n_{min} = 25.95\%$, corresponding to tetrahedral packing, to a maximum possible porosity $n_{max} = 47.64\%$, corresponding to a simple cubic packing. Moreover, dense sands can dilate and become loose upon shearing and vice versa, this cycle can be better appreciated in Fig. 4-5.

$$n_c = \frac{8 \cdot \sin(90^\circ - \varnothing'_{cs,ps}) - \frac{4}{3}\pi}{8 \cdot \sin(90^\circ - \varnothing'_{cs,ps})} \quad (4-11)$$

$$n_c = \frac{8 \cdot \sin(\varnothing'_{cs,ps}) - \frac{4}{3}\pi}{8 \cdot \sin(\varnothing'_{cs,ps})} \quad (4-12)$$

$$n_0 = \frac{8 \cdot \sin(90^\circ - \theta'_{cv,ps}) - \frac{4}{3}\pi}{8 \cdot \sin(90^\circ - \theta'_{cv,ps})} \quad (4-13)$$

$$n_0 = \frac{8 \cdot \sin(\theta'_{cv,ps}) - \frac{4}{3}\pi}{8 \cdot \sin(\theta'_{cv,ps})} \quad (4-14)$$

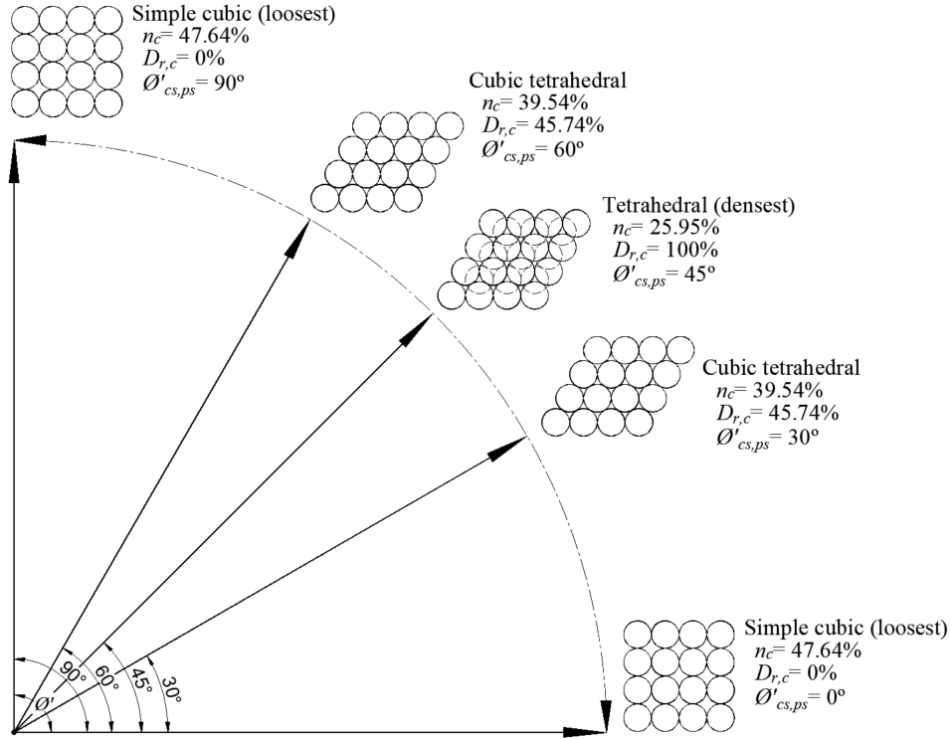


Fig. 4-5 Cycle of porosity or relative density involved by Eqs. (4-11) to (4-14).

Given the porosity of the packing, it is possible then to identify the zones in Fig. 4-6, where dilative and contractive behaviors occur, as determined by the threshold porosity $n_s = 39.54\%$, along with the collapsible zone for the critical porosity $n_0^* = 43.61\%$ where the pore pressure becomes positive according to Eq. (4-20). Moreover, this porosity n_0^* corresponds to a theoretical $\theta'_{cs,ps} = 21.8^\circ$ which consequently becomes the minimum shear strength attainable by the shear failure mechanism in cohesionless soils. This value can be determined from Fig. 4-8, which presents the

pore pressure coefficient $A_{cs,ps}$ of Eq. (4-20) versus the plane-strain critical state friction angle $\phi'_{cs,ps}$ of Eq. (4-9). The value at which $A_{cs,ps} = 0$ is the point where the pore pressure coefficient $A_{cs,ps}$ becomes positive and where the risk of collapse during loading becomes critical.

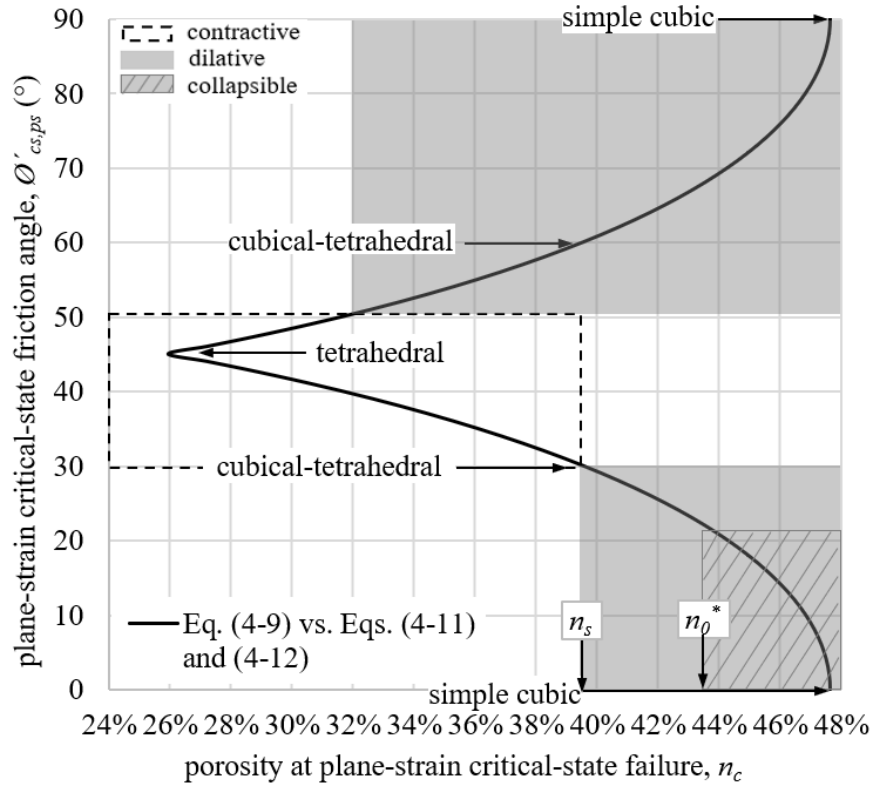


Fig. 4-6 Developed plane-strain critical state friction angle $\phi'_{cs,ps}$ versus the critical state porosity n_c , annotated with three distinctive behaviors: contractive, dilative, and collapsible.

4.2.4. Pore pressure coefficient

The geometrical interference at constant volume or the plane-strain angle of pushing or rearrangement $\phi'_{p,ps}$ is the only parameter with the potential to mobilize either additional internal effective friction at failure (i.e., $\phi'_{cs,ps}$) or pore water pressure at failure under undrained shearing.

Thus, and by analogy with Eq. (2-4), it is possible to define the pore pressure expression given in Eq. (4-15); however, considering that dilation appears positive in Eq. (2-4), it is necessary to apply the negative sign in Eq. (4-15) to be consistent with the corresponding negative pore pressures. Under the undrained condition, the coefficient of pore pressure at plane-strain critical state failure, denoted here as $A_{cs,ps}$, can be defined as the sum of the coefficient of pore pressure accounting for the geometrical interference, $A_{p,ps}$, and the so-called intrinsic or steady pore pressure coefficient $A_{cv,ps}$; see Eq. (4-15). The intrinsic or steady pore pressure coefficient $A_{cv,ps}$ is the pore pressure corresponding to the normal compressive stress only without the influence of shear, which comes from the theory of elasticity and was also presented and discussed in (Skempton, 1954) to be 1/3.

$$A_{cs,ps} = -(A_{cv,ps} + A_{p,ps}) \quad (4-15)$$

The effective shear strength developed at failure is the same for the total stress framework as well as for the effective stress framework as given by Eqs. (4-16) and (4-17), respectively. Considering that the shear strength of soils is controlled by the effective stress, regardless of whether failure occurs under drained or undrained conditions; consequently, the shear strength parameters used in Eqs. (4-16) and (4-17) correspond to effective parameters. However, in the total stress analysis, i.e. Eq. (4-16), the pore pressures are not subtracted from the total stresses because the shear strength parameter is related to the undrained condition; that is $\phi'_{cv,ps}$. In the effective stress analysis, i.e. Eq. (4-17), the shear strength parameter is related to the drained condition; that is, $\phi'_{cs,ps}$.

$$\Delta\tau' = \Delta\sigma_3 \cdot \tan(\phi'_{cv,ps}) \quad (4-16)$$

$$\Delta\tau' = \Delta\sigma'_3 \cdot \tan(\phi'_{cs,ps}) \quad (4-17)$$

By equating Eqs. (4-16) and (4-17) and substituting the value of Δu as a function of the pore pressure coefficient $A_{p,ps}$, we obtain Eq. (4-18). Rearranging for the pore pressure coefficient $A_{p,ps}$ yields Eq. (4-19):

$$\Delta\sigma'_3 \cdot \tan(\phi'_{cs,ps}) = \left(\Delta\sigma'_3 + A_{p,ps} \cdot (\Delta\sigma'_1 - \Delta\sigma'_3) \right) \cdot \tan(\phi'_{cv,ps}) \quad (4-18)$$

$$A_{p,ps} = \frac{\tan(\phi'_{cs,ps}) - \tan(\phi'_{cv,ps})}{\tan(\phi'_{cs,ps}) \cdot \tan(\phi'_{cv,ps})} \quad (4-19)$$

Furthermore, substituting Eq. (4-19) and $A_{cv,ps} = 1/3$ into Eq. (4-15) yields Eq. (4-20) for the pore pressure coefficient of plane-strain critical state shear failure, $A_{cs,ps}$.

$$A_{cs,ps} = -\frac{1}{3} - \frac{\tan(\phi'_{cs,ps}) - \tan(\phi'_{cv,ps})}{\tan(\phi'_{cs,ps}) \cdot \tan(\phi'_{cv,ps})} \quad (4-20)$$

4.2.4.1. Validation of the pore pressure coefficient $A_{cs,ps}$ as given by present expression (4-20)

(Bjerrum et al., 1961) developed a series of drained and undrained triaxial tests in a fine uniform natural quartz sand composed by well-rounded and polished particles. The uniformity of that sand plus the well-rounded and polish character of its particles constitutes a granular material that naturally coincides with the characteristics of the herein defined theoretical assemblage of spherical particles (see numeral 4.2.2); as a consequence, the experimental results from (Bjerrum

et al., 1961) holds direct positive comparison with present theory without the need of porosity correlations as indicated in numeral 4.2.5.

In the context of the pore pressure coefficient, (Bjerrum et al., 1961) found experimentally that the turning point between negative and positive pore pressure is at a porosity $n_0^* = 44\%$ observed in the range of very loose sands. As explained before, the present analytical model in Eq. (4-20) provides virtually the same critical porosity found experimentally; in fact, an exact theoretical figure for this porosity of $n_0^* = 43.61\%$ can be computed. This neat agreement shown in Fig. 4-7 is a further demonstration of the capacity of present model to capture the fundamental frictional behavior of granular soils in critical state. Moreover, according to (Mittal, 1963) “*The value of the pore pressure parameter A_f at failure, in plane strain (i.e., the same annotated as $A_{cs,ps}$ in the present Thesis) is definitely greater than that for the corresponding conventional triaxial test*” which further confirms the present result.

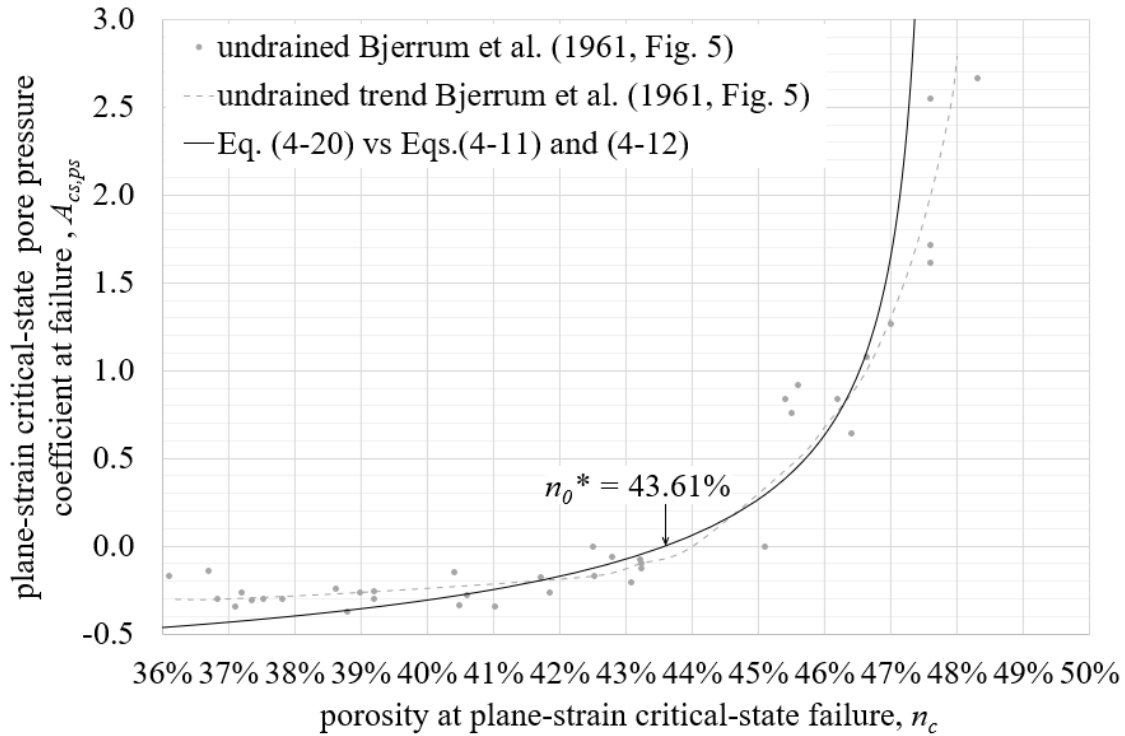


Fig. 4-7 Pore pressure coefficient $A_{cs,ps}$ at plane-strain critical state shear failure given by Eq. (4-20) compared with experimental results adopted from (Bjerrum et al., 1961, fig. 5).

Soil looser than this critical porosity $n_0^* = 43.61\%$ correspond to very loose soil under imminent risk of *collapse* due to the substantial increase in pore pressure and loss of strength that could eventually result in liquefaction (see Fig. 4-6), notice the asymptotic grow toward positive infinite over this critical porosity or $\phi'_{cs,ps} < 21.8^\circ$ in Fig. 4-8. This same critical porosity $n_0^* \approx 44\%$ was suggested as well by the experiments developed by (Castro, 1969) in his study on liquefaction of sands. The critical porosity according to this author occurred in a relative density of 20% to 30% for low confining pressure (i.e., up to 10 kPa). And present theory agrees well with this

experimental result given that for the here determined theoretical critical porosity $n_0^* = 43.61\%$ the relative density is 24.4%.

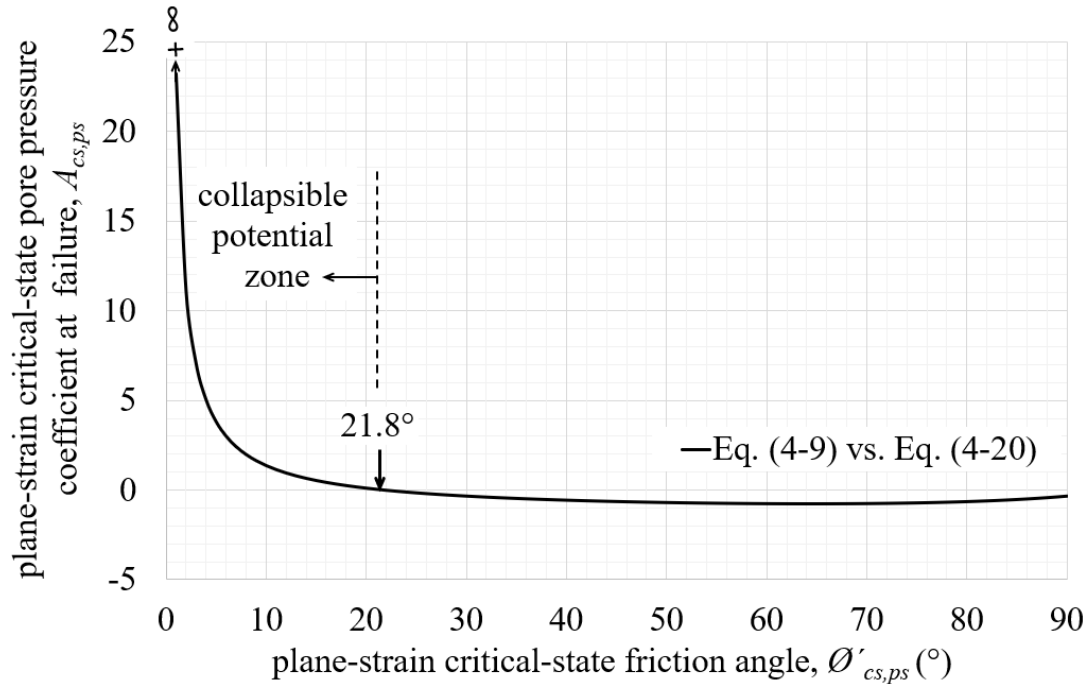


Fig. 4-8 Present pore pressure coefficient $A_{cs,ps}$ versus its corresponding plane-strain critical state friction angle $\phi'_{cs,ps}$.

(Bjerrum et al., 1961) additionally stated that “Another characteristic property of the loose sand is the high pore pressures developed in undrained tests. The pore pressure parameter, A , was found to be as high as 2.7 in the very loose sand with initial porosity 47 to 48 per cent.” On this regard, the present theoretical Eq. (4-20) for the pore pressure coefficient at plane-strain critical state predicts the same result given that a pore pressure coefficient $A_{cs,ps} = 2.7$ can be obtained within the range of porosity 47% to 48% as can be corroborated in Fig. 4-9.

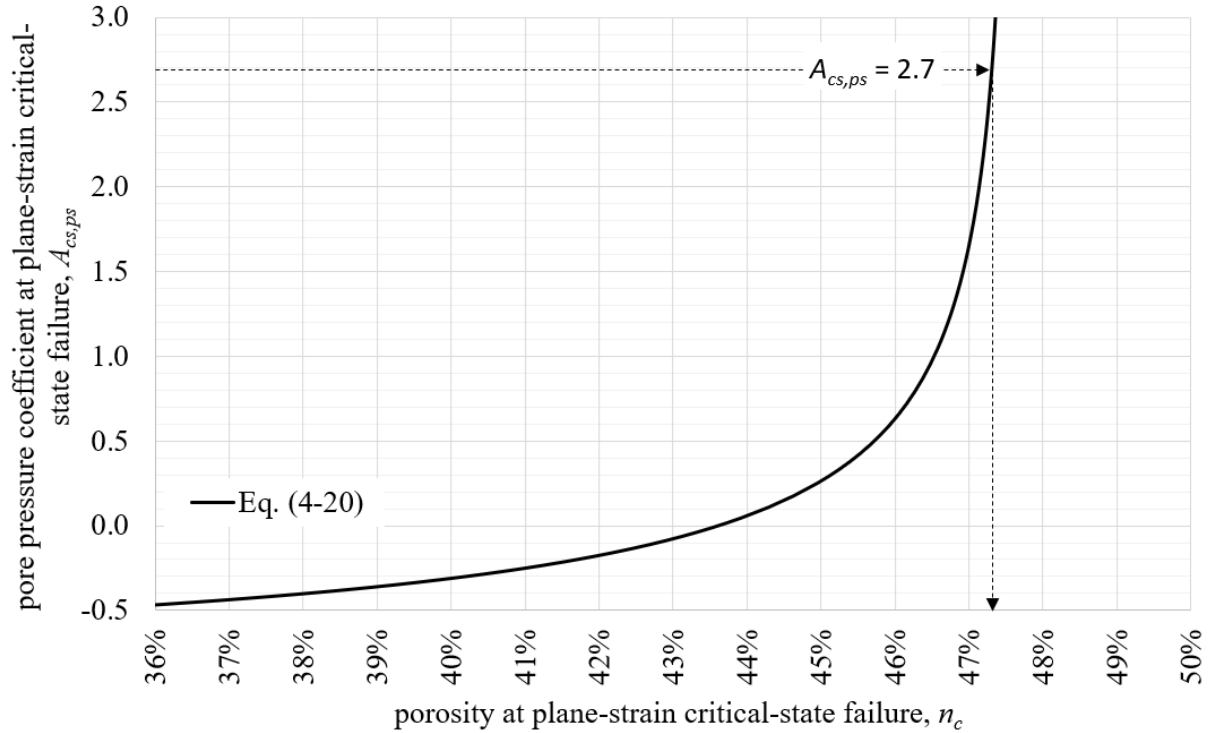


Fig. 4-9 Characteristic pore pressure $A_{cs,ps}$ for very loose sand according to (Bjerrum et al., 1961) and present Eq. (4-20).

4.2.5. Critical state shear strength and critical state porosity in natural sands correlated to present *flow rule* in Eq. (4-9)

As explained in the literature review (see numeral 2.2). The finally mobilized angle of shearing resistance $\theta'_{cs,ps}$ corresponds to the critical porosity n_c at which the change of volumetric strain or dilatancy rate becomes zero under constant stress. In a more general sense, for each initial state $(\theta'_{cv,ps}, n_0)$ there is a unique critical porosity n_c at which a soil reaches its ultimate final state $\theta'_{cs,ps}$. For the case of a pile of silica sand standing at rest, for instance, the initial state $\theta'_{cv,ps} = \theta'_\mu = 33.46^\circ$ develops a final state $\theta'_{cs,ps} = \beta = 36.5^\circ$ at a theoretical critical state porosity equal to $n_c = 34.86\%$. This theoretical critical state porosity n_c can be correlated to actual porosity in silica sand

by means of the relative porosity n_r previously defined by (Hanna, 2001) and adopted for the present assemblage of particles as in Eq. (4-21); where n_c is given in Eqs. (4-11) and (4-12). Thus, the relative porosity is $n_{c,r} = 0.57$. Then, the critical state porosity reached by the pile of silica sand is $n_{c,sand} = 38.61\%$ as determined from Eq. (4-22) after applying the known maximum and minimum porosities of silica sand as reported in numeral 3.2; furthermore, this critical state porosity corresponds to a relative density at failure equal to $D_{r,c,sand} = 62.09\%$ as given by the known expression (4-23) for relative density in terms of porosity.

$$n_{c,r} = \frac{47.64\% - n_{c,model}}{47.64\% - 25.95\%} \quad (4-21)$$

$$n_{c,sand} = n_{max,sand} - n_{c,r} \cdot (n_{max,sand} - n_{min,sand}) \quad (4-22)$$

$$D_{r,c,sand} = \frac{\left(\frac{n_{max,sand}}{1 - n_{max,sand}}\right) - \left(\frac{n_{c,sand}}{1 - n_{c,sand}}\right)}{\left(\frac{n_{max,sand}}{1 - n_{max,sand}}\right) - \left(\frac{n_{min,sand}}{1 - n_{min,sand}}\right)} \times 100\% \quad (4-23)$$

The same correlation between the *assemblage of particles* and *natural sand* by means of the relative porosity n_r criteria can be applied for the initial state; in this case, the Eqs. (4-21) to (4-23) can be rewritten as in Eqs (4-24) to (4-26); where n_0 is given in Eqs. (4-13) and (4-14).

$$n_{0,r} = \frac{n_{max} - n_{0,model}}{n_{max} - n_{min}} = \frac{47.64\% - n_{0,model}}{47.64\% - 25.95\%} \quad (4-24)$$

$$n_{0,sand} = n_{max,sand} - n_{0,r} \cdot (n_{max,sand} - n_{min,sand}) \quad (4-25)$$

$$D_{r,0,sand} = \frac{\left(\frac{n_{max,sand}}{1 - n_{max,sand}}\right) - \left(\frac{n_{0,sand}}{1 - n_{0,sand}}\right)}{\left(\frac{n_{max,sand}}{1 - n_{max,sand}}\right) - \left(\frac{n_{min,sand}}{1 - n_{min,sand}}\right)} \times 100\% \quad (4-26)$$

Chapter 5: At-rest Lateral Earth Pressure Coefficient K_0 and K_{0-OC}

5.1. General

The previous *Chapter 4*: derived and validated an expression for the plane-strain critical state friction angle as a function of the plane-strain constant-volume friction angle $\phi'_{cs,ps}(\phi'_{cv,ps})$, see Eq. (4-8) and Eq. (4-9). The present chapter uses that expression as an input to formulate an at-rest coefficient of lateral earth pressure for both normally and overconsolidated conditions. This formulation is based on a limit equilibrium analysis of a slope of cohesionless soil standing at-rest. The main assumption of this analytical model is the use of the angle of repose $\beta = \phi'_{cs,ps}$ as the angle at which the slope stands at-rest.

5.2. Derivation of K_0

In the fill or pile resting at-rest, as illustrated in Fig. 5-1, the line \overline{AB} remains vertical (i.e., zero lateral strain). It means the strength provided by the wedge of soil ABC necessarily must counterbalance the horizontal pressure exerted by the fill on the line \overline{AB} .

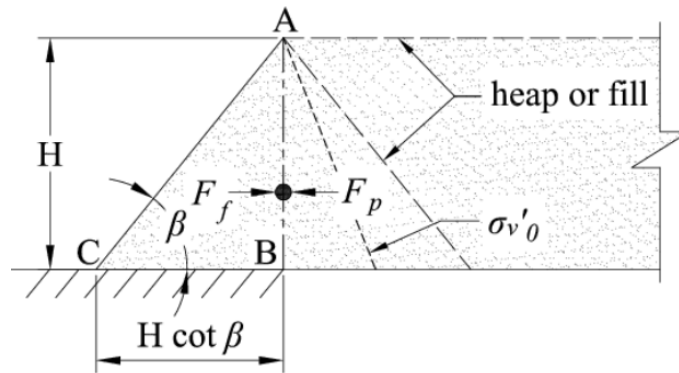


Fig. 5-1 Cross-sectional model used to analytically derive K_0 .

This balance between horizontal stresses can be expressed in terms of the limit equilibrium between the resisting frictional force on the side of the wedge ABC and the lateral earth pressure acting from the opposite side on the line AB, this is: $F_f = F_p$ as illustrated in Fig. 5-1. Considering a slice with unitary thickness, the resultant resisting frictional force F_f is given by the equation (5-1).

$$F_f = \frac{\gamma \cdot H^2 \cdot \tan \varnothing'_\mu \cdot \cot \beta}{4} \quad (5-1)$$

On the other side, the resultant of the acting forces due to the at-rest lateral earth pressure is given in Eq. (5-2):

$$F_p = \frac{\gamma \cdot H^2}{2} \cdot K_0 \quad (5-2)$$

Finally, by equating (5-1) and (5-2); Eq. (5-3) can be obtained:

$$K_0 = \frac{\tan \varnothing'_\mu}{2 \cdot \tan \beta} = \frac{\tan \varnothing'_{cv,ps}}{2 \cdot \tan \varnothing'_{cs,ps}} \quad (5-3)$$

The present expression (5-3) provides the at-rest lateral earth pressure coefficient as a function of the interparticle sliding friction angle \varnothing'_μ and the angle of repose β . Additionally, by substituting Eq. (4-9) in Eq. (5-3), the at-rest lateral earth pressure coefficient can be exclusively expressed in terms of the effective normally consolidated plane-strain critical state friction angle $\varnothing'_{cs,ps}$ as given in Eq. (5-4).

$$K_0 = \frac{\sqrt{3/4} - \sin(\phi'_{cs,ps})}{2 \cdot \cos(\phi'_{cs,ps}) - 1} \quad (5-4)$$

Fig. 5-2 shows the at-rest lateral earth pressure K_0 as given by the previously derived equation (5-3) compared with the simplified expression (2-18) according to (Jaky, 1948) which is known to be a good empirical fit for natural soils.

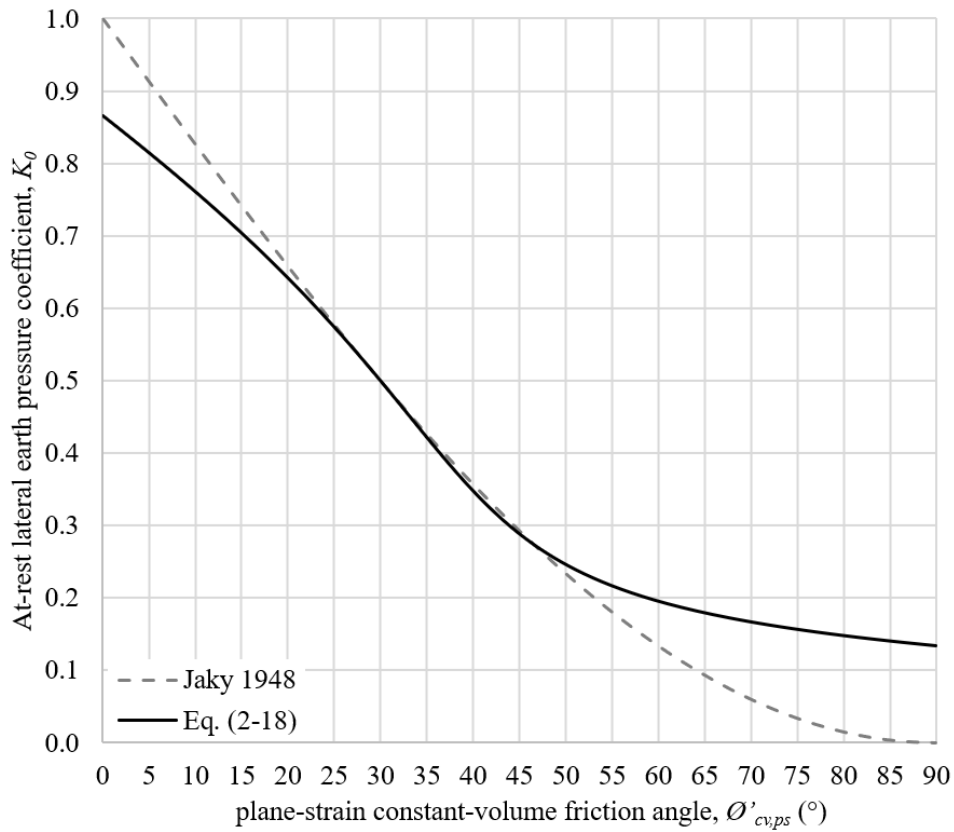


Fig. 5-2 At-rest lateral earth pressure coefficient K_0 according to Eq. (5-3) compared with the expression (2-18) since (Jaky, 1948).

Fig. 5-2 shows how the Jaky's simplified expression (2-18) is approximately coincident with present expression (5-3) or (5-4) in the interval of angles of shearing resistance commonly found in natural soils; this is $20^\circ < \phi' < 40^\circ$ according to (Terzaghi et al., 1996, p. 146). Probably, this local overlap could explain the coincidental results obtained from Eq. (2-18) as pointed out by (Michalowski, 2005, p. 1429) among others, see numeral 2.5.

The range of the equation (5-3) is $(1 - \sqrt{3/4}) \leq K_\theta \leq \sqrt{3/4}$ within the complete domain for the angle of shearing resistance $0 \leq \phi' \leq 90^\circ$. While the range of Jaky's simplified expression (2-18) is $0 \leq K_\theta \leq 1$ for the same domain as can be seen in Fig. 5-2. This difference in ranges is specially marked toward the ends of the domain and out of the local sub range associated with natural soils. Given that a granular soil like sand is neither liquid nor solid matter it seems more reasonable the range exhibited by the present Eq. (5-3).

From the relationship established between friction and the state parameter porosity and the relationship between porosity and relative density as explained in *Chapter 4*: is possible to plot the relationship between the at-rest coefficient of lateral earth pressure K_θ versus the relative density D_r of the silica sand under study see Fig. 5-3.

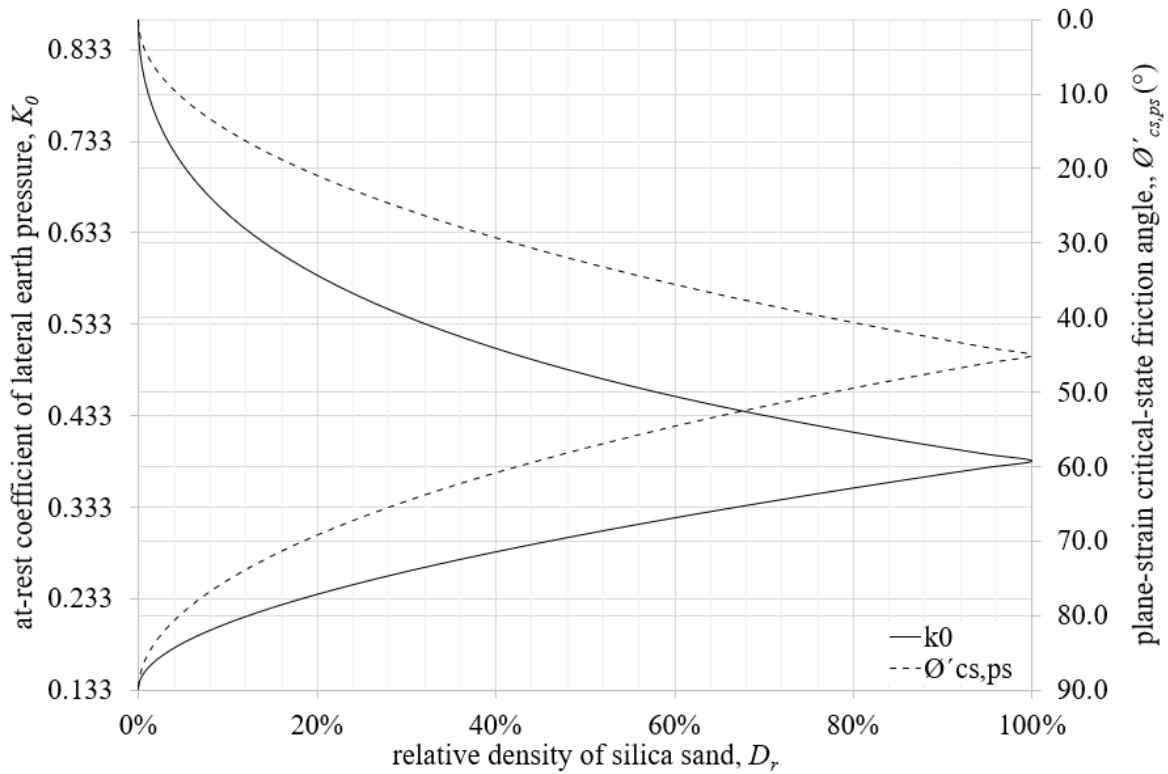


Fig. 5-3 At-rest lateral earth pressure coefficient K_0 according to Eq. (5-3) versus relative density for silica sand.

5.2.1. Validation of present expression (5-3) for K_0 with existing experimental results

As exposed in the literature review, several researchers have confirmed the empirical validity of the results of Jaky's simplified expression (2-18) when applied in natural soils (Brooker and Ireland, 1965), (Mayne and Kulhawy, 1982), (Mesri and Hayat, 1993, p. 664), (Michalowski and Park, 2004), (Michalowski, 2005), (Federico et al., 2008), (Lee et al., 2013), (Khosravi et al., 2013). Now, considering that Jaky's simplified expression is coincident with present equation (5-3) in the interval of shearing resistance angles in the range $20^\circ < \phi' < 40^\circ$ commonly found in

naturally occurring soils (*i.e.* just a small difference of +/- 0.035), see Fig. 5-2. By extension it follows that the present expression (5-3) shares this same empirical validation.

(Terzaghi, 1923) observed the at-rest lateral earth pressure coefficient K_0 as a case of the active lateral earth pressure mechanism where the mobilized angle of internal friction ϕ'_o associated with the at-rest condition acts along a straight plane of failure, see equation (5-5).

$$K_0 = \frac{1 - \sin \phi'_o}{1 + \sin \phi'_o} \quad (5-5)$$

Experimental measurements of K_0 in clays and granular soils after the application of equations (2-5) and (2-18) leads to ratios of ϕ'_o/ϕ'_{cv} in the range of 0.59 to 0.73, (Mesri and Hayat, 1993, p. 651). Back calculating this same ratio ϕ'_o/ϕ'_{cv} using the K_0 from herein equation (5-3) in the range of naturally occurring soils yields ratios of ϕ'_o/ϕ'_{cv} in a very similar range of 0.60 to 0.73, see computations in the Table 5-1. The ϕ'_o/ϕ'_{cv} ratios suggested by (Terzaghi, 1923) and (Rowe, 1954) and (Rowe, 1958) are within this same range (Mesri and Hayat, 1993, p. 651). It should be noted that normally consolidated clays and loose sand specimens behave similarly (Mesri and Hayat, 1993) thus for those clays Eq. (5-4) holds present comparison.

ϕ'	K_0	ϕ'_o	ϕ'_o/ϕ'_{cv}
20	0.60	14.67	0.73
21	0.59	15.16	0.72
22	0.58	15.65	0.71
23	0.57	16.13	0.70
24	0.56	16.61	0.69

θ'	K_0	θ'_o	θ'_o/θ'_{cv}
25	0.55	17.09	0.68
26	0.54	17.57	0.68
27	0.53	18.05	0.67
28	0.52	18.53	0.66
29	0.51	19.00	0.66
30	0.50	19.47	0.65
31	0.49	19.94	0.64
32	0.48	20.41	0.64
33	0.47	20.88	0.63
34	0.47	21.35	0.63
35	0.46	21.81	0.62
36	0.45	22.28	0.62
37	0.44	22.74	0.61
38	0.43	23.21	0.61
39	0.43	23.67	0.61
40	0.42	24.14	0.60

Table 5-1 Theoretical θ'_o/θ'_{cv} ratios for the interval of naturally occurring soils according to the present study.

(Mesri and Hayat, 1993) plotted own and existing experimental data from (Stroud, 1988), (Díaz-Rodríguez et al., 1992) and (Terzaghi, 1920) for the coefficient of at-rest lateral earth pressure in sedimented, normally consolidated young deposits. This figure was adapted in Fig. 5-4 to include the present Eq. (5-3) or Eq. (5-4). Fig. 5-4 shows that present derivation adheres well to that experimental data.

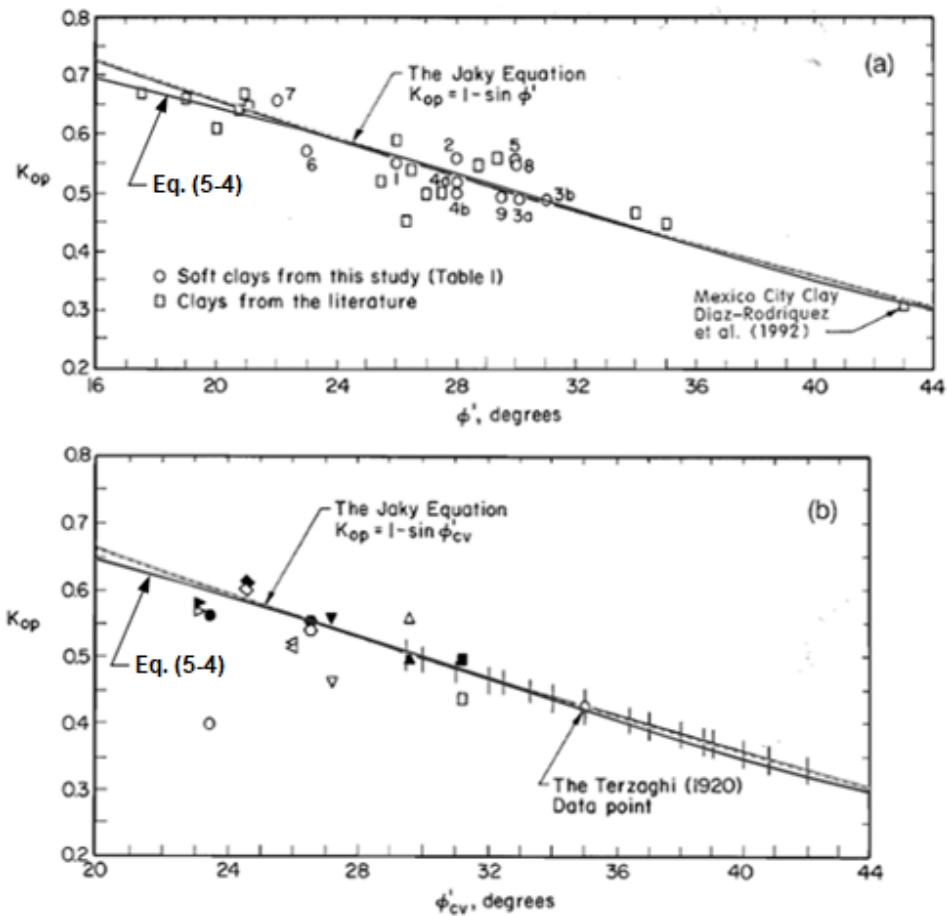


Fig. 5-4 K_0 according to present Eq. (5-4) superimposed on data for K_0 : (a) for clays; and (b) for loose sands. Adapted from (Mesri and Hayat, 1993, fig. 7).

(Bjerrum et al., 1961) developed a series of triaxial tests in sand as analyzed in *Chapter 8*. As part of the sample preparation, these authors developed consolidation under an all-around cell pressure caring the principal stress ratio to guaranty no change of the sample diameter. In this way, they obtained direct measurement of the at-rest lateral earth pressure coefficient K_0 . Then, they plotted the observed values of K_0 versus their corresponding initial porosities n_0 . These results are adopted in Fig. 5-5 to compared with present work in Eq. (5-3) or Eq. (5-4). As observed in Fig. 5-5, the

present Eq (5-4) makes a good prediction of that experimental data set. Moreover, (5-4) in Fig. 5-5 predicts the upper envelope as expected for the normally consolidated condition.

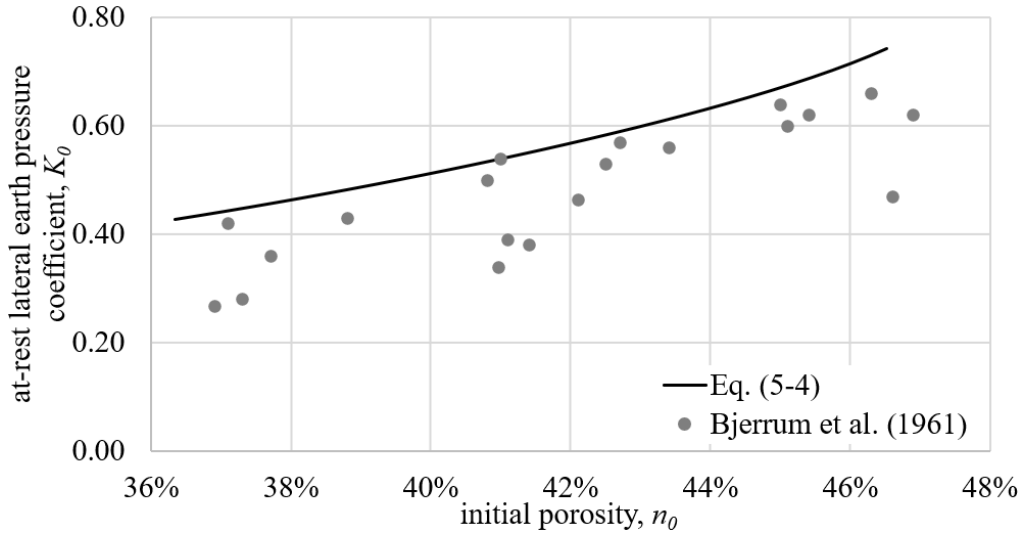


Fig. 5-5 K_0 according to present equation (5-4) versus initial porosity compared to original data for K_0 obtained experimentally in loose sands by (Bjerrum et al., 1961, fig. 12).

(Chu and Gan, 2004) found that K_0 values for loose to very loose sand as obtained from their laboratory tests were significantly lower than that predicted by Jaky's simplified expression (2-18). On this regard is interesting to note that present solution in Eq. (5-3) or Eq. (5-4) agrees well with this finding since present K_0 consistently plots below Jaky's simplified expression (2-18) specifically for the range of $\theta' < 25^\circ$ (i.e., loose and very loose sand), see Fig. 5-2.

5.3. Derivation of K_{0-oc}

The overconsolidation can be easily introduced in the present model through multiplying the weight of the column " m " given in present equation (4-5) by OCR , in this way an equivalent angle

of repose corresponding to the historical condition is obtained. Then, this angle of repose is passed through the derivation for the at-rest lateral earth pressure explained before to get in this way the maximum past at-rest lateral earth pressure (i.e., loading phase), see equation (5-6).

$$K_{0-loading} = K_0 \cdot OCR \quad (5-6)$$

After the loading phase, the unloading phase starts where a part of the lateral earth pressure is lost due to plastic relaxation of the granular soil mass. However, the elastic component of the soil can store elastic energy resulting in a higher coefficient of at-rest lateral earth pressure (i.e., K_{0-OC}). This elastic soil behavior given by Hook's law has also been experimentally observed in soils (Sherif et al., 1984, p. 55), (Zhao et al., 2010). Accordingly, by subtracting the losses due to unloading from the loading phase (5-6) is possible to obtain the expression (5-7) for the at-rest lateral earth pressure coefficient incorporating the OCR parameter. This Eq. (5-7) for K_{0-OC} becomes K_0 (5-3) for the normally consolidated state where $OCR = 1$.

$$K_{0-OC} = K_{0-OCR} \cdot OCR - K_{0-OCR} \cdot (OCR - 1) \cdot \Lambda \quad (5-7)$$

Where:

$$K_{0-OCR} = \frac{\sqrt{3/4} - \sin(\varnothing'_{cs,ps,OCR})}{2 \cdot \cos(\varnothing'_{cs,ps,OCR}) - 1} \quad (5-8)$$

$$\tan(\varnothing'_{cv,ps,OCR}) = \tan(\varnothing'_{cs,ps,OCR}) \frac{\sin 60^\circ - \sin(\varnothing'_{cs,ps,OCR})}{\cos(\varnothing'_{cs,ps,OCR}) - \cos 60^\circ} \quad (5-9)$$

$$\varnothing'_{cv,ps,OCR} = \tan^{-1} \left(\frac{\tan(\varnothing'_{cv,ps})}{OCR} \right) \quad (5-10)$$

Or

$$\phi'_{cs,ps,OCR} = \tan^{-1} \left(\frac{\tan(\phi'_{cs,ps})}{OCR} \right) \quad (5-11)$$

Where $K_{\theta-OCR}$ is the equivalent normally consolidated at-rest coefficient of lateral earth pressure given by Eq. (5-8) after substituting the effective normally consolidated critical state plane-strain friction equivalent to the given overconsolidated condition $\phi'_{cs,ps,OCR}$. In turn, this $\phi'_{cs,ps,OCR}$ can be computed from Eq. (5-9) after substituting the effective normally consolidated plane-strain constant-volume friction equivalent to the given overconsolidated condition $\phi'_{cv,ps,OCR}$ determined by the Eq. (5-10) or $\phi'_{cs,ps,OCR}$ can also be computed directly from Eq. (5-11). And A is the plastic volumetric strain ratio defined as $(1 - \kappa/\lambda)$; where, λ and κ are the volumetric compression indices for the plastic and elastic deformations of soil, respectively. Alternatively, A can also be estimated as $(1 - C_s/C_c)$; where, C_c and C_s are the slopes of the compression and swelling lines under vertical loading in oedometer tests. (Mayne, 1980) published a range of A based on 105 tests. Mayne indicated that regardless of the clay composition, there was an upper bound around 0.9 and a lower bound around 0.2 for A . (Atkinson, 1993) suggested a typical interval for A between 0.99 and 0.61, see Fig. 5-6. In general, plastic volumetric strain ratio in natural soils ranges within a wider interval between 0.99 and 0.2. In conclusion, three CSSM parameters (i.e., OCR , κ , λ) are necessary for a more complete estimation of $K_{\theta-OC}$.

Soil	LL	PL	Typical soil parameters					
			λ	Γ	N	M	ϕ'	κ/λ
Fine-grained clay soils								
London clay	75	30	0.16	2.45	2.68	0.89	23°	0.39
Kaolin clay	65	35	0.19	3.14	3.26	1.00	25°	0.26
Glacial till	35	17	0.09	1.81	1.98	1.18	29°	0.16
Coarse-grained soils								
River sand			0.16	2.99	3.17	1.28	32°	0.09
Decomposed granite			0.09	2.04	2.17	1.59	39°	0.06
Carbonate sand			0.34	4.35	4.80	1.65	40°	0.01

Fig. 5-6 Critical state parameters of some soil types in (Atkinson, 1993).

5.3.1. Validation of present expression (5-7) for K_{0-OC} with existing experimental results

(Hanna and Al-Romhein, 2008) based on experimental investigation for the at-rest lateral earth pressure in overconsolidated silica sand, proposed the formula given in Eq. (5-12). By applying a plastic volumetric strain ratio for this silica sand λ in the interval between 0.973 and 0.977 for relative densities between 21% and 75% as reported by (Hanna and Diab, 2017), see numeral 3.2. Fig. 5-7 presents comparison between the results obtained by Eq. (5-7) and the experimental results in Eq. (5-12).

$$K_{0-OC} = (1 - \sin \phi') \cdot OCR^{(\sin \phi' - 0.18)} \quad (5-12)$$

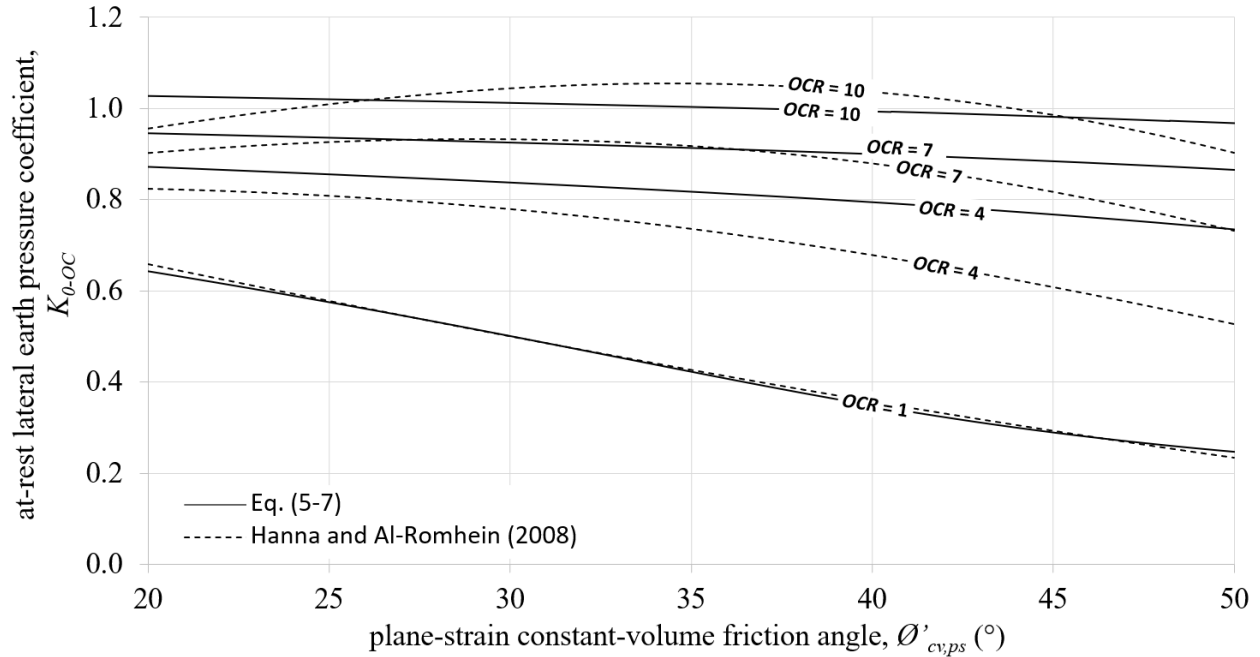


Fig. 5-7 At-rest lateral earth pressure coefficient K_{0-OC} according to present Eq. (5-7) compared with the empirical formula (5-12) according to (Hanna and Al-Romhein, 2008).

(El-Emam, 2011) conducted experimental and numerical investigations on the at-rest lateral earth pressure on overconsolidated sandy soil (olivine sand). A specially instrumented container of 1.0 m high was used for this purpose. The sandy soil was compacted by vibration to increase the overconsolidation ratio. He reported that the horizontal force was about three times the value calculated from Eq. (2-18) (Jaky, 1948) for the sandy soil of $\phi' = 46^\circ$ and the compaction procedures used were in perfect agreement with an $OCR = 4$. By using an average $A = 0.95$ for sand estimated by (Atkinson, 1993), see Fig. 5-6, it was possible to compute the horizontal to vertical force ratio of 2.93 found by (El-Emam, 2011). Previous estimation was computed as follows: the horizontal force is a direct function of the coefficient of lateral earth pressure; consequently, the ratio between overconsolidated and at-rest horizontal forces is given by K_{0-OC}/K_0 .

Now, by applying Jaky simplified expression (2-18) for the given constant-volume friction angle for this olivine sand, $\phi'_{cv} = 46^\circ$, results an at-rest lateral earth pressure coefficient equal to $K_0 = 0.28$. On the other hand, after applying present expression (5-7) for the given overconsolidation ratio $OCR = 4$ and the plastic volumetric strain ratio $A = 0.95$ results an at-rest lateral earth pressure for overconsolidated sand equal to $K_{0-OC} = 0.82$. Finally, this yields $K_{0-OC}/K_0 = 0.82/0.28 = 2.93$.

(Santana and Candeias, 2015) presented an experimental technique, using a computer controlled triaxial test to evaluate the at-rest lateral earth pressure coefficient K_0 with the OCR effect. They reported their method has the advantages of being free from any side friction effect and automatically ensures the diameter change remains zero. Based on results from those laboratory tests, they determined a characteristic relationship for K_{0-OC} of the Toyoura sand as a function of OCR , given in Eq. (5-13).

$$K_{0-OC} = 0.38 \cdot OCR^{(0.447)} \quad (5-13)$$

By using a plastic volumetric strain ratio of $A = 0.98$ for the Toyoura sand (Uchida et al., 2016) and a friction angle $\phi' = 38^\circ$ as reported by these authors. Fig. 5-8 shows a satisfactory comparison between the present theoretical prediction using (5-7) and the experimental result as given by these authors in (5-13).

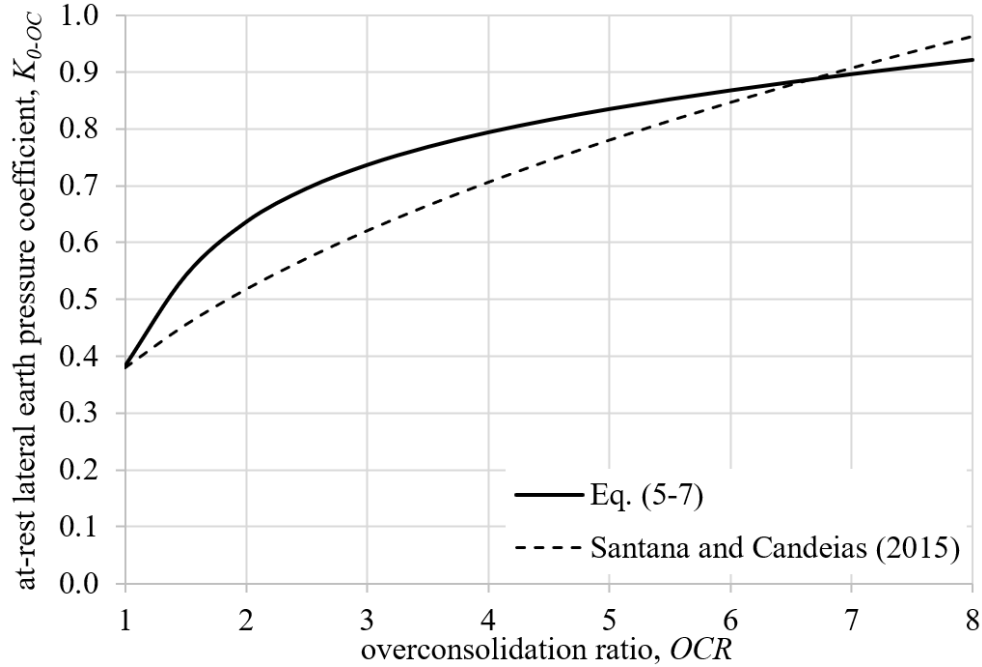


Fig. 5-8 At-rest lateral earth pressure coefficient $K_{\theta-OC}$ after present equation (5-7) compared with the experimental result for Toyoura sand given by equation (5-13) according to (Santana and Candeias, 2015).

5.4. Experimental verification of present expressions for K_{θ} (5-3) and $K_{\theta-OC}$ (5-7)

This is the analysis of the experimental results for lateral stress presented in numeral 3.4. Table 5-2 compares experimental results versus corresponding theoretical predictions for the at-rest lateral earth pressure in a non-compacted sample of silica sand. The first line in Table 5-2 corresponds to the normally consolidated condition and the following lines are independent unloading steps. The outputs are presented in (kPa) after correlating outputs with the corresponding calibration functions, see numeral 3.4.2.2. The experimental at-rest coefficient of lateral earth pressure K_{θ} or $K_{\theta-OC}$ was computed as the ratio between the average horizontal stress

given by the pressure sensors $\overline{\sigma'_h}$ and the known applied vertical stress $\sigma'_{v,0}$ at each step, see Eq. (2-1). The experimental overconsolidation ratio OCR associated to each step was calculated as the ratio between the known maximum historic vertical consolidation stress which is $\sigma'_{v,max} = 24.06$ kPa for these tests on non-compacted silica sand, and the known applied effective vertical stress or current stress at each unloading step which is given in the column “ $\sigma'_{v,0}$ ” in Table 5-2, see Eq. (5-14).

$$OCR = \frac{\sigma'_{v,max}}{\sigma'_{v,0}} \quad (5-14)$$

The OCR was additionally back computed by applying Eqs. (5-7) to (5-10) and the known initial friction angle $\phi'_{cv,ps}$, see Eq. (4-9). Accordingly, the OCR reported in the Table 5-2 (theoretical results part) is the one associated to a theoretical K_{0-OC} that equals that obtain from present experimental study. Finally, a direct comparison between the experimental OCR and the theoretical OCR permits to conclude there is a good agreement between experimental results and theoretical predictions for both the normal Eq. (5-3) and the overconsolidated Eq. (5-7) at-rest coefficients of lateral earth pressure. The previous conclusion under a relative error of about +/- 5%. *Appendix G* presents all previous computations in an Excel spreadsheet.

Experimental results			Theoretical results		
$\sigma'_{v,0}$	$\overline{\sigma'_h}$	$K_{\theta-OC}$	OCR	OCR	Relative error
(kPa)	(kPa)			(5-7)	
24.056	10.53	0.438	1.000	0.970	-3.00%
21.313	10.01	0.470	1.129	1.117	-1.00%
18.570	9.31	0.501	1.295	1.280	-1.20%
15.771	8.47	0.537	1.525	1.492	-2.18%
13.028	7.76	0.596	1.846	1.921	4.04%
10.065	6.70	0.666	2.390	2.620	9.62%
average (SD):					1.0% (+/-5.0%)

Table 5-2 Experimental verification of present expressions for K_{θ} Eq. (5-3) and $K_{\theta-OC}$ Eq. (5-7) on a non-compacted sample of silica sand.

5.5. Experimental determination of the $\sigma'_{v,max}$ corresponding to the standard, the reduced modified and the modified Proctor energies of compaction in silica sand

Table 5-3 and Table 5-4 report the experimental results for the three standard compacted samples. The output horizontal stress in (kPa) corresponds to the average of the three sensors after correlating with the corresponding calibration functions, see numeral 3.4.2.2. The overconsolidated at-rest coefficient of lateral earth pressure $K_{\theta-OC}$ at each step was computed as the ratio between the horizontal stress given by the average of the three pressure sensors $\overline{\sigma'_h}$ and the current known applied vertical stress $\sigma'_{v,0}$ at each step, see Eq. (2-1).

The parameter OCR associated to each step was back computed by applying Eqs. (5-7) to (5-10) and the known initial friction angle $\phi'_{cv,ps}$, see Eq. (4-9). In this way, the OCR reported in the Table 5-3 and Table 5-4 is the one correlated to a theoretical $K_{\theta-OC}$ equal to that obtain from this experimental work. Finally, the maximum historic vertical consolidation stress $\sigma'_{v,max}$ equivalent to each of the energies of compaction was determined by multiplying the known applied vertical stress or current stress $\sigma'_{v,0}$ by the OCR theoretically determined as explain before. The *Appendix F* contains all the computations involved in this analysis in a spreadsheet.

This equivalent maximum historic vertical consolidation stress $\sigma'_{v,max}$ is then a direct function of the energy of compaction and the type of sand. For the herein observed silica sand, the standard Proctor energy leads to a $\sigma'_{v,max} = 101.56$ kPa (SD = 6.63 kPa) and the modified Proctor energy to a $\sigma'_{v,max} = 517.17$ kPa (SD = 15.81 kPa). As expected, the resultant maximum historic vertical consolidation stress $\sigma'_{v,max}$ is virtually constant for each energy of compaction.

Table 5-5 shows the corresponding for the reduced modified Proctor energy. This test was added to the rest of the experimental tests to build the general conclusive trend shown in Fig. 5-9.

Experimental results			Theoretical results	
$\sigma'_{v,0}$	$\overline{\sigma'_h}$	$K_{\theta-OC}$	OCR	$\sigma'_{v,max}$
(kPa)	(kPa)		(5-7)	(kPa)
24.056	18.25	0.758	4.187	100.716
21.313	16.88	0.792	4.894	104.309
18.570	15.11	0.814	5.406	100.382
15.771	13.81	0.876	7.112	112.164

Experimental results			Theoretical results	
$\sigma'_{v,0}$	$\overline{\sigma'_h}$	K_{0-oc}	OCR	$\sigma'_{v,max}$
(kPa)	(kPa)		(5-7)	(kPa)
13.028	11.82	0.907	8.129	105.905
10.065	9.47	0.941	9.289	93.497
7.377	7.60	1.031	12.735	93.943
average (SD):				101.56 (6.63)

Table 5-3 Experimental determination of the maximum historic vertical consolidation stress

$\sigma'_{v,max}$ equivalent to the standard Proctor energy.

Experimental results			Theoretical results	
$\sigma'_{v,0}$	$\overline{\sigma'_h}$	K_{0-oc}	OCR	$\sigma'_{v,max}$
(kPa)	(kPa)		(5-7)	(kPa)
13.030	20.28	1.557	40.008	521.310
10.070	18.13	1.800	52.632	530.003
7.380	15.22	2.063	66.348	489.645
4.470	13.54	3.028	117.230	524.018
1.730	11.25	6.501	301.072	520.854
average (SD):				517.17 (15.81)

Table 5-4 Experimental determination of the maximum historic vertical consolidation stress

$\sigma'_{v,max}$ equivalent to the modified Proctor energy.

Experimental results			Theoretical results	
$\sigma'_{v,0}$	$\overline{\sigma'_h}$	K_{0-OCR}	OCR	$\sigma'_{v,max}$
(kPa)	(kPa)		(5-7)	(kPa)
18.570	18.34	0.988	11.521	213.938
15.771	16.58	1.052	14.142	223.041
13.028	14.80	1.136	17.842	232.446
10.065	11.92	1.184	20.041	201.721
7.377	10.07	1.365	28.530	210.461
4.470	8.18	1.831	51.399	229.750
average (SD):				218.56 (11.91)

Table 5-5 Experimental determination of the maximum historic vertical consolidation stress

$\sigma'_{v,max}$ equivalent to the reduced modified Proctor energy.

5.6. Conclusion

The constitutive framework for plane-strain critical state shear resistance derived in *Chapter 4*: was satisfactorily applied to a limit equilibrium analysis for the obtention of two new expressions for the at-rest lateral earth pressure coefficient. These two new expressions were proved experimentally and cross-validated with existing experimental results. The first expression for K_0 accounts for the normally consolidated condition and the second extends the first into a more general form that incorporates the soil parameter OCR . Finally, a methodology to estimate OCR in backfills with standard compaction was presented and illustrated with samples of silica sand.

The analysis of the experimental results within the present chapter also permitted the empirical determination of the “maximum historic vertical consolidation stress” $\sigma'_{v,max}$ equivalent to two standard energies of compaction in silica sand, namely: the standard Proctor energy that yields an equivalent $\sigma'_{v,max} = 101.56$ kPa and the modified Proctor energy that yields an equivalent $\sigma'_{v,max} = 517.17$ kPa.

In general, as Fig. 5-9 shows, all the results from the four experimental tests align to a unique trend that reveals a tie between OCR , $K_{\theta-OC}$, and relative density D_r . Fundamentally, as shown in Fig. 5-10 OCR is a direct function of the relative density D_r reached after a given energy of compaction. The energy of compaction is then just a nominal descriptor of the medium used to obtain each relative density. Accordingly, two conclusions can be drawn: the greater D_r the greater the OCR the soil can hold; and the overconsolidated state ($OCR > 1$) can only exist where $\sigma'_{cv,ps} > \sigma'_{\mu}$. The previous is valid only under current or in-situ vertical stresses $\sigma'_{v,0} < \sigma'_{v,max}$ (i.e., elastic response) otherwise the soil may become normally consolidated or underconsolidated which may trigger a process of densification (i.e., creep) or particle crushing.

Present comprehensive solution could be found for any other sand by applying present theoretical model and an experimental test like the one described in the numeral 3.4. However, the fact that the plastic volumetric strain ratio A for cohesionless soils has a small variability (see Fig. 5-6) in the present results constitute a general indication of order or magnitude for quartz sand.

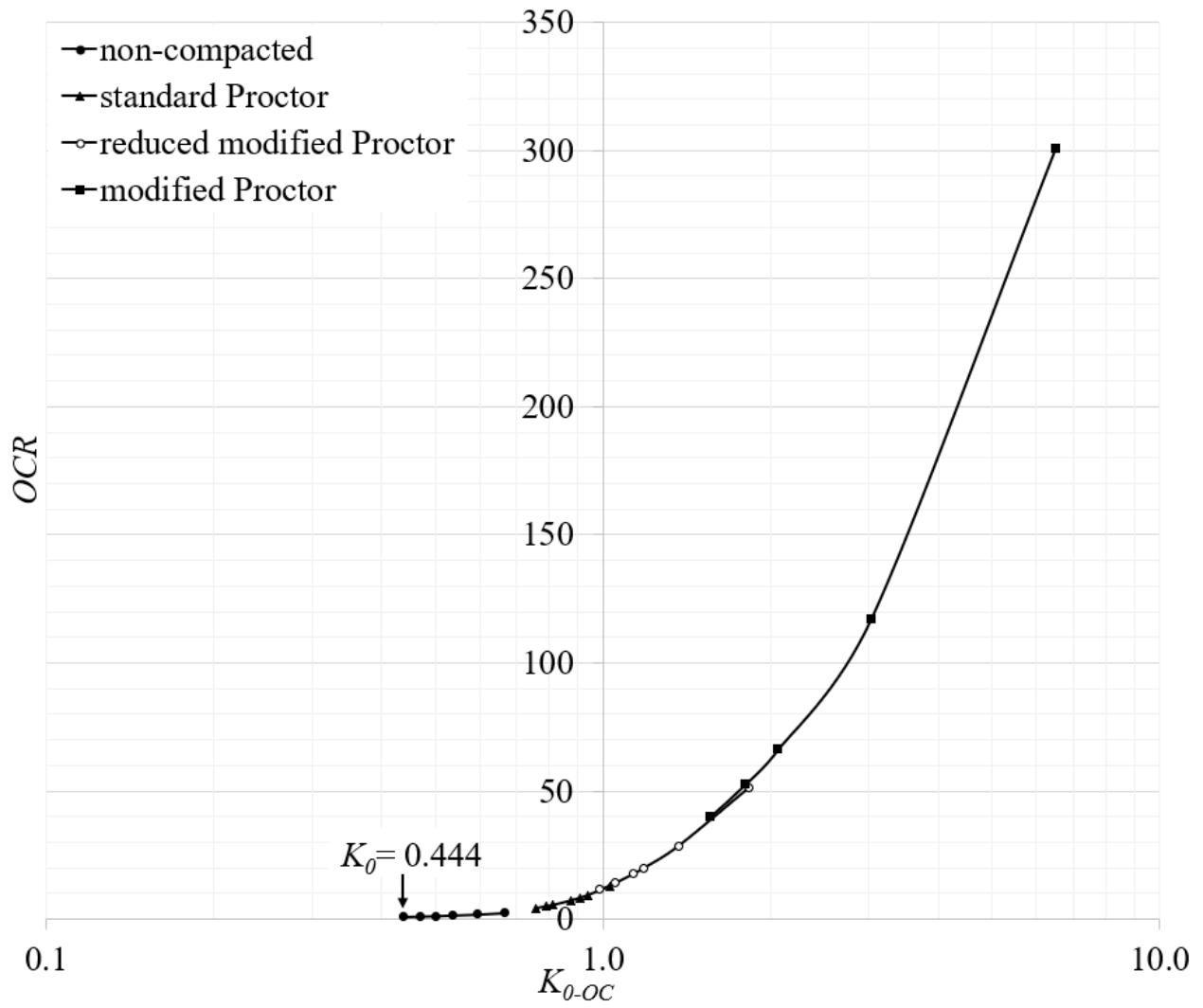


Fig. 5-9 Experimental results exhibiting a common alignment or link among OCR , $K_{\theta-OC}$, and D_r in present silica sand (see *Appendix G*).

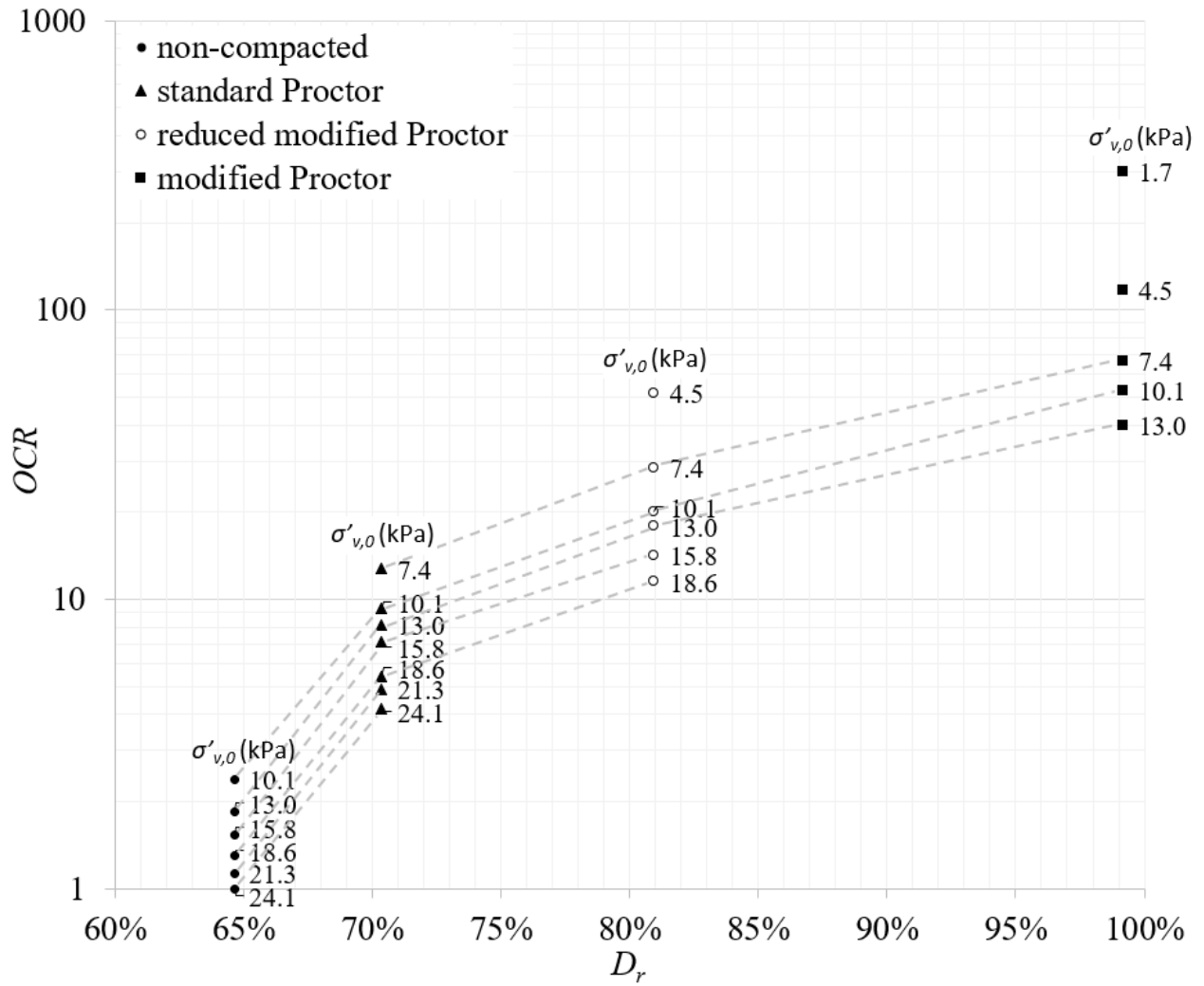


Fig. 5-10 OCR versus D_r for silica sand (see Appendix G).

Chapter 6: Active and Passive Coefficients of Lateral Earth Pressure K_a and K_p

6.1. General

This chapter presents the coefficients K_a and K_p for the plane-strain critical state backfill failure behind a retaining wall. A model was developed for the nonlinear geometry of active and passive slip-failure surface in cohesionless soils, and accordingly the determination of the appropriate coefficient of lateral earth pressure. The variational limit equilibrium method applied to a normally consolidated dry granular media and the plane-strain critical state friction angle at failure were adopted to develop the model for the failure behind a retaining wall. Finally, the influence of the parameter OCR in K_a and K_p is discussed and incorporated.

6.2. K_a and K_p in a wall backfill under plane-strain critical state failure

The observation of experimental slips indicates that no momentum is transferred through the failing mass of soil since the initially horizontal lines of reference remained horizontal after failure (Koudelka, 2016), (Hu et al., 2019), (Yang et al., 2020); in other words, no evidence of angular strain associated to moments was observed. In the absence of momentum, there is no need to check for equilibrium of momentums. On the other side, for the present problem, the vertical forces will be necessarily in equilibrium when the equilibrium of the horizontal forces is given; in other words, the vertical equilibrium is a consequence of the horizontal equilibrium. In conclusion, the induced horizontal force due to wall rotation is the main source of lateral disbalance in a soil-wall interaction; thus, the equilibrium of horizontal forces is the main condition considered in present analysis. Other assumptions associated to this model are:

- a) The wall back face is initially vertical and the backfill surface is horizontal;

- b) The wall is rigid and rotates around its base (or outward translation) in active state and around its top in passive state (or inward translation, or around its base);
- c) Coulomb is used as the failure criterion;
- d) The soil along the slip-failure surface is to develop the effective critical state plane-strain friction $\phi'_{cs,ps}$;
- e) The soil is in a normally consolidated state; and
- f) The cohesionless soil is dry.

The slope stability problem is known to adhere to the least action principle as observed by (Chen and Snitbhan, 1975) and others (Li and Liu, 2006), (Xinggao and Weining, 2010), (Yang et al., 2020). This same variational limit equilibrium approach is used here to determine the slip geometry associated to the stationary lateral force necessary to observe equilibrium of horizontal forces under the active and passive states. Using the Coulomb criterion and the differential soil element shown in Fig. 6-1, the equilibrium of the horizontal forces can be written as in Eqs. (6-1)-(6-3). The first term in Eq. (6-2) accounts for the shear resistance developed along the slip-failure surface and the second term accounts for the corresponding unbalanced horizontal stress.

$$\sum F_H = 0 \quad (6-1)$$

$$\int_0^x \int_0^y \sigma' \tan \phi'_{cs,ps} dy dx - \int_0^x \sigma' y' dx = 0 \quad (6-2)$$

$$\int_0^x (y \sigma' \tan \phi'_{cs,ps} - \sigma' y') dx = 0 \quad (6-3)$$

$$I = y \sigma' \tan \phi'_{cs,ps} - \sigma' y' \quad (6-4)$$

Where:

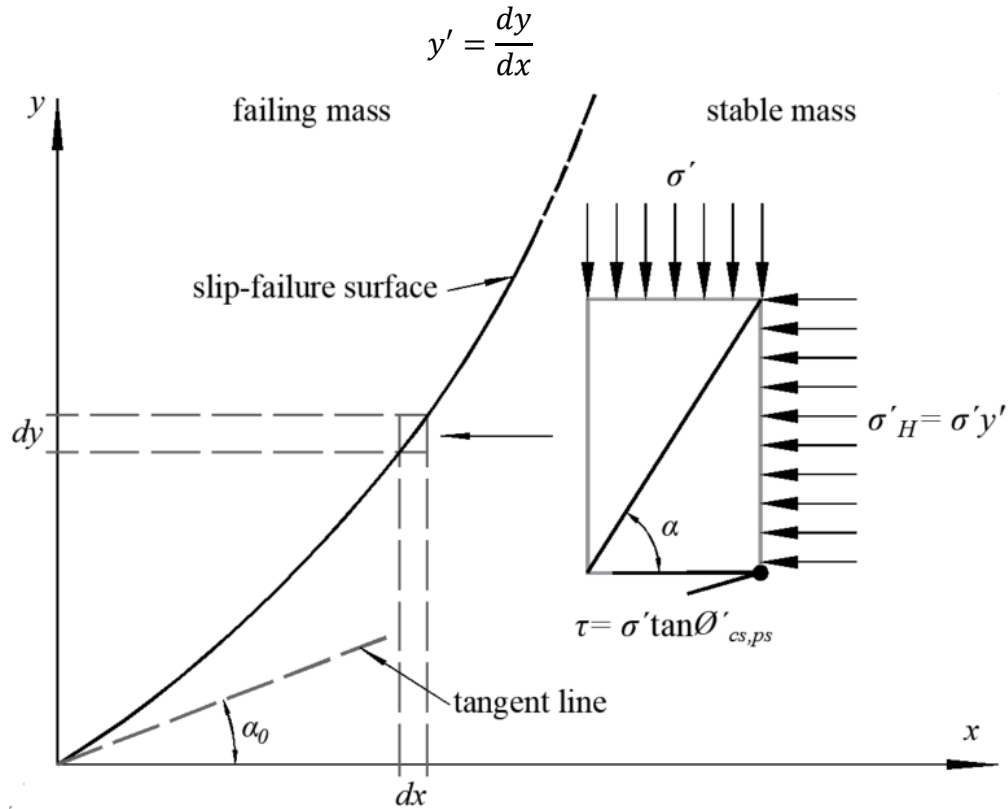


Fig. 6-1 Slip-failure surface in cartesian coordinates and differential soil element.

Since the integrand “ I ”, extracted from Eq. (6-3), incorporates the functions for: the slip geometry $y(x)$, the vertical effective stress $\sigma'(x)$ and the first derivative of the geometry $y'(x)$, the Euler differential equation will be first order, and “ I ” has a stationary value if the following Euler-Lagrange differential equations are satisfied:

$$\frac{\partial I}{\partial y(x)} - \frac{d}{dx} \left(\frac{\partial I}{\partial y'(x)} \right) = 0 \quad (6-5)$$

$$\frac{\partial I}{\partial \sigma'(x)} - \frac{d}{dx} \left(\frac{\partial I}{\partial \sigma'(x)} \right) = 0 \quad (6-6)$$

Substituting Eq. (6-4) into Eqs. (6-5) and (6-6) these two conditions are satisfied by the following first order differential equations (6-7) and (6-8):

$$y \tan \phi'_{cs,ps} - y' = 0 \quad (6-7)$$

$$\sigma' \tan \phi'_{cs,ps} + \sigma'' = 0 \quad (6-8)$$

The geometry of the slip surface Eq. (6-9) can be then obtained by solving Eq. (6-7):

$$y(x) = C_1 e^{x \cdot \tan \phi'_{cs,ps}} \quad (6-9)$$

The plane-strain critical state friction angle for normally consolidated soils is equal to the angle of repose $\beta = \phi'_{cs,ps}$ (Lambe and Whitman, 1969), (Terzaghi et al., 1996, p. 104), (Cornforth, 1973), (Santamarina and Cho, 2001), (Sadrekarimi and Olson, 2011). Beyond this point, the soil mass stands at rest as illustrated in the Fig. 6-2(a) and consequently is delimited by the angle of repose $\alpha_0 = \beta = \phi'_{cs,ps}$. Therefore, to ensure at-rest equilibrium in the active condition, the tangent of the slip-failure surface geometry at the base must be equal to the tangent of the plane-strain critical state friction angle $y'(0) = \tan(\phi'_{cs,ps})$. This condition is applied to Eq. (9) to determine the constant $C_1 = 1$. Substituting C_1 in Eq. (9) yields the geometry of the slip-failure surface Eq. (6-10) under the active state:

$$y(x) = e^{x \cdot \tan \phi'_{cs,ps}} \quad (6-10)$$

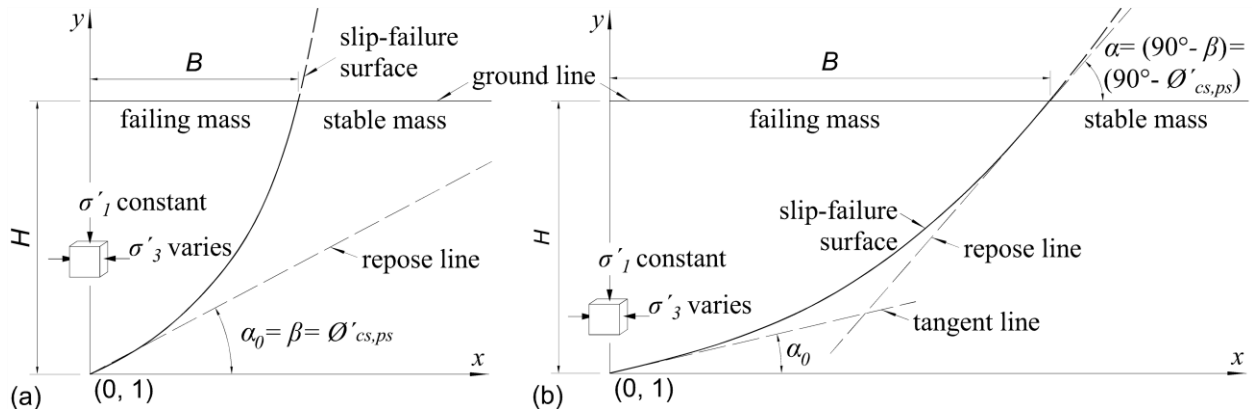


Fig. 6-2 Slip-failure surface and known boundary conditions: (a) active state; (b) passive state.

The horizontal distance B between the wall back face and the point where the slip-failure surface outcrops ground given in Eq. (6-11) can be derived from Eq. (6-10) after applying the condition $y(B) = (H + 1)$:

$$B = \frac{\ln(H + 1)}{\tan \phi'_{cs,ps}} \quad (6-11)$$

Similarly, the vertical stress $\sigma'(x)$ in Eq. (6-12) can be obtained by solving Eq. (6-8):

$$\sigma'(x) = C_2 e^{-x \cdot \tan \phi'_{cs,ps}} \quad (6-12)$$

By applying the known vertical stress at any point $(H + 1 - y)\gamma$ the constant C_2 can be determined as $(H + 1 - y)\gamma$; where: γ is the dry unit weight of the cohesionless soil. The vertical stress in Eq. (6-13) satisfies the vertical stress equal to zero at the top of the wall, i.e. $\sigma'(B) = 0$ where $y = (H + 1)$, and the vertical stress equal to γH at the base of the wall, i.e. $\sigma'(0) = \gamma H$ where $y = 1$.

$$\sigma'(x) = (H + 1 - y) \gamma \quad (6-13)$$

For the passive state, the above analysis remains applicable until Eq. (6-9). However, due to the 90°-rotation of the principal stress state, the friction angle developed at the origin is not longer $\phi'_{cs,ps}$ but the unknown angle α_0 as denoted in Fig. 6-2(b). Accordingly, Eq. (6-9) becomes:

$$y(x) = C_1 e^{x \cdot \tan \alpha_0} \quad (6-14)$$

Given the wall height H , the passive case will have three unknowns and three knowns. The unknowns are: α_0 , B , and C_1 . And the knowns from Fig. 2(b) are: $y(0) = 1$, $y(B) = (H+1)$, and $y'(B) = \tan(90^\circ - \phi'_{cs,ps})$. By applying these conditions in Eq. (6-14) turns out the geometry for the slip-failure surface in the passive state is Eq. (6-15). Where the integral constant results to be $C_1 = 1$, the distance B is determined by Eq. (6-16) and the generatrix angle α_0 is determined by Eq. (6-17).

$$y(x) = e^{\left(\frac{x \cdot \tan(90^\circ - \phi'_{cs,ps})}{(H+1)}\right)} \quad (6-15)$$

$$B = \frac{(H+1) \ln(H+1)}{\tan(90^\circ - \phi'_{cs,ps})} \quad (6-16)$$

$$\alpha_0 = \tan^{-1} \left(\frac{\tan(90^\circ - \phi'_{cs,ps})}{(H+1)} \right) \quad (6-17)$$

Since the vertical stress boundary conditions in the passive state are the same as for the active state, that is: $\sigma(0) = \gamma H$ for $y = 1$ and $\sigma(B) = 0$ for $y = (H+1)$, it follows the differential equation Eq. (6-8) is also satisfied by Eq. (6-12) as demonstrated above. Additionally, from the governing geometry it is possible to determine the area A_f of the failing mass by means of Eq. (6-18).

$$A_f = (H+1)B - \frac{e^{B \tan \alpha_0} - 1}{\tan \alpha_0} \quad (6-18)$$

Having the horizontal and vertical stresses defined in Fig. 6-1 and Eq. (6-13) it is possible to determine the associated horizontal earth pressure distribution. The failing mass undergoes in extension, as shown in Fig. 6-2, where the intermediate stress is equal to the *major* principal stress $\sigma'_3 = \sigma'_{max}$ and $\sigma'_1 = \sigma'_{min}$; accordingly, the lateral earth pressure at failure is given by $K = \sigma'_1 / \sigma'_3$. For a dx and according to Fig. 6-1 we have that $\sigma'_3 = \sigma'_y$ and $\sigma'_1 = \sigma'$; consequently, the lateral earth pressure coefficient can be given by $K = 1 / y'$ or, after integrating, by Eq. (6-19); where, the generatrix angle is $\alpha_0 = \theta'_{cs,ps}$ for the active state and Eq. (6-17) for the passive state. Moreover, the lateral earth pressure distribution behind the wall given in Eq. (6-20) is the product between the lateral earth pressure coefficient from Eq. (6-19) and the vertical stress from Eq. (6-13).

$$K(x) = \frac{x}{\tan \alpha_0 e^{x \cdot \tan \alpha_0}} \quad (6-19)$$

$$\sigma'_H(x) = \frac{\gamma(H + 1 - y)x}{\tan \alpha_0 e^{x \cdot \tan \alpha_0}} \quad (6-20)$$

Fig. 6-3 presents the proposed solution applied to the large-scale experiment of (Tsagareli, 1965) where the $\theta'_{cs,ps} = 45.2^\circ$ is given by the $atan(y'(0))$ of the equation number one in (Tsagareli, 1965). The resultant active force for each of the five tests reported by (Tsagareli, 1965) after applying present solution is: 42.18 kN, 31.65 kN, 22.56 kN, 14.98 kN and 8.94 kN for the wall heights 4.0 m, 3.5 m, 3.0 m, 2.5 m and 2.0 m, respectively. These resultant forces agree positively with the empirical result of 4.00 t, 2.85 t, 2.02 t, 1.39 t and 0.9 t, respectively. In general, the herein theoretical prediction was 8% over the experimental measurement. On the other side, the average location of the resultant force as per present solution is $0.38H$ while the average experimentally determined by (Tsagareli, 1965) was $0.42H$.

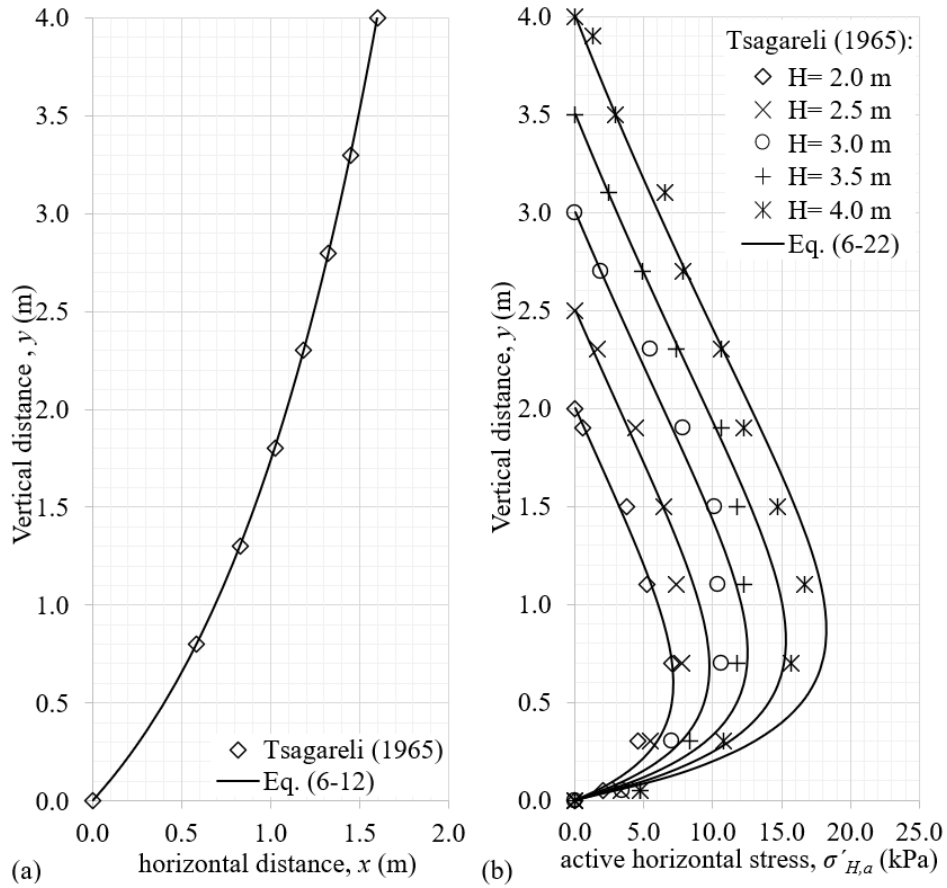


Fig. 6-3 Present solution applied to experimental results of Tsagareli (1965): (a) slip-failure geometry; (b) lateral earth pressure distribution.

In conclusion, Fig. 6-4 to Fig. 6-7 shows a selected family of curves to illustrate the variation of present solution with friction and wall height for the active and passive cases; friction angles from 20° to 60° with 5° increments were plotted. *Appendix H* presents a spreadsheet with all the calculations. From this analysis is possible to establish the following general conclusions:

- The slip-failure surface geometry for the active case is unique for each $\phi'_{cs,ps}$ being the cutting level the given wall height H . The small-scale models are not enough to capture the complete governing geometry as previously pointed by (Tsagareli, 1965).
- The slip-failure surface geometry is relatively more curved in the active state than for the passive where it results more flattened.
- The lateral stress distribution is curved and in general proportional to friction and wall height; however, for the passive state the lateral stress appears particularly sensitive to the wall height.
- The location of the resultant force is an inverse function of the wall height and varies as illustrated in Fig. 6-8. Consequently, there is not a unique relative location of the resultant force in terms of wall height H like the $H/3$ since Coulomb or Rankine or the $0.42H$ suggested in (Tsagareli, 1965).

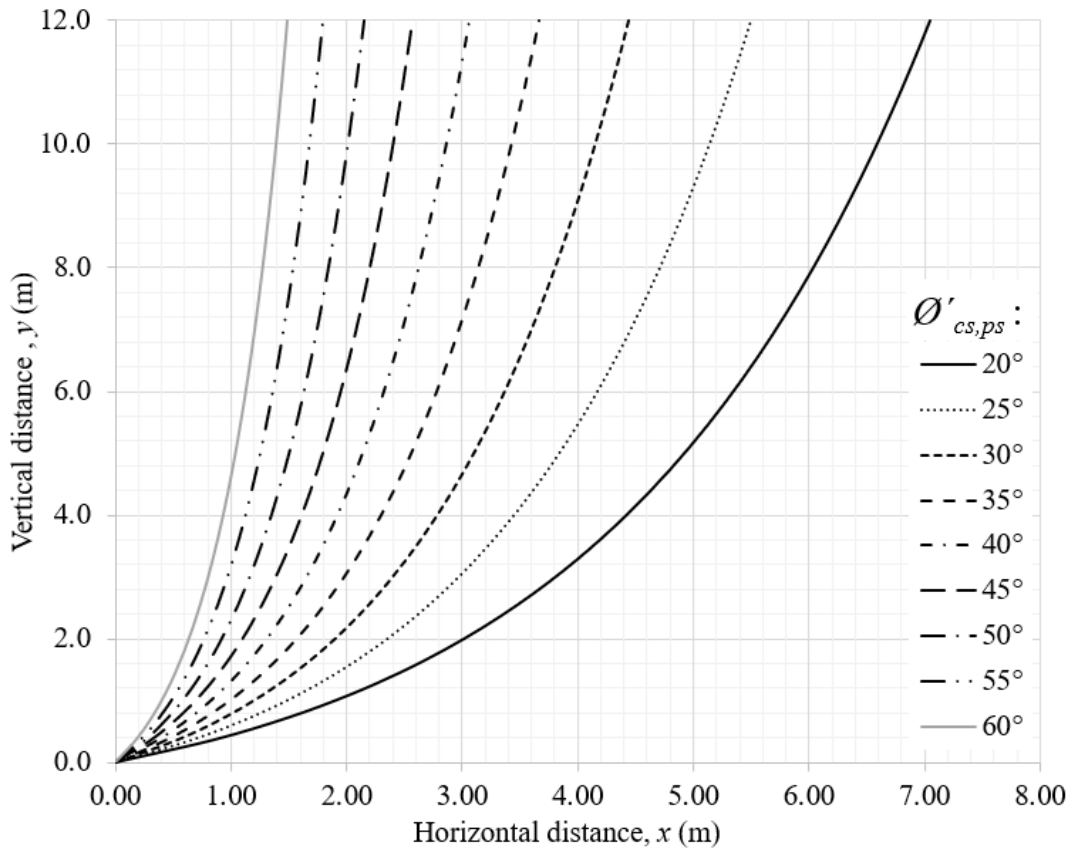


Fig. 6-4 Active slip geometry as per Eq. (6-10) illustrated with a selection of $\varnothing'_{cs,ps}$.

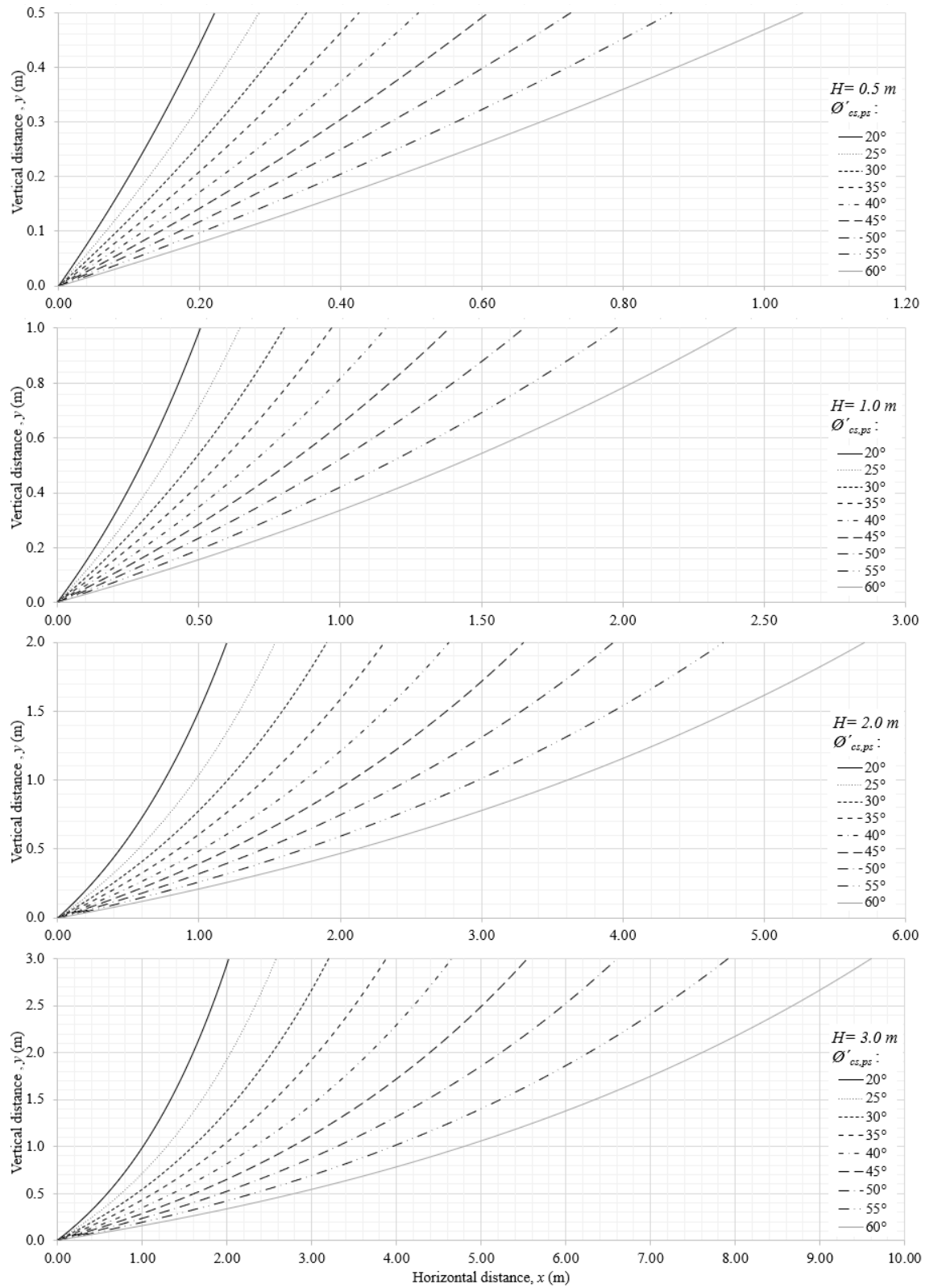


Fig. 6-5 Passive slip geometry as per Eq. (6-15) illustrated with a selection of $\theta'_{cs,ps}$ and H .

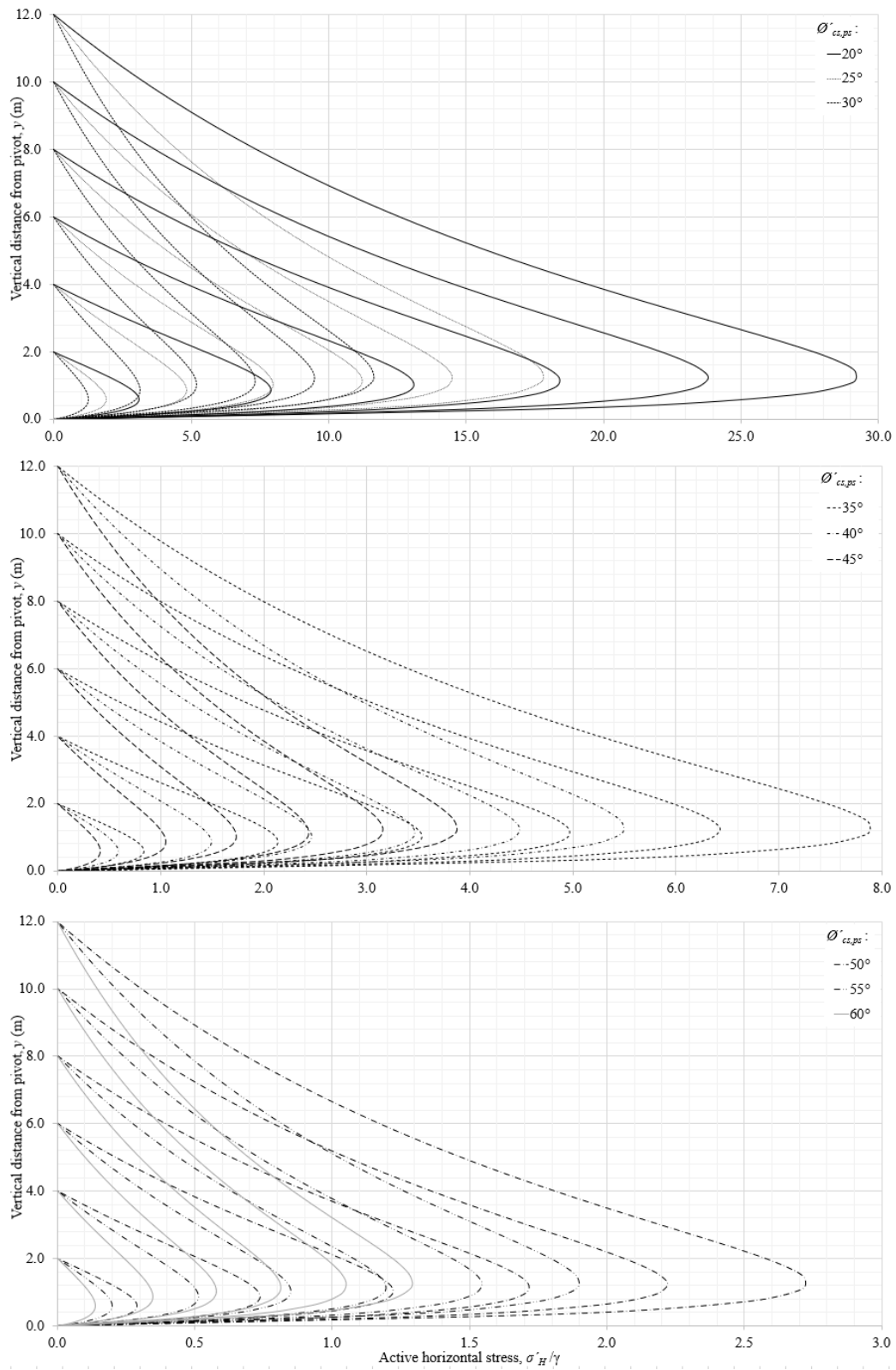


Fig. 6-6 Active pressure as per Eq. (6-20) illustrated with a selection of $\theta'_{cs,ps}$ and H .

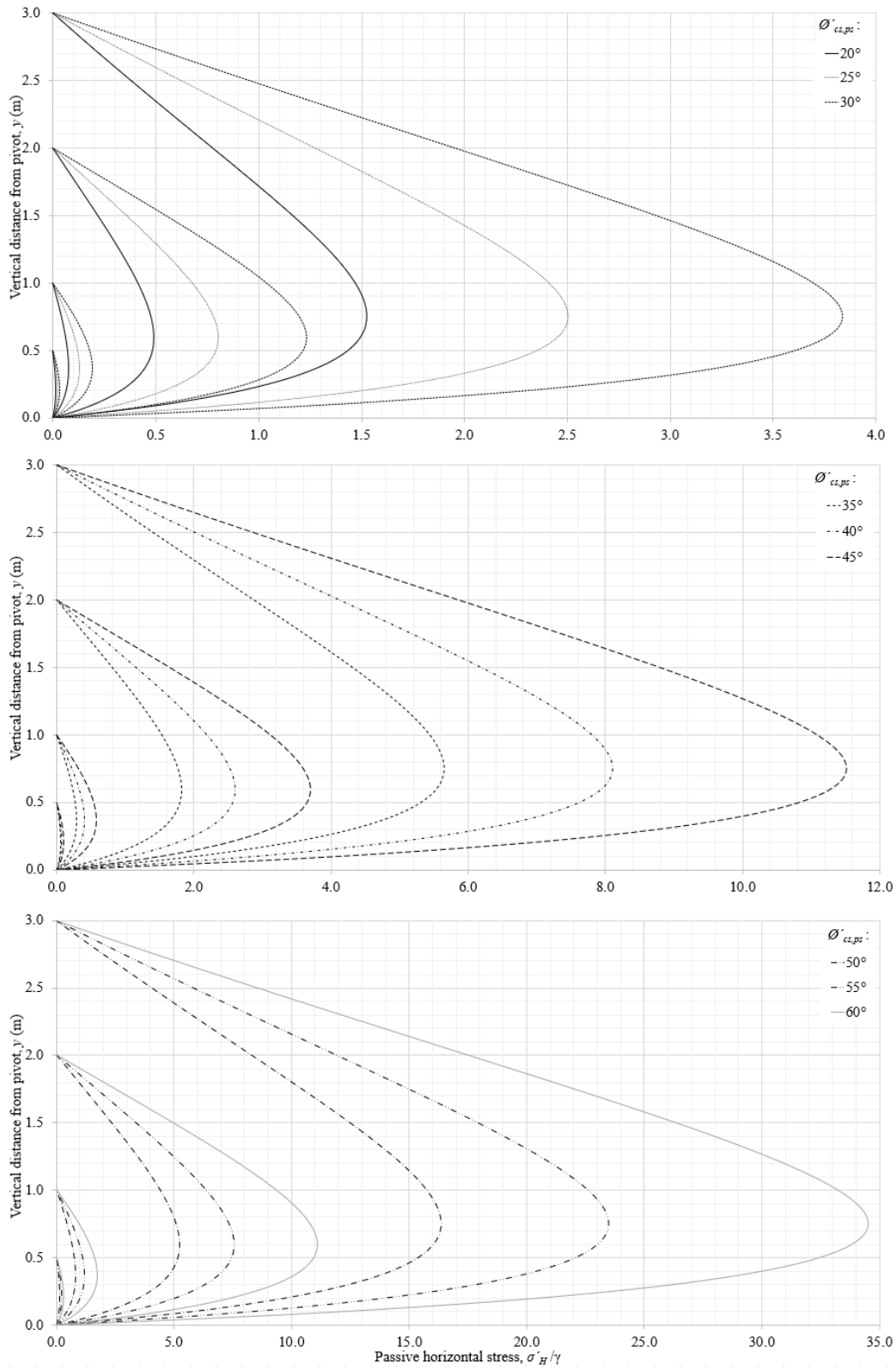


Fig. 6-7 Passive pressure as per Eq. (6-20) illustrated with a selection of $\theta'_{cs,ps}$ and H .

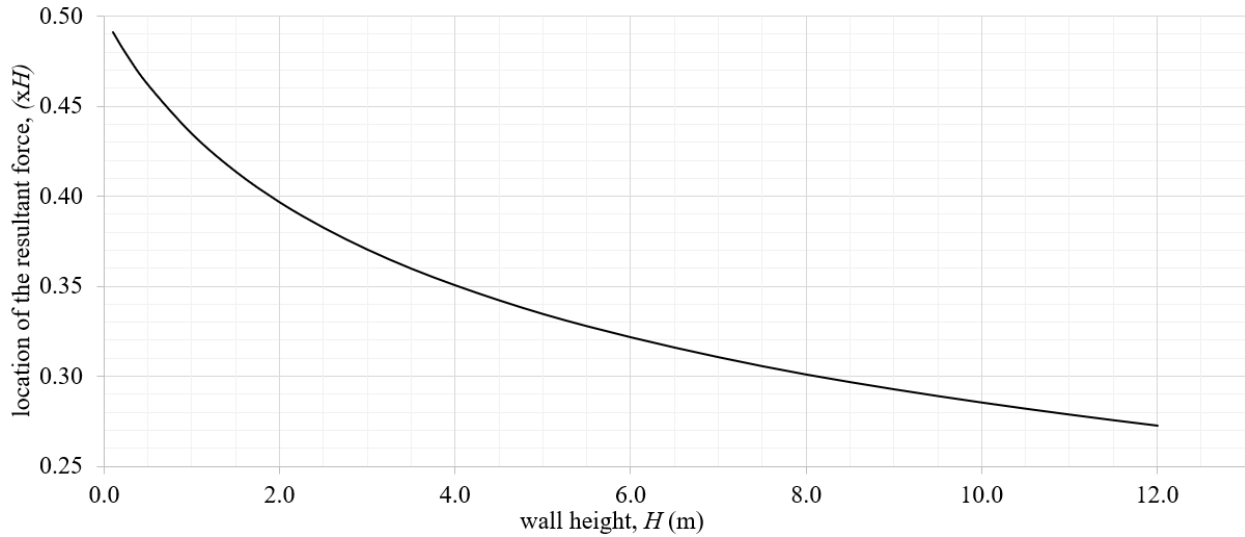


Fig. 6-8 Location of the resultant horizontal force.

6.3. K_a and K_p incorporated with the OCR effect

For the active case, the process of failure involves distension of the soil mass and as a result any stress history will be destroyed or unlocked; consequently, the granular mass will end up in a normally consolidated state. In other words, the solution can be approached as a normally consolidated condition (i.e., $OCR = 1$); that is K_a is given by Eqs. (6-20) and (6-10).

For the passive state, the process of failure involves compression and as a result any stress history will be the first to offset; thus, the granular mass will first oppose resistance base on its original overconsolidated condition as given by its OCR parameter. In this case, there is an initial peak lateral stress $\sigma_{p,H,OC}$ which comes before the ultimate or residual provided by Eq. (6-20) and can be determined from Eq. (6-21).

$$\sigma_{p,H,OC} = \gamma \cdot H \cdot K_{0-OC} \quad (6-21)$$

6.4. Conclusion

Present chapter described a simple closed-form explicit nonlinear solution in cartesian coordinates to the critical slip-failure surface and its associated lateral stress distribution for the active and passive states in normally consolidated cohesionless soil. The governing geometry parameters are the natural exponential function and the plane-strain critical state friction angle $\theta'_{cs,ps}$. The value of present solution lies in the deterministic obtention of the slip-failure surface; thus, there is not need for arbitrary assumptions like the straight line or the logarithmic spiral commonly adopted in actual practice. Moreover, the lateral stress is here presented as an associated consequence of the slip-failure geometry resulting in this way a more rational and standalone solution. In addition, the *OCR* effect was discussed and incorporated. *Appendix C* presents direct comparison between present lateral earth pressure theory for active and passive states and “classical theory” since (Coulomb, 1776) and (Rankine, 1857).

Chapter 7: Stress–Strain: A CSSM Plane-Strain Incremental Numerical Model

7.1. General

Previous chapters resolved and verified a theoretical relationship between friction and dilation in the framework of plane strain. Moreover, a deeper connection between the frictional components of the soil in plane strain, porosity (or relative density) and *OCR* was also established. The present chapter incorporates the stress–strain associated to present CSSM model. With this, the full relationship between friction, dilation, density, *OCR*, pore pressure, stress, and strain is finally established for the plane-strain condition of cohesionless soils as illustrated in Fig. 7-1. The complete model was implanted in a spreadsheet for practical applications, see *Appendix I*.

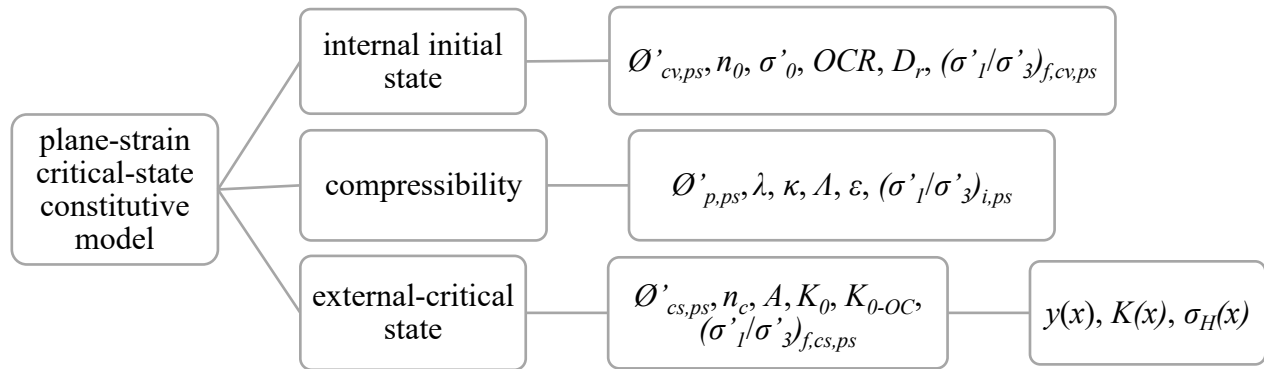


Fig. 7-1 Complete plane-strain critical state constitutive model developed by present study.

7.2. Incremental flow rule

The present *flow rule* (4-9) developed in the *Chapter 4*: accounts for the dilation developed at the plane-strain critical state failure in terms of cardinal parameters. However, by means of an incremental model is possible to observe the complete stress-strain path associated to the

development of dilatancy. Thus, the present *flow rule* (4-9) is used here in an incremental way in terms of the auxiliary angle α . This auxiliary angle α is a variable angle that represents the transit of friction between the initially available plane-strain constant-volume friction angle $\alpha_{initial} = \emptyset'_{cv,ps}$ and the finally developed plane-strain critical state friction angle $\alpha_{final} = \emptyset'_{cs,ps}$; consequently, the incremental transit of this auxiliary angle, developed within a given total number of steps N , can be denoted by α_i and ranges in the interval $\emptyset'_{cv,ps} \leq \alpha_i \leq \emptyset'_{cs,ps}$ as given by Eq. (7-1). Where: the index i stands for the actual step.

$$\alpha_i = \emptyset'_{cv,ps} + (i - 1) \cdot \Delta\alpha \quad (7-1)$$

Where:

$$\Delta\alpha = \frac{\emptyset'_{cs,ps} - \emptyset'_{cv,ps}}{(N - 1)} \quad (7-2)$$

$$1 \leq i \leq N$$

7.3. The principal stress ratio $(\sigma'_1/\sigma'_3)_f$ at plane-strain constant-volume failure of a prismatic soil element

The principal stress ratio at constant-volume is known, see numeral 2.4.1.2. For the constant-volume plane-strain condition $(\sigma'_1/\sigma'_3)_{f,cv,ps}$ was initially developed by (Rankine, 1857), then suggested by (Terzaghi, 1923) and afterwards rediscovered by (Rowe, 1962, p. 521) based on his research on equilibrium of assemblies of particles in contact which probed that for the constant-volume plane-strain condition the effective principal stress ratio at failure is a function of the plane-strain constant-volume friction angle $\emptyset'_{cv,ps}$ (Rowe, 1969) which was originally presented in terms of \emptyset'_μ as shown in Eq. (7-3). Moreover, Rowe showed that there exists an angle between failure

plane and the principal stress direction which minimizes the energy of the particulate system, namely $\beta = (45^\circ - \phi'/2)$, the same angle previously derived mathematically by (Rankine, 1857).

$$\left(\frac{\sigma'_1}{\sigma'_3}\right)_{f,cv,ps} = \frac{\tan(\phi'_\mu + \beta)}{\tan \beta} = \tan^2\left(45^\circ + \frac{\phi'_\mu}{2}\right) \quad (7-3)$$

Where:
$$\beta = \left(45^\circ - \frac{\phi'_\mu}{2}\right)$$

For plane-strain test conditions ($\varepsilon_2 = 0$) and after replacing ϕ'_μ by $\phi'_{cv,ps}$ in Eq. (7-3) and adding a dilatancy factor defined for present incremental model yields a general stress–strain relationship as suggested by (Rowe, 1962, p. 514), see Eq. (7-4). Where: $\dot{\varepsilon}_v$ is the volumetric strain increment and ε_1 is the major principal strain.

$$\begin{aligned} \left(\frac{\sigma'_1}{\sigma'_3}\right)_{i,ps} &= \left(\frac{\sigma'_1}{\sigma'_3}\right)_{f,cv,ps} \cdot \left(1 + \frac{\dot{\varepsilon}_v}{\varepsilon_1}\right) \\ \left(\frac{\sigma'_1}{\sigma'_3}\right)_{i,ps} &= \tan^2\left(45^\circ + \frac{\phi'_{cv,ps}}{2}\right) \cdot \left(1 + \frac{\dot{\varepsilon}_v}{\varepsilon_1}\right) \end{aligned} \quad (7-4)$$

Where:
$$\dot{\varepsilon}_v = -(\dot{\varepsilon}_{1,i} + \dot{\varepsilon}_{3,i}) \quad (7-5)$$

$$\varepsilon_1 = \sum_{i=1}^i \dot{\varepsilon}_1 \quad (7-6)$$

As suggested by Eq. (7-4), the principal stress ratio at critical state plane-strain failure $(\sigma'_1/\sigma'_3)_{f,cs,ps}$ can differ from the principal stress ratio at constant-volume plane-strain failure $(\sigma'_1/\sigma'_3)_{f,cv,ps}$ depending on the stress–strain path developed by the soil. Present incremental numerical model for the stress–strain path then offers a solution to the $(\sigma'_1/\sigma'_3)_{f,cs,ps}$ associated to present CSSM constitutive framework (see Fig. 7-1).

7.4. Stress–strain simulation of the critical state plane-strain case ($\epsilon_2 = 0$)

Fig. 7-2(a) shows the deformation mechanism of the unitary pack of particles or *soil element* considered for the herein particle-scale model (see Fig. 4-1). And Fig. 7-2(b) shows a sketch of a corresponding idealized sample under critical state plane-strain failure.

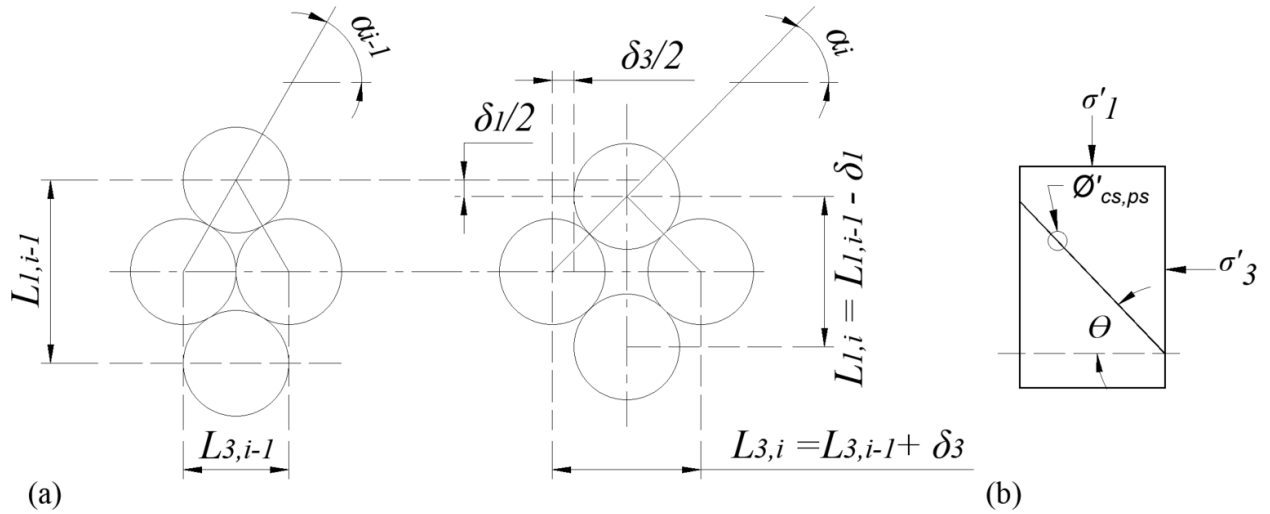


Fig. 7-2 Deformation mechanism: (a) the unitary pack of particles; (b) prismatic sample under the critical state plane-strain failure ($\epsilon_2 = 0$).

Based on the principal axial deflexion δ_1 shown in Fig. 7-2(a) and the theory of elasticity for the plane-strain case; the principal axial strain rate $\dot{\epsilon}_1$ can be expressed with Eqs. (7-7) and (7-8) for the ranges 0° to 45° and 45° to 90° , respectively. The principal axial strain rate is positive in compression and negative in extension, and the volumetric strain rate is positive in dilation and negative in contraction. Having the principal axial strain rate, the secondary strain rate $\dot{\epsilon}_3$ can be determined using Eq. (7-9). Finally, by applying present definition for strain in the stress–strain

relationship in (7-4) is possible to simulate the stress–strain behavior of a granular material as per present model.

$$\dot{\varepsilon}_1 = \frac{\cos(90 - \alpha_{i-1}) - \cos(90 - \alpha_i)}{\cos(90 - \alpha_{i-1}) (1 - \nu)} \quad (7-7)$$

$$\dot{\varepsilon}_1 = \frac{\cos(\alpha_{i-1}) - \cos(\alpha_i)}{\cos(\alpha_{i-1}) (1 - \nu)} \quad (7-8)$$

$$\dot{\varepsilon}_3 = -\dot{\varepsilon}_1 \cdot \nu \quad (7-9)$$

It should be noted that Eq. (7-4) alone requires all its variables to be measured independently. While present study integrates deformation as a function of the state parameter porosity n [see Eqs. (4-11) to (4-14)]. And with porosity a complete constitutive connection can be established to other soil parameters as illustrated in Fig. 7-1. The previous via the Poisson ratio ν which correlates to the angle of shearing resistance and to porosity by means of the elastic definition for the at-rest lateral earth pressure coefficient K_0 , see Eq. (2-28). Since present study offers an explicit solution for K_0 as an exclusive function of the friction angle, see Eq. (5-4); consequently, there exist an explicit solution for the incrementally updated Poisson ratio ν as a unique function of the friction angle or porosity (i.e., plasticity = rearrangement), see Eq. (7-10).

$$\nu = \frac{K_0}{1 + K_0} \quad (7-10)$$

In summary, the present formulation accounts for a continuous nonlinear stress–strain path in an incremental way with the auxiliary angle α which simultaneously controls the continuous evolution of porosity n . In other words, the continuous plastic behavior is modeled as a sequence of multiple

elastic steps updated with Poisson ratio ν . In addition, due to the incremental nature of present simulation, there is an intrinsic precision involved. This precision is given in percentage by the expression (7-11). In general, the precision indicates how much of the initial theoretical principal stress ratio at failure has been considered by the simulation.

$$precision = \left(1 - \frac{\left(\frac{\sigma'_1}{\sigma'_3}\right)_{f,cv,ps} - \left(\frac{\sigma'_1}{\sigma'_3}\right)_{i,cv}}{\left(\frac{\sigma'_1}{\sigma'_3}\right)_{f,cv,ps}} \right) \cdot 100 \quad (7-11)$$

The resultant principal stress ratio at critical state plane-strain failure $(\sigma'_1/\sigma'_3)_{f,cs,ps}$ is finally given by (7-12); where: N is the total number of steps considered by the incremental simulation and $(\sigma'_1/\sigma'_3)_{i,ps}$ is the incremental plane-strain principal stress ratio according to Eq. (7-4).

$$\left(\frac{\sigma'_1}{\sigma'_3}\right)_{f,cs,ps} = \left(\frac{\sigma'_1}{\sigma'_3}\right)_{i,ps=N} \quad (7-12)$$

7.4.1. Stress–strain and other characteristic paths according to present CSSM incremental model for cohesionless soil

Depending on the initial state of the soil sample (e.g., $\emptyset'_{cv,ps}$) the stress–strain path can follow a different rout. Table 7-1 classifies all these potential behaviors in five distinct groups properly identify in the column “description”. Various characteristic curves can be plotted for each distinct behavior from results that can be obtained via the application of the CSSM incremental model described in present chapter. Four curves were selected to illustrate the five characteristic behaviors under critical state plane-strain test. The curves selected are: (i) principal stress ratio

$(\sigma'_1/\sigma'_3)_{i,ps}$ versus principal axial strain ϵ_l , (ii) void ratio e versus principal axial strain ϵ_l , (iii) pore pressure coefficient A versus principal axial strain ϵ_l , and (iv) volumetric strain ϵ_v versus principal axial strain ϵ_l . Fig. 7-3 to Fig. 7-7 show this set of characteristic curves for each of the five distinct groups of behavior as described in Table 7-1. The arbitrary initial state friction angles (i.e., $\theta'_{cv,ps}$) selected to illustrate these characteristic groups are 23° , 27° , 34° , 39° and 42° for extensive/collapsible, extensive/dilative, compressive/contractive, compressive/dilative, and extensive/suction-dilative behavior, respectively. The resultant principal stress ratio at critical state plane-strain failure $(\sigma'_1/\sigma'_3)_{f,cs,ps}$ resulted to be 2.28 (2.28), 2.65 (2.66), 3.52 (3.54), 4.46 (4.40), and 5.03 (5.04), respectively, where the number within the parenthesis corresponds to the expected as per Eq. (7-3) and by using $N = 200$ (i.e., precision over 99%). For the compressive/dilative behavior of dense soil the principal stress ratio at critical state plane-strain failure results greater than the principal stress ratio at constant-volume plane-strain failure; that is $4.46 > 4.40$.

Initial state	Class	\mathcal{E}'_l	\mathcal{E}'_v	A	Description
$0^\circ < \theta'_{cv,ps} < 24.78^\circ$	Very loose	-	+	-/+	extensive/collapsible
$24.78^\circ \leq \theta'_{cv,ps} < 30^\circ$	Loose	-	+	-	extensive/dilative
30°		0	0	$(-1/3)^*$	nor dilative or contractive
$30^\circ < \theta'_{cv,ps} \leq 37.5^\circ$	Medium	+	-	-	compressive/contractive
$37.5^\circ < \theta'_{cv,ps} \leq 39.94^\circ$	Dense	+/- (net +)	-/+	-	compressive/dilative
$39.94^\circ < \theta'_{cv,ps} < 45^\circ$	Very dense	+/- (net -)	-/+	-	extensive/suction-dilative
$45^\circ \leq \theta'_{cv,ps} < 90^\circ$		-	+	-	extensive/suction-dilative

*(Skempton, 1954)

Table 7-1 Types of soil behavior according to present CSSM incremental model.

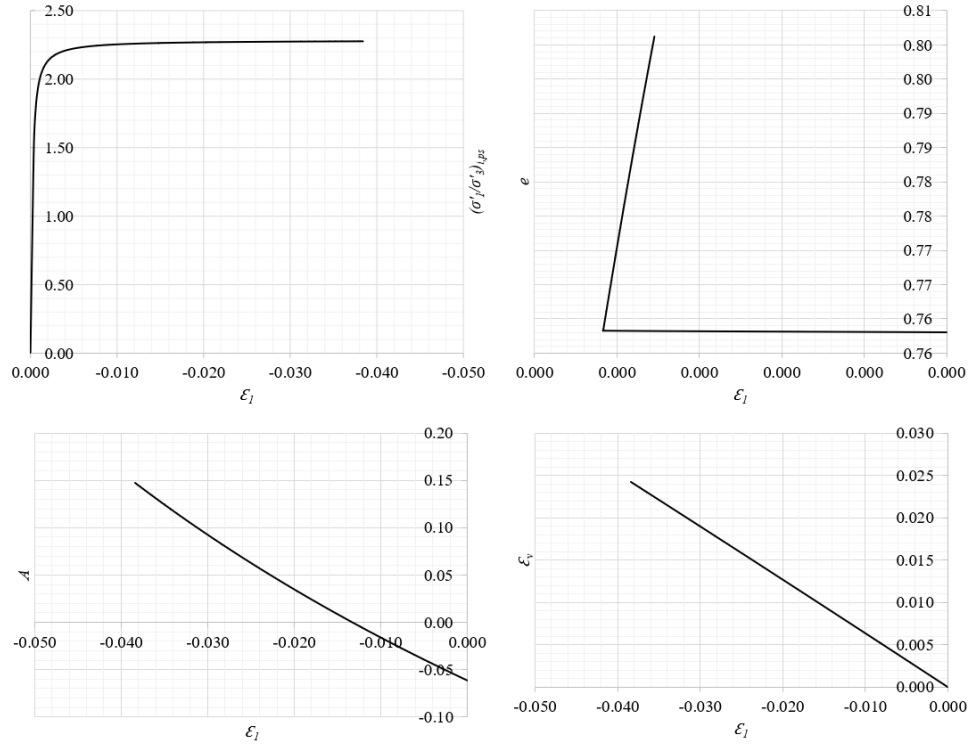


Fig. 7-3 Characteristic curves for extensive/collapsible cohesionless granular material.

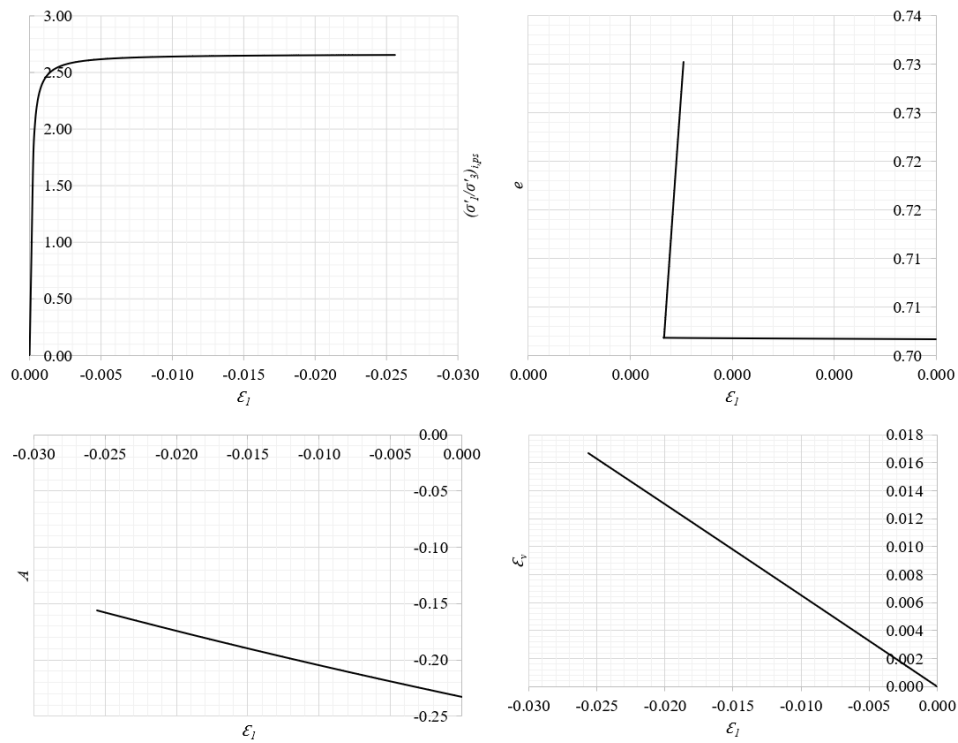


Fig. 7-4 Characteristic curves for extensive/dilative cohesionless granular material.

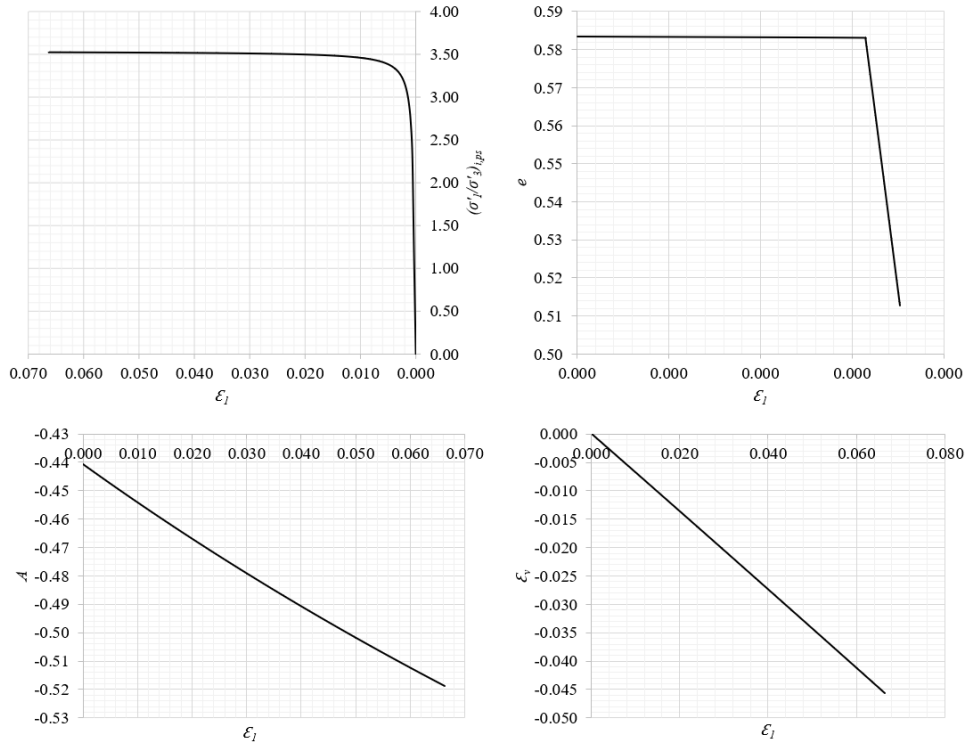


Fig. 7-5 Characteristic curves for compressive/contractive cohesionless granular material.

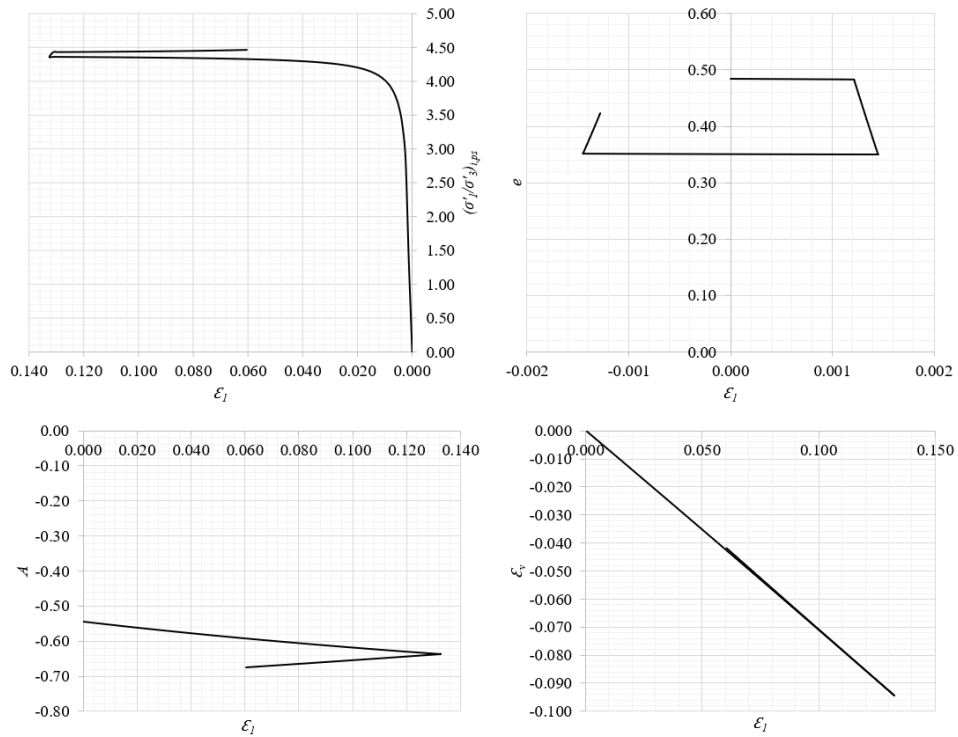


Fig. 7-6 Characteristic curves for compressive/dilative cohesionless granular material.

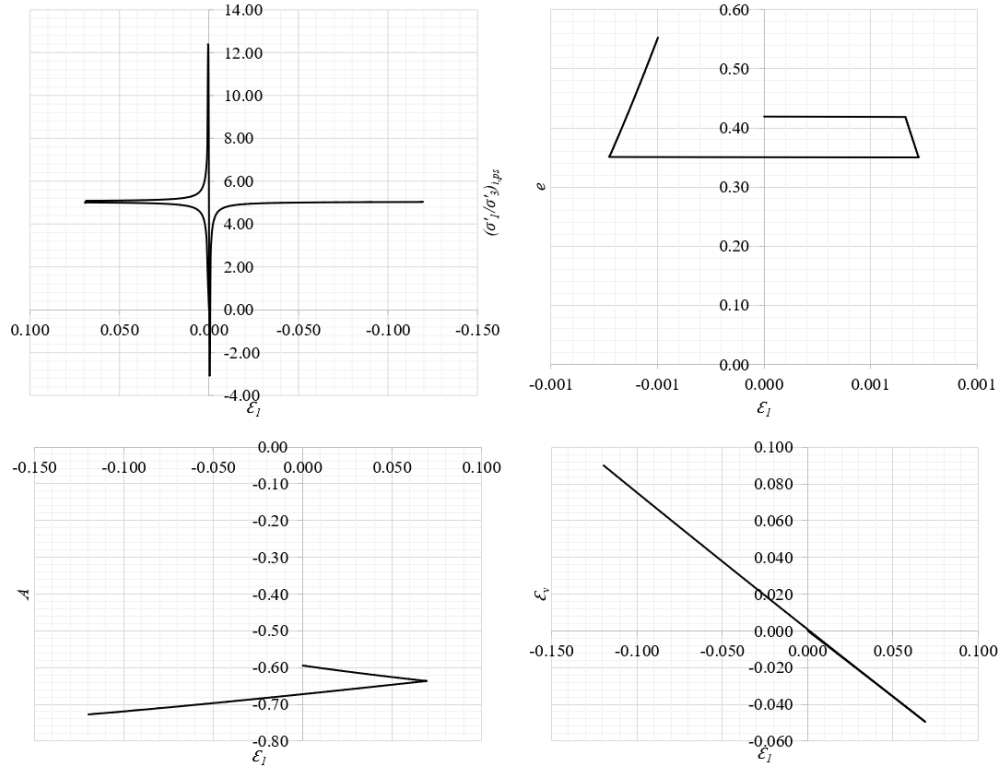


Fig. 7-7 Characteristic curves for extensive/suction-dilative cohesionless granular material.

7.4.2. Validation of the Stress–Strain incremental model with existing experimental results

(Alshibli et al., 2004) tested natural uniform silica sand by means of a plane-strain apparatus (i.e., a biaxial test) on two equal prismatic samples (i.e., 57 mm x 121 mm x 180 mm) having both the same initial density, from that study the principal stress ratio at failure in drained condition is 4.59 [i.e., $(\sigma'_1/\sigma'_3)_{f,cs,ps}$]. The previous by considering the failure is in the point where the volumetric strain becomes constant (Cetin and Gökoğlu, 2013). The net axial displacement at failure was measured to be 3.5 mm which corresponds to a final axial strain of 0.0194.

After performing a numerical simulation by means of present CSSM Incremental Numerical Model with the number of steps equal to $N = 200$ and a precision of 99.22%, see Fig. 7-8. A theoretical critical state plane-strain principal stress ratio at failure of $(\sigma'_1/\sigma'_3)_{f,cs,ps} = 4.69$ can be determined. Moreover, previous numerical result corresponds to a principal axial strain of $\varepsilon_1 = 0.02118$ which is also in the same order found experimentally.

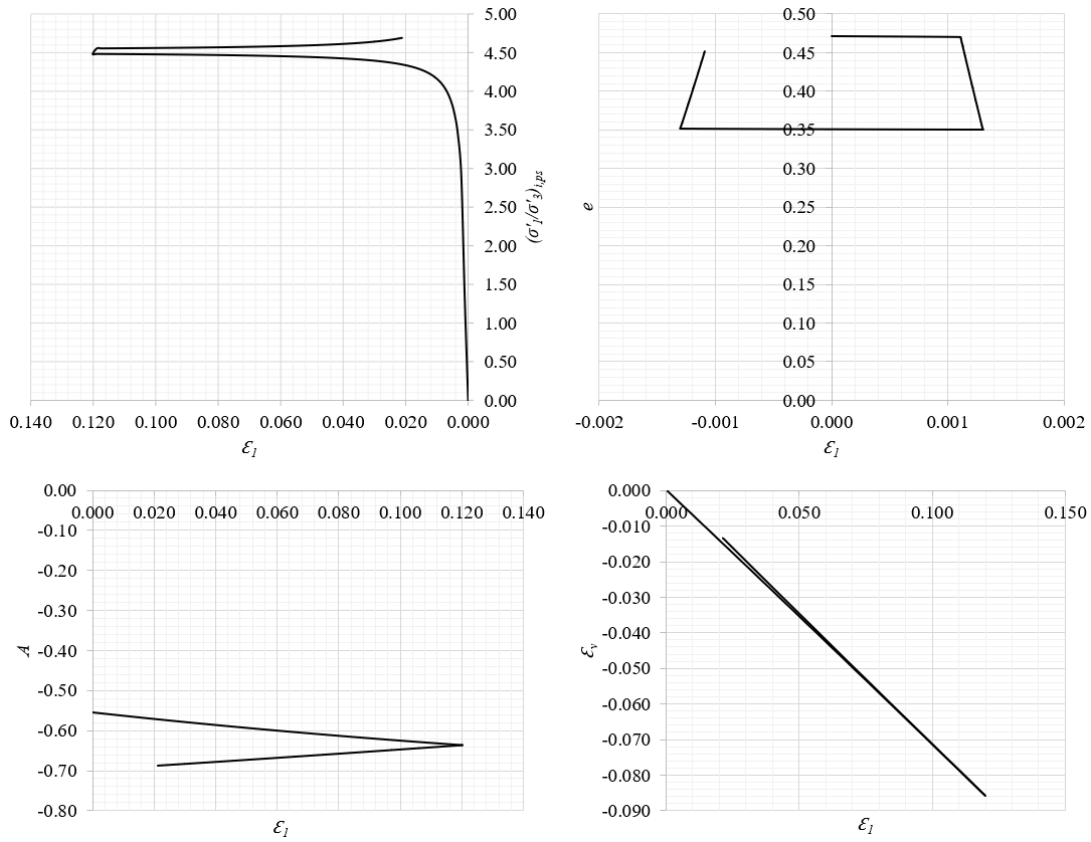


Fig. 7-8 Present CSSM incremental model applied to experimental results from (Alshibli et al., 2004).

(Alshibli et al., 2004) described the specimen undergoes initial contraction followed by continuous dilation toward approaching failure. This behavior corresponds to the “compressive/dilative”

behavior described in the previous numeral 7.4.1. Indeed, the initial constant-volume plane-strain friction angle as determined with present simulation is $\phi'_{cv,ps} = 39.61^\circ$ consequently falls in the range for “compressive/dilative” behavior described in Table 7-1. This model result for $\phi'_{cv,ps}$ matches the residual friction determined by (Alshibli et al., 2004) with the “unrestrained bottom” version of their plane-strain biaxial test; that is $\phi'_{r,U} = 39.8^\circ$. On the other hand, the developed critical state plane-strain friction angle as determined with present simulation is $\phi'_{cs,ps} = 49.51^\circ$ which matches the peak friction determined by (Alshibli et al., 2004) with the “restrained” version of their plane-strain biaxial test; that is $\phi'_{p,R} = 49.5^\circ$. Moreover, the inclination of the failure plane that corresponds to the developed critical state plane-strain friction angle as determined with present simulation is $\theta = 69.7^\circ$. This modeled inclination of the failure plane positively corresponds with $\theta = 69^\circ$ reported in (Alshibli et al., 2004, fig. 11).

7.5. Conclusion

This chapter described the integration of knowledge developed in previous chapters within an incremental numerical model to simulate the stress–strain path of cohesionless soil under plane-strain critical state failure. Present model improves the capabilities of present general CSSM constitutive framework with the principal stress ratio and strain at failure. Moreover, present model permitted a theoretical general classification of the soil behavior based on five observed distinct responses namely: extensive/collapsible, extensive/dilative, compressive/contractive, compressive/dilative, and extensive/suction-dilative behavior. Predictions using this stress–strain model was positively compared with existing experimental results on natural silica sand.

The present chapter also finalizes the description of the general CSSM constitutive framework pursued by this study. With this, a more complete and linked understanding of friction at critical

state was provided. This new mathematical interpretation of friction at critical state accounts for the role of the geometrical interference and interconnects all the soil parameters with the state parameter porosity n .

Chapter 8: Practical Applications of Present Design Theory

8.1. General

The present chapter initially summarizes the practical methodology to determine the analytical CSSM parameters for cohesionless soils as proposed by present study. All the parameters considered by the present constitutive framework for critical state are summarized graphically in Fig. 7-1. Then some example problems are presented and solved in a step-by-step approach to illustrate the application of present theory for Lateral Earth Pressure in terms of CSSM plane-strain parameters.

8.2. Methodology to determine soil parameters according to present CSSM framework

The herein derived analytical constitutive framework for plane-strain critical state of cohesionless granular materials is initially composed by two parts: (i) the relationship between constant-volume and critical state plane-strain frictions or *flow rule* given in Eq. (4-9), and (ii) the relationship between friction and porosity given in Eqs. (4-11) to (4-14). Within this constitutive framework and given the soil porosity established as indicated in Fig. 8-1, the frictional parameters and other associated parameters can be computed as indicated in Fig. 8-2.

Once porosity and its corresponding frictional parameters are determined as explained before; then, it is possible to determine the rest of the associated soil parameters. Most of these associated parameters can be determined by direct application of the appropriate equation, that is: the relative density D_r from Eqs. (4-23) or (4-26), the pore pressure coefficient $A_{cs,ps}$ from Eq. (4-20) and the at-rest lateral earth pressure coefficient K_0 from Eq. (5-3). By adding the basic property plastic volumetric strain ratio λ [i.e., $(1 - \kappa/\lambda)$] the at-rest coefficient of lateral earth pressure of an

overconsolidated or compacted soil deposit $K_{\theta-OC}$ can be determined from Eq. (5-7). If the soil constitutes the backfill behind a retaining wall, the corresponding nonlinear lateral earth pressure coefficient $K(x)$ (i.e., K_p and K_a) can be determined from Eq. (6-19) and its associated lateral earth pressure distribution $\sigma'_H(x)$ and slip-failure surface geometry $y(x)$ from Eq. (6-20) and Eqs. (6-10) or (6-15), respectively. Finally, the stress–strain response can be determined by applying the CSSM Incremental Numerical Model described in the *Chapter 7: (see Appendix I)*.

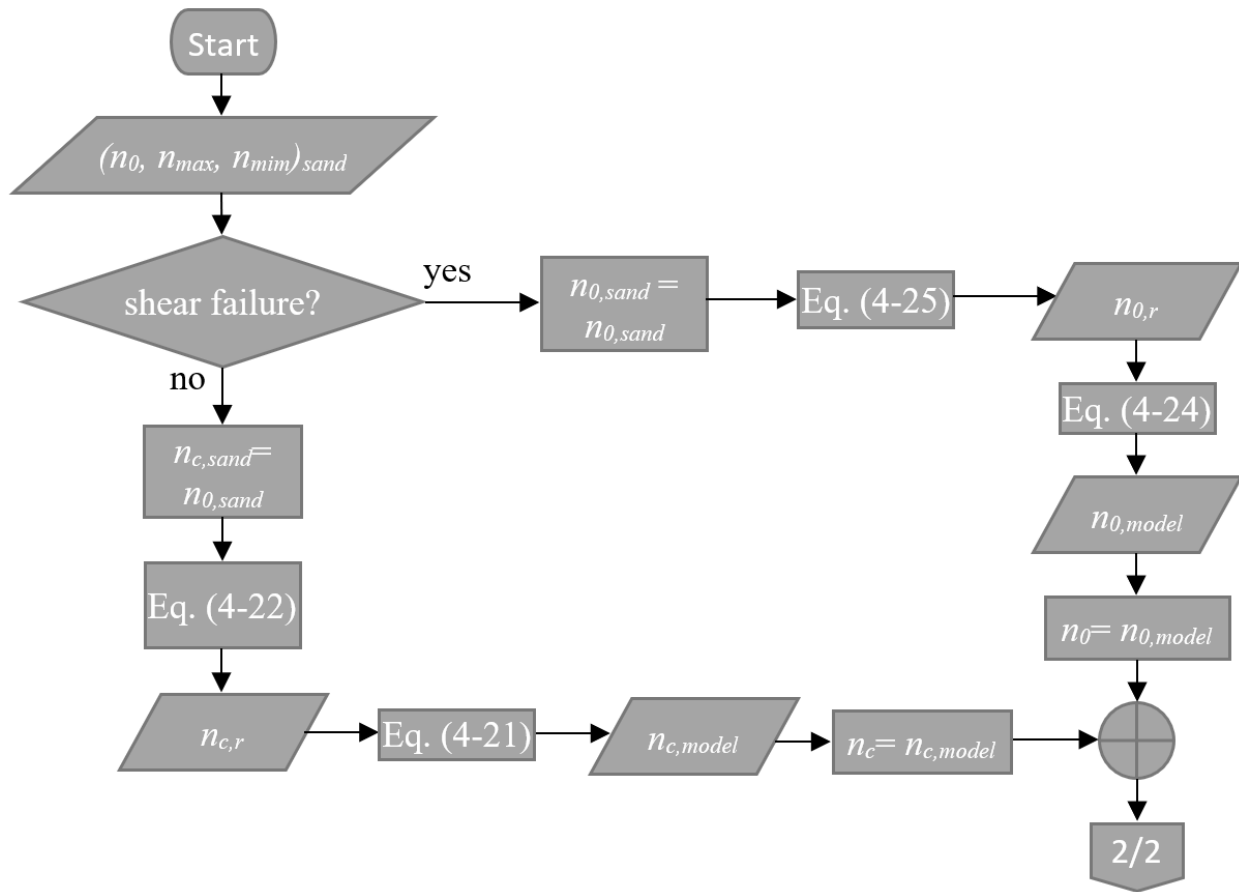


Fig. 8-1 Flowchart to establish porosity for present CSSM framework.

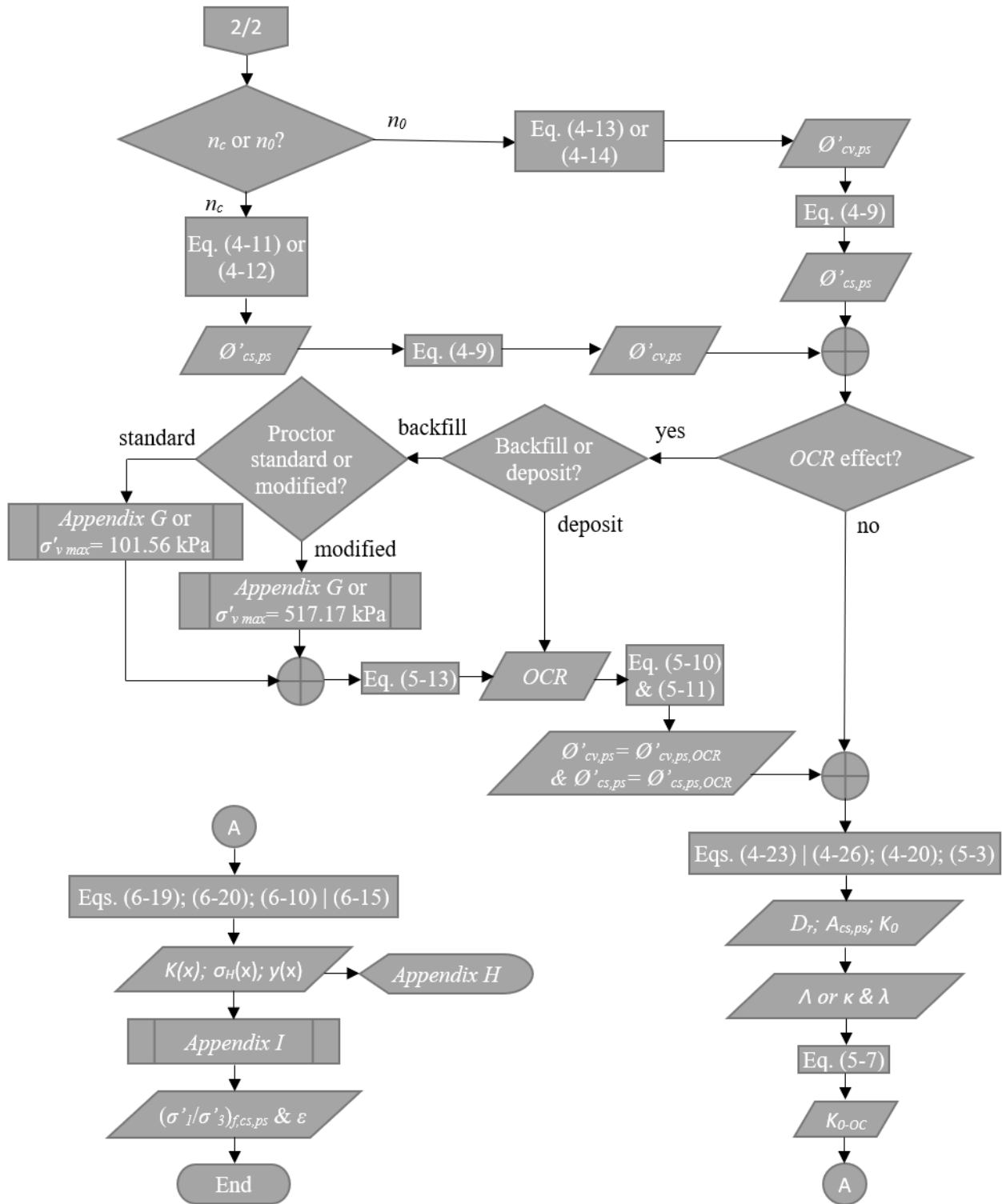


Fig. 8-2 Flowchart to determine friction and other parameters in present CSSM framework.

8.3. Soil parameters from laboratory testing

Present analytical $\phi'_{cv,ps}$ corresponds to a friction that can be determined in laboratory by techniques like constant-volume RS test (Sadrekarimi and Olson, 2011), undrained TxC shear test for the special case of very loose sands or by means of measuring the residual friction in a plane-strain (biaxial test with unrestrained bottom) apparatus (Alshibli et al., 2004). On the other hand, present analytical $\phi'_{cs,ps}$ corresponds to a friction that can be approached in laboratory by techniques like the RS test (Sadrekarimi and Olson, 2011), the large displacement DS test (Lings and Dietz, 2004) or by means of measuring the peak friction in a plane-strain (biaxial test with restrained bottom) apparatus (Alshibli et al., 2004). Unfortunately, all these are experimental approaches which methodology and associated equipment are neither still standardized or commercially available. In the absence of appropriate and accessible laboratory testing to measure $\phi'_{cs,ps}$ and $\phi'_{cv,ps}$ directly, present analytical framework for CSSM offers an alternative methodology to determine $\phi'_{cs,ps}$ and $\phi'_{cv,ps}$ and other associated parameters all from a more accessible parameter, porosity n , as described in previous numeral 8.2 (see Fig. 8-1 and Fig. 8-2).

Other approach to the plane-strain parameters $\phi'_{cs,ps}$ and $\phi'_{cv,ps}$ is by means of analytical or empirical expressions that correlated the plane-strain parameters with frictional properties obtained from simpler tests like *triaxial test* (TX) or *direct shear test* (DS) e.g., (Taylor, 1948), (Davis, 1968), (Rowe, 1969), (Dietz, 2000), (Hanna, 2001), (Lings and Dietz, 2004). In line with previous approach, present CSSM plane-strain framework can also be correlated to angles of shearing resistance coming from TX or DS tests.

The *direct shear test* is the component of the plane-strain test along the principal stress direction, see Fig. 7-2(b). Accordingly, the $\phi'_{cs,ps}$ can be obtained from Eq. (8-1).

$$\varnothing'_{cs,ps} = \frac{\varnothing'_{ds}}{\sin(\Theta)} \quad (8-1)$$

Where: $\Theta \cong \bar{\alpha}_{H_a \rightarrow \infty} \cong \left(45^\circ + \frac{\varnothing'_{cs,ps}}{2} \right)$

A *triaxial test* develops simultaneously the complete range of resistance between $\varnothing'_{cs,ps}$ and $\varnothing'_{cv,ps}$ as illustrated in Fig. 8-3. From this and assuming uniform distribution is possible to derive the relationship in Eq. (8-2) between the triaxial test friction angle \varnothing'_t and present plane-strain parameters. Moreover, by plotting Eq. (8-2) against the present plane-strain parameters obtained from Eq. (4-9) for the complete domain of friction yields the graphical relationship shown in the Fig. 8-4. On average, for the complete domain of friction, Fig. 8-4 indicates that $\overline{\varnothing'_{cs,ps}} = 1.07 \overline{\varnothing'_t}$ which confirms the known rule $\varnothing'_{ps} \approx 1.1 \varnothing'_t$.

$$\varnothing'_t = \frac{\varnothing'_{cs,ps} + \varnothing'_{cv,ps}}{2} \quad (8-2)$$

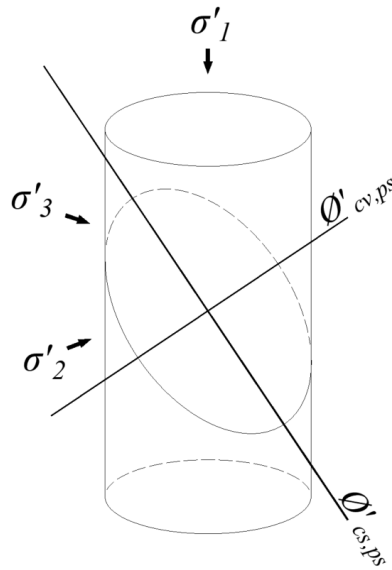


Fig. 8-3 Plane-strain frictional parameters embedded in a single triaxial test.

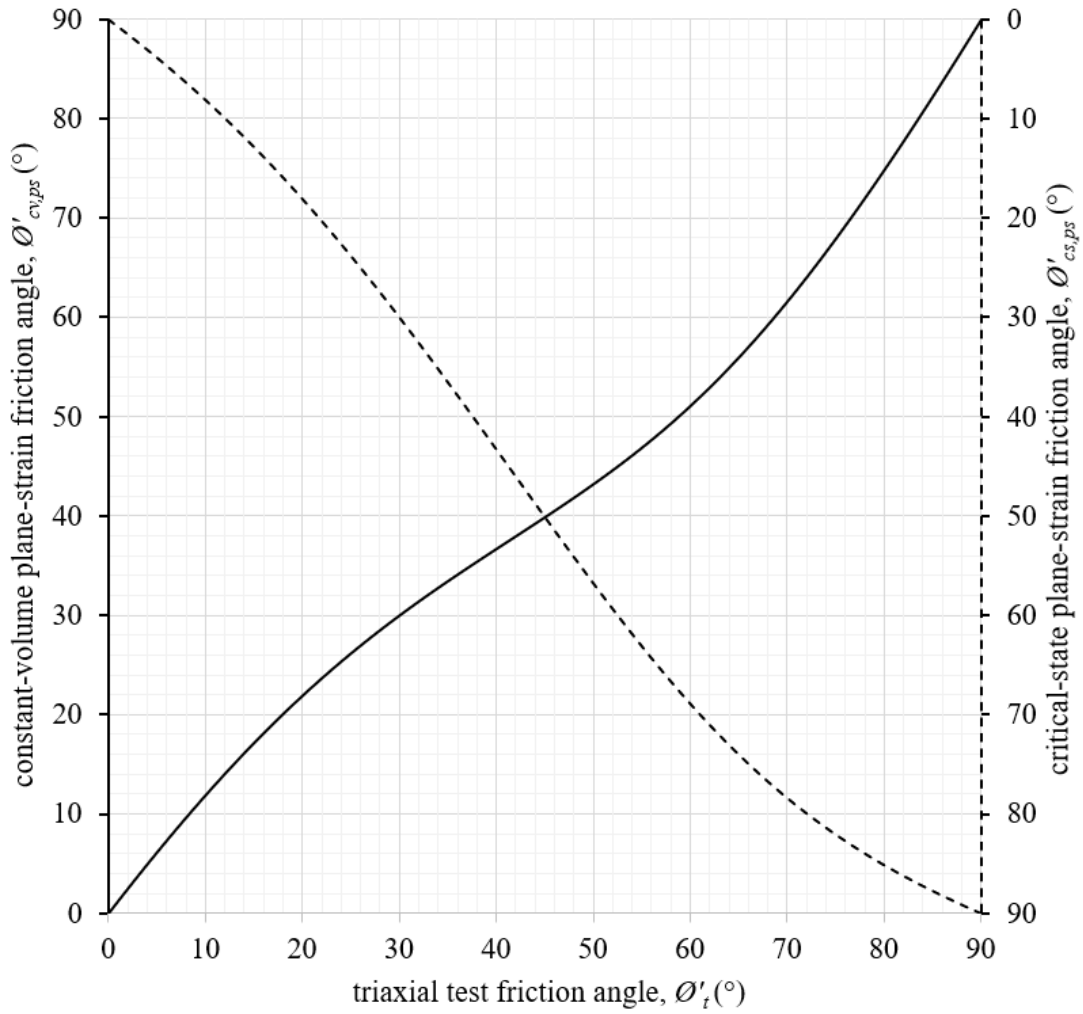


Fig. 8-4 Plane-strain frictional parameters versus triaxial test friction.

The expression Eq. (8-2) can be further validated by means of experimental results produced and collected in (Hanna, 2001). Thus, Table 8-1 presents results according to present Eq. (8-2) comparing well with these existing experimental results from (Hanna, 2001).

n_r	θ'_t (°)	$\theta'_{cs,ps}$ (°)	$\theta'_{cv,ps}$ (°) Eq. (4-9)	θ'_t (°) predicted with Eq. (8-2)	Relative error
Mersey River quartz sand (Rowe, 1962); ($\sigma_3 = 28$ kPa)					
1.00	42.0	46.5	38.2	42.3	-0.83%
0.80	40.6	43.5	36.8	40.2	1.11%
0.60	38.0	40.0	35.1	37.6	1.12%
0.40	36.9	38.0	34.2	36.1	2.19%
0.20	34.5	35.0	32.7	33.8	1.91%
0.00	32.0	32.0	31.1	31.6	1.39%
Brasted sand (Cornforth, 1961); ($\sigma_3 = 276$ kPa)					
1.00	42.0	46.0	38.0	42.0	0.04%
0.67	40.0	43.0	36.6	39.8	0.54%
0.33	35.5	37.0	33.7	35.3	0.44%
0.17	34.0	35.0	32.7	33.8	0.46%
0.00	33.0	33.5	31.9	32.7	0.90%

Average: 0.84%

Table 8-1 Results from Eq. (8-2) compared to existing experimental results on natural sand from (Hanna, 2001).

For a sample of natural soil, it is commonly known that the shear strength measured from plane-strain test is greater than that measured from direct shear test and that measured from the triaxial test: that is, $\theta'_{cs,ps} > \theta'_{ds}$ and $\theta'_{cs,ps} > \theta'_t$. However, according to Eqs. (8-1) and (8-2) and for the complete domain of friction this aspect actually depends on relative density D_r as can be seen in the general view provided in Fig. 8-5 and Table 7-1.

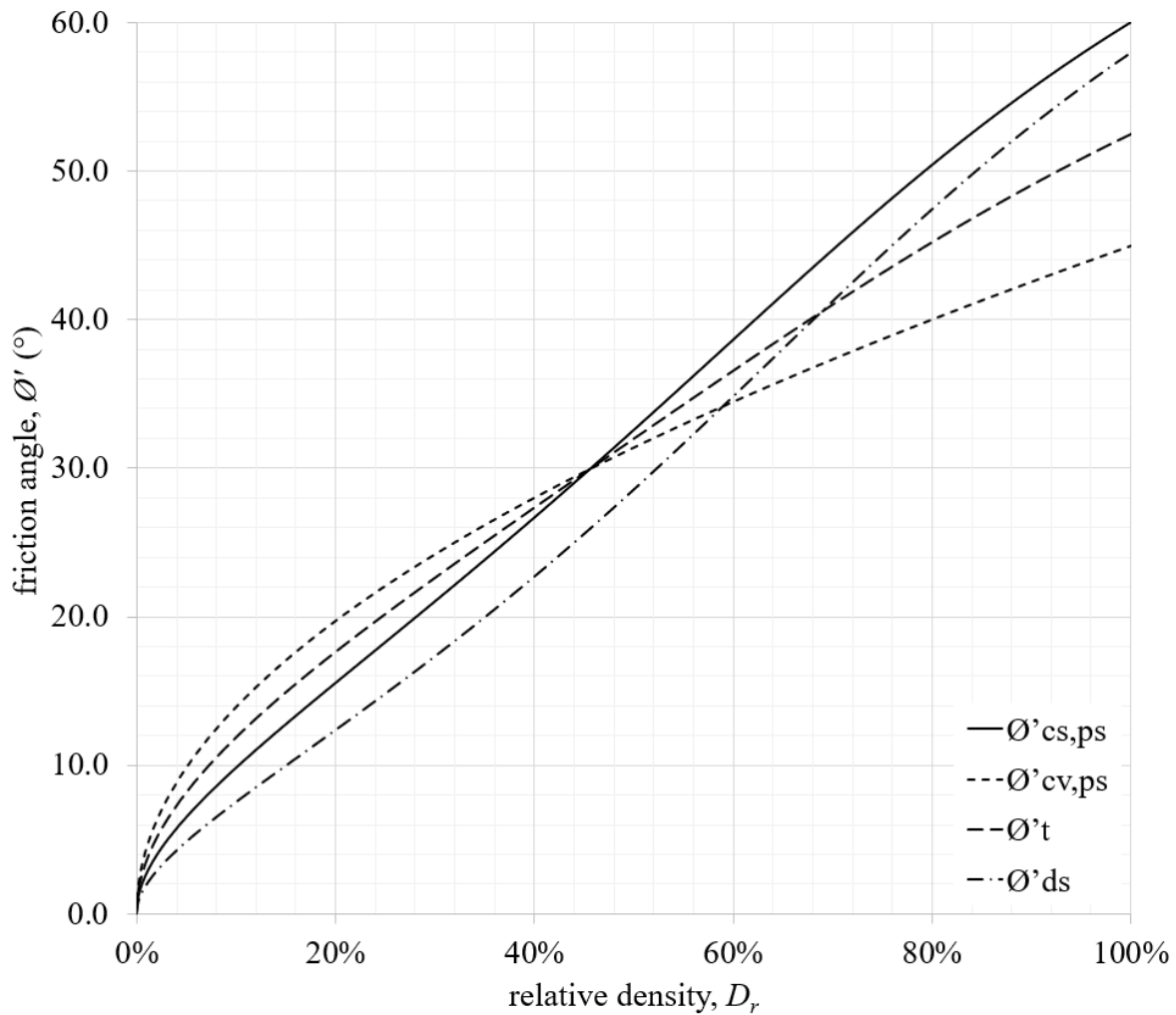


Fig. 8-5 Comparison between the angle of shearing resistance for different tests.

8.4. Design criteria for the lateral earth pressure acting against a retaining wall

The design criteria held and proposed by the present study is to design for the critical state of the soil (i.e., backfill). This criterion implies that any potential peak before ultimate critical state is ignored (e.g., the one identified in the numeral 6.3). In this way, the final design will be more standalone and safer because such design can be deemed independent of strain limits tied to peak resistance. In this regard, for instance, (Fang et al., 2002) concluded that (passive) earth pressure

at a large wall displacement can be adequately approximated by introducing the critical state concept to Coulomb theory (i.e., what present study does) to offer a reasonable conservative design approach more appropriate to keep the retaining wall on the safe side. In short, for the present design criterion the drained condition is determined by $\phi'_{cs,ps}$ and the undrained condition by $\phi'_{cv,ps}$.

8.5. Example problems

This numeral presents the step-by-step solution of some hypothetical example problems selected to illustrate the capabilities and practical scope of present theory applied to obtain the lateral earth pressure on walls. All the example problems incorporate the *OCR* effect and curved failure surface and lateral stress distribution as proposed in present study.

8.5.1. Problem #1: At-rest lateral earth pressure

For the massive retaining wall shown in Fig. 8-6(a) which backfill was compacted under the Proctor standard effort, determine the lateral earth force at-rest per unit length of the wall. Also determine the location of the resultant force measured from the bottom of the wall.

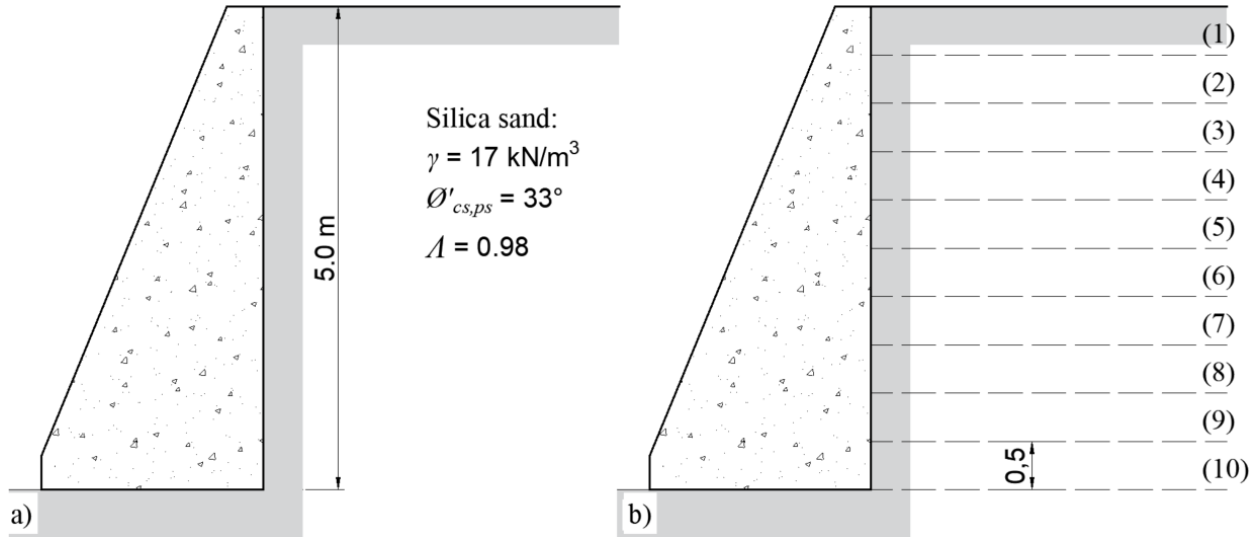


Fig. 8-6 Problem #1: (a) wall and backfill properties; and (b) sublayers to determine *OCR*

Solution:

Step #1: Subdivide the backfill in various equal-thickness auxiliary sublayers as indicated in Fig. 8-6(b). The total number of sublayers adopted for present solution is $N = 10$ and the pack of sublayers is labeled consecutively from top ($i = 1$) to bottom ($i = N$). The resultant constant thickness of the sublayers is then 0.50 m as indicated in Fig. 8-6(b).

Step #2: Determine the *OCR* at each sublayer by using Eq. (5-14) [or Eq. (8-3) in terms of the sublayer i] and the equivalent maximum past vertical stress corresponding to the standard Proctor energy $\sigma'_{v,max} = 101.56 \text{ kPa}$.

$$OCR_i = \frac{\sigma'_{v,max}}{\sigma'_{v0,i}} \quad (8-3)$$

Step #3: Determine the critical state plane-strain friction equivalent to the given overconsolidated condition $\phi'_{cs,ps,OCR}$ at each sublayer by using Eq. (5-11) [or Eq. (8-4) in terms of the sublayer i].

$$\phi'_{cs,ps,OCR,i} = \tan^{-1} \left(\frac{\tan(\phi'_{cs,ps})}{OCR_i} \right) \quad (8-4)$$

Step #4: Determine the equivalent normally consolidated at-rest coefficient of lateral earth pressure K_{0-OCR} at each sublayer by using Eq. (5-8) [or Eq. (8-5) in terms of the sublayer i].

$$K_{0-OCR,i} = \frac{\sqrt{3/4} - \sin(\phi'_{cs,ps,OCR,i})}{2 \cdot \cos(\phi'_{cs,ps,OCR,i}) - 1} \quad (8-5)$$

Step #5: Determine the at-rest coefficient of lateral earth pressure for compacted soil K_{0-OC} at each sublayer by using Eq. (5-7) [or Eq. (8-6) in terms of the sublayer i].

$$K_{0-OC,i} = K_{0-OCR,i} \cdot OCR_i - K_{0-OCR,i} \cdot (OCR_i - 1) \cdot \lambda \quad (8-6)$$

Step #6: Determine the at-rest lateral earth pressure at each sublayer with Eq. (8-7).

$$\sigma'_{0,H,i} = \sigma'_{v0,i} \cdot K_{0-OC,i} \quad (8-7)$$

Step #7: Determine the at-rest lateral earth force at each sublayer by multiplying the previous at-rest horizontal stress by the known the constant thickness of each sublayer which is 0.5 m. And the resultant force by means of adding the at-rest lateral earth force from all the sublayers. The Table 8-2 shows the results for present *Step #7* in conjunction with previous steps. The total lateral earth force at-rest per unit length of the wall is $F_0 = 132.74$ kN/m.

layer <i>i</i>	depth (m)	$\sigma'_{v,0}$ (kPa)	OCR	$\theta'_{cs,ps,OCR}$ (°)	$K_{\theta-OCR}$	$K_{\theta-OC}$	$\sigma'_{\theta,H}$ (kPa)	$F_{\theta,H}$ (kN)	lever arm (m)	moment (kN*m)
1	0.25	4.25	23.90	1.56	0.84	1.22	5.20	2.60	4.75	12.35
2	0.75	12.75	7.97	4.66	0.79	0.90	11.48	5.74	4.25	24.39
3	1.25	21.25	4.78	7.74	0.74	0.80	17.03	8.51	3.75	31.93
4	1.75	29.75	3.41	10.77	0.70	0.74	21.95	10.98	3.25	35.67
5	2.25	38.25	2.66	13.74	0.67	0.69	26.34	13.17	2.75	36.22
6	2.75	46.75	2.17	16.64	0.63	0.65	30.27	15.13	2.25	34.05
7	3.25	55.25	1.84	19.46	0.60	0.61	33.80	16.90	1.75	29.57
8	3.75	63.75	1.59	22.18	0.57	0.58	36.99	18.49	1.25	23.12
9	4.25	72.25	1.41	24.80	0.55	0.55	39.89	19.94	0.75	14.96
10	4.75	80.75	1.26	27.31	0.52	0.53	42.54	21.27	0.25	5.32
Total:								132.74	Total:	247.58

Table 8-2 Problem #1: summary of results per unit length of wall.

Step #8: Determine the location of the resultant with Eq. (8-8); where: Y_i is the vertical distance between the base of the wall and the location of each force at the center of each sublayer (i.e., the lever arm) and \bar{Y} is the location of the resultant force. By replacing the summations presented in Table 8-2 the location of the resultant force from the base of the wall is 1.86 m as described below.

$$\bar{Y} = \frac{\sum_{i=1}^N (F_{\theta,H,i} \cdot Y_i)}{\sum_{i=1}^N (F_{\theta,H,i})} \quad (8-8)$$

$$\bar{Y} = \frac{247.58 \text{ kN} \cdot \text{m}}{132.74 \text{ kN}} = 1.86 \text{ m}$$

Step #9: Finally, it is also possible plot the at-rest lateral earth pressure distribution obtained in *Step #6* alongside with the resultant lateral force from *Step #7*, see Fig. 8-7.

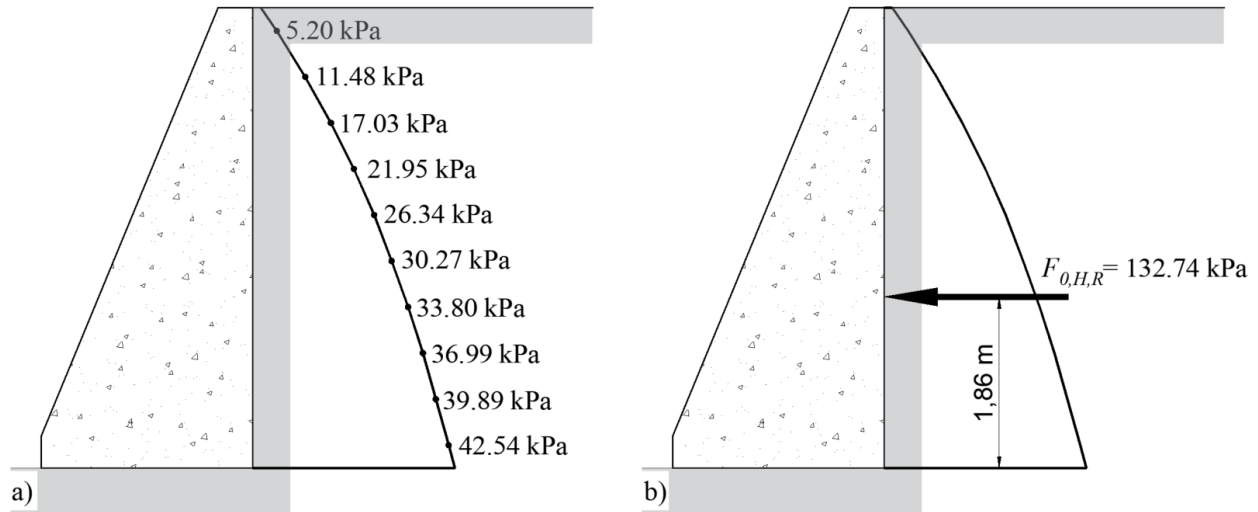


Fig. 8-7 Problem #1: at-rest lateral earth pressure per unit length of wall: (a) distribution; and (b) resultant.

8.5.2. Problem #2: Active lateral earth pressure

For the cantilever retaining wall shown in Fig. 8-8(a), determine the nonlinear active lateral earth pressure distribution and the resultant force per unit length of the wall indicating its location measured from the bottom of the wall. Also determine the nonlinear slip-failure surface, the horizontal outcrop distance, and the volume of the failing mass per unit length of the wall.

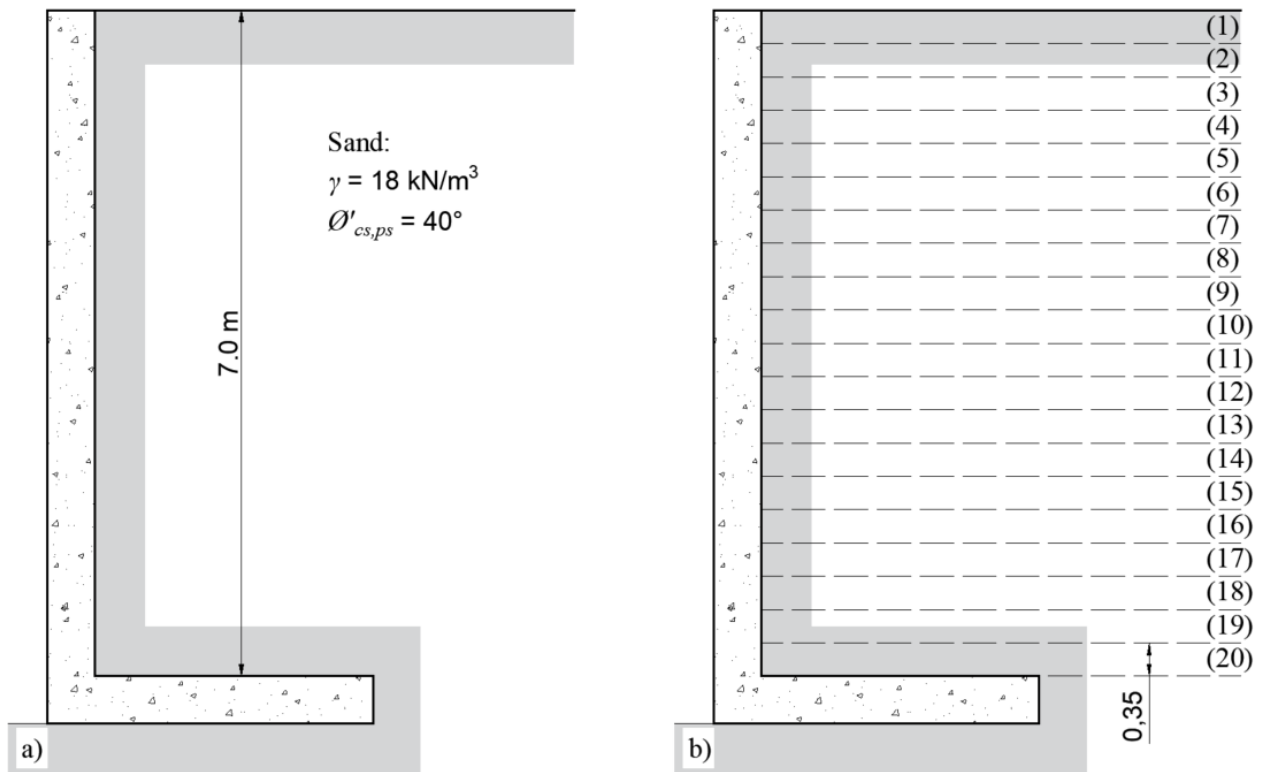


Fig. 8-8 Problem #2: (a) wall and backfill properties; and (b) sublayers to determine the lateral stress distribution and the slip-failure surface geometry.

Solution:

Step #1: Subdivide the backfill in various equal-thickness auxiliary sublayers as indicated in Fig. 8-8(b). The total number of sublayers adopted for present solution is $N = 20$ and the pack of sublayers is labeled consecutively from top ($i = 1$) to bottom ($i = N$). The resultant constant thickness of the sublayers is then 0.35 m as indicated in Fig. 8-8(b).

Step #2: Determine the ordinate x associated to each predefined height y using Eq. (6-10).

Step #3: Determine the active lateral stress $\sigma'_{a,H}$ at each predefined height y using Eq. (6-20).

Step #4: Determine the active force $F_{a,H}$ at each sublayer by multiplying the active lateral stress $\sigma'_{a,H}$ at each predefined height by the constant thickness of the sublayer (i.e., 0.35 m). Table 8-3 shows the results for present *Step #4* along with previous steps. The total active lateral earth force per unit length of the wall is 194.0 kN/m.

y (m)	x (m)	$\sigma'_{a,H}$ (kPa)	$F_{a,H}$ (kN)	lever arm (m)	moment (kN*m)
0.00	0.00	0.00			
0.35	0.36	37.79	6.61	0.18	1.16
0.70	0.63	50.27	15.41	0.53	8.09
1.05	0.86	53.26	18.12	0.88	15.85
1.40	1.04	52.22	18.46	1.23	22.61
1.75	1.21	49.37	17.78	1.58	28.00
2.10	1.35	45.72	16.64	1.93	32.03
2.45	1.48	41.75	15.31	2.28	34.82
2.80	1.59	37.72	13.91	2.63	36.51
3.15	1.70	33.75	12.51	2.98	37.21
3.50	1.79	29.91	11.14	3.33	37.04
3.85	1.88	26.22	9.82	3.68	36.09
4.20	1.96	22.70	8.56	4.03	34.45
4.55	2.04	19.34	7.36	4.38	32.18
4.90	2.12	16.15	6.21	4.73	29.35

y (m)	x (m)	$\sigma'_{a,H}$ (kPa)	$F_{a,H}$ (kN)	lever arm (m)	moment (kN*m)
5.25	2.18	13.12	5.12	5.08	25.99
5.60	2.25	10.23	4.09	5.43	22.17
5.95	2.31	7.49	3.10	5.78	17.91
6.30	2.37	4.87	2.16	6.13	13.25
6.65	2.42	2.38	1.27	6.48	8.22
7.00	2.48	0.00	0.42	6.83	2.84
		Total:	194.00	Total:	475.80

Table 8-3 Problem #2: summary of results per unit length of wall.

Step #5: Determine the location of the resultant with Eq. (8-8); where: Y_i is the vertical distance between the base of the wall and the location of each force at the center of each sublayer (i.e., the lever arm) and \bar{Y} is the location of the resultant force. By replacing the summations presented in Table 8-3 the location of the resultant force from the base of the wall is 2.45 m as described below.

$$\bar{Y} = \frac{\sum_{i=1}^N (F_{a,H,i} \cdot Y_i)}{\sum_{i=1}^N (F_{a,H,i})}$$

$$\bar{Y} = \frac{475.80 \text{ kN} \cdot \text{m}}{194.00 \text{ kN}} = 2.45 \text{ m}$$

Step #6: Finally, it is also possible plot the active lateral earth pressure distribution obtained in *Step #3* alongside with the slip-failure surface geometry from *Step #2*, see Fig. 8-9. The horizontal outcrop distance is calculated with Eq. (6-11) to be 2.48 m and the volume of the failing mass per unit length of the wall is calculated with Eq. (6-18) to be 11.48 m³.

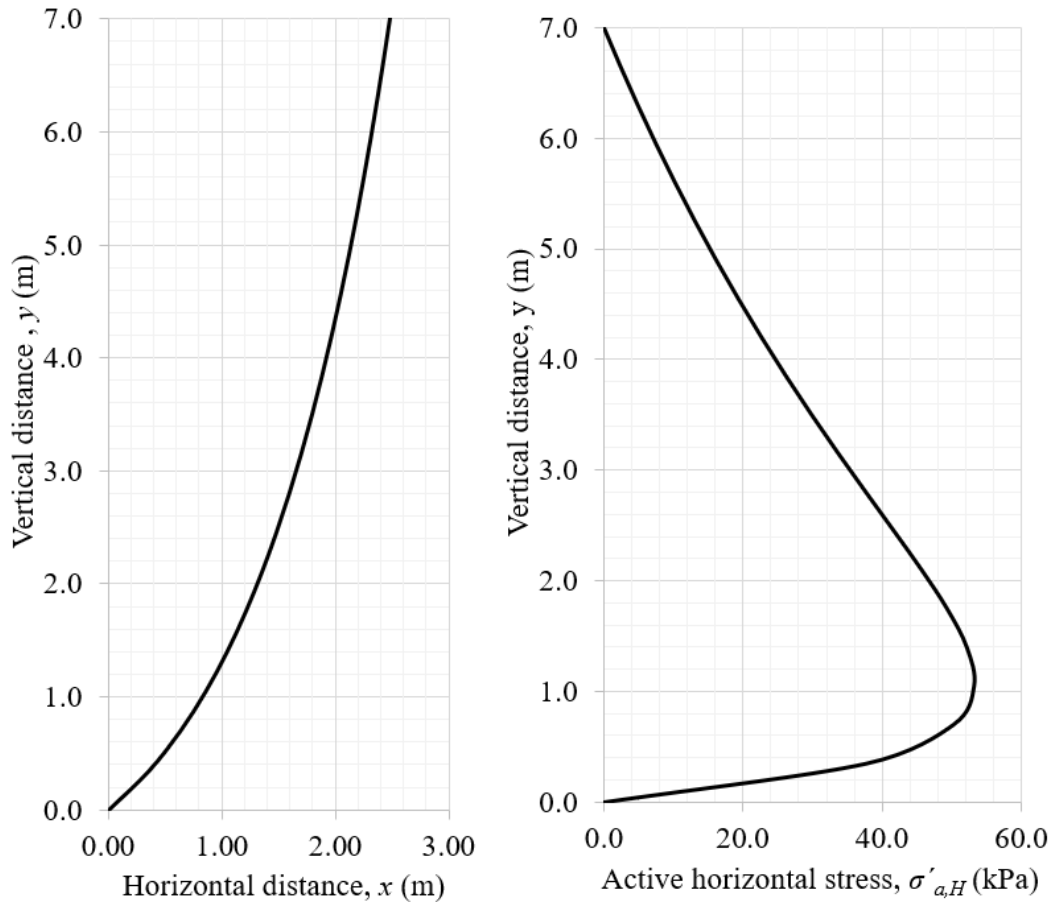


Fig. 8-9 Problem #2: (a) slip-failure surface geometry; and (b) active lateral earth pressure distribution.

8.5.3. Problem #3: Passive lateral earth pressure

For the cantilever retaining wall shown in Fig. 8-10(a), determine the nonlinear passive lateral earth pressure distribution and the resultant force per unit length of the wall indicating its location measured from the bottom of the wall. Also determine the nonlinear slip-failure surface, the horizontal outcrop distance, and the volume of the failing mass per unit length of the wall.

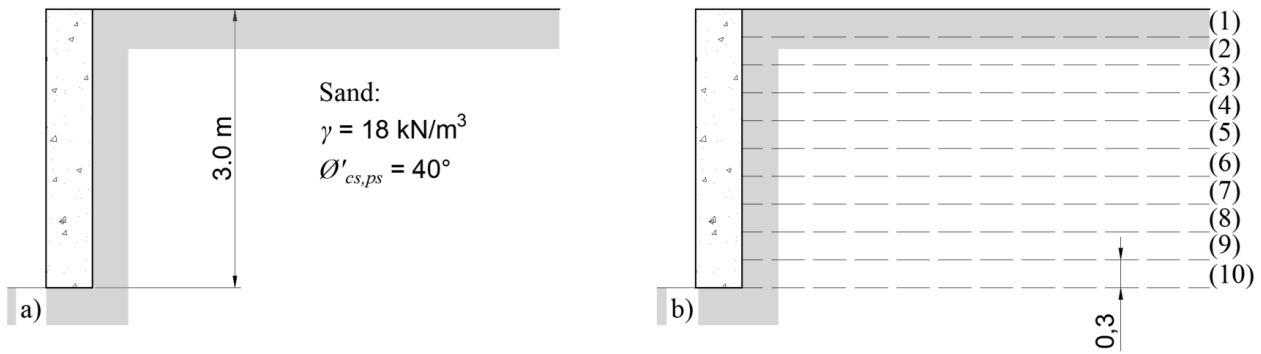


Fig. 8-10 Problem #3: (a) wall and backfill properties; and (b) sublayers to determine the lateral stress distribution and the slip-failure surface geometry.

Solution:

Step #1: Subdivide the backfill in various equal-thickness auxiliary sublayers as indicated in Fig. 8-10(b). The total number of sublayers adopted for present solution is $N = 10$ and the pack of sublayers is labeled consecutively from top ($i = 1$) to bottom ($i = N$). The resultant constant thickness of the sublayers is then 0.30 m as indicated in Fig. 8-10(b).

Step #2: Determine the ordinate x associated to each predefined height y using Eq. (6-15).

Step #3: Determine the passive lateral stress $\sigma'_{p,H}$ at each predefined height y using Eq. (6-20).

Step #4: Determine the passive force $F_{p,H}$ at each sublayer by multiplying the passive lateral stress $\sigma'_{p,H}$ at each predefined height by the constant thickness of the sublayer (i.e., 0.30 m). Table 8-4

shows the results for present *Step #4* along with previous steps. The total active lateral earth force per unit length of the wall is 258.3 kN/m.

y (m)	x (m)	$\sigma'_{p,H}$ (kPa)	$F_{p,H}$ (kN)	lever arm (m)	moment (kN*m)
0.00	0.00	0.00			
0.30	0.88	110.50	16.57	0.15	2.49
0.60	1.58	142.96	38.02	0.45	17.11
0.90	2.15	143.85	43.02	0.75	32.27
1.20	2.65	130.81	41.20	1.05	43.26
1.50	3.08	111.48	36.34	1.35	49.06
1.80	3.46	89.48	30.14	1.65	49.74
2.10	3.80	66.61	23.41	1.95	45.65
2.40	4.11	43.79	16.56	2.25	37.26
2.70	4.39	21.51	9.80	2.55	24.98
3.00	4.65	0.00	3.23	2.85	9.20
		Total:	258.30	Total:	311.01

Table 8-4 Problem #3: summary of results per unit length of wall.

Step #5: Determine the location of the resultant with Eq. (8-8); where: Y_i is the vertical distance between the base of the wall and the location of each force at the center of each sublayer (i.e., the lever arm) and \bar{Y} is the location of the resultant force. By replacing the summations presented in Table 8-4 the location of the resultant force from the base of the wall is 1.20 m as described below.

$$\bar{Y} = \frac{\sum_{i=1}^N (F_{p,H,i} \cdot Y_i)}{\sum_{i=1}^N (F_{p,H,i})}$$

$$\bar{Y} = \frac{311.01 \text{ kN} \cdot \text{m}}{258.30 \text{ kN}} = 1.20 \text{ m}$$

Step #6: Finally, it is also possible plot the passive lateral earth pressure distribution obtained in *Step #3* alongside with the slip-failure surface geometry from *Step #2*, see Fig. 8-11. The horizontal outcrop distance is calculated with Eq. (6-16) to be 4.65 m and the volume of the failing mass per unit length of the wall is calculated with Eq. (6-18) to be 8.54 m³.

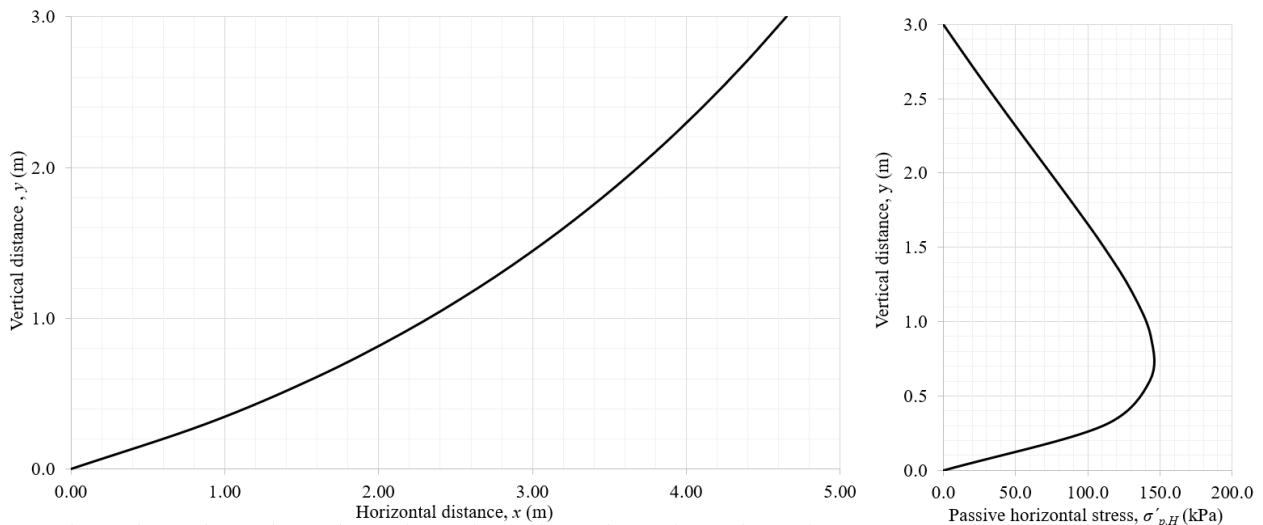


Fig. 8-11 Problem #3: (a) slip-failure surface geometry; and (b) passive lateral earth pressure distribution.

8.5.4. Problem #4: wall rotation Δ_x/H for active lateral earth pressure

For a vertical wall 3.0 m height, determine the minimum wall rotation and wall displacement Δ_x/H in percentage required to fully develop the active lateral earth pressure if the backfill is made from:

(a) dense sand with $\phi'_{cs,ps} = 48^\circ$; and (b) loose sand with $\phi'_{cs,ps} = 25^\circ$.

Solution:

Step #1: Subdivide the backfill in various equal-thickness auxiliary sublayers. The total number of sublayers adopted for present solution is $N = 10$ and the pack of sublayers is labeled consecutively from top ($i = 1$) to bottom ($i = N$). The resultant constant thickness of the sublayers is then 0.30 m.

Step #2: Determine the ordinate x associated to each predefined height y using Eq. (6-10).

Step #3: Determine the lateral strain ε_H at critical state plane-strain failure by means of applying the spreadsheet in *Appendix I* (see *Chapter 7*:). The lateral strain is $\varepsilon_H = -0.02024$ for the dense sand and $\varepsilon_H = -0.02577$ for the loose sand.

Step #4: Determine the displacement δ imposed by the wall. Considering a rigid wall, the displacement δ_i at the middle of each layer can be determined by applying linear distribution. For the case of outward rotation around the base, this linear distribution varies from zero at the wall bottom up to Δ_x at the wall top. For the case of horizontal outward translation, the lateral

displacement remains constant and is equal to Δ_x . In both cases, the displacement at the top Δ_x is the free variable used to find the critical state condition all along the slip-failure surface.

Step #5: Determine the strain imposed by the wall $\varepsilon_{3,wall}$ at each sublayer with Eq. (8-9).

$$\varepsilon_{3,wall} = -\frac{\delta_i}{x_i} \quad (8-9)$$

Step #6: By progressively increasing Δ_x determine the minimum value of Δ_x for which all the layers reach the critical state condition. Table 8-5 shows the results from *Steps #1 to #6* for both wall displacement conditions in dense sand. And Table 8-6 shows the results from *Steps #1 to #6* for both wall displacement conditions in loose sand.

depth avg.	y (m)	wall δ (mm)	wall $\delta_{avg.}$ (mm)	x (m)	$\varepsilon_{3,wall}$	CS ?
Outward rotation about the base:						
0.00		51.00				
0.30	2.85	45.90	48.45	1.21	-0.03992	yes
0.60	2.55	40.80	43.35	1.14	-0.03800	yes
0.90	2.25	35.70	38.25	1.06	-0.03604	yes
1.20	1.95	30.60	33.15	0.97	-0.03403	yes
1.50	1.65	25.50	28.05	0.88	-0.03197	yes
1.80	1.35	20.40	22.95	0.77	-0.02983	yes
2.10	1.05	15.30	17.85	0.65	-0.02762	yes
2.40	0.75	10.20	12.75	0.50	-0.02530	yes
2.70	0.45	5.10	7.65	0.33	-0.02287	yes

depth avg.	y (m)	wall δ (mm)	wall $\delta_{avg.}$ (mm)	x (m)	$\mathcal{E}_{3,wall}$	CS ?
3.00	0.15	0.00	2.55	0.13	-0.02026	yes
Outward translation:						
0.00		25.00				
0.30	2.85	25.00	25.00	1.21	-0.02060	yes
0.60	2.55	25.00	25.00	1.14	-0.02192	yes
0.90	2.25	25.00	25.00	1.06	-0.02356	yes
1.20	1.95	25.00	25.00	0.97	-0.02567	yes
1.50	1.65	25.00	25.00	0.88	-0.02849	yes
1.80	1.35	25.00	25.00	0.77	-0.03250	yes
2.10	1.05	25.00	25.00	0.65	-0.03868	yes
2.40	0.75	25.00	25.00	0.50	-0.04961	yes
2.70	0.45	25.00	25.00	0.33	-0.07473	yes
3.00	0.15	25.00	25.00	0.13	-0.19866	yes

Table 8-5 Problem #4: summary of results for dense sand under active state.

depth avg.	y (m)	wall δ (mm)	wall $\delta_{avg.}$ (mm)	x (m)	$\mathcal{E}_{3,wall}$	CS ?
Outward rotation about the base:						
0.00		155.00				
0.30	2.85	139.50	147.25	2.89	-0.05093	yes
0.60	2.55	124.00	131.75	2.72	-0.04849	yes
0.90	2.25	108.50	116.25	2.53	-0.04599	yes
1.20	1.95	93.00	100.75	2.32	-0.04343	yes
1.50	1.65	77.50	85.25	2.09	-0.04079	yes
1.80	1.35	62.00	69.75	1.83	-0.03806	yes

depth avg.	y (m)	wall δ (mm)	wall $\delta_{avg.}$ (mm)	x (m)	$\mathcal{E}_{3,wall}$	CS ?
2.10	1.05	46.50	54.25	1.54	-0.03524	yes
2.40	0.75	31.00	38.75	1.20	-0.03229	yes
2.70	0.45	15.50	23.25	0.80	-0.02918	yes
3.00	0.15	0.00	7.75	0.30	-0.02586	yes
Outward translation:						
0.00		75.00				
0.30	2.85	75.00	75.00	2.89	-0.02594	yes
0.60	2.55	75.00	75.00	2.72	-0.02760	yes
0.90	2.25	75.00	75.00	2.53	-0.02967	yes
1.20	1.95	75.00	75.00	2.32	-0.03233	yes
1.50	1.65	75.00	75.00	2.09	-0.03588	yes
1.80	1.35	75.00	75.00	1.83	-0.04093	yes
2.10	1.05	75.00	75.00	1.54	-0.04872	yes
2.40	0.75	75.00	75.00	1.20	-0.06249	yes
2.70	0.45	75.00	75.00	0.80	-0.09412	yes
3.00	0.15	75.00	75.00	0.30	-0.25022	yes

Table 8-6 Problem #4: summary of results for loose sand under active state.

Step #7: Determine the ratio Δ_x/H at critical state for both wall displacement conditions and densities. Accordingly, for dense sand and wall rotation $\Delta_x/H = 1.7\%$; for dense sand and wall translation $\Delta_x/H = 0.83\%$; for loose sand and wall rotation $\Delta_x/H = 5.17\%$; and for loose sand and wall translation $\Delta_x/H = 2.5\%$.

Step #8: Finally, it is also possible to compare these results with popular reference values since (Clough and Duncan, 1991). According to those authors, the rotation or lateral translation to reach minimum active earth pressure in dense soil is in the order of $\Delta_x/H = 0.1\%$ while for loose soil is in the order of $\Delta_x/H = 0.4\%$. However, according to present analysis the computed average value is $\overline{\Delta_x/H} = 1.27\%$ for dense sand and the corresponding computed average value for loose sand is $\overline{\Delta_x/H} = 3.83\%$. In conclusion, for the present problem, the rotation required to reach critical state plane-strain failure under the active state is about 10 times greater than that suggested by (Clough and Duncan, 1991) and associated to classic lateral earth pressure theories.

8.5.5. Problem #5: wall rotation Δ_x/H for passive lateral earth pressure

For a vertical wall 3.0 m height, determine the minimum wall rotation and wall displacement Δ_x/H in percentage required to fully develop the passive lateral earth pressure if the backfill is made from: (a) dense sand with $\phi'_{cs,ps} = 48^\circ$; and (b) loose sand with $\phi'_{cs,ps} = 25^\circ$.

Solution:

Step #1: Subdivide the backfill in various equal-thickness auxiliary sublayers. The total number of sublayers adopted for present solution is $N = 10$ and the pack of sublayers is labeled consecutively from top ($i = 1$) to bottom ($i = N$). The resultant constant thickness of the sublayers is then 0.30 m.

Step #2: Determine the ordinate x associated to each predefined height y using Eq. (6-15).

Step #3: Determine the lateral strain ε_H at critical state plane-strain failure by means of applying the spreadsheet in *Appendix I* (see *Chapter 7*:). The lateral strain is $\varepsilon_H = 0.02024$ for the dense sand and $\varepsilon_H = 0.02577$ for the loose sand.

Step #4: Determine the displacement δ imposed by the wall. Considering a rigid wall, the displacement δ_i at the middle of each layer can be determined by applying linear distribution. For the case of inward rotation around the base, this linear distribution varies from zero at the wall bottom up to Δ_x at the wall top. For the case of horizontal inward translation, the lateral displacement remains constant and is equal to Δ_x . In both cases, the displacement at the top Δ_x is the free variable used to find the critical state condition all along the slip-failure surface.

Step #5: Determine the strain imposed by the wall $\varepsilon_{3,wall}$ at each sublayer with Eq. (8-10).

$$\varepsilon_{3,wall} = \frac{\delta_i}{x_i} \quad (8-10)$$

Step #6: By progressively increasing Δ_x determine the minimum value of Δ_x for which all the layers reach the critical state condition. Table 8-7 shows the results from *Steps #1* to *#6* for both wall displacement conditions in dense sand. And Table 8-8 shows the results from *Steps #1* to *#6* for both wall displacement conditions in loose sand.

depth avg.	y (m)	wall δ (mm)	wall $\delta_{avg.}$ (mm)	x (m)	$\mathcal{E}_{H,wall}$	CS ?
Inward rotation about the base:						
0.00		252.00				
0.30	2.85	226.80	239.40	5.99	0.03998	yes
0.60	2.55	201.60	214.20	5.63	0.03806	yes
0.90	2.25	176.40	189.00	5.24	0.03610	yes
1.20	1.95	151.20	163.80	4.81	0.03408	yes
1.50	1.65	126.00	138.60	4.33	0.03201	yes
1.80	1.35	100.80	113.40	3.80	0.02988	yes
2.10	1.05	75.60	88.20	3.19	0.02766	yes
2.40	0.75	50.40	63.00	2.49	0.02534	yes
2.70	0.45	25.20	37.80	1.65	0.02290	yes
3.00	0.15	0.00	12.60	0.62	0.02029	yes
Inward translation:						
0.00		122.00				
0.30	2.85	122.00	122.00	5.99	0.02037	yes
0.60	2.55	122.00	122.00	5.63	0.02168	yes
0.90	2.25	122.00	122.00	5.24	0.02330	yes
1.20	1.95	122.00	122.00	4.81	0.02539	yes
1.50	1.65	122.00	122.00	4.33	0.02818	yes
1.80	1.35	122.00	122.00	3.80	0.03214	yes
2.10	1.05	122.00	122.00	3.19	0.03826	yes
2.40	0.75	122.00	122.00	2.49	0.04907	yes
2.70	0.45	122.00	122.00	1.65	0.07391	yes
3.00	0.15	122.00	122.00	0.62	0.19650	yes

Table 8-7 Problem #5: summary of results for dense sand under passive state.

depth avg.	y (m)	wall δ (mm)	wall $\delta_{avg.}$ (mm)	x (m)	$\mathcal{E}_{H,wall}$	CS ?
Inward rotation about the base:						
0.00		135.00				
0.30	2.85	121.50	128.25	2.51	0.05101	yes
0.60	2.55	108.00	114.75	2.36	0.04856	yes
0.90	2.25	94.50	101.25	2.20	0.04606	yes
1.20	1.95	81.00	87.75	2.02	0.04349	yes
1.50	1.65	67.50	74.25	1.82	0.04085	yes
1.80	1.35	54.00	60.75	1.59	0.03812	yes
2.10	1.05	40.50	47.25	1.34	0.03529	yes
2.40	0.75	27.00	33.75	1.04	0.03234	yes
2.70	0.45	13.50	20.25	0.69	0.02922	yes
3.00	0.15	0.00	6.75	0.26	0.02589	yes
Inward translation:						
0.00		65.00				
0.30	2.85	65.00	65.00	2.51	0.02585	yes
0.60	2.55	65.00	65.00	2.36	0.02751	yes
0.90	2.25	65.00	65.00	2.20	0.02957	yes
1.20	1.95	65.00	65.00	2.02	0.03222	yes
1.50	1.65	65.00	65.00	1.82	0.03576	yes
1.80	1.35	65.00	65.00	1.59	0.04079	yes
2.10	1.05	65.00	65.00	1.34	0.04855	yes
2.40	0.75	65.00	65.00	1.04	0.06228	yes
2.70	0.45	65.00	65.00	0.69	0.09379	yes
3.00	0.15	65.00	65.00	0.26	0.24936	yes

Table 8-8 Problem #5: summary of results for loose sand under passive state.

Step #7: Determine the ratio Δ_x/H at critical state for both wall displacement conditions and densities. Accordingly, for dense sand and wall rotation $\Delta_x/H = 8.40\%$; for dense sand and wall translation $\Delta_x/H = 4.07\%$; for loose sand and wall rotation $\Delta_x/H = 4.50\%$; and for loose sand and wall translation $\Delta_x/H = 2.17\%$.

Step #8: Finally, it is also possible to compare these results with popular reference values (Clough and Duncan, 1991). According to these authors, the rotation or lateral translation to reach maximum passive earth pressure in dense soil is in the order of $\Delta_x/H = 1\%$ while for loose soil is in the order of $\Delta_x/H = 4\%$. However, according to present analysis the computed average value is $\overline{\Delta_x/H} = 6.23\%$ for dense sand and the corresponding computed average value for loose sand is $\overline{\Delta_x/H} = 3.33\%$. In conclusion, for the present problem, the rotation required to reach critical state plane-strain failure under the passive state is about 2 times greater than that suggested by (Clough and Duncan, 1991) and associated to classic lateral earth pressure theories.

Chapter 9: Conclusion and Recommendations

9.1. General

The lateral earth pressure of normally NC and overconsolidated OC cohesionless soils under the CSSM plane-strain concept has been investigated experimentally, analytically, and numerically in this thesis. Emphasis was set on the nonlinearity natural to this phenomenon and the constitutive integration to other soil parameters.

Experimentally, laboratory tests were performed to measure the static angle of repose or critical state plane-strain friction angle, the interparticle sliding friction angle or constant-volume plane-strain friction and the at-rest lateral earth pressure transmitted by normally and overconsolidated cohesionless soils. A total of 134 single experimental tests was performed.

Analytically, the limit equilibrium technique, the law of energy conservation and the variational limit equilibrium method were applied on a granular particle-scale media to derive a new plane-strain *flow rule* and close-form solutions for the nonlinear at-rest (see *Appendix G*), active and passive coefficients of lateral earth pressure (i.e., NC and OC) and other associated plane-strain parameters namely: pore pressure coefficient; porosity; relative density; nonlinear at-rest, active and passive horizontal stress distribution (see *Appendix H*); and nonlinear slip-failure surface geometry (see *Appendix H*). Relationships between the present plane-strain frictional parameters and the corresponding angles of shearing resistance produced from the triaxial test or direct shear test were established. All the previous constitutes a new analytical CSSM plane-strain framework that was validated by means of present experimental research and additionally validated by means of multiple instances of direct comparison with data collected from the literature.

Numerically, a new incremental numerical model was also developed to simulate the complete stress–strain behavior associated to the present *flow rule* and CSSM plane-strain framework. This numerical model was implanted in a spreadsheet (see *Appendix I*) that permits stress-strain simulations for obtention the strain and principal stress ratio at failure as well as other characteristic curves and linked soil parameters given the initial state of the soil sample.

9.2. Main conclusion

The critical state concept was satisfactorily formulated in terms of friction and porosity to establish a complete CSSM framework for critical state of cohesionless soils. The application of this new CSSM plane-strain framework on the specific problem of retaining walls yielded an improved lateral earth pressure theory.

The soil shearing resistance and its associated failure surface in many geotechnical applications involving cohesionless soils is commonly better approximated by the plane-strain condition. Geotechnical projects like retaining walls, landslide stability, earth dams, box culverts, continuous footings, piles under lateral loads, pipelines, railroads, bridge abutments, tunnels, and road embankments are all applications where the plane-strain condition better represents the soil behavior. However, the complex behavior of cohesionless soil under plane-strain shearing and the difficulties to develop equipment and methods to perform plane-strain tests have kept lagged the application of the plane-strain shear resistance. In fact, this situation has left geotechnical engineering practitioners with the only option of less suitable approaches like *direct shear test* or *triaxial test*. In the absence of appropriate and accessible laboratory plane-strain tests, present research offers an alternative via a complete analytical CSSM plane-strain micromechanical

framework that links all relevant soil parameters to soil porosity facilitating in this way plane-strain applications.

The micromechanical approach (or particle-scale) adopted for this study resulted to be good enough to describe the soil behavior under the critical-state plane strain, active, at-rest and passive lateral earth pressure conditions. On this regard (Bolton, 2000) presented “micromechanics” as the appropriate tool to overcome difficulties in geotechnical engineering like “*to overcome shortcomings in the classical continuum approach to soil mechanics*” and “*to improve empirical correlations, to relate previously unrelated mechanisms, to define appropriate tests and to assist in the proper definition of parameters*” (Bolton, 2000). The present thesis understands and agrees with the points posited by (Bolton, 2000). In fact, the present thesis obtained some results in the scope of the “lateral earth pressure theory” as predicted by (Bolton, 2000); that is, for instance, by means of using the “micromechanics” tool: we improved a classical empirical formula for K_0 in NC by providing an alternative novel equation supported with rational derivation; we related the “pore water pressure coefficient A ” to friction in PS which was previously unrelated; we identified and delimited five distinct soil behaviors in PS which will help in defining more appropriate tests procedures and apparatuses; and within the thesis we also presented more solid definitions for the frictional components in PS and with this we are helping to disambiguate the yet ambiguous terminology that is currently affecting Geomechanics.

9.3. Specific conclusions

Based on the results produced in the present experimental, analytical, and numerical investigations, the following conclusions were made:

- 1) The use of artificial granular materials to investigate friction below and over the typical range of natural sands permitted a more comprehensive understanding of friction.
- 2) The interparticle sliding friction angle ϕ'_μ can also be measured with the inclined plane method and properly prepared blocks of sand.
- 3) The true static angle of repose β is a maximum limit that occurs only under zero energy of particle accommodation.
- 4) The static angle of repose β of a freestanding pile of loose granular material is the critical state plane-strain angle developed from the initial state provided by the interparticle sliding friction angle ϕ'_μ which can be referred to as the constant-volume plane-strain friction angle $\phi'_{cv,ps}$ in an ampler sense.
- 5) The plane-strain dilation $\phi'_{p,ps}$ is associated to the initial state of the soil (i.e., the constant-volume plane-strain friction angle). Accordingly, dilation is not an independent variable.
- 6) Due to compaction effort, backfills can be deemed as overconsolidated deposits and the consequent *OCR* effect is represented in an increase of the at-rest lateral earth pressure and in a resultant curve at-rest lateral earth pressure distribution.
- 7) A sand deposit under the at-rest state is overconsolidated if $\phi'_{cv,ps} > \phi'_\mu$ (or $\phi'_{cs,ps} > \beta$); in that case, *OCR* is greater than one in proportion to the relative density reached after a given energy of compaction. On the other side, in the case where $\phi'_{cv,ps} = \phi'_\mu$ (or $\phi'_{cs,ps} = \beta$) the soil deposit is normally consolidated (i.e., *OCR* is equal to one).
- 8) Present *flow rule* in Eq. (4-9) improves past expressions given that present solution reduces by one the number of unknowns (see Table 4-2) and links other soil parameters (see Fig. 7-1) in addition to the mere relationship between the components of friction.

- 9) The application of a micromechanical or particle-scale approach to investigate cohesionless granular materials is more advantageous than the traditional continuous approach.
- 10) The pore pressure coefficient A associated to the undrained behavior of cohesionless soil can be determined from the plane-strain frictional components $\phi'_{cv,ps}$ and $\phi'_{cs,ps}$ as given in the Eq. (4-20). Moreover, present solution includes the known pore pressure at constant-volume (i.e., $A_{cv} = -1/3$) previously determine by (Skempton, 1954).
- 11) The porosity n is a state parameter (i.e., an independent variable) from which is possible to determine the rest of soil parameters and the general CSSM plane-strain response of cohesionless soils.
- 12) As proved experimentally, the soil porosity correlates to present CSSM plane-stain framework by means of the relative porosity n_r previously defined by (Hanna, 2001).
- 13) The soil porosity varies in closed cycle in which dense soil can become loose and vice verse upon shear stress as illustrated in Fig. 4-5 and as defined by Eqs. (4-11) to (4-14).
- 14) The at-rest coefficient of lateral earth pressure K_0 for normally consolidated soils herein derived [see Eqs. (5-3) or (5-4)] and validated from the present experimental investigation agreed well with the empirical simplified formula proposed by (Jaky, 1948) in the range of friction of natural sands, which validates the present experimental and analytical investigation.
- 15) The equivalent maximum historic vertical consolidation stress $\sigma'_{v,max}$ associated to the compaction of cohesionless soils is a direct function of the energy of compaction and the type of sand. For the herein investigated silica sand, the standard Proctor energy leads a

$\sigma'_{v,max} = 101.56$ kPa (SD = 6.63 kPa) and the modified Proctor energy a $\sigma'_{v,max} = 517.17$ kPa (SD = 15.81 kPa).

- 16) The constant maximum historic vertical consolidation stress $\sigma'_{v,max}$ for any given energy of compaction and soil type is necessary to determine *OCR* in backfills. A methodology to determine $\sigma'_{v,max}$ was presented in numeral 3.4 and the associated calculations were conveniently implanted in a spreadsheet to easy applications (see *Appendix F*).
- 17) The nonlinear slip-failure surface geometry $y(x)$ is deterministic, and the governing parameters are the natural exponential function and the critical state plane-strain friction angle $\phi'_{cs,ps}$ as given in Eqs. (6-10) or (6-15).
- 18) The nonlinear horizontal earth pressure distribution behind a retaining wall $\sigma'_H(x)$ is deterministic and a function of the critical state plane-strain friction angle $\phi'_{cv,ps}$ as given in Eq. (6-20).
- 19) The nonlinear active and passive lateral earth pressure theory herein developed revealed that lateral earth pressure can be either substantially overestimated or underestimated by classical theory since Coulomb or Rankine.
- 20) The slip-failure surface geometry for the active case is unique for each $\phi'_{cs,ps}$ being the cutting level the given wall height H . Consequently, the small-scale models are not enough to capture the complete governing geometry as previously pointed by (Tsagareli, 1965).
- 21) The slip-failure surface geometry is relatively more curved for the active state than for the passive where geometry curved but more flattened.

- 22) The lateral stress distribution is curved and in general proportional to friction $\phi'_{cs,ps}$ and wall height H ; however, for the passive state the lateral stress appears particularly sensitive to the wall height.
- 23) The location of the resultant force is an inverse function of the wall height and varies as illustrated in Fig. 6-8. As a result, it is not a unique relative location of the resultant force in terms of wall height H like the popular $H/3$ since Coulomb or Rankine or the empirical $0.42H$ suggested in (Tsagareli, 1965).
- 24) From the application of the present Incremental Numerical Model for stress-strain simulation was possible to differentiate five distinct behaviors of cohesionless soils (see Table 7-1) namely: extensive/collapsible, extensive/dilative, compressive/contractive, compressive/dilative, and extensive/suction-dilative behavior.
- 25) The stress-strain path within the shear band as herein determined differs from the net stress-strain path measured in laboratory tests on the sample surface.
- 26) Present CSSM plane-strain framework is summarized in the algorithm presented in Fig. 8-1 and Fig. 8-2 and the soil properties integrated by this framework are summarized in Fig. 7-1 which sorts the variables in three main stages namely: a initial constant-volume state, a final critical state and an intermediate zone representing the transit between initial and final states.
- 27) Present plane-strain frictional components $\phi'_{cv,ps}$ and $\phi'_{cs,ps}$ can also be estimated from direct shear results with Eq. (8-1) and from triaxial test results with Eq. (8-2).

28) The minimum wall rotation required to reach critical state plane-strain failure under passive and active states is substantially greater than that suggested by (Clough and Duncan, 1991) to trigger active and passive states in classical theories.

9.4. Recommendation for Future Work

Given demonstrated capabilities general applicability of present CSSM plane-strain framework the following recommendations are suggested for future work:

- 1) To integrate present CSSM plane-strain framework in the solution to other geotechnical applications (e.g., investigate the slope stability analysis incorporated with dilative-contractive response, the effect of *OCR* on the capacity of closed-end displacement piles in cohesionless soil, bearing capacity of footings on dense to very dense cohesionless soil).
- 2) To experimentally explore new laboratory apparatuses and methodologies to perform plane-strain tests.
- 3) To evaluate appropriate factor of safety suitable for present design criteria for critical state.
- 4) To integrate present constitutive CSSM plane-strain framework in FEM or DEM modeling.
- 5) To integrate present constitutive CSSM plane-strain framework to numerical simulation of pushover analysis of soil-structure interactions such as bridge abutments and piles or basement walls under lateral loading (e.g., passive p-y curves).
- 6) To incorporate cohesion to the active and passive states (e.g., by applying Bell's extension).
- 7) To evaluate non-homogeneous solutions by applying present theory in a layer-by-layer basis.

References

- Alharthi, Y.M., 2018. Shaft Resistance of Driven Piles in Overconsolidated Cohesionless Soils (PhD Thesis). Concordia University.
- Alshibli, K.A., Godbold, D.L., Hoffman, K., 2004. The Louisiana Plane Strain Apparatus for Soil Testing. *Geotech. Test. J.* 27, 337–346. <https://doi.org/10.1520/GTJ19103>
- ASTM D06 Committee, 2007. Test Method for Coefficient of Static Friction of Uncoated Writing and Printing Paper by Use of the Inclined Plane Method (No. ASTM D4918-97 (withdrawn 2010)). ASTM International, West Conshohocken, PA.
- ASTM D698-12e2, 2012. Test Methods for Laboratory Compaction Characteristics of Soil Using Standard Effort (12 400 ft-lbf/ft³ (600 kN-m/m³)). ASTM International, West Conshohocken, PA. <https://doi.org/10.1520/D0698-12E02>
- ASTM D1557-12e1, 2012. Test Methods for Laboratory Compaction Characteristics of Soil Using Modified Effort (56,000 ft-lbf/ft³ (2,700 kN-m/m³)). ASTM International, West Conshohocken, PA. <https://doi.org/10.1520/D1557-12E01>
- ASTM D4254-16, 2016a. Test Methods for Minimum Index Density and Unit Weight of Soils and Calculation of Relative Density. <https://doi.org/10.1520/D4254-16>
- ASTM D4254-16, 2016b. Test Methods for Minimum Index Density and Unit Weight of Soils and Calculation of Relative Density ((active standard)). ASTM International, West Conshohocken, PA. <https://doi.org/10.1520/D4254-16>

- Atkinson, J., 1993. An Introduction to the Mechanics of Soils and Foundations: Through Critical State Soil Mechanics. McGraw-Hill Book Company (UK) Ltd.
- Atkinson, J.H., 2017. The Mechanics of Soils and Foundations, 2nd ed. ed. CRC Press, Abingdon, UK.
- Atkinson, J.H., 1973. The deformation of undisturbed London clay.
- Beakawi Al-Hashemi, H.M., Baghabra Al-Amoudi, O.S., 2018. A Review on the Angle of Repose of Granular Materials. Powder Technol. 330, 397–417.
<https://doi.org/10.1016/j.powtec.2018.02.003>
- Benmebarek, N., Labdi, H., Benmebarek, S., 2016. A Numerical Study of the Active Earth Pressure on a Rigid Retaining Wall for Various Modes of Movements. Soil Mech. Found. Eng. 53, 39–45. <https://doi.org/10.1007/s11204-016-9362-z>
- Bishop, A.W., 1954. Correspondence on Shear Characteristics of a Saturated Silt, Measured in Triaxial Compression. Géotechnique 4, 43–45.
- Bjerrum, L., Kringstad, S., Kummeneje, O., 1961. The Shear Strength of a Fine Sand, in: Proc. 5th Int. Conf. Soil Mech. Paris, pp. 29–37.
- Bolton, M.D., 2000. The role of micro-mechanics in soil mechanics (Monograph). Cambridge University Engineering Department, Cambridge.
- Bolton, M.D., 1987. Discussion: The strength and dilatancy of sands. Géotechnique 37, 219–226.
<https://doi.org/10.1680/geot.1987.37.2.219>
- Bolton, M.D., 1986. The Strength and Dilatancy of Sands. Geotechnique 36, 65–78.

- Bolton, M.D., Arthur, J.R.F., 1987. The Strength and Dilatancy of Sands [(1986). *Géotechnique* 36, No. 1, 65-78.]. Discussion. *Geotechnique* 36.
- Boussinesq, J., 1885. Application des potentiels à l'étude de l'équilibre et du mouvement des solides élastiques: principalement au calcul des déformations et des pressions que produisent, dans ces solides, des efforts quelconques exercés sur une petite partie de leur surface ou de leur intérieur: mémoire suivi de notes étendues sur divers points de physique, mathématique et d'analyse. Gauthier-Villars.
- Brezzi, L., Cola, S., Gabrieli, F., Gidoni, G., 2017. Spreading of Kaolin and Sand Mixtures on a Horizontal Plane: Physical Experiments and SPH Numerical Modelling. *Procedia Eng.* 175, 197–203. <https://doi.org/10.1016/j.proeng.2017.01.008>
- Brooker, E.W., Ireland, H.O., 1965. Earth Pressures At-rest Related to Stress History. *Can. Geotech. J.* 2, 1–15. <https://doi-org.lib-ezproxy.concordia.ca/10.1139/t65-001>
- C08.03 Subcommittee, 2000. Standard Test Method for Measuring the Angle of Repose of Free-Flowing Mold Powders (Withdrawn 2005) (Withdrawn Standard No. ASTM C1444-00). ASTM International, West Conshohocken, PA. <https://doi.org/10.1520/C1444-00>
- Cao, W., Liu, T., Xu, Z., 2019. Calculation of Passive Earth Pressure Using the Simplified Principal Stress Trajectory Method on Rigid Retaining Walls. *Comput. Geotech.* 109, 108–116. <https://doi.org/10.1016/j.compgeo.2019.01.021>
- Caquot, A.I., 1934. Équilibre des Massifs à Frottement Interne: Stabilité des Terres, Pulvérulentes ou Cohérentes. Gauthier-Villars.

- Castro, G., 1969. Liquefaction of Sands. Harv. Soil Mech. Ser. Harv. Univ. Camb. Mass., Harvard Soil Mechanics Series.
- Cavarretta, I., Rocchi, I., Coop, M.R., 2011. A new interparticle friction apparatus for granular materials. *Can. Geotech. J.* 48, 1829–1840. <https://doi-org.lib-ezproxy.concordia.ca/10.1139/t11-077>
- Cetin, H., Gökoğlu, A., 2013. Soil Structure Changes During Drained and Undrained Triaxial Shear of a Clayey Soil. *Soils Found.* 53, 628–638. <https://doi.org/10.1016/j.sandf.2013.08.002>
- Chakraborty, T., Salgado, R., 2010. Dilatancy and Shear Strength of Sand at Low Confining Pressures. *J. Geotech. Geoenvironmental Eng.* 136, 527–532. [https://doi.org/10.1061/\(ASCE\)GT.1943-5606.0000237](https://doi.org/10.1061/(ASCE)GT.1943-5606.0000237)
- Chen, W.F., Snitbhan, N., 1975. On Slip Surface and Slope Stability Analysis. 土質工学会論文報告集 15, 41–49. https://doi.org/10.3208/sandf1972.15.3_41
- Chik, Z., Vallejo, L.E., 2005. Characterization of the Angle of Repose of Binary Granular Materials. *Can. Geotech. J.* 42, 683–692. <https://doi-org.lib-ezproxy.concordia.ca/10.1139/t04-118>
- Chu, J., Gan, C.L., 2004. Effect of Void Ratio on K_0 of Loose Sand. *Geotechnique* 54, 285–288. <https://doi-org.lib-ezproxy.concordia.ca/10.1680/geot.2004.54.4.285>

- Cinicioglu, O., Altunbas, A., Soltanbeigi, B., Gezgin, A.T., 2015. Characterization of Active Failure Wedge for Cohesionless Soils. The British Geotechnical Association Edinburgh, UK.
- Clough, G.W., Duncan, J.M., 1991. Earth Pressures, in: Fang, H.-Y. (Ed.), *Foundation Engineering Handbook*. Springer US, Boston, MA, pp. 223–235. https://doi.org/10.1007/978-1-4757-5271-7_6
- Coetzee, C.J., 2017. Review: Calibration of the Discrete Element Method. *Powder Technol.* 310, 104–142. <https://doi.org/10.1016/j.powtec.2017.01.015>
- Cornforth, D.H., 1973. Prediction of Drained Strength of Sands from Relative Density Measurements. *Eval. Relat. Density Its Role Geotech. Proj. Involv. Cohesionless Soils*. <https://doi.org/10.1520/STP37878S>
- Cornforth, D.H., 1961. Plane strain failure characteristics of saturated sand (PhD Thesis). Imperial College London.
- Coulomb, C.A., 1776. *Essai Sur une Application des Regles de Maximis et Minimis a Quelques Problemes de Statique Relatifs a L'architecture* (Essay on Maximums and Minimums of Rules to Some Static Problems Relating to Architecture). *Memoires Math. Phys. Present. Acad. R. Sci.* 3, 343–382.
- D18 Committee, 2014. Test Method for Bulk Solids Characterization by Carr Indices (Active Standard No. ASTM D6393). ASTM International. <https://doi.org/10.1520/D6393-14>
- Davis, E.H., 1968. Theories of plasticity and failures of soil masses. *Soil Mech. Sel. Top.*

- Di Camillo, F., 2014. Effects of Stress History of Sand on the Shaft Resistance of Large Displacement Piles (PhD Thesis). Concordia University.
- Díaz-Rodríguez, J.A., Leroueil, S., Alemán, J.D., 1992. Yielding of Mexico City Clay and Other Natural Clays. *J. Geotech. Eng.* 118, 981–995. [https://doi.org/10.1061/\(ASCE\)0733-9410\(1992\)118:7\(981\)](https://doi.org/10.1061/(ASCE)0733-9410(1992)118:7(981))
- Diaz-Segura, E.G., 2016. The coefficient of earth pressure at rest. *Electron. J. Geotech. Eng.* 21, 1775–1785.
- Dietz, M.S., 2000. Developing an holistic understanding of interface friction using sand with direct shear apparatus (PhD Thesis). University of Bristol.
- Duncan, J.M., Chang, C.Y., 1970. Nonlinear Analysis of Stress and Strain in Soils. *J. Soil Mech. Found. Div.*
- El Sharif, M., Taha, Y.K., Eweada, S.N., 2011. Theoretical Study of Earth Pressure At–Rest for Sandy Soils. *J. Eng. Sci.* 39, 1–13.
- El-Emam, M., 2011. Experimental and Numerical Study of At-rest Lateral Earth Pressure of Overconsolidated Sand. *Adv. Civ. Eng.* 2011, 12. <http://dx.doi.org/10.1155/2011/524568>
- Evesque, P., 1999. On Jaky Constant of Oedometers, Rowe’s Relation and Incremental Modeling. *Poudres Grains* 6, 1–9.
- Fang, Y., Ishibashi, I., 1986. Static Earth Pressures with Various Wall Movements. *J. Geotech. Eng.* 112, 317–333. [https://doi.org/10.1061/\(ASCE\)0733-9410\(1986\)112:3\(317\)](https://doi.org/10.1061/(ASCE)0733-9410(1986)112:3(317))

- Fang, Y.-S., Ho, Y.-C., Chen, T.-J., 2002. Passive Earth Pressure with Critical State Concept. *J. Geotech. Geoenvironmental Eng.* 128, 651–659. [https://doi.org/10.1061/\(ASCE\)1090-0241\(2002\)128:8\(651\)](https://doi.org/10.1061/(ASCE)1090-0241(2002)128:8(651))
- Federico, A., Elia, G., Germano, V., 2008. A Short Note on the Earth Pressure and Mobilized Angle of Internal Friction in One-Dimensional Compression of Soils. *J. Geoenviron. Eng.* 3, 41–46.
- Fellenius, W.K.A., 1948. *Erdstatische Berechnungen: Mit Reibung und Kohäsion (Adhäsion) und Unter Annahme Kreiszyklindrischer Gleitflächen.* W. Ernst.
- Froehlich, D.C., 2011. Mass Angle of Repose of Open-Graded Rock Riprap. *J. Irrig. Drain. Eng.* 137, 454–461. [https://doi.org/10.1061/\(ASCE\)IR.1943-4774.0000316](https://doi.org/10.1061/(ASCE)IR.1943-4774.0000316)
- Garga, V.K., Sedano, J.-A.I., 2002. Steady State Strength of Sands in a Constant Volume Ring Shear Apparatus. *Geotech. Test. J.* 25, 414–421. <https://doi.org/10.1520/GTJ11291J>
- Guo, P., 2010. Effect of Density and Compressibility on K_0 of Cohesionless Soils. *Acta Geotech.* 5, 225–238. <https://doi.org/10.1007/s11440-010-0125-0>
- Hamidi, A., Alizadeh, M., Soleymani, S., 2009. Effect of Particle Crushing on Shear Strength and Dilation Characteristics of Sand-Gravel Mixtures. *Int. J. Civ. Eng. Iran Univ. Sci. Technol.* 7, 61–72.
- Handy Richard L., 1985. The Arch in Soil Arching. *J. Geotech. Eng.* 111, 302–318. [https://doi.org/10.1061/\(ASCE\)0733-9410\(1985\)111:3\(302\)](https://doi.org/10.1061/(ASCE)0733-9410(1985)111:3(302))

- Hanna, A.M., 2001. Determination of plane-strain shear strength of sand from the results of triaxial tests. *Can. Geotech. J.* 38, 1231–1240. <https://doi-org.lib-ezproxy.concordia.ca/10.1139/t01-064>
- Hanna, A.M., Al-Romhein, R., 2008. At-rest Earth Pressure of Overconsolidated Cohesionless Soil. *J. Geotech. Geoenvironmental Eng.* 134, 408–412. [https://doi.org/10.1061/\(ASCE\)1090-0241\(2008\)134:3\(408\)](https://doi.org/10.1061/(ASCE)1090-0241(2008)134:3(408))
- Hanna, A.M., Diab, R., 2017. Passive Earth Pressure of Normally and Overconsolidated Cohesionless Soil in Terms of Critical-State Soil Mechanics Parameters. *Int. J. Geomech.* 17, 04016028. [https://doi.org/10.1061/\(ASCE\)GM.1943-5622.0000683](https://doi.org/10.1061/(ASCE)GM.1943-5622.0000683)
- Hanna, A.M., Khoury Imad, A., 2005. Passive Earth Pressure of Overconsolidated Cohesionless Backfill. *J. Geotech. Geoenvironmental Eng.* 131, 978–986. [https://doi.org/10.1061/\(ASCE\)1090-0241\(2005\)131:8\(978\)](https://doi.org/10.1061/(ASCE)1090-0241(2005)131:8(978))
- Harrop-Williams, K.O., 1989. Geostatic Wall Pressures. *J. Geotech. Eng.* 115, 1321–1325.
- Hendron Jr, A.J., 1963. The Behavior of Sand in One-Dimensional Compression. (Technical Report No. AD0424192). Illinois Univ Urbana, United States.
- Hettiaratchi, D.R.P., Reece, A.R., 1974. The Calculation of Passive Soil Resistance. *Géotechnique* 24, 289–310. <https://doi.org/10.1680/geot.1974.24.3.289>
- Hettiaratchi, D.R.P., Witney, B.D., Reece, A.R., 1966. The Calculation of Passive Pressure in Two-dimensional Soil Failure. *J. Agric. Eng. Res.* 11, 89–107. [https://doi.org/10.1016/S0021-8634\(66\)80045-8](https://doi.org/10.1016/S0021-8634(66)80045-8)

- Horne, M.R., 1969. The Behaviour of an Assembly of Rotund, Rigid, Cohesionless Particles. III. Proc. R. Soc. Lond. Ser. Math. Phys. Sci. 310, 21–34.
- Hu, H., Yang, M., Lin, P., Lin, X., 2019. Passive Earth Pressures on Retaining Walls for Pit-in-Pit Excavations. IEEE Access 7, 5918–5931. <https://doi.org/10.1109/ACCESS.2018.2889991>
- Huang, W.-X., Wu, W., Sun, D.-A., Sloan, S., 2006. A Simple Hypoplastic Model for Normally Consolidated Clay. Acta Geotech. 1, 15–27. <https://doi.org/10.1007/s11440-005-0003-3>
- Jaky, J., 1948. Pressure in Silos, in: Proc. 2nd ICSM, 1948.
- Jaky, J., 1944. The Coefficient of Earth Pressure at Rest. J Soc. Hung. Archit. Eng. 355–358.
- Jamiolkowski, M., Lo Presti, D.C.F., Manassero, M., 2012. Evaluation of Relative Density and Shear Strength of Sands from CPT and DMT 201–238. [https://doi.org/10.1061/40659\(2003\)7](https://doi.org/10.1061/40659(2003)7)
- Janssen, H.A., 1895. Versuche Ober Getreidedruck in Silozellen. Z. Ver. Dtsch. Ingenieure 39, 1045–1049.
- Jerves, A.X., Andrade, J.E., 2016. A micro-mechanical study of peak strength and critical state. Int. J. Numer. Anal. Methods Geomech. 40, 1184–1202. <https://doi.org/10.1002/nag.2478>
- Jones, R., 2003. From single particle AFM studies of adhesion and friction to bulk flow: forging the links. Granul. Matter 4, 191–204. <https://doi.org/10.1007/s10035-002-0122-6>
- Khosravi, M.H., Pipatpongsa, T., Takemura, J., 2013. Experimental Analysis of Earth Pressure Against Rigid Retaining Walls under Translation Mode. Géotechnique 63, 1020–1028. <https://doi.org/10.1680/geot.12.P.021>

- Kleinhans, M.G., Markies, H., Vet, S.J. de, Veld, A.C. in 't, Postema, F.N., 2011. Static and Dynamic Angles of Repose in Loose Granular Materials under Reduced Gravity. *J. Geophys. Res. Planets* 116. <https://doi.org/10.1029/2011JE003865>
- Kötter, F., 1903. Die Bestimmung des Druckes an gekrümmten Gleitflächen, eine Aufgabe aus der Lehre vom Erddruck. *Ber Akad Wiss Berl.* 229 223.
- Koudelka, P., 2016. Experiment E7/0,3 – Time Behaviour of Active Pressure of Non-Cohesive Sand after Wall Translative Motion. *Appl. Mech. Mater.* 821, 512–517. <https://doi.org/10.4028/www.scientific.net/AMM.821.512>
- Lambe, T.W., Whitman, R.V., 1969. *Soil Mechanics*, 553 pp. John Wiley, New York.
- Lazebnik, G., 1974. Some Factors that Affect the Magnitude of the Lateral Pressure “At-rest” of the Granular. *Izv VNIIG* 105, 64–72.
- Lazebnik, G., Tsinker, G., 1997. *Monitoring of Soil-Structure Interaction: Instruments for Measuring of Soil Pressures*. Springer Science & Business Media.
- Lee, J., Herrmann, H.J., 1993. Angle of Repose and Angle of Marginal Stability: Molecular Dynamics of Granular Particles. *J. Phys. Math. Gen.* 26, 373–383. <https://doi.org/10.1088/0305-4470/26/2/021>
- Lee, J., Yun, T.S., Lee, D., Lee, J., 2013. Assessment of K_0 Correlation to Strength for Granular Materials. *Soils Found.* 53, 584–595. <https://doi.org/10.1016/j.sandf.2013.06.009>

- Lee, S.-H., 2019. Computation of Passive Earth Pressure Coefficient considering Logarithmic Spiral Arc. *J. Korea Acad.-Ind. Coop. Soc.* 20, 425–433.
<https://doi.org/10.5762/KAIS.2019.20.2.425>
- Li, X.G., Liu, W.N., 2006. Study on limit earth pressure by variational limit equilibrium method, in: *Advances in Earth Structures: Research to Practice*. pp. 356–363.
- Li, Y., Xu, Y., Thornton, C., 2005. A Comparison of Discrete Element Simulations and Experiments for ‘Sandpiles’ Composed of Spherical Particles. *Powder Technol.* 160, 219–228. <https://doi.org/10.1016/j.powtec.2005.09.002>
- Liffman, K., Chan, D.Y., Hughes, B.D., 1992. Force Distribution in a Two-Dimensional Sandpile. *Powder Technol.* 72, 255–267.
- Lings, M.L., Dietz, M.S., 2004. An improved direct shear apparatus for sand. *Géotechnique* 54, 245–256. <https://doi.org/10.1680/geot.2004.54.4.245>
- Liu, S., Xia, Y., Liang, L., 2018. A Modified Logarithmic Spiral Method for Determining Passive Earth Pressure. *J. Rock Mech. Geotech. Eng.* 10, 1171–1182.
<https://doi.org/10.1016/j.jrmge.2018.03.011>
- Liu, Z., 2011. Measuring the Angle of Repose of Granular Systems Using Hollow Cylinders (PhD Thesis). University of Pittsburgh.
- Livingston, C.W., 1961. The Natural Arch, the Fracture Pattern, and the Sequence of Failure in Massive Rocks Surrounding an Underground Opening, in: *The 4th US Symposium on Rock Mechanics (USRMS)*. American Rock Mechanics Association.

- Lowe, D.R., 1976. Grain Flow and Grain Flow Deposits. *J. Sediment. Res.* 46, 188–199.
- Matsuo, M., Kenmochi, S., Yagi, H., 1978. Experimental Study on Earth Pressure of Retaining Wall by Field Tests. *Soils Found.* 18, 27–41.
- Mayne, P.W., 1980. Cam-Clays Predictions of Undrained Strength. *J. Geotech. Geoenvironmental Eng.* 106.
- Mayne, P.W., Kulhawy, F.H., 1982. K₀-OCR Relationships in Soil. *J. Soil Mech. Found. Div.* 108, 851–872.
- Mehta, A., Barker, G.C., 1994. The Dynamics of Sand. *Rep. Prog. Phys.* 57, 383.
- Mesri, G., Hayat, T.M., 1993. The Coefficient of Earth Pressure At-rest. *Can. Geotech. J.* 30, 647–666. <https://doi.org/10.1139/t93-056>
- Meyerhof, G.G., 1976. Bearing Capacity and Settlement of Pile Foundations. *J. Geotech. Eng. Div.* 102, 195–228.
- Michalowski, R.L., 2005. Coefficient of Earth Pressure At-rest. *J. Geotech. Geoenvironmental Eng.* 131, 1429–1433. [https://doi.org/10.1061/\(ASCE\)1090-0241\(2005\)131:11\(1429\)](https://doi.org/10.1061/(ASCE)1090-0241(2005)131:11(1429))
- Michalowski, R.L., Park, N., 2004. Admissible Stress Fields and Arching in Piles of Sand. *Geotechnique* 54, 529–538.
- Mittal, H.K., 1963. Effect of plane strain on pore pressure parameters (PhD Thesis). University of British Columbia.
- Miura, K., Maeda, K., Toki, S., 1997. Method of Measurement for the Angle of Repose of Sands. *Soils Found.* 37, 89–96. https://doi.org/10.3208/sandf.37.2_89

- Moroto, N., 1987. On Deformation of Granular Material in Simple Shear. *Soils Found.* 27, 77–85.
- Narain, J., Saran, S., Nandakumaran, P., 1969. Model Study of Passive Pressure in Sand. *J. Soil Mech. Found. Div.*
- Paik, K.H., Salgado, R., 2003. Estimation of Active Earth Pressure Against Rigid Retaining Walls Considering Arching Effects. *Geotechnique* 53, 643–654.
- Pipatpongsa, T., Heng, S., Iizuka, A., Ohta, H., 2009. Rationale for Coefficient of Earth Pressure At-rest Derived from Prismatic Sand Heap. *J. Appl. Mech.* 12, 383–394.
- Pohlman, N.A., Severson, B.L., Ottino, J.M., Lueptow, R.M., 2006. Surface Roughness Effects in Granular Matter: Influence on Angle of Repose and the Absence of Segregation. *Phys. Rev. E* 73, 031304. <https://doi.org/10.1103/PhysRevE.73.031304>
- Prandtl, L., 1920. Über die Härte Plastischer Körper. Göttingen. *Nachrichten Math.-Phys. Kl.* 12, 74–85.
- Pruska, L., 1978. At-rest Lateral Earth Pressure Coefficient of a Granular Medium. *Soil Mech. Found. Eng.* 15, 56–61. <https://doi.org/10.1007/BF02145334>
- Rahardjo, H., Fredlund, D.G., 1984. General Limit Equilibrium Method for Lateral Earth Force. *Can. Geotech. J.* 21, 166–175.
- Rankine, W.J., 1857. II. On the Stability of Loose Earth. *Philos. Trans. R. Soc. Lond.* 147, 9–27. <https://doi.org/10.1098/rstl.1857.0003>
- Reece, A.R., Hettiaratchi, D.R.P., 1989. A Slip-line Method for Estimating Passive Earth Pressure. *J. Agric. Eng. Res.* 42, 27–41. [https://doi.org/10.1016/0021-8634\(89\)90037-1](https://doi.org/10.1016/0021-8634(89)90037-1)

- Rendulic, L., 1940. Gleitflaechen, Pruefflaechen und Erddruck. Verlag nicht ermittelbar.
- Roessler, T., Katterfeld, A., 2018. Scaling of the Angle of Repose Test and its Influence on the Calibration of DEM Parameters Using Upscaled Particles. *Powder Technol.* 330, 58–66. <https://doi.org/10.1016/j.powtec.2018.01.044>
- Roscoe, K.H., Schofield, A.N., Thurairajah, A., 1963. Yielding of Clays in States Wetter than Critical. *Géotechnique* 13, 211–240. <https://doi.org/10.1680/geot.1963.13.3.211>
- Roscoe, K.H., Schofield, A.N., Wroth, C.P., 1958. On the Yielding of Soils. *Geotechnique* 8, 22–53. <https://doi-org.lib-ezproxy.concordia.ca/10.1680/geot.1958.8.1.22>
- Rousé, P.C., 2013. Comparison of Methods for the Measurement of the Angle of Repose of Granular Materials. *Geotech. Test. J.* 37, 164–168. <https://doi.org/10.1520/GTJ20120144>
- Rowe, P.W., 1969. The Relation Between the Shear Strength of Sands in Triaxial Compression, Plane Strain and Direct Shear. *Géotechnique* 19, 75–86. <https://doi.org/10.1680/geot.1969.19.1.75>
- Rowe, P.W., 1963. Stress-Dilatancy, Earth Pressures, and Slopes. *J. Soil Mech. Found. Div.* 89, 37–62.
- Rowe, P.W., 1962. The Stress-Dilatancy Relation for Static Equilibrium of an Assembly of Particles in Contact. *Proc. R. Soc. Lond. Ser. Math. Phys. Sci.* 269, 500–527. <https://doi.org/10.1098/rspa.1962.0193>
- Rowe, P.W., 1958. General report on papers in section 1, in: *Proceedings of the Brussels Conf. on Earth Pressure Problems, Brussels, Belgium.* pp. 25–30.

- Rowe, P.W., 1954. A Stress-Strain Theory for Cohesionless Soil with Applications to Earth Pressures at Rest and Moving Walls. *Géotechnique* 4, 70–88. <https://doi.org/10.1680/geot.1954.4.2.70>
- Sadrekarami, A., Olson, S.M., 2011. Critical State Friction Angle of Sands. *Geotech. Lond.* 61, 771–783. <https://doi.org/10.1680/geot.9.P.090>
- Sadrekarami, A., Olson, S.M., 2009. A New Ring Shear Device to Measure the Large Displacement Shearing Behavior of Sands. *Geotech. Test. J.* 32, 1–12. <https://doi.org/10.1520/GTJ101733>
- Santamarina, J.C., Cho, G.C., 2001. Determination of Critical State Parameters in Sandy Soils-Simple Procedure. *Geotech. Test. J.* 24, 185–192. <https://doi.org/10.1520/GTJ11338J>
- Santamarina, J.C., Shin, H., 2009. Friction in granular media. *Meso-Scale Shear Phys. Earthq. Landslide Mech.* CRC Press Lond. 157–188.
- Santana, T., Candeias, M., 2015. K₀ Measurement in a Sand Using Back Volume Change. *Soils Rocks* 38, 3–8.
- Senetakis, K., Coop, M., 2014. The Development of a New Micro-Mechanical Inter-Particle Loading Apparatus. *Geotech. Test. J.* 37, 1028–1039. <https://doi.org/10.1520/GTJ20120187>
- Senetakis, K., Coop, M.R., Todisco, M.C., 2013. The inter-particle coefficient of friction at the contacts of Leighton Buzzard sand quartz minerals. *Soils Found.* 53, 746–755. <https://doi.org/10.1016/j.sandf.2013.08.012>

- Senoon, A.A.A., 2013. Passive Earth Pressure Against Retaining Wall Using Log-spiral Arc. *J. Eng. Sci. Assiut Univ.* 41.
- Shamsabadi, A., Rollins, K.M., Kapuskar, M., 2007. Nonlinear Soil–abutment–bridge Structure Interaction for Seismic Performance-based Design. *J. Geotech. Geoenvironmental Eng.* 133, 707–720.
- Shen, C., Liu, S., 2018. Micromechanical Analysis of the At-Rest Lateral Pressure Coefficient of Granular Materials, in: Wu, W., Yu, H.-S. (Eds.), *Proceedings of China-Europe Conference on Geotechnical Engineering, Springer Series in Geomechanics and Geoengineering.* Springer International Publishing, Cham, pp. 207–210. https://doi.org/10.1007/978-3-319-97112-4_47
- Sherif, M.A., Fang, Y., Sherif, R.I., 1984. K_a and K_o Behind Rotating and Non-Yielding Walls. *J. Geotech. Eng.* 110, 41–56. [https://doi.org/10.1061/\(ASCE\)0733-9410\(1984\)110:1\(41\)](https://doi.org/10.1061/(ASCE)0733-9410(1984)110:1(41))
- Skempton, A.W., 1954. The Pore-Pressure Coefficients A and B. *Géotechnique* 4, 143–147.
- Sokolovskii, V.V., 1965. *Statics of Granular Media.* Pergamon, Oxford.
- Spangler, M.G., Handy, R.L., 1984. *Soil Engineering.* Harper & Row Publishers.
- Stevic, M., Jasarevic, I., Ramiz, F., 1979. Arching in Hanging Walls over Leached Deposits of Rock Salt, in: 4th ISRM Congress. International Society for Rock Mechanics and Rock Engineering.
- Stewart, J.P., Taciroglu, E., Wallace, J.W., Lemnitzer, A., Hilson, C.H., Nojoudi, A., Keowan, S., Nigbor, R.L., Salamanca, A., 2011. Nonlinear Load-deflection Behavior of Abutment

- Backwalls with Varying Height and Soil Density. (No. CA12-2040). California. Dept. of Transportation. Division of Research and Innovation.
- Stroud, M.A., 1988. The Standard Penetration Test - its Application and Interpretation, in: Penetration Testing in the UK. Proceedings of the Geotechnology Conference, Birmingham, U.K. Institution of Civil Engineers. Presented at the Thomas Telford, London, U.K., pp. 29–49.
- Sun, Y., Song, E., 2016. Active Earth Pressure Analysis Based on Normal Stress Distribution Function Along Failure Surface in Soil Obeying Nonlinear Failure Criterion. *Acta Geotech.* 11, 255–268. <https://doi.org/10.1007/s11440-015-0390-z>
- Szypcio, Z., 2017. Stress-Dilatancy for Soils. Part III: Experimental Validation for the Biaxial Condition. *Stud. Geotech. Mech.* 39, 73–80. <https://doi.org/10.1515/sgem-2017-0007>
- Tatsuoka, F., 1976. Stress-Dilatancy Relations of Anisotropic Sands in Three Dimensional Stress Condition. *Soils Found.* 16, 1–18. https://doi.org/10.3208/sandf1972.16.2_1
- Tatsuoka, F., Sakamoto, M., Kawamura, T., Fukushima, T.B.S., 1986. Strength and Deformation Characteristics of Sand in Plane Strain Compression at Extremely Low Pressures. *Soils Found* 26, 65–84. <https://doi.org/10.3208/sandf1972.26.65>
- Taylor, D.W., 1948. 1948, *Fundamentals of soil mechanics*. Wiley, New York.
- Terzaghi, K., 1943. *Theoretical Soil Mechanics*. JohnWiley & Sons, Inc. <https://doi.org/10.1002/9780470172766>

- Terzaghi, K., 1923. Discussion of Lateral Earth Pressure: The Accurate Experimental Determination of the Lateral Earth Pressure, together with a Resume of Previous Experiments. *Trans. Am. Soc. Civ. Eng.* 86, 1525–1543.
- Terzaghi, K., 1920. Old Earth Pressure Theories and New Test Results. *Eng. News Rec.* 85, 632–637.
- Terzaghi, K., Peck, R.B., Mesri, G., 1996. *Soil Mechanics in Engineering Practice*. John Wiley & Sons, Inc.
- Tsagareli, Z.V., 1965. Experimental Investigation of the Pressure of a Loose Medium on Retaining Walls with a Vertical Back face and Horizontal Backfill Surface. *Soil Mech. Found. Eng.* 2, 197–200. <https://doi.org/10.1007/BF01706095>
- Tyrrell, J.W.G., Cleaver, J.A.S., 2001. Development of an instrument for measuring inter-particle forces. *Adv. Powder Technol.* 12, 1–15. <https://doi.org/10.1163/156855201744895>
- Uchida, S., Xie, X.-G., Leung, Y.F., 2016. Role of Critical State Framework in Understanding Geomechanical Behavior of Methane Hydrate-Bearing Sediments. *J. Geophys. Res. Solid Earth* 121, 5580–5595. <https://doi.org/10.1002/2016JB012967>
- Vakili, R., 2015. *Load Sharing Mechanism of Piled-Raft Foundation in Sand* (PhD Thesis). Concordia University.
- Vosler, G., 2006. Coefficient of static friction (slide angle) of packaging and packaging materials (including shipping sack papers, corrugated and solid fiberboard; inclined plane method)

- [WWW Document]. TAPPI Web Site. URL <http://www.tappi.org/content/sarg/t815.pdf> (accessed 6.22.20).
- Walker, D.M., 1966. An Approximate Theory for Pressures and Arching in Hoppers. *Chem. Eng. Sci.* 21, 975–997.
- Wan, R.G., Guo, P.J., 2004. Stress Dilatancy and Fabric Dependencies on Sand Behavior. *J. Eng. Mech.* 130, 635–645. [https://doi.org/10.1061/\(ASCE\)0733-9399\(2004\)130:6\(635\)](https://doi.org/10.1061/(ASCE)0733-9399(2004)130:6(635))
- Wroth, C.P., 1972a. General Theories of Earth Pressure and Deformation, in: *Proceedings of 5th European Conference on Soil Mechanics and Foundation Engineering*. pp. 33–52.
- Wroth, C.P., 1972b. General theories of earth pressure and deformation, in: *Proceedings of 5th European Conference on Soil Mechanics and Foundation Engineering*. pp. 33–52.
- Wu, A., Sun, Y., 2008. *Granular Dynamic Theory and its Applications*, 1st ed. Springer-Verlag Berlin Heidelberg, Beijing.
- Xiang-Song, L., Defalias, Y.F., Zhi-Liang, W., 1999. State-Dependent Dilatancy in Critical-State Constitutive Modelling of Sand. *Can. Geotech. J. Ott.* 36, 599–611.
- Xinggao, L., Weining, L., 2010. Study on the action of the active earth pressure by variational limit equilibrium method. *Int. J. Numer. Anal. Methods Geomech.* 34, 991–1008. <https://doi.org/10.1002/nag.840>
- Yang, M., Tang, X., Wu, Z., 2020. Slip Surface and Active Earth Pressure of Cohesionless Narrow Backfill behind Rigid Retaining Walls under Translation Movement Mode. *Int. J. Geomech.* 20, 04020115. [https://doi.org/10.1061/\(ASCE\)GM.1943-5622.0001746](https://doi.org/10.1061/(ASCE)GM.1943-5622.0001746)

Zhao, X., Zhou, G., Tian, Q., Kuang, L., 2010. Coefficient of Earth Pressure At Rest for Normal, Consolidated soils. *Min. Sci. Technol.* 20, 406–410. [https://doi.org/10.1016/S1674-5264\(09\)60216-7](https://doi.org/10.1016/S1674-5264(09)60216-7)

Zhou, Y.C., Xu, B.H., Yu, A.B., Zulli, P., 2002. An Experimental and Numerical Study of the Angle of Repose of Coarse Spheres. *Powder Technol.* 125, 45–54. [https://doi.org/10.1016/S0032-5910\(01\)00520-4](https://doi.org/10.1016/S0032-5910(01)00520-4)

Appendices

Appendix A Critical Review of the Empirical K_0 Since (Jaky, 1944).

This is a critical review of Jaky’s derivation for the at-rest lateral earth pressure coefficient for normally consolidated soil deposits K_0 . This analysis is based on the translation from Hungarian done by (Diaz-Segura, 2016) of the original paper. Jaky started by defining the stress state of a soil element pertaining to an infinite horizon as illustrated in Fig. A-1.

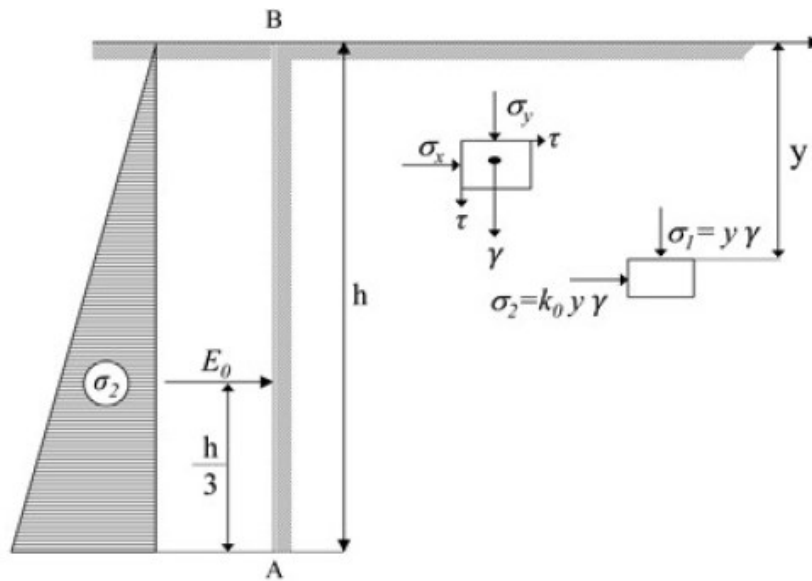


Fig. A-1 Stress state in a mass of earth of infinite horizontal extension taken from (Diaz-Segura, 2016)

Then Jaky invokes the geometric model of a pile of sand as shown in Fig. A-2. On this model Jaky assumes that the angle of the pile or angle of repose is the same angle of shearing resistance of the soil. Additionally, Jaky establishes that the lateral stress acting on the line \overline{OC} is necessarily defined by the at-rest coefficient of lateral earth pressure and consequently is a function of the angle of shearing resistance of the soil.

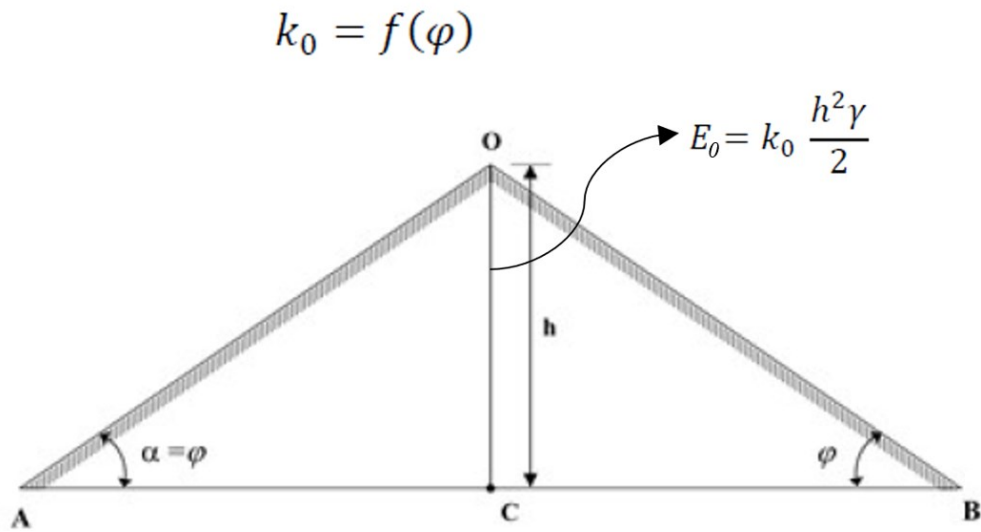


Fig. A-2 Model of a pile of granular soil assumed by (Jaky, 1944) taken from (Diaz-Segura, 2016)

Jaky continues by assuming that this pile of sand can be divided in two zones, a plastic zone labeled as (I) and an elastic zone labeled as (II), see Fig. A-3. However, the author does not provide physical experimental evidence of those two zones within a pile of granular material standing at rest. In addition, Jaky assumes that the line \overline{OB} that separates these two zones is the same planar failure surface for the active state according to (Rankine, 1857) which is assumed to cross through the apex of the pile of sand (or point O). The slip lines within the zone (I) or plastic zone are assumed to be parallel to the pile face. The blue point labeled with the number “1” represents any point along the line \overline{OB} . Jaky uses this adjoining point “1” to derive his expression for K_0 . Basically, Jaky develops an expression for the horizontal stress $\sigma_{x,I-I}$ from the zone (I) on the point “1” and another expression for the horizontal stress $\sigma_{x,I-II}$ on the same point “1” but from the zone

(II). Then, to guaranty equilibrium at the point “1”, Jaky equals these two expressions and simplifies until obtains his expression for K_0 as publish in (Jaky, 1944).

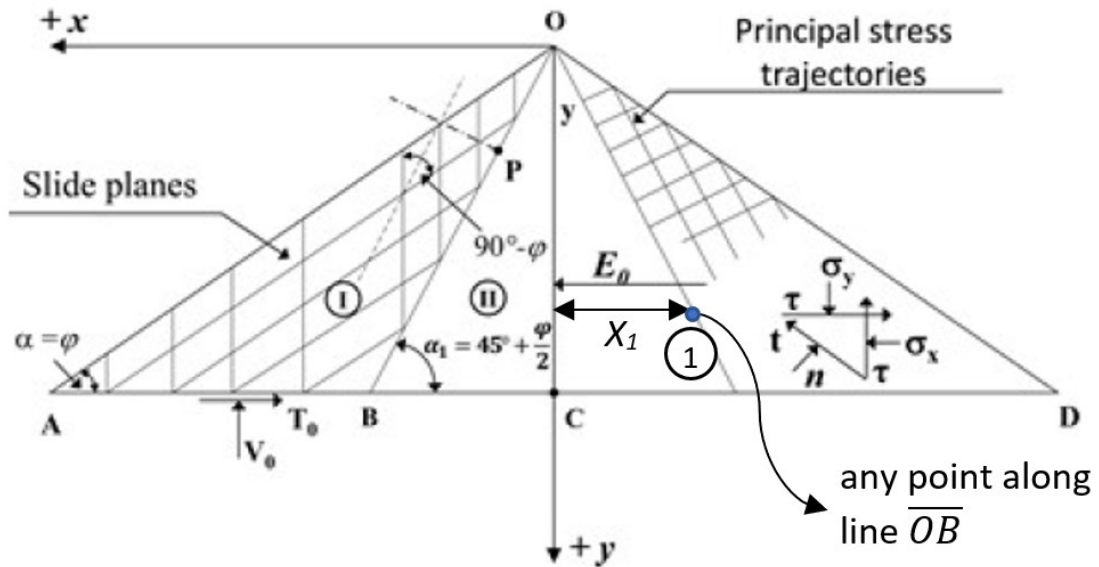


Fig. A-3 Slide planes in a motionless mass of earth taken from (Diaz-Segura, 2016)

From the simplified and assumed geometry for the pile of sand and the “plastic zone” or zone I shown in Fig. A-4 and from the stress state defined by Jaky in Fig. A-3 within zone I, it follows the next stress definitions at the point “1” but from the zone I:

The normal force n in Eq. (A-2) and the shear force action on the assumed slip shear planes t in Eq. (A-2).

Normal force:
$$n = X_1 \cdot \gamma \tag{A-1}$$

Shear force on slip plane:
$$t = n \cdot \tan \phi'$$

$$t = X_1 \cdot \gamma \cdot \tan \phi' \quad (\text{A-2})$$

From the stresses state in Fig. A-3 and by replacing Eq. (A-2) the shear stress can be defined as in Eq. (A-3):

$$\cos \phi' = \frac{\tau}{t}$$

$$\tau = t \cdot \cos \phi'$$

$$\tau_1 = X_1 \cdot \gamma \cdot \sin \phi' \quad (\text{A-3})$$

Now, by using Eq. (A-3), the horizontal stress at point “1” can be then defined with Eq. (A-4):

$$\tan \phi' = \frac{\tau}{\sigma_x}$$

$$\sigma_{x,1} = \tau_1 \cdot \cot \phi'$$

$$\sigma_{x,1} = X_1 \cdot \gamma \cdot \cos \phi' \quad (\text{A-4})$$

From the geometry presented in Fig. A-4 we can determine the distance X_1 to be given by Eq. (A-5):

$$X_1 = y \cdot \tan \left(45^\circ - \frac{\phi'}{2} \right) \quad (\text{A-5})$$

Now, by replacing Eq. (A-5) into Eq. (A-4), the horizontal stress at point “1” can be rewritten as in Eq. (A-6):

$$\sigma_{x,1} = y \cdot \gamma \cdot \tan\left(45^\circ - \frac{\phi'}{2}\right) \cdot \cos \phi' \quad (\text{A-6})$$

To further simplify Eq. (A-6) the term $\tan(45^\circ - \phi'/2)$ can be redefined with the angle Ψ as presented in Eqs. (A-7) and (A-8):

$$\Psi = \left(45^\circ - \frac{\phi'}{2}\right) \quad (\text{A-7})$$

$$\sigma_{x,1} = y \cdot \gamma \cdot \tan \Psi \cdot \cos \phi' \quad (\text{A-8})$$

Now, for the isolated term $\tan \Psi$ and from the double-angle identity for the tangent function we know Eq. (A-9):

$$\tan(2\Psi) = \frac{2 \cdot \tan \Psi}{1 - \tan^2 \Psi} \quad (\text{A-9})$$

By rearranging Eq. (A-9) is possible to obtain the following expression Eq. (A-10) for the term $\tan \Psi$:

$$\tan \Psi = \frac{\tan(2\Psi) \cdot (1 - \tan^2 \Psi)}{2} \quad (\text{A-10})$$

Now we can put Eq. (A-10) in terms ϕ' .

The term $\tan(2\Psi)$ in the numerator of Eq. (A-10) becomes $\cot \phi'$ after applying the co-function identity $\tan(\theta) = \cot(90^\circ - \theta)$ where $\theta = 2\Psi$; and replacing the expression of Ψ previously defined in Eq. (A-7); as explained in detail as follows:

$$\tan(2\Psi) = \cot(90^\circ - (2\Psi))$$

$$\tan(2\Psi) = \cot\left(90^\circ - 2 \cdot \left(45^\circ - \frac{\phi'}{2}\right)\right)$$

$$\tan(2\Psi) = \cot(\phi') \tag{A-11}$$

Accordingly, Eq. (A-10) can be then rewritten as in Eq. (A-12) after replacing previous equality in Eq. (A-11):

$$\tan \Psi = \frac{\cot(\phi') \cdot (1 - \tan^2 \Psi)}{2} \tag{A-12}$$

As demonstrated in the *Appendix B*, the term $\tan^2(\Psi)$ is identical to the term $((1 - \sin \phi') / (1 + \sin \phi'))$, so by using this identity in Eq. (A-12) follows:

$$\tan \Psi = \frac{\cot(\phi') \cdot \left(1 - \frac{1 - \sin \phi'}{1 + \sin \phi'}\right)}{2} \tag{A-13}$$

Resuming, Eq. (A-12) can be replaced by the term $\tan \Psi$ in Eq. (A-8) to obtain the new Eq. (A-14) for the horizontal stress at point “1”:

$$\sigma_{x,1} = \gamma \cdot y \cdot \frac{\cot(\phi') \cdot \left(1 - \frac{1 - \sin \phi'}{1 + \sin \phi'}\right)}{2} \cdot \cos \phi' \tag{A-14}$$

Finally, by simplifying Eq. (A-14) we can obtain the shorter expression in Eq. (A-15):

$$\sigma_{x,1} = y \cdot \gamma \cdot \frac{\cot(\varnothing') \cdot \cos \varnothing' \cdot \left(1 - \frac{1 - \sin \varnothing'}{1 + \sin \varnothing'}\right)}{2}$$

$$\sigma_{x,1} = y \cdot \gamma \cdot \frac{\cot(\varnothing') \cdot \cos \varnothing' \cdot \left(\frac{1 + \sin \varnothing' - 1 + \sin \varnothing'}{1 + \sin \varnothing'}\right)}{2}$$

$$\sigma_{x,1} = y \cdot \gamma \cdot \frac{\cot(\varnothing') \cdot \cos \varnothing' \cdot \left(\frac{2 \cdot \sin \varnothing'}{1 + \sin \varnothing'}\right)}{2}$$

$$\sigma_{x,1} = y \cdot \gamma \cdot \frac{\cos^2 \varnothing'}{1 + \sin \varnothing'}$$

$$\sigma_{x,1} = y \cdot \gamma \cdot \frac{1 - \sin^2 \varnothing'}{1 + \sin \varnothing'}$$

$$\sigma_{x,1} = y \cdot \gamma \cdot \frac{(1 + \sin \varnothing')(1 - \sin \varnothing')}{1 + \sin \varnothing'}$$

$$\sigma_{x,1} = y \cdot \gamma \cdot (1 - \sin \varnothing') \tag{A-15}$$

As derived above, Eq. (A-15) represents the horizontal stress associated to the stress-state defined for the “plastic zone” (i.e., zone I); accordingly, the stress $\sigma_{x,1}$ can be further denoted as $\sigma_{x,1-I}$ as presented in Eq. (A-16):

$$\sigma_{x,1-I} = y \cdot \gamma \cdot (1 - \sin \varnothing') \tag{A-16}$$

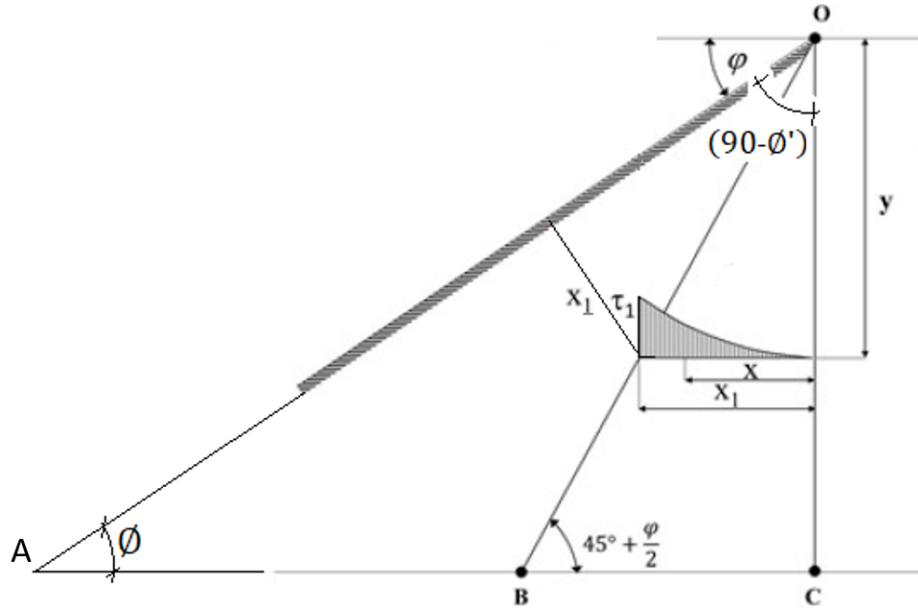


Fig. A-4 Geometry properties and arbitrary assumption of the shear stress distribution within the zone II, figure adopted from (Diaz-Segura, 2016).

From Fig. A-4 should be noticed that the angle $\angle BOC$ is equal than $\angle AOC/2$ via the geometric assumptions previously commented, namely: (i) the angle of repose of the pile is the same angle of shearing resistance $\beta = \phi'$; and (ii) the angle $\angle OBC$ has the same inclination as the slip-failure surface in the active case according to (Rankine, 1857). In other words, the line \overline{OB} bisects the angle $\angle AOC$ and consequently the horizontal distance X_1 between the line \overline{OC} and the point “1” as shown in Fig. A-3 and Fig. A-4 is by geometry the same normal distance between the pile surface and the point “1”. Consequently, the normal force acting on the “slip lines” at the point “1” can be expressed as a direct function of the distance X_1 as presented in Eq. (A-1).

On the other side, for the so-called “elastic zone” or zone II, Jaky states: “Assuming that the variation of τ between \overline{OB} and \overline{OC} can be represented as a second order parabolic function in terms of x ”, see Eq. (A-17). However, the previous constitutes an additional arbitrary assumption since there is none experimental, analytical, or numerical evidence proving the shear stress distribution within zone I is governed by the expression Eq. (A-17).

$$\tau = \tau_1 \cdot \left(\frac{x^2}{X_1^2} \right) \quad (\text{A-17})$$

By replacing the shear stress previously define by Eq. (A-3) at the point “1” in Eq. (A-17) follows Eq. (A-18):

$$\tau = \frac{(X_1 \cdot \gamma \cdot \sin \phi') \cdot x^2}{X_1^2} \quad (\text{A-18})$$

From the geometry shown in Fig. A-4 is possible to derive $X_1 = y \tan(45 - \phi'/2)$; thus, by replacing this into Eq. (A-18) yields:

$$\tau = \frac{\left(y \cdot \tan \left(45^\circ - \frac{\phi'}{2} \right) \cdot \gamma \cdot \sin \phi' \right) \cdot x^2}{y^2 \cdot \tan^2 \left(45^\circ - \frac{\phi'}{2} \right)}$$

By simplifying the previous expression, the shear stress in Zone II becomes Eq. (A-19):

$$\tau = \frac{x^2}{y} \cdot \gamma \cdot \sin \phi' \cdot \tan \left(45^\circ + \frac{\phi'}{2} \right) \quad (\text{A-19})$$

Then Jaky invokes the Cauchy Eq. (A-20) based in the fact that for an infinite mass of earth the directions of the principal stresses are vertical and horizontal.

$$\left. \begin{aligned} \frac{\partial \sigma_y}{\partial y} + \frac{\partial \tau}{\partial x} &= \gamma \\ \frac{\partial \sigma_x}{\partial x} + \frac{\partial \tau}{\partial y} &= 0 \end{aligned} \right\} \quad (\text{A-20})$$

Now, by replacing Eq. (A-19) in Eq. (A-20) and solving for the horizontal stress we have:

$$\frac{d\sigma_x}{dx} = -\frac{d\tau}{dy} = \frac{x^2}{y^2} \cdot \gamma \cdot \sin \phi' \cdot \tan \left(45^\circ + \frac{\phi'}{2} \right)$$

By integrating the previous it follows:

$$\sigma_x = \frac{x^3}{3 \cdot y^2} \cdot \gamma \cdot \sin \phi' \cdot \tan \left(45^\circ + \frac{\phi'}{2} \right) + C$$

For $x = 0$, the boundary condition on the line \overline{OC} forces the constant of integration C to be the same at-rest horizontal stress $\sigma_{x,0}$ (see Fig. A-2). Thus, by replacing this constant of integration in the previous expression; and reading the horizontal stress on the boundary \overline{OB} , that is $\sigma_{x,1-II}(X_1)$; yields Eq. (A-21) which is the horizontal stress associated to the stress-state defined for the “elastic zone” (i.e., zone II) at the point “1”:

$$\sigma_{x,1-II} = \frac{X_1^3}{3 \cdot y^2} \cdot \gamma \cdot \sin \phi' \cdot \tan \left(45^\circ + \frac{\phi'}{2} \right) + \sigma_{x,0} \quad (\text{A-21})$$

After having the horizontal stress at point “1” derived from zone I [i.e., $\sigma_{x,1-I}$ given in Eq. (A-16)] and the horizontal stress at point “1” derived from zone II [i.e., $\sigma_{x,1-II}$ given in Eq. (A-21)] is possible to establish the equilibrium of horizontal stresses at the point “1” indicated by Eq. (A-22):

$$\sigma_{x,1-I} = \sigma_{x,1-II} \quad (\text{A-22})$$

Accordingly, after replacing both sides of Eq. (A-22) follows:

$$y \cdot \gamma \cdot (1 - \sin \phi') = \frac{X_1^3}{3 \cdot y^2} \cdot \gamma \cdot \sin \phi' \cdot \tan \left(45^\circ + \frac{\phi'}{2} \right) + \sigma_{x,0}$$

Now, by replacing $X_1 = y \tan(45 - \phi'/2)$ as previously explained and defined from the geometry shown in Fig. A-4, the previous expression becomes:

$$y \cdot \gamma \cdot (1 - \sin \phi') = \frac{y^3 \cdot \tan^3 \left(45^\circ - \frac{\phi'}{2} \right)}{3 \cdot y^2} \cdot \gamma \cdot \sin \phi' \cdot \tan \left(45^\circ + \frac{\phi'}{2} \right) + \sigma_{x,0}$$

Now simplifying the previous and clearing for at-rest lateral earth pressure $\sigma_{x,0}$ follows:

$$\sigma_{x,0} = y \cdot \gamma \cdot \left((1 - \sin \phi') - \frac{\left(\frac{1 - \sin \phi'}{1 + \sin \phi'} \right) \cdot \sin \phi'}{3} \right)$$

$$\sigma_{x,0} = y \cdot \gamma \cdot (1 - \sin \phi') \cdot \left(1 - \frac{\left(\frac{\sin \phi'}{1 + \sin \phi'} \right)}{3} \right)$$

$$\sigma_{x,0} = y \cdot \gamma \cdot (1 - \sin \phi') \cdot \left(\frac{3 + 2 \cdot \sin \phi'}{3 + 3 \cdot \sin \phi'} \right)$$

$$\sigma_{x,0} = y \cdot \gamma \cdot (1 - \sin \phi') \cdot \left(\frac{1 + \frac{2}{3} \cdot \sin \phi'}{1 + \sin \phi'} \right) \quad (\text{A-23})$$

By fundamental definition we know that $K_0 = \sigma_{x,0}/\sigma_{y,0}$; where: $\sigma_{y,0} = \gamma y$. Consequently, after reading Eq. (A-23) in the context of this fundamental definition, the at-rest lateral earth pressure coefficient K_0 is given by Eq. (A-24) as it was originally published in (Jaky, 1944). Then, in 1948 Jaky published the popular simplified form for K_0 presented in Eq. (A-25) after removing the right factor from Eq. (A-24), see (Jaky, 1948). Neither derivation nor explanation was presented to support this simplification other than the short form (A-25) better matches empirical results.

$$K_0 = (1 - \sin \phi') \cdot \left(\frac{1 + \frac{2}{3} \cdot \sin \phi'}{1 + \sin \phi'} \right) \quad (\text{A-24})$$

$$K_0 = (1 - \sin \phi') \quad (\text{A-25})$$

In conclusion, the most widely used expression for the at-rest lateral earth pressure in normally consolidated soil deposits or Eq. (A-25) is controversial since it is a simplified version of the

originally derived Eq. (A-24). This simplified form (A-25) differs by about +/-10% from the originally derived Eq. (A-24), the one having an explicit derivation. However, the original Eq. (A-24) could also be considered controversial because it is based on many arbitrary assumptions lacking phenomenological link or permitting parallel interpretations and solutions other than Eqs. (A-24) or (A-25).

Appendix B Proof of Coincidence Between Common Solutions According to (Coulomb, 1776) and (Rankine, 1857).

For the most general case of a vertical retaining wall ($\Theta = 0^\circ$) with horizontal backfill ($\alpha = 0^\circ$) and frictionless soil-structure interface ($\delta' = 0^\circ$), the theoretical solutions according to (Coulomb, 1776) and (Rankine, 1857) are identical solutions. This can be demonstrated by applying trigonometry as shown below for the following identity for passive state:

$$K_p = \tan^2 \left(45^\circ + \frac{\phi'}{2} \right) \equiv \frac{1 + \sin \phi'}{1 - \sin \phi'}$$

By applying the known identity for the *tangent of the addition of two angles* in the square tangent side which is the K_p according to Rankine (i.e., left side of the identity), we get:

$$\left(\frac{\tan 45^\circ + \tan(\phi'/2)}{1 - \tan 45^\circ \cdot \tan(\phi'/2)} \right)^2 = \left(\frac{1 + \tan(\phi'/2)}{1 - \tan(\phi'/2)} \right)^2 \equiv \frac{1 + \sin \phi'}{1 - \sin \phi'}$$

Now, by applying the *tangent of half-angle identity* in the term “ $\tan(\phi'/2)$ ”, it follows:

$$\left(\frac{1 + \sqrt{\frac{1 - \cos \phi'}{1 + \cos \phi'}}}{1 - \sqrt{\frac{1 - \cos \phi'}{1 + \cos \phi'}}} \right)^2 \equiv \frac{1 + \sin \phi'}{1 - \sin \phi'}$$

Then, by solving the square binomials and multiplying the two parts of the fraction within the square root by the term $(1 + \cos \phi')$ we get:

$$\frac{1 + 2 \sqrt{\frac{(1 - \cos \varphi')(1 + \cos \varphi')}{(1 + \cos \varphi')(1 + \cos \varphi')} + \frac{1 - \cos \varphi'}{1 + \cos \varphi'}}{1 - 2 \sqrt{\frac{(1 - \cos \varphi')(1 + \cos \varphi')}{(1 + \cos \varphi')(1 + \cos \varphi')} + \frac{1 - \cos \varphi'}{1 + \cos \varphi'}} \equiv \frac{1 + \sin \varphi'}{1 - \sin \varphi'}$$

The previous can be further simplified as:

$$\frac{1 + 2 \sqrt{\frac{(1 - \cos^2 \varphi')}{(1 + \cos \varphi')^2} + \frac{1 - \cos \varphi'}{1 + \cos \varphi'}}{1 - 2 \sqrt{\frac{(1 - \cos^2 \varphi')}{(1 + \cos \varphi')^2} + \frac{1 - \cos \varphi'}{1 + \cos \varphi'}} \equiv \frac{1 + \sin \varphi'}{1 - \sin \varphi'}$$

Finally, applying the *Pythagorean identity* in the numerator within the square root and simplifying is possible to confirm the identity; that is, to obtain on the left side the same expression for K_p presented on the right side of the identity (i.e., K_p according to Coulomb):

$$\frac{1 + 2 \sqrt{\frac{\sin^2 \varphi'}{(1 + \cos \varphi')^2} + \frac{1 - \cos \varphi'}{1 + \cos \varphi'}}{1 - 2 \sqrt{\frac{\sin^2 \varphi'}{(1 + \cos \varphi')^2} + \frac{1 - \cos \varphi'}{1 + \cos \varphi'}} \equiv \frac{1 + \sin \varphi'}{1 - \sin \varphi'}$$

$$\frac{1 + 2 \frac{\sin \varphi'}{1 + \cos \varphi'} + \frac{1 - \cos \varphi'}{1 + \cos \varphi'}}{1 - 2 \frac{\sin \varphi'}{1 + \cos \varphi'} + \frac{1 - \cos \varphi'}{1 + \cos \varphi'}} \equiv \frac{1 + \sin \varphi'}{1 - \sin \varphi'}$$

$$\frac{1 + \cos \varphi' + 2 \cdot \sin \varphi' + 1 - \cos \varphi'}{1 + \cos \varphi' - 2 \cdot \sin \varphi' + 1 - \cos \varphi'} \equiv \frac{1 + \sin \varphi'}{1 - \sin \varphi'}$$

$$\frac{2 + 2 \cdot \sin \varphi'}{2 - 2 \cdot \sin \varphi'} \equiv \frac{1 + \sin \varphi'}{1 - \sin \varphi'}$$

$$\frac{1 + \sin \varphi'}{1 - \sin \varphi'} \equiv \frac{1 + \sin \varphi'}{1 - \sin \varphi'}$$

Appendix C Comparison of Lateral Earth Pressure Distribution and Slip-Failure Geometry Between Present Theory and Classical Theory According to (Coulomb, 1776) or (Rankine, 1857).

A simple retaining wall of 3.0 meters height is adopted here to perform a direct comparison between the present Theory and the “classical theory” according to (Coulomb, 1776) or (Rankine, 1857). This “classical theory” is to provide identical solutions given the most general case of a vertical retaining wall ($\theta = 0^\circ$) with horizontal backfill ($\alpha = 0^\circ$) and frictionless soil-structure interface ($\delta' = 0^\circ$) is also adopted for this comparison (see *Appendix B*). The arbitrary initial state friction angles (i.e., $\phi'_{cv,ps}$) selected to illustrate this comparison are 23° , 27° , 34° , 39° and 42° . These angles represent the five distinct soil behaviors previously identify and described in the numeral 7.4.1 for extensive/collapsible, extensive/dilative, compressive/contractive, compressive/dilative, and extensive/suction-dilative behavior, respectively. The governing frictional parameter for present theory is $\phi'_{cs,ps}$ while for the “classical theory” is its corresponding $\phi'_{cv,ps}$ as provided by Eq. (4-9).

The active state is illustrated with the figures Fig. C-1 to Fig. C-5 and the passive state with the figures Fig. C-6 to Fig. C-10. The figures are self-explanatory and reveal substantial differences between both approaches.

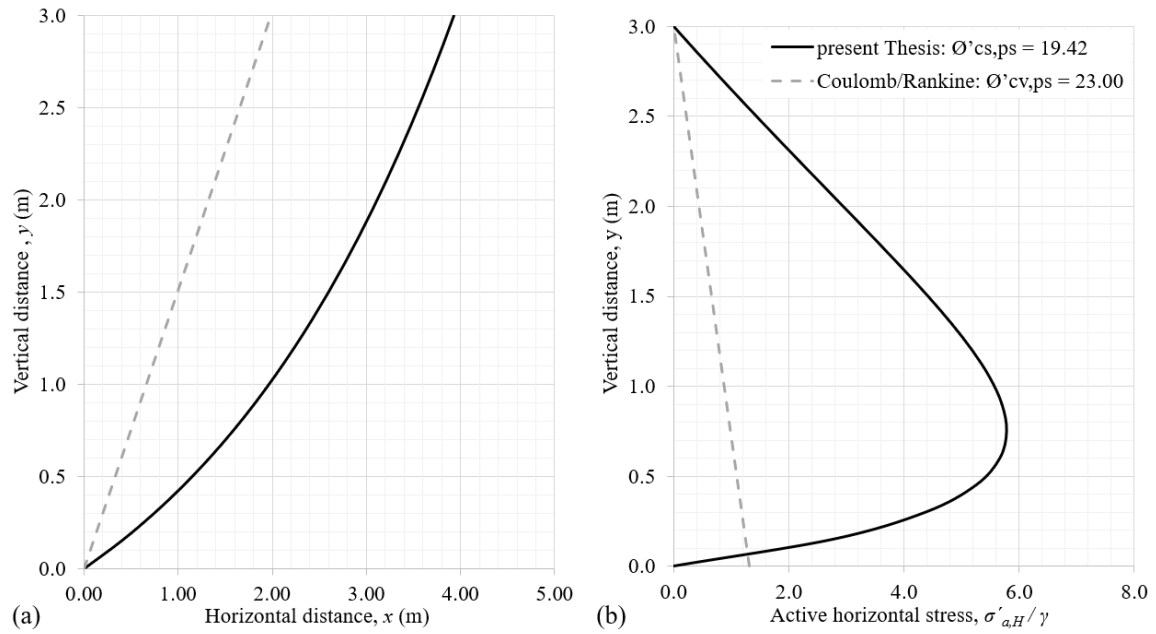


Fig. C-1 Active state characteristic curves for an extensive/collapsible cohesionless granular material: (a) slip-failure surface geometry; and (b) lateral earth pressure distribution.

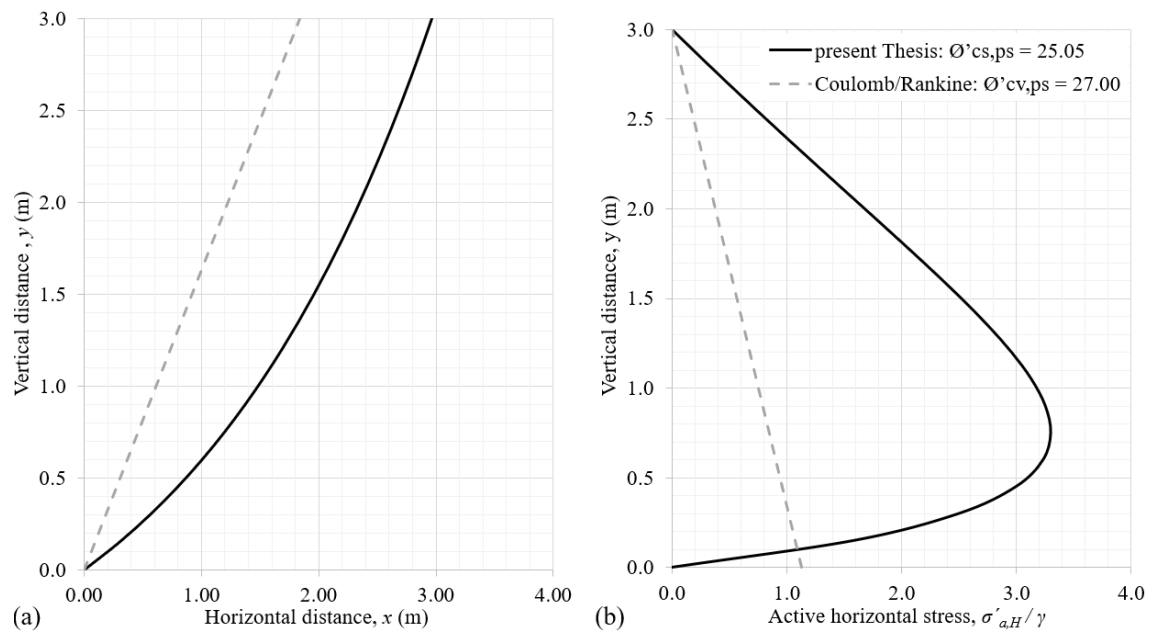


Fig. C-2 Active state characteristic curves for an extensive/dilative cohesionless granular material: (a) slip-failure surface geometry; and (b) lateral earth pressure distribution.

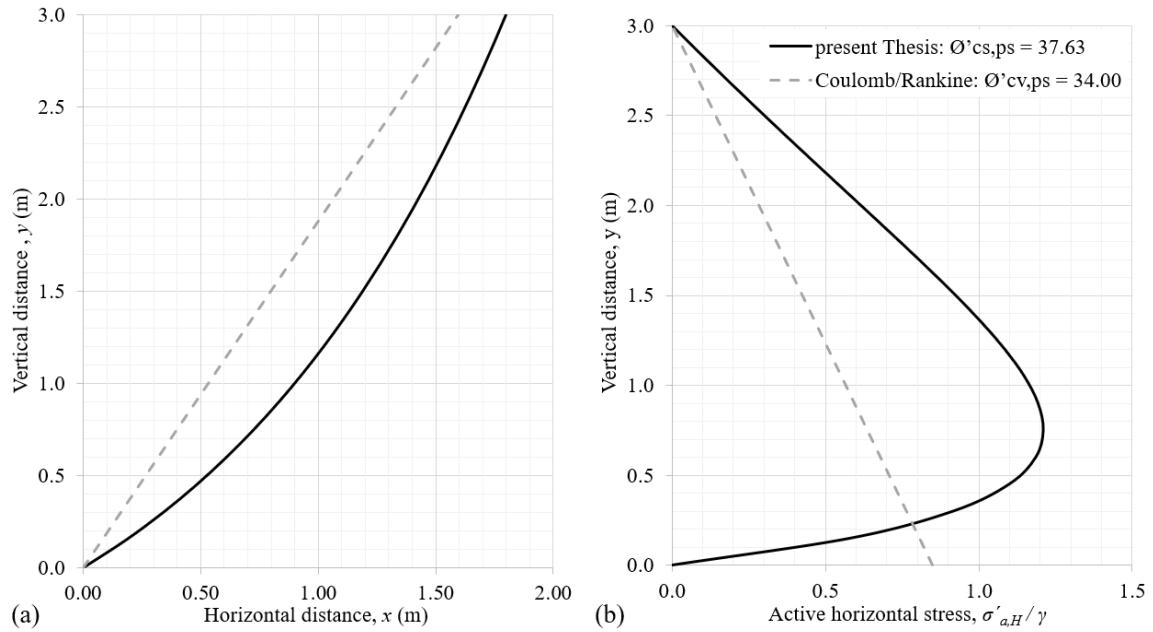


Fig. C-3 Active state characteristic curves for a compressive/contractive cohesionless granular material: (a) slip-failure surface geometry; and (b) lateral earth pressure distribution.

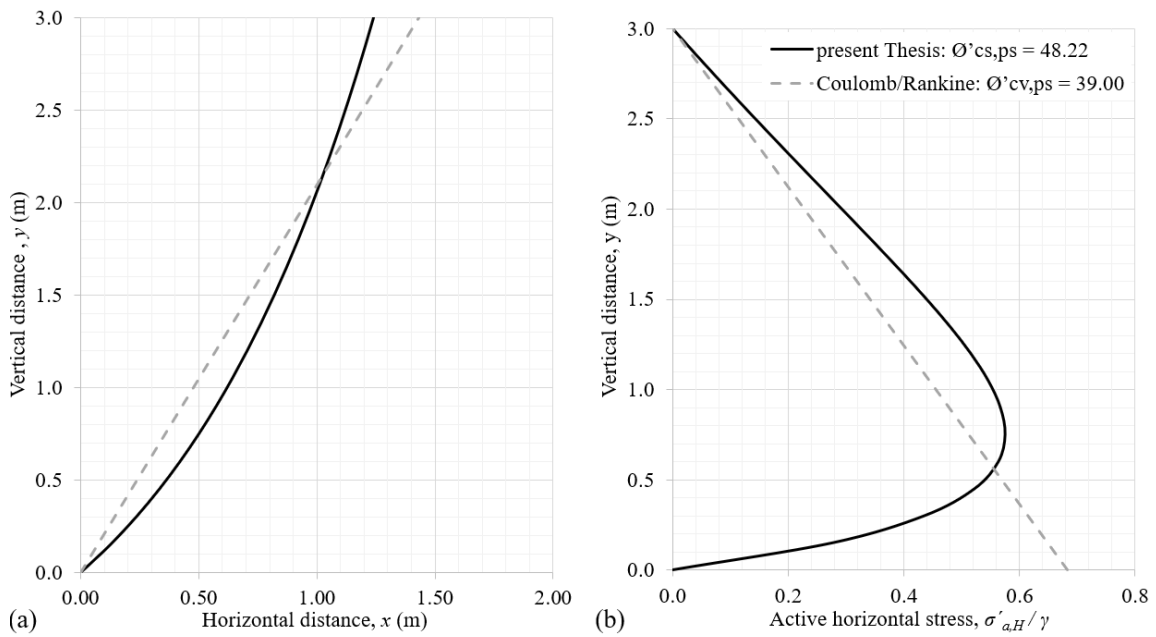


Fig. C-4 Active state characteristic curves for a compressive/dilative cohesionless granular material: (a) slip-failure surface geometry; and (b) lateral earth pressure distribution.

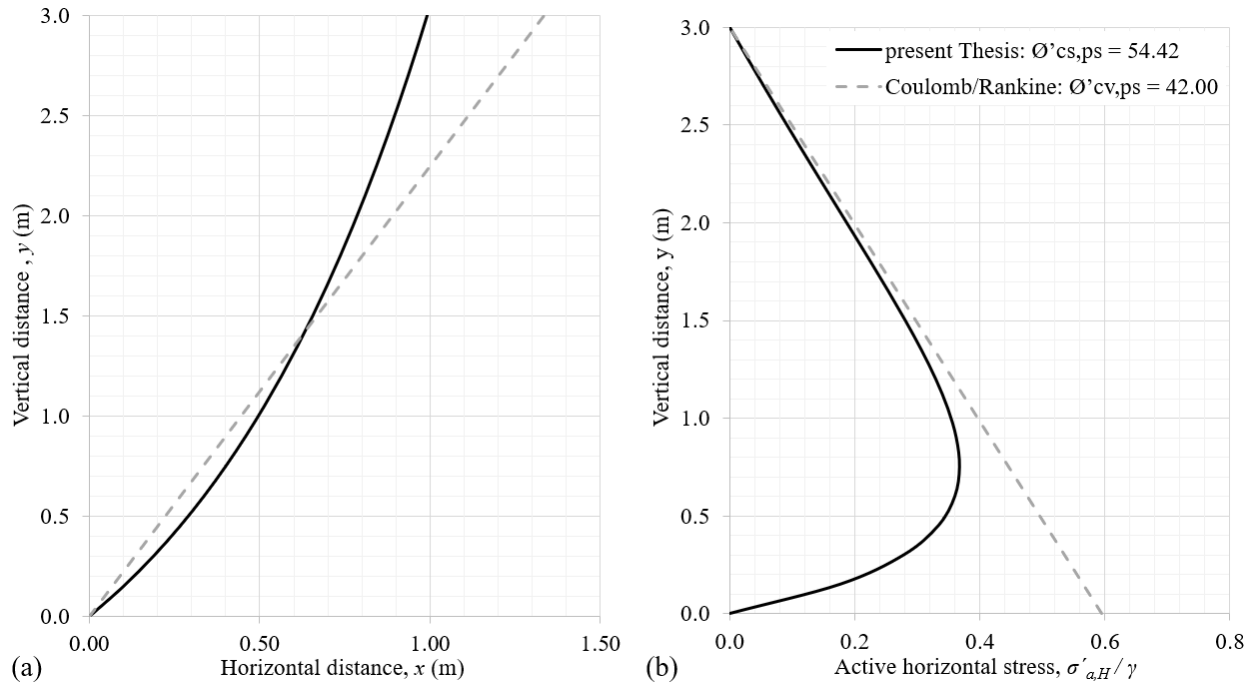


Fig. C-5 Active state characteristic curves for an extensive/suction-dilative cohesionless granular material: (a) slip-failure surface geometry; and (b) lateral earth pressure distribution.

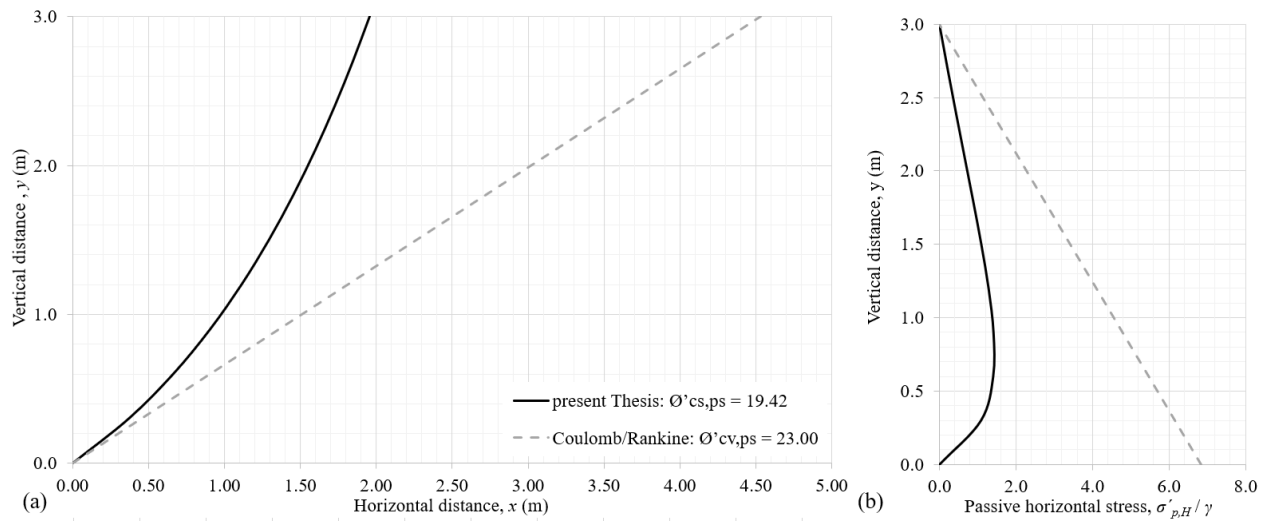


Fig. C-6 Passive state characteristic curves for an extensive/collapsible cohesionless granular material: (a) slip-failure surface geometry; and (b) lateral earth pressure distribution.

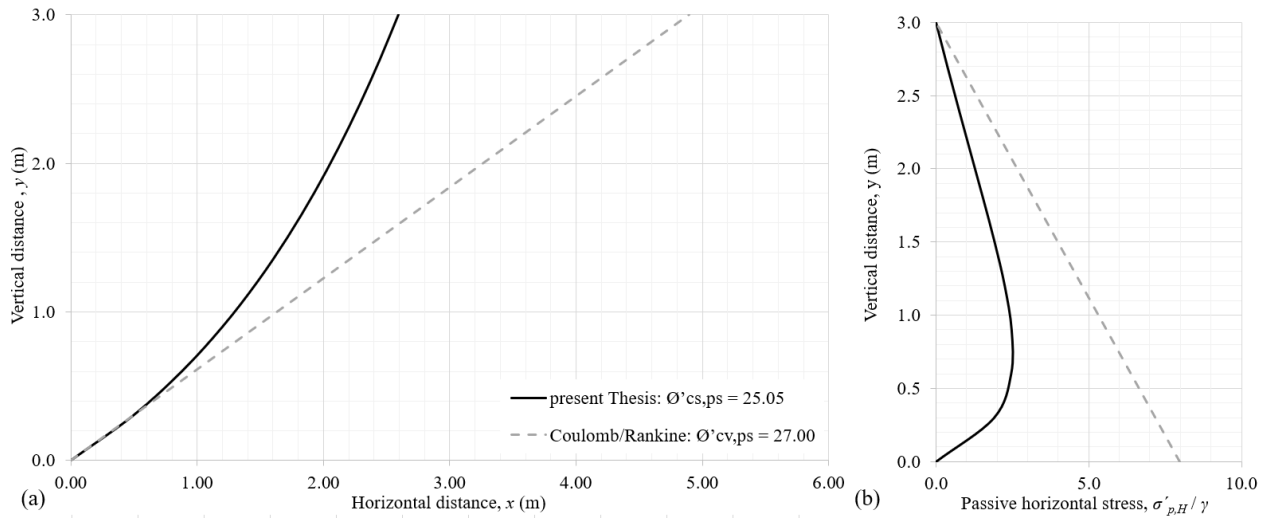


Fig. C-7 Passive state characteristic curves for an extensive/dilative cohesionless granular material: (a) slip-failure surface geometry; and (b) lateral earth pressure distribution.

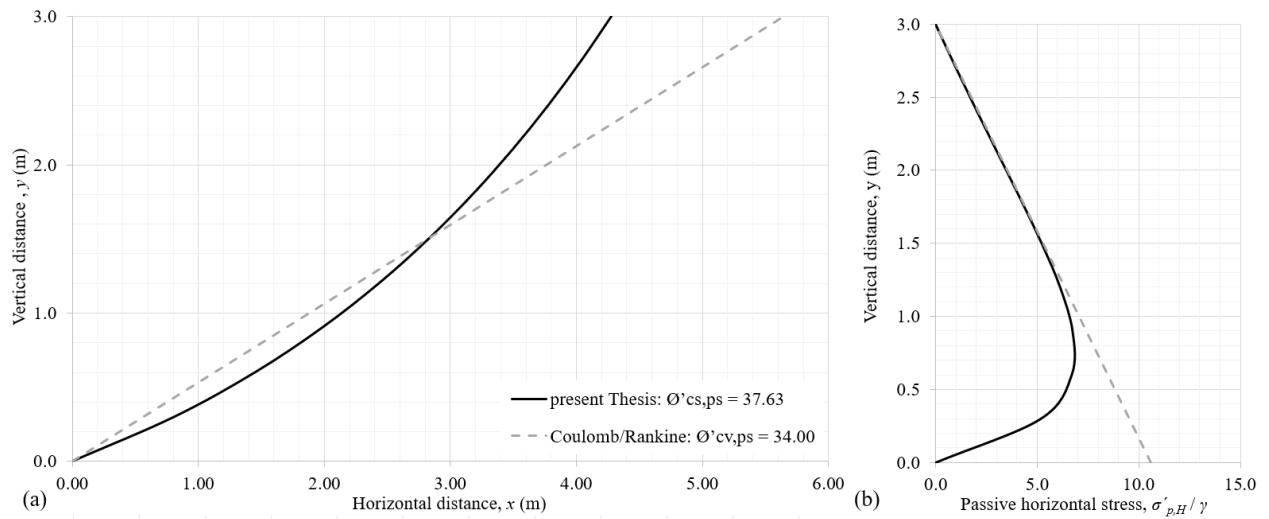


Fig. C-8 Passive state characteristic curves for a compressive/contractive cohesionless granular material: (a) slip-failure surface geometry; and (b) lateral earth pressure distribution.

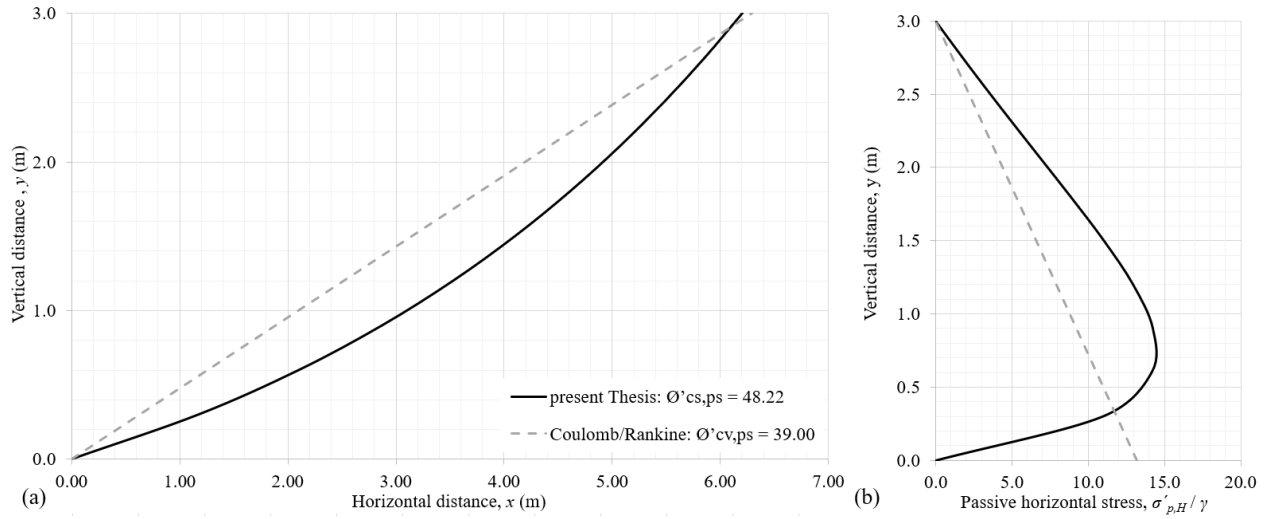


Fig. C-9 Passive state characteristic curves for a compressive/dilative cohesionless granular material: (a) slip-failure surface geometry; and (b) lateral earth pressure distribution.

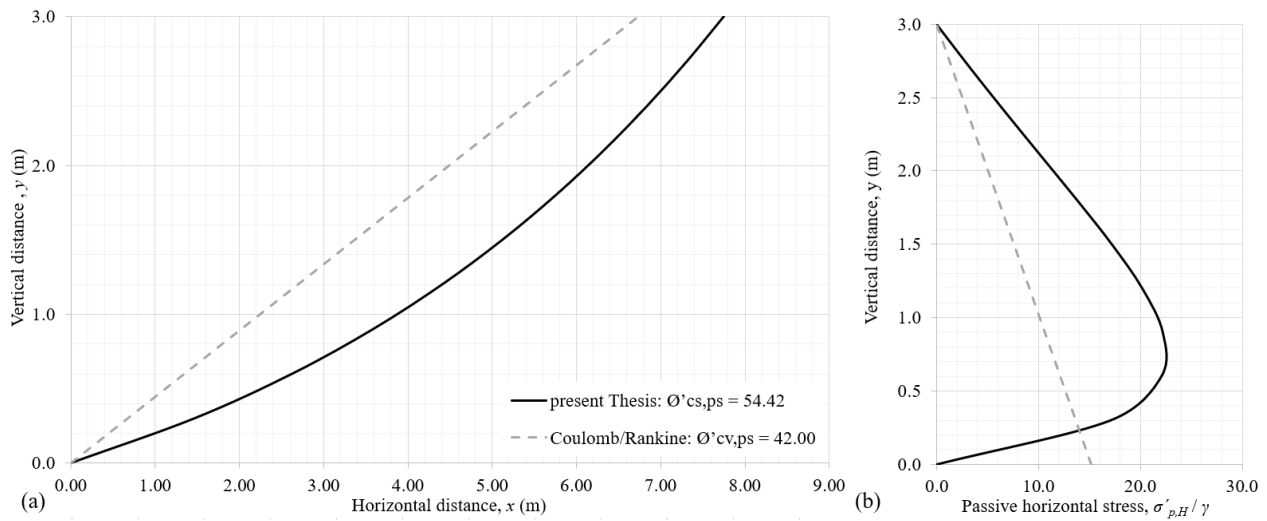


Fig. C-10 Passive state characteristic curves for an extensive/suction-dilative cohesionless granular material: (a) slip-failure surface geometry; and (b) lateral earth pressure distribution.

Appendix D Video Recording of the Plane-Strain Constant-Volume Friction Angle Tests.

The file “*Appendix D Video Recording of the Plane-Strain Constant-Volume Friction Angle Tests. MP4*” attached to present Thesis contains a video recording of 13’ and 49” duration presenting the tests developed to measure the initial state plane-strain constant-volume friction angle of the three granular materials under investigation, namely: silica sand, P50 sandpaper and UHMW polyethylene. These results are also presented in the numeral 3.3.3.1.

Appendix E Video Recording of the Plane-Strain Critical-State Friction Angle Tests.

The file “*Appendix E Video Recording of the Plane-Strain Critical-State Friction Angle Tests. MP4*” attached to present Thesis contains a video recording of 61’ and 26” duration presenting the tests developed to measure the final state plane-strain critical state friction angle of the three granular materials under investigation, namely: silica sand, P50 sandpaper and UHMW polyethylene. These results are also presented in the numeral 3.3.3.2.

Appendix F Video Recording of the Angle of Repose Tests in Silica Sand.

The file “*Appendix F Video Recording of the Angle of Repose Tests in Silica Sand. MP4*” attached to present Thesis contains a video recording of 19’ and 17” duration presenting the tests developed to measure the angle of repose in silica sand. These results are also presented in the numeral 3.3.4.

Appendix G Spreadsheet to Calculate $\sigma'_{v,max}$ from Experimental Results for K_{0-OC} .

The file “Appendix G Spreadsheet to Calculate $\sigma'_{v,max}$ from Experimental Results for K_{0-OC} . xlsx” attached to present Thesis contains all the calculations required to determine the maximum historic vertical stress $\sigma'_{v,max}$ associated to any given energy of compaction. The values presented in this spreadsheet correspond to the data processing of the experimental tests presented in the numeral 3.4.

All the formulas within the spreadsheet are properly labelled to correspond with the captions used within present Thesis for each equation, this to facilitate easy connection between the theory and practical applications. In addition, the spreadsheet contains instructions to properly identify inputs and outputs and where to perform numerical solution (i.e., the *Solver* function) to determine implicit values. Initially, as shown in the figures Fig. G-1 and Fig. G-2, the spreadsheet presents the inputs, the code of colors for each type of cell and the basic parameters and data processing for the silica sand and for the samples of silica sand.

	A	B	C	D	E	F	G	H	I	J
1	1) silica sand basic parameters (see numeral 3.2):									
2		silica sand	spheres							
3		n_{max}	0,46	0,476401224		Code of colors for cells:				
4		n_{min}	0,33	0,25951951		###	input from silica sand data set			
5		G_r	2,62			###	input from experimental/lab measurement			
6		γ_{max}	17,16	kN/m ³		###	calculation			
7		γ_{min}	13,98	kN/m ³			equation used for each calculation			
8		γ_w	9,81	kN/m ³		###	solver target			
9						###	output			
10										
11	2) model parameters for the four samples of silica sand:									
12										
13	case	Energy	Weight	Height	Volume, V_T	γ	V_s	e_e	$n_{c,sand}$	$n_{c,r}$
14		(kJ/m ³)	(gr)	(m)	(x 10 ⁻⁴ m ³)	(kN/m ³)	(x 10 ⁻⁴ m ³)		(%)	
15					$V = A * H$	$\gamma = \frac{W}{V}$	$V_s = \frac{W_s}{G_s \cdot \gamma_w}$	$e = \frac{V_T - V_s}{V_s}$	$n = \frac{e}{1 + e}$	Eq. (4-22)
16	non-compacted	N/A	524,41	0,040	3,24	15,86	2,00	0,620	38,28%	0,598
17	standard Proctor	590	517,52	0,039	3,16	16,05	1,98	0,601	37,53%	0,659
18	reduced modified Proctor	1346	556,57	0,041	3,32	16,42	2,12	0,565	36,09%	0,776
19	modified Proctor	2787	636,05	0,045	3,65	17,10	2,43	0,503	33,46%	0,990

Fig. G-1 Spreadsheet screenshot showing the inputs and initial data processing.

	A	B	C	D	K	L	M	N	O	P	Q	R
1	1) silica sand basic parameters (see numeral 3.2):											
2		silica sand	spheres									
3		n_{max}	0,46	0,476401224								
4		n_{min}	0,33	0,25951951								
5		G_s	2,62									
6		γ_{max}	17,16	kN/m ³								
7		γ_{min}	13,98	kN/m ³								
8		γ_w	9,81	kN/m ³								
9												
10												
11	2) model parameters for the four samples of silica sand:											
12												
13	case	Energy	Weight	Height	$n_{c,model}$	$D_{r,c,sand}$	A	n_c	solver target	$\theta'_{cv,ps}$	$\theta'_{cv,ps}$	K_θ
14		(kJ/m ³)	(gr)	(m)	(%)	(%)		(%)		(°)	(°)	
15					$n = \frac{e}{1+e}$	Eq. (4-23)	see numeral 3.2	Eq. (4-11)	(must be equal to 1)	solver result	Eq. (4-9)	Eq. (5-4)
16	non-compacted	N/A	524,41	0,040	34,66%	64,63%	0,97605	34,66%	1,00000	36,740	33,562	0,444
17	standard Proctor	590	517,52	0,039	33,34%	70,36%	0,97641	33,34%	1,00000	38,236	34,298	0,433
18	reduced modified Proctor	1346	556,57	0,041	30,81%	80,94%	0,97707	30,81%	1,00000	40,821	35,540	0,413
19	modified Proctor	2787	636,05	0,045	26,17%	99,16%	0,97822	26,17%	1,00000	44,829	37,420	0,385

Fig. G-2 Spreadsheet screenshot showing the inputs and initial data processing (continued).

Then, the spreadsheet continues by processing the lateral stresses obtained from the experimental investigation on the four tested samples, as it appears illustrated in the figures Fig. G-3 and Fig. G-4 for the standard Proctor instance.

	A	B	C	D	E	F	G	H	I	J
38	Experimental results									
39	step	$\sigma'_{v,\theta}$	voltage output from datalogger (V)			σ'_h (kPa)				$K_{\theta-oc}$
40	no.	(kPa)	PSR # 1	PSR # 2	PSR # 3	PSR # 1	PSR # 2	PSR # 3	average	
41						see calibration functions in numeral 3.4.2.2				Eq. (2-1)
42	0,0	24,1	4,42	4,39	4,42	18,10	18,23	18,41	18,25	0,758
43	1,0	21,3	4,34	4,32	4,29	16,98	17,28	16,39	16,88	0,792
44	2,0	18,6	4,18	4,18	4,15	15,08	15,61	14,65	15,11	0,814
45	3,0	15,8	3,89	4,14	4,05	12,60	15,18	13,64	13,81	0,876
46	4,0	13,0	3,76	3,77	3,76	11,81	12,09	11,57	11,82	0,907
47	5,0	10,1	2,90	3,23	3,22	9,09	9,61	9,72	9,47	0,941
48	6,0	7,4	1,76	2,29	2,40	6,95	7,78	8,09	7,60	1,031

Fig. G-3 Spreadsheet screenshot showing the cells and formulas to process the lateral stress.

	K	L	M	N	O	P	Q	R
38	Model calculations							relative error
39	$\theta'_{cs,p5,OCR}$	$\theta'_{cs,p5,OCR}$	$K_{\theta-OCR}$	$K_{\theta-OC}$	solver target	OCR	$\sigma'_{v,max}$	
40	(°)	(°)					(kPa)	
41	Eq. (5-10)	Eq. (5-11)	Eq. (5-8)	Eq. (5-7)	(must be equal to 1)	solver result	Eq. (5-14)	
42	9,253	10,658	0,705	0,758	1,00000	4,187	100,716	0,83%
43	7,934	9,146	0,726	0,792	1,00000	4,894	104,309	-2,71%
44	7,192	8,293	0,737	0,814	1,00000	5,406	100,382	1,16%
45	5,478	6,322	0,765	0,876	1,00000	7,112	112,164	-10,44%
46	4,796	5,536	0,777	0,907	1,00000	8,129	105,905	-4,28%
47	4,200	4,848	0,787	0,941	1,00000	9,289	93,497	7,94%
48	3,066	3,540	0,807	1,031	1,00000	12,735	93,943	7,50%
49						average (SD):	101.56 (6.63)	+/-7.0%

Fig. G-4 Spreadsheet screenshot showing the cells and formulas to process the lateral stress

(continued).

Appendix H Spreadsheet to Calculate Nonlinear Slip-Failure Surface and Lateral Stress Distribution Geometry.

The file “Appendix H Spreadsheet to Calculate Nonlinear Slip-Failure Surface and Lateral Stress Distribution Geometry. xls” attached to present Thesis contains all the calculations required to determine the nonlinear slip-failure surface geometry and its associated lateral earth pressure distribution as established in the Chapter 6:. From the input parameters wall height H and the $\phi'_{cs,ps}$ friction, the figure Fig. H-1 shows an instance of calculation for the slip-failure surface geometry in active and passive conditions. The equation used in the columns “B-D-F-H” to determine $y(m)$ is “=B7+(\$B\$3/33)”, basically the wall height was discretized in 34 points.

	A	B	C	D	E	F	G	H
3	H	12,00	H	12,00	H	12,00	H	12,00
4	$\phi'_{cs,ps}$	20,00	$\phi'_{cs,ps}$	25,00	$\phi'_{cs,ps}$	30,00	$\phi'_{cs,ps}$	35,00
5	x (m)	y (m)						
6	Eq. (6-12)		Eq. (6-12)		Eq. (6-12)		Eq. (6-12)	
7	0,000	0,000	0,000	0,000	0,000	0,000	0,000	0,000
8	0,852	0,364	0,665	0,364	0,537	0,364	0,443	0,364
9	1,502	0,727	1,172	0,727	0,947	0,727	0,781	0,727
10	2,027	1,091	1,582	1,091	1,278	1,091	1,053	1,091
11	2,467	1,455	1,926	1,455	1,555	1,455	1,282	1,455
12	2,847	1,818	2,222	1,818	1,795	1,818	1,480	1,818
13	3,180	2,182	2,482	2,182	2,005	2,182	1,653	2,182
14	3,477	2,545	2,714	2,545	2,192	2,545	1,808	2,545
15	3,746	2,909	2,924	2,909	2,361	2,909	1,947	2,909
16	3,990	3,273	3,114	3,273	2,515	3,273	2,074	3,273
17	4,214	3,636	3,290	3,636	2,657	3,636	2,191	3,636
18	4,422	4,000	3,451	4,000	2,788	4,000	2,299	4,000
19	4,615	4,364	3,602	4,364	2,909	4,364	2,399	4,364
20	4,795	4,727	3,743	4,727	3,023	4,727	2,492	4,727
21	4,964	5,091	3,875	5,091	3,129	5,091	2,580	5,091
22	5,123	5,455	3,999	5,455	3,230	5,455	2,663	5,455
23	5,274	5,818	4,117	5,818	3,325	5,818	2,741	5,818
24	5,417	6,182	4,228	6,182	3,415	6,182	2,816	6,182
25	5,553	6,545	4,334	6,545	3,500	6,545	2,886	6,545
26	5,682	6,909	4,435	6,909	3,582	6,909	2,953	6,909
27	5,805	7,273	4,531	7,273	3,660	7,273	3,018	7,273
28	5,924	7,636	4,624	7,636	3,734	7,636	3,079	7,636
29	6,037	8,000	4,712	8,000	3,806	8,000	3,138	8,000
30	6,146	8,364	4,797	8,364	3,874	8,364	3,195	8,364
31	6,250	8,727	4,879	8,727	3,940	8,727	3,249	8,727
32	6,351	9,091	4,957	9,091	4,004	9,091	3,301	9,091
33	6,448	9,455	5,033	9,455	4,065	9,455	3,352	9,455
34	6,542	9,818	5,107	9,818	4,124	9,818	3,401	9,818
35	6,633	10,182	5,177	10,182	4,182	10,182	3,448	10,182
36	6,721	10,545	5,246	10,545	4,237	10,545	3,494	10,545
37	6,806	10,909	5,313	10,909	4,291	10,909	3,538	10,909
38	6,889	11,273	5,377	11,273	4,343	11,273	3,581	11,273
39	6,969	11,636	5,440	11,636	4,393	11,636	3,623	11,636
40	7,047	12,000	5,501	12,000	4,443	12,000	3,663	12,000

	A	B	C	D	E	F	G	H
3	H (m)	0,50						
4	$\phi'_{cs,ps}$ (°)	20,00	$\phi'_{cs,ps}$ (°)	25,00	$\phi'_{cs,ps}$ (°)	30,00	$\phi'_{cs,ps}$ (°)	35,00
5	x (m)	y (m)						
6	Eq. (6-17)		Eq. (6-17)		Eq. (6-17)		Eq. (6-17)	
7	0,000	0,000	0,000	0,000	0,000	0,000	0,000	0,000
8	0,008	0,015	0,011	0,015	0,013	0,015	0,016	0,015
9	0,016	0,030	0,021	0,030	0,026	0,030	0,031	0,030
10	0,024	0,045	0,031	0,045	0,038	0,045	0,047	0,045
11	0,032	0,061	0,041	0,061	0,051	0,061	0,062	0,061
12	0,040	0,076	0,051	0,076	0,063	0,076	0,077	0,076
13	0,048	0,091	0,061	0,091	0,075	0,091	0,091	0,091
14	0,055	0,106	0,071	0,106	0,087	0,106	0,106	0,106
15	0,062	0,121	0,080	0,121	0,099	0,121	0,120	0,121
16	0,070	0,136	0,089	0,136	0,111	0,136	0,134	0,136
17	0,077	0,152	0,099	0,152	0,122	0,152	0,148	0,152
18	0,084	0,167	0,108	0,167	0,133	0,167	0,162	0,167
19	0,091	0,182	0,117	0,182	0,145	0,182	0,175	0,182
20	0,098	0,197	0,126	0,197	0,156	0,197	0,189	0,197
21	0,105	0,212	0,135	0,212	0,167	0,212	0,202	0,212
22	0,112	0,227	0,143	0,227	0,177	0,227	0,215	0,227
23	0,119	0,242	0,152	0,242	0,188	0,242	0,228	0,242
24	0,125	0,258	0,160	0,258	0,198	0,258	0,241	0,258
25	0,132	0,273	0,169	0,273	0,209	0,273	0,253	0,273
26	0,138	0,288	0,177	0,288	0,219	0,288	0,266	0,288
27	0,145	0,303	0,185	0,303	0,229	0,303	0,278	0,303
28	0,151	0,318	0,193	0,318	0,239	0,318	0,290	0,318
29	0,157	0,333	0,201	0,333	0,249	0,333	0,302	0,333
30	0,163	0,348	0,209	0,348	0,259	0,348	0,314	0,348
31	0,169	0,364	0,217	0,364	0,269	0,364	0,326	0,364
32	0,175	0,379	0,225	0,379	0,278	0,379	0,337	0,379
33	0,181	0,394	0,232	0,394	0,288	0,394	0,349	0,394
34	0,187	0,409	0,240	0,409	0,297	0,409	0,360	0,409
35	0,193	0,424	0,247	0,424	0,306	0,424	0,371	0,424
36	0,199	0,439	0,255	0,439	0,315	0,439	0,383	0,439
37	0,205	0,455	0,262	0,455	0,324	0,455	0,394	0,455
38	0,210	0,470	0,269	0,470	0,333	0,470	0,404	0,470
39	0,216	0,485	0,277	0,485	0,342	0,485	0,415	0,485
40	0,221	0,500	0,284	0,500	0,351	0,500	0,426	0,500

Fig. H-1 Spreadsheet screenshot showing the tabulation for the slip-failure surface geometry: (a) active; and (b) passive.

All the formulas within the spreadsheet were properly labelled to correspond with the captions used within present Thesis for each equation, this to facilitate easy connection between the theory and practical applications. From the input parameters wall height H , unit weight of soil γ and the $\phi'_{cs,ps}$ friction, the figure Fig. H-2 shows an instance of calculation for the lateral earth pressure distribution in active and passive conditions. The equation used in the columns “B” to determine $y(m)$ is “=B7+(\$B\$3/33)”, basically the wall height was discretized in 34 points.

	A	B	C	D	E	F
85	$\phi'_{cs,ps}$ (°)	30,00	γ	1,00	H (m)	2,00
86	α_θ (°)	30,00				
87	$\sigma_{H,a}$	y (m)	x (m)	P_a	cumu. P_a	\bar{P}_a Location (xH)
88	Eq. (6-22)		Eq. (6-12)			
89	0,000	0,000	0,000			
90	0,323	0,061	0,102	0,010	0,006	
91	0,575	0,121	0,198	0,027	0,024	
92	0,771	0,182	0,289	0,041	0,050	
93	0,921	0,242	0,376	0,051	0,084	
94	1,034	0,303	0,458	0,059	0,122	
95	1,117	0,364	0,537	0,065	0,164	
96	1,174	0,424	0,613	0,069	0,209	
97	1,210	0,485	0,685	0,072	0,256	
98	1,229	0,545	0,754	0,074	0,304	
99	1,234	0,606	0,821	0,075	0,353	
100	1,226	0,667	0,885	0,075	0,401	
101	1,208	0,727	0,947	0,074	0,449	
102	1,182	0,788	1,006	0,072	0,496	
103	1,148	0,848	1,064	0,071	0,542	0,397
104	1,109	0,909	1,120	0,068	0,586	
105	1,064	0,970	1,174	0,066	0,629	
106	1,015	1,030	1,227	0,063	0,670	
107	0,962	1,091	1,278	0,060	0,708	
108	0,906	1,152	1,327	0,057	0,745	
109	0,848	1,212	1,375	0,053	0,780	
110	0,788	1,273	1,422	0,050	0,812	
111	0,726	1,333	1,468	0,046	0,842	
112	0,663	1,394	1,512	0,042	0,869	
113	0,599	1,455	1,555	0,038	0,894	
114	0,533	1,515	1,598	0,034	0,916	
115	0,468	1,576	1,639	0,030	0,936	
116	0,401	1,636	1,679	0,026	0,953	
117	0,334	1,697	1,718	0,022	0,967	
118	0,268	1,758	1,757	0,018	0,979	
119	0,201	1,818	1,795	0,014	0,988	
120	0,134	1,879	1,831	0,010	0,995	
121	0,067	1,939	1,868	0,006	0,999	
122	0,000	2,000	1,903	0,002	1,000	
123	Resultant horizontal force →			1,542		

	A	B	C	D	E	F
85	$\phi'_{cs,ps}$ (°)	30,00	γ	1,00	H (m)	0,50
86	α_θ (°)	49,11				
87	$\sigma_{H,p}$	y (m)	x (m)	P_p	cumu. P_p	\bar{P}_p Location (xH)
88	Eq. (6-22)		Eq. (6-17)			
89	0,000	0,000	0,000			
90	0,005	0,015	0,013	0,000	0,004	
91	0,010	0,030	0,026	0,000	0,014	
92	0,014	0,045	0,038	0,000	0,031	
93	0,018	0,061	0,051	0,000	0,053	
94	0,022	0,076	0,063	0,000	0,079	
95	0,024	0,091	0,075	0,000	0,110	
96	0,027	0,106	0,087	0,000	0,144	
97	0,029	0,121	0,099	0,000	0,182	
98	0,031	0,136	0,111	0,000	0,222	
99	0,032	0,152	0,122	0,000	0,264	
100	0,033	0,167	0,133	0,000	0,307	
101	0,034	0,182	0,145	0,001	0,352	
102	0,034	0,197	0,156	0,001	0,397	
103	0,034	0,212	0,167	0,001	0,443	
104	0,034	0,227	0,177	0,001	0,489	
105	0,034	0,242	0,188	0,001	0,535	0,462
106	0,033	0,258	0,198	0,001	0,579	
107	0,032	0,273	0,209	0,000	0,623	
108	0,031	0,288	0,219	0,000	0,666	
109	0,030	0,303	0,229	0,000	0,707	
110	0,029	0,318	0,239	0,000	0,746	
111	0,027	0,333	0,249	0,000	0,783	
112	0,025	0,348	0,259	0,000	0,818	
113	0,023	0,364	0,269	0,000	0,850	
114	0,021	0,379	0,278	0,000	0,880	
115	0,019	0,394	0,288	0,000	0,907	
116	0,017	0,409	0,297	0,000	0,931	
117	0,014	0,424	0,306	0,000	0,951	
118	0,012	0,439	0,315	0,000	0,969	
119	0,009	0,455	0,324	0,000	0,982	
120	0,006	0,470	0,333	0,000	0,992	
121	0,003	0,485	0,342	0,000	0,998	
122	0,000	0,500	0,351	0,000	1,000	
123	Resultant horizontal force →			0,011		

Fig. H-2 Spreadsheet screenshot showing the tabulation for lateral earth pressure distribution: (a) active; and (b) passive.

The equation used to the determine the resultant lateral force at each height as indicated in Fig. H-2 is “=((A90+A89)/2)*(B90-B89)” which at the end was totalized at the row “123” by means of

the equation “=SUM(D90:D122)”. The column labeled as “*cumu. Pa*” contains the relative cumulative lateral force applied from the wall base and each row as given by the equation “=SUM(\$D\$89:D90)/SUM(\$D\$89:\$D\$122)”. Finally, the location of the resultant lateral force was found in the column “F” by the algorithm:

```
“=IF.ERROR(IF(AND(E89<0,5;E90>0,5);B89+((0,5-E89)*((B90-B89)/(E90-E89)));  
"")/$F$85;””
```

Finally, this spreadsheet also contains an additional *Sheet* to present the simulation of the large-scale experiments from (Tzagareli, 1965) used to validate theory presented in the numeral 6.2. The calculations for this case were done by means of the same spreadsheets described before, see figures Fig. H-1 and Fig. H-2.

Appendix I Spreadsheet Implanted with Present CSSM Plane–Strain Numerical Simulation for Granular Cohesionless Soil.

The file “Appendix I Spreadsheet Implanted with Present CSSM Plane–Strain Numerical Simulation for Granular Cohesionless Soil. xlsx” attached to present Thesis contains all the calculations required by present incremental numerical model to simulate CSSM stress–strain paths along with the evolution of other related soil properties as established in present Thesis and as shown in the figure Fig. I-1.

step # i	$(\sigma'_1/\sigma'_3)_{cvpz}$	σ'_1 (kPa)	α_i (°)	α_{0i} (°)	A	u (kPa)	n	e	Dr	K_0	v	ϵ'_1	ϵ_1	ϵ'_3	ϵ_3	ϵ'_v	ϵ_v	ϵ_y
	Eq. (7-4)	$(\sigma'_1/\sigma'_3) \cdot \sigma'_1$	Eq. (7-1)	Eq. (4-9)	Eq. (4-20)	$(\sigma'_1 \cdot \sigma'_3) \cdot A$	Eq. (4-11) to (4-14)	$e = \frac{n}{1-n}$	Eq. (4-23) or (4-26)	Eq. (5-4)	$k_0/(1+k_0)$ Eq. (7-10)	Eq. (7-7) or Eq. (7-8)	CUSUM Eq. (7-6)	$\epsilon'_3 - \epsilon'_1 \cdot v$ Eq. (7-9)	CUSUM	$-(\epsilon'_1 + \epsilon'_3)$ Eq. (7-5)	CUSUM	$(\epsilon_1 - \epsilon_3)$
1	0,0000	0,00	39,6100	34,9622	-0,56	0,00	0,32036	0,47136	78,39%	0,42246	0,29699	0,00000	0,00000	0,00000	0,00000	0,00000	0,00000	0,00000
2	1,3409	40,23	39,6639	34,9880	-0,56	-5,69	0,31983	0,47021	78,59%	0,42206	0,29679	0,00111	0,00111	-0,00033	-0,00033	-0,00078	-0,00078	0,00144
3	2,9278	87,83	39,7178	35,0139	-0,56	-32,21	0,31930	0,46907	78,80%	0,42165	0,29659	0,00111	0,00222	-0,00033	-0,00066	-0,00078	-0,00156	0,00288
4	3,4567	103,70	39,7717	35,0397	-0,56	-41,12	0,31876	0,46792	79,01%	0,42125	0,29639	0,00111	0,00333	-0,00033	-0,00099	-0,00078	-0,00234	0,00432
5	3,7212	111,64	39,8256	35,0655	-0,56	-45,62	0,31823	0,46677	79,21%	0,42085	0,29620	0,00111	0,00444	-0,00033	-0,00132	-0,00078	-0,00312	0,00576
6	3,8799	116,40	39,8795	35,0913	-0,56	-48,36	0,31769	0,46562	79,42%	0,42045	0,29600	0,00111	0,00556	-0,00033	-0,00165	-0,00078	-0,00391	0,00720
7	3,9857	119,57	39,9334	35,1171	-0,56	-50,22	0,31716	0,46446	79,62%	0,42005	0,29580	0,00112	0,00667	-0,00033	-0,00198	-0,00079	-0,00470	0,00865
8	4,0613	121,84	39,9873	35,1429	-0,56	-51,58	0,31662	0,46331	79,83%	0,41964	0,29560	0,00112	0,00779	-0,00033	-0,00231	-0,00079	-0,00548	0,01010
9	4,1179	123,54	40,0412	35,1686	-0,56	-52,62	0,31608	0,46215	80,04%	0,41924	0,29540	0,00112	0,00891	-0,00033	-0,00264	-0,00079	-0,00627	0,01155
10	4,1620	124,86	40,0951	35,1944	-0,56	-53,45	0,31554	0,46100	80,24%	0,41884	0,29520	0,00112	0,01003	-0,00033	-0,00297	-0,00079	-0,00706	0,01301
11	4,1973	125,92	40,1490	35,2201	-0,56	-54,14	0,31499	0,45984	80,45%	0,41844	0,29500	0,00112	0,01116	-0,00033	-0,00330	-0,00079	-0,00786	0,01446

Fig. I-1 Spreadsheet Implanted with Present CSSM Plane–Strain Numerical Simulation for Granular Cohesionless Soil.

All the formulas within the spreadsheet are properly labelled to correspond with the captions used within present Thesis for each equation, this to facilitate easy connection between the theory and practical applications. In addition, the spreadsheet contains instructions to properly identify inputs and outputs (see the code of colors for each type of cell shown in the Fig. G-1) and where to perform numerical solution (i.e., the *Solver* function) to determine implicit values like the $\phi'_{cs,ps}$ from Eq. (4-9). In addition, the spreadsheet contains two additional *Sheets* to calculate the minimum active and passive wall displacement (i.e., Δ_x/H) required to fully mobilize the plane-strain critical state failure in the backfill as it was explained in detail in the numerals 8.5.4 and 8.5.5.